ACTIVE METASURFACE DESIGNS FOR TUNABLE SCATTERING PROPERTIES

A Dissertation Submitted to
the The Graduate School of
İzmir Institute of Technology
in Partial Fulfillment of the Requirements for the Degree of

DOCTOR OF PHILOSOPHY

in Electronics and Communication Engineering

by
Hasan Önder YILMAZ

November 2024
İZMİR

We approve the thesis of **Hasan Önder YILMAZ**

Examining Committee Members:

Prof. Dr. Mustafa Aziz Altınkaya
Department of Electrical and Electronics Engineering, İzmir Institute of Technology

Prof. Dr. Mehmet Salih Dinleyici
Department of Electrical and Electronics Engineering, İzmir Institute of Technology

Assoc. Prof. Dr. Avni Aksoy
Institute of Accelerator Technologies, Ankara University

Prof. Dr. Alp Kuştepeli
Department of Electrical and Electronics Engineering, İzmir Institute of Technology

Prof. Dr. Emine Yeşim Zoral
Department of Electrical and Electronics Engineering, Dokuz Eylül University

8 November 2024

Prof. Dr. Mustafa Aziz Altınkaya
Supervisor
Dept. of Electrical and Electronics Eng.
İzmir Institute of Technology

Assoc. Prof. Dr. Fatih Yaman
Co-Supervisor
Dept. of Electrical and Electronics Eng.
İzmir Institute of Technology
ASTeC, UKRI-STFC Daresbury Lab.

Prof. Dr. Mustafa Aziz Altınkaya
Head of the Department of
Electrical and Electronics Engineering

Prof. Dr. Mehtap Eanes
Dean of The Graduate School

ACKNOWLEDGMENTS

First and foremost, I extend my sincere gratitude to my supervisor, Assoc. Prof. Dr. Fatih Yaman, for his expert guidance, mentorship, and support throughout this research journey. I am deeply thankful for his dedication and encouragement, which have consistently motivated me in my academic endeavors.

I would like to express my sincere gratitude to our department's current chair, Prof. Dr. Mustafa Altınkaya, for accepting my supervision solely to carry out the bureaucratic procedures of the graduate institute.

I am grateful to my thesis monitoring committee members, Prof. Dr. Mehmet Salih Dinleyici and Assoc. Prof. Dr. Avni Aksoy, for their valuable feedback, contributions, and suggestions, as well as their critical reviews of my research. I also appreciate the contributions of the other thesis defense jury members, Prof. Dr. Alp Kuştepeli and Prof. Dr. Emine Yeşim Zoral, whose expertise and insights have significantly enhanced the quality and rigor of this thesis.

I wish to express my deepest gratitude to my colleagues and close friends who have supported and contributed to completing my Ph.D. thesis. Special thanks go to my friend, Ceren Özkal, for her motivational talks and unwavering support and patience throughout my Ph.D. journey. Additionally, I extend heartfelt thanks to my former roommate, Çağın Ekici, for his continuous encouragement and valuable wisdom whenever I needed it. I am also grateful to my close friends Dr. Oğuzhan Takıcak, Dr. Enes Ataç, Fatih Onay, Dr. Bilal Orkan Olcay, Mehmet Sergen Çatal, Mehmet Çalı, Dr. Esra Tunçer Çalı, Barış Yazar, Metin Sağık, İrem Cumalı, and Mert İlgüy as well as all my colleagues, for their support, valuable discussions, and shared experiences. Their guidance and encouragement have been truly invaluable.

The experimental aspect of this thesis was supported by the Scientific and Technological Research Council of Türkiye (TUBİTAK) under Grant 123E112.

Finally, I extend my deepest gratitude and love to my beloved family, Halime and Hüseyin Yılmaz, for their unwavering love and unconditional support throughout the years. Their strength and presence have been my pillars, and I am profoundly grateful for their constant support in my life.

ABSTRACT

ACTIVE METASURFACE DESIGNS FOR TUNABLE SCATTERING PROPERTIES

Advancing technologies require artificially designed dynamic surfaces with capabilities beyond the natural ones to control electromagnetic wave scattering and properties for complex applications. This thesis presents a novel method for dynamic control of propagating waves through surface waves and its implementation to nonreciprocal transmission and reconfigurable radiation problems. This study contributes to the literature by proposing a design methodology for the analytical model based on phase-conjugate surfaces and bianisotropy, and its three-dimensional (3D) realization model in the microwave domain involving the metasurface concept based on the double-negative index medium. It begins with analytical solutions supported by numerical simulations, and proceeds with the designs and simulation results of passive and dynamic 3D models. Impedance-based characterization is applied to both time-invariant and time-variant unit cell models. It is followed by developing and constructing the time-domain-based equivalent circuit via the retrieved impedances, which are employed in the numerical solution of the time-modulated unit cell. For nonreciprocal transmission, a novel method was introduced based on time modulation, which is applied to the generated anti-symmetric surface waves on bianisotropic metasurfaces, depending on the excitation direction. This method is demonstrated on the penetrable unit cell bounded by a surface cavity incorporating a variable capacitor. Numerical simulation results show both phase-coherent and phase-incoherent nonreciprocal transmission via time modulation, which is supported by consistent experimental results. The final chapter explores wavefront manipulation through phase variations on unit cells of the metasurface by using surface waves for reconfigurable radiation applications. Specifically, it focuses on steering the radiated beam from the metasurface, fed by a horn antenna. A novel 3D model based on the proposed method is introduced, offering a simplified control scheme with variable capacitors placed on etched slits, which electrically separate columns. A numerical eigenmode analysis is conducted to examine the excited surface modes under periodic boundary conditions, followed by simulations of its integration with a horn antenna for beam-steering applications. The results from both simulations and proof-of-concept experiments demonstrate the steering of the radiated beam.

ÖZET

AYARLANABİLİR SAÇILMA ÖZELLİKLERİ İÇİN AKTİF METAYÜZEY TASARIMLARI

Gelişen teknolojiler, elektromanyetik dalgaların saçılmasını ve özelliklerini kontrol etmek için, doğal yapıların ötesinde özelliklere sahip yapay olarak tasarlanmış dinamik yüzeylere ihtiyaç duymaktadır. Bu tez, geçirgen bir metayüzey üzerinde oluşturulan yüzey dalgaları aracılığıyla yayılan dalgaların dinamik kontrolü için yeni bir yöntem önererek, bunun karşıt olmayan iletim ve yeniden yapılandırılabilir radyasyon problemlerine uygulanmasını içermektedir. Bu çalışma, faz eşlenik yüzeyler ve bianizotropiye dayalı analitik model için bir tasarım metodolojisi ve çift negatif indeks ortamına dayalı metayüzey kavramını içeren mikrodalga alanındaki üç boyutlu gerçekleştirme modeli önererek literatüre katkıda bulunmaktadır. Tez, ilk olarak sayısal simülasyonlarla desteklenen analitik çözümleri ve ardından pasif ve dinamik üç boyutlu modellerin tasarımları ve simülasyon sonuçlarını sunmaktadır. Empedans tabanlı karakterizasyon hem zaman bağımlı ve hem de zaman bağımsız birim hücre modelleri için uygulanmaktadır. Bunu, elde edilen empedanslar aracılığıyla zamana dayalı eşdeğer devrenin geliştirilmesi ve oluşturulması izlemektedir. Geliştirilen bu eşdeğer devre, zaman modülasyonlu birim hücrenin sayısal çözümünde kullanılmaktadır. Karşıt olmayan iletim için, uyarım yönüne bağlı olarak bianizotropik metayüzey üzerinde üretilen antisimetrik yüzey dalgalarına uygulanan zaman modülasyonuna dayalı yeni bir yöntem önerilmiştir. Bu yöntemin uygulanabilirliği, değişken bir kapasitör içeren bir yüzey kavitesi ile sınırlanmış geçirgen birim hücre üzerinde gösterilmiştir. Sayısal simülasyon sonuçları zaman modülasyonu yoluyla hem faz uyumlu hem de faz uyumsuz karşıt olmayan iletimi göstermektedir ve bunlar tutarlı deney sonuçlarıyla desteklenmektedir. Son bölümde, yeniden yapılandırılabilir radyasyon uygulamaları için yüzey dalgalarını kullanarak metayüzeyin birim hücrelerindeki faz değişimleri yoluyla dalga cephesi manipülasyonu araştırılmaktadır. Özel olarak, bir korna anten tarafından beslenen metayüzeyden yayılan hüzmenin açısal yönlendirilmesine odaklanılmaktadır. Önerdiğimiz yönteme dayalı yeni bir 3B tasarım modeli tanıtılmaktadır. Bu tasarım ile, kolonları elektriksel olarak ayıran kazınmış yarıklara yerleştirilmiş değişken kapasitörler ile basitleştirilmiş bir kontrol şeması önerilmektedir. Periyodik sınır koşulları altında uyarılmış yüzey modlarını incelemek için numerik özdeğer analizleri, ve ardından hüzme yönlendirme uygulaması için korna antenle entegrasyonunun simülasyonları gerçekleştirilmiştir. Simülasyonlardan ve kavram kanıtı deneylerinden elde edilen sonuçlar yayılan hüzmenin yönlendirilmesini göstermektedir.

To my lovely family and
the memory of my beloved brother, Öncül YILMAZ

TABLE OF CONTENTS

LIST OF FIGURES

LIST OF TABLES

LIST OF ABBREVIATIONS

EM	Electromagnetic
RF	Radio Frequency
MW	Microwave
TL	Transmission Line
DNG	Double Negative
DPS	Double Positive
LHM	Left Handed Medium
RHM	Right Handed Medium
ENG	Epsilon Negative
MNG	Mu Negative
NZI	Near-Zero Index
TE	Transerve Electric
TM	Transerve Magnetic
TEM	Transerve Electromagnetic
ITMM	Impedance Transfer Matrix Method
HB	Harmonic Balance
FSS	Frequency Selective Surface
HIS	High Impedance Surface
GSTCs	Generalized Sheet Transition Conditions
PEC	Perfect Electric Conductor
PMC	Perfect Magnetic Conductor
PML	Perfect Match Layer
IBC	Impedance Boundary Condition
UBC	Unit Cell Boundary Condition
SIW	Substrate Integrated Waveguide
CPW	Co-Planar Waveguide
SMA	Sub-Miniature version A
VNA	Vector Network Analyzer
RA	Reflectarray
TA	Transmitarray

CHAPTER 1

INTRODUCTION

Electromagnetic (EM) waves are fundamental to modern technologies, from RF and microwave to far-optic regions, particularly in communication systems and remote energy-based applications. Reshaping free-space waves after being emitted from antennas or light sources is crucial in developing these technologies. This allows the achievement of desired wave properties, such as wavefront, direction, polarization, intensity, frequency, and reflectivity/transmissivity. Advances in material science and EM engineering now enable precise and sophisticated wave shaping using natural and artificial materials, which are often designed with thicknesses much smaller than the wavelength, classified as surface.

Throughout history, the initial examples of structures based on natural materials are for light waves, as predictable—the earliest documented example dates back to the 5th century BCE. The Aristophanes' Lens is a famous example of such a transmissive optical device for focusing or dispersing light beams through the principle of refraction (Hickie, 2023). Following significant advancements in analytical wave theory, further developments included Huygens' Eyepiece and Fresnel's compact lens, which were constructed using concentric annular sections during the 17th and 18th centuries (Pietrow, 2023; Boutry, 1948). During the 19th and 20th centuries, developments extended beyond light collimation, including controllable polarization and frequency filtering (Shurcliff, 1962). After J. C. Maxwell introduced his renowned equations in 1865 that demonstrated light is an EM wave, J.C. Bose 1894 presented one of the earliest microwave lenses, which enhanced antenna directivity (Bose, 1897). This was soon followed by Marconi's development of polarization reflectors in the 1910s (Achouri and Caloz, 2021). Significant progress in this field occurred in tandem with the advancement of radar technology during World War II, extending into the 1950s and 1960s. The developments grew new systems and technologies, such as a Fresnel zone plate reflector commonly employed in radio transmitters and operating on the Fresnel lens principle (Buskirk and Hendrix, 1961). Subsequently, frequency selective surfaces (FSS) and reflectarrays/transmitarrays (RA and TA) emerged as new technologies. FSS has been utilized as microwave frequency filters (Munk, 2000), while RAs and TAs, composed of microstrip patch arrays, replicate the function of traditional parabolic reflectors (B. H. Fong and Sievenpiper, 2010; Mc-

Grath, 1986; Kahrilas, 1968). Beyond space-to-space wave converters, early examples like near-field plates (Anthony Grbic and Merlin, 2008) and impedance surfaces (D. Berry and Kennedy, 2010) demonstrated the conversion between free-space and surface waves. While some of these structures relied solely on natural materials for their wave conversion properties through geometry or layering, others represented the first passive microwave surfaces based on artificial media.

In recent decades, research in artificial EM materials (or structures) has expanded significantly due to the limitations of natural constituent capabilities. They are utilized to precisely control the wave propagation and scattering (reflection, transmission, absorption) in progress as well as other wave properties. Designing these structures to be multi-functional, cost-effective, and readily producible are among the engineering challenges critical for future technologies. Artificial EM surfaces are typically constructed by engineering the geometries and compositions of ordinary medium. They generally consist of periodic or gradient arrays of electrically small (subwavelength) unit cells. The concept of manipulating EM wave propagation through thin artificial structures has been explored for over a century. An early example, introduced by Lamb in the late 19th century, investigated the scattering behavior of a metallic strip array (Lamb, 1897). In the literature, these structures are referred to by various names depending on the research area and the wavelength-to-unit-cell size ratio. Common examples include diffraction gratings, FSS, high impedance surfaces (HIS) (Sievenpiper, 1999), Huygens surfaces, and metasurfaces (A. Li and Sievenpiper, 2018).

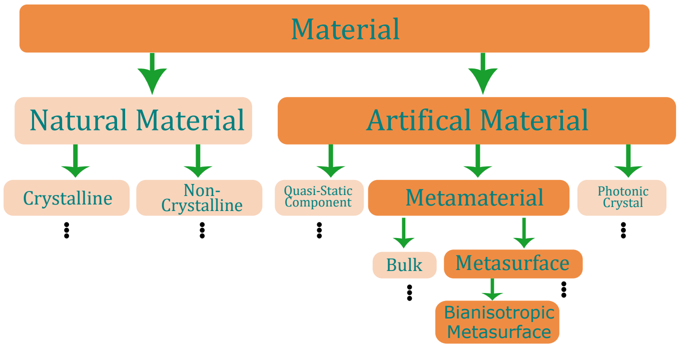

Figure 1.1. General chart of the EM material research in today (Albooyeh, 2015).

While some classifications overlap, the term ’metasurface’ is now commonly used for homogenizable, electrically thin surfaces with outstanding properties, representing the two-dimensional counterpart of metamaterials. The prefix ’meta’ signifies a departure from traditional terminology, as metamaterials exhibit EM responses beyond those of conventional materials. Figure 1.1 illustrates a classification chart of EM materials. Further, dynamic structures can be designed to address complex microwave and optical engineering challenges by introducing new dimensions to the effective parameters. However, designing dynamic artificial structures presents the challenge of systematically generalizing analytical expressions to control and determine their effective medium properties.

1.1. Homogenization and Effective Medium Parameters

The homogenization approach helps analyze and design particular complex structures by effective constitutive parameters, enabling unique properties which cannot be found in natural materials. This method defines averaged macroscopic quantities by representing the effective parameters of periodic or random collections of molecules or unit cell scatterers, such as split-ring resonators (Smith and Pendry, 2011). It allows for determining the effective electric and magnetic responses of artificial structures on a macro scale, thereby facilitating wave interaction calculations using effective medium parameters (ϵ_{eff} and μ_{eff}) and eliminating the need to analyze each individual in microscale. The homogenization is an analytical approach and it effectively defines a continuous artificial medium made from subwavelength-sized unit cells with subwavelength periods. The accuracy depends on factors such as medium continuity at boundaries, the type of inclusions (resonant or non-resonant), and spatial dispersion. Classical mixing methods, like Clausius–Mossotti and Maxwell–Garnett formulas, are limited to specific geometries and structures (Smith and Pendry, 2006). They may become inaccurate for metamaterials with conductive, resonant elements, especially when periodicity approaches the free-space wavelength. Improved techniques, such as quasi-static and dynamic field averaging, are proposed for such cases (Simovski, 2018). J. B. Pendry and D. R. Smith have proposed a field averaging technique called by their names for acquiring the effective medium response of metamaterials (Smith and Pendry, 2006). They use the averaged electric (E and D) and magnetic (H and B) field and fluxes or medium impedance (z) and refractive index (n) from the subwavelength unit cube illustrated in Figure 1.2. Effective permittivity (ϵ) and permeability (μ) can be calculated using constitutive relations, either between fluxes and fields or impedance and refractive index.

The averaging of field $\vec{F}^{true}$ over the volume $V = d^3$ centered at the observation point $\vec{R}_i$ is given by

$$\vec{F}(\vec{R}_i) = \frac{1}{V}\int_V \vec{F}^{true}(\vec{R}')dV, \tag{1.1}$$

where the $true$ refers to the microscopic field and $(kd) << 1$, where k is the wave number, and d is the periodicity of the point dipoles, it means that $d << \frac{\lambda}{2\pi}$. It is called quasi-static averaging or Ewald's definition of the mean field (Simovski, 2018).

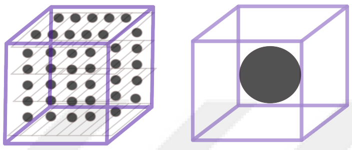

Figure 1.2. Equivalent homogenization models according to field averaging technique (Smith and Pendry, 2006).

The averaged electric field and flux density over length (L_x) and surface are (A_x) defined by

$$\langle E_x\rangle_L = \frac{1}{L_x}\int_{L_x} \vec{E}(\vec{r})\cdot d\vec{s} \qquad \text{and} \qquad \langle D_x\rangle_A = \frac{1}{A_x}\int_{A_x} \vec{D}(\vec{r})\cdot d\vec{A}, \tag{1.2}$$

where $\langle\ \rangle$ refers to the mean of the field. $\vec{D}(C/m^2)$ is the electric displacement vector and $\vec{E}(V/m)$ is the electric field vector. The effective permittivity for the related principle axis can be expressed as

$$\epsilon_x = \frac{\langle D_x\rangle_A}{\langle E_x\rangle_L}. \tag{1.3}$$

For discrete numerical analysis of a two dimensional (2D) surface (e.g., normal to $\hat{z}$), the average scalar electric and magnetic fields can be expressed as

$$E_x^{ave} = \frac{1}{N_x \times N_y}\sum_{N_x}\sum_{N_y} E_x^{true}(x, y). \tag{1.4}$$

The accuracy of the averaged fields technique depends on the unit cell dimensions (s_x

and s_y, with $s_{x,y} \leq \lambda/2$), periodicity d ($kd << 1$), and the number of discrete points (N_x and N_y). The first two are related to the unit cell design, while the third depends on the resolution of numerical simulations, such as mesh density and data point evaluation.

An alternative method for determining effective parameters uses reflection and transmission coefficients. This approach calculates the complex coefficients for a unit cell and compares them with analytical formulas for a homogeneous slab of the same thickness. Applicable to simulated and measured S-parameter data, this technique allows practical measurement of the medium's scattering response. While straightforward, it may lack deeper insights into artificial materials, as the coefficients analyzed in S-parameter data do not always align with analytical homogenization theories based on local-field and current distributions. The impedance and phase terms are calculated as outlined by (Lubkowski, 2009; Önder Yılmaz and Yaman, 2022)

$$z_{eff} = \pm\sqrt{\frac{(1+S_{11})^2 - S_{21}^2}{(1-S_{11})^2 - S_{21}^2}} \qquad \text{and} \qquad e^{jnk_0d} = X \pm j\sqrt{1-X^2}, \tag{1.5}$$

where

$$X = \frac{1}{2S_{21}(1 - S_{11}^2 + S_{21}^2)}. \tag{1.6}$$

1.2. Metamaterial Concept and Metasurfaces

Metamaterials are engineered structures inspired by atomic arrangements to obtain desired macroscopic electric and/or magnetic properties. These structures consist of periodic or gradual arrangements of inclusions, known as 'meta-atoms' or 'unit cells'. The unit cell size and period must be subwavelength, typically $\leq \lambda_0/2$ (Achouri and Caloz, 2021). It is often designed smaller than $\lambda_0/10$ to minimize spatial dispersion. Studies span metamaterials, metasurfaces (electrically thin 2D counterparts), and meta-atoms (unit cells) and include across frequencies from microwave to optical. Each frequency range requires specific design methods influenced by factors such as electrical surface currents and the influence of magnetic fields. Material properties and fabrication complexity present additional challenges, especially at nanometer wavelengths. In the microwave region, unit cells typically consist of metallic inclusions within a dielectric host.

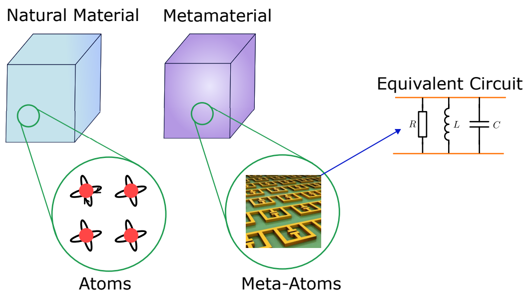

Figure 1.3. Illustration of analogy between natural material with atomic structures and metamaterial with meta-atoms (Vardaxoglou, 2017).

Figure 1.3 illustrates the analogy between natural material and meta-atoms in metamaterials. Although V. G. Veselago outlined the theoretical foundations of the left-handed metamaterial in the 1960s (Veselago, 1968), their physical realization did not emerge until the late 1990s and early 2000s (J. B. Pendry and Youngs, 1996; J. B. Pendry and Stewart, 1999; D. R. Smith and Schultz, 2000). Indeed, early examples date back before, with chiral (Bose, 1898), dielectric (Lindman, 1920), and magnetic materials (Schelkunoff and Friis, 1952) introduced in the 1890s, 1910s, and 1940s, respectively.

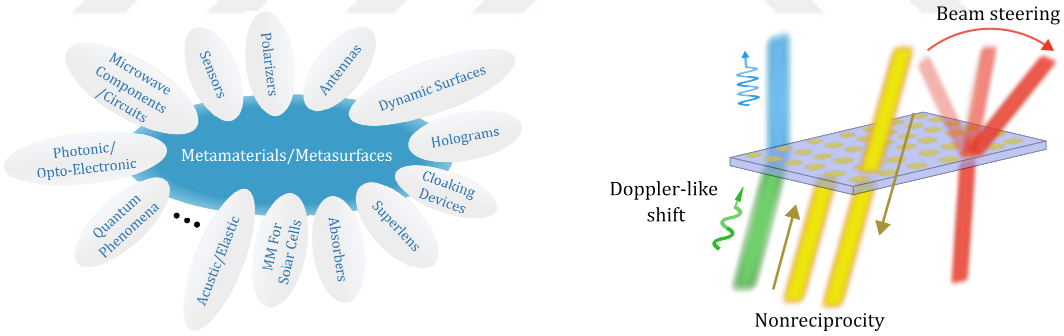

(a) (b)

Figure 1.4. Example applications of (a) metamaterial concepts for today and future directions, (b) today's research on time-varying metasurfaces (Shaltout et al., 2019).

Initial research focused on passive, time-invariant structures, but since the early 2010s, interest has shifted to dynamic, time-varying designs. Dynamic control enhances flexibility and introduces new variables into modeling. Simultaneously, electrically thin metasurfaces have gained attention due to their ease of production and the demands of modern communication technologies. Current research primarily focuses on Huygens' surfaces, hyperbolic, gradient, and bianisotropic metasurfaces, as well as their time-varying and nonlinear variations. Figure 1.4a outlines current and future engineering applications and academic research directions. Figure 1.4b highlights specific dynamic metasurface applications, such as nonreciprocity and beam steering, which are the application objectives of the thesis. A comprehensive classification of metamaterial and metasurface concepts is crucial for developing a theoretical framework. Figure 1.5 provides an overview of these classifications.

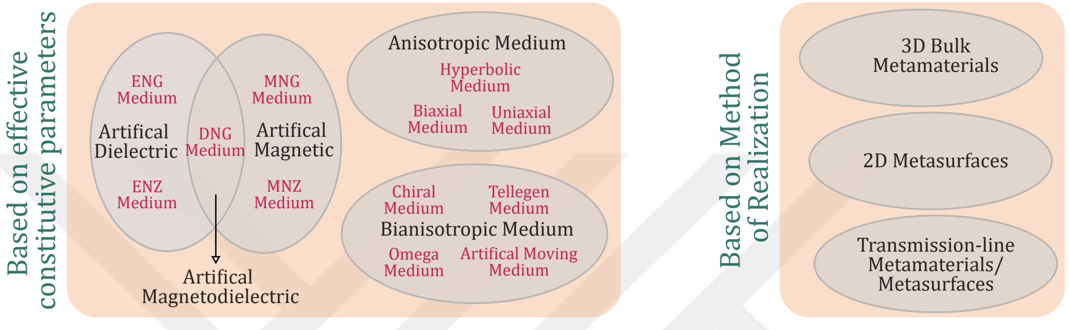

(a) (b)

Figure 1.5. Types of classifications for metamaterial concept: based on (a) effective parameters, (b) method of realization (Vehmas, 2015). ENG, MNG, ENZ, and MNZ are electric and magnetic negative, and near-zero abbreviations, respectively.

1.3. Spatial Dispersion and Bianisotropy

Metamaterials, like crystals, are inevitably anisotropic unless unit cells are randomly mixed, as their response depends on the direction of the excitation field (Sihvola, 2007; Önder Yılmaz and Yaman, 2022). In anisotropic media, permittivity ($\bar{\bar{\epsilon}}$) and permeability ($\bar{\bar{\mu}}$) are represented as 3 × 3 tensors (Balanis, 1989). The constitutive relation and corresponding tensors are given as follows

$$\vec{D} = \bar{\bar{\epsilon}}\vec{E} \qquad \text{and} \qquad \vec{B} = \bar{\bar{\mu}}\vec{H}, \tag{1.7}$$

$$\bar{\bar{\epsilon}} = \begin{bmatrix} \epsilon_{xx} & \epsilon_{xy} & \epsilon_{xz} \\ \epsilon_{yx} & \epsilon_{yy} & \epsilon_{yz} \\ \epsilon_{zx} & \epsilon_{zy} & \epsilon_{zz} \end{bmatrix} \qquad \text{and} \qquad \bar{\bar{\mu}} = \begin{bmatrix} \mu_{xx} & \mu_{xy} & \mu_{xz} \\ \mu_{yx} & \mu_{yy} & \mu_{yz} \\ \mu_{zx} & \mu_{zy} & \mu_{zz} \end{bmatrix}. \tag{1.8}$$

A medium can exhibit both electrical and magnetic anisotropy. Expanding Equation 1.7 for a general medium with both electric and magnetic polarizations, the macroscopic constitutive relation is expressed as

$$\begin{aligned} \vec{D} &= \epsilon_0 \vec{E} + \vec{P}, \\ \vec{B} &= \mu_0(\vec{H} + \vec{M}), \end{aligned} \tag{1.9}$$

where $\vec{D}(C/m^2)$ and $\vec{B}(Wb/m^2)$ are, respectively, the electric displacement vector and the magnetic flux density vector, $\vec{E}(V/m)$ and $\vec{H}(A/m)$ are, respectively, electric field vector and the magnetic field vector. $\vec{P}(C/m^2)$ and $\vec{M}(A/m)$ are, respectively, the electric polarization density vector and the magnetic polarization density vector. ϵ_0 and μ_0 are permittivity and permeability of the vacuum, respectively.

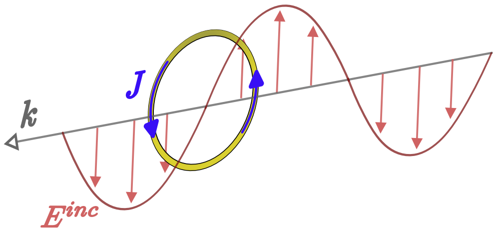

Figure 1.6. An illustrated example of spatial dispersion effect by a loop of metal wire illuminated by a plane wave (Asadchy, 2017).

The metamaterial concept is closely linked to spatial dispersion. When the unit cell's inclusion size and periodicity approach the wavelength, the structure's polarization responses become non-local and cannot be fully described by effective permittivity and permeability. For instance, if the wavelength equals the double loop diameter as in Figure 1.6, the electric fields at opposite sides oscillate out of phase, it will generate circulating currents and magnetic polarization. In contrast, if the wavelength is much larger, the electric field is uniform across the loop, and spatial dispersion can be ignored

(A. Serdyukov and Sihvola, 2001; Asadchy, 2017). In this case, the local electric field cannot independently induce a dipole moment; the entire field within the inclusion is required. Understanding spatial dispersion, including the electric field and its spatial derivatives, is essential to studying bianisotropy. We now review the literature to investigate spatial dispersion and its relation with bianisotropy (Asadchy, 2017). Taylor's series expansion of the electric field at the center ($\vec{r}_0$) is given by

$$\vec{E}(\vec{r}+\vec{r}_0) = \vec{E}(\vec{r}_0) + \nabla_j \vec{E}(\vec{r}_0) r_j + \frac{1}{2}\nabla_j \nabla_k \vec{E}(\vec{r}_0) r_j r_k + \dots \tag{1.10}$$

where ∇_j represents the spatial derivative with respect to r_j. If the local field at $\vec{r}_0$ throughout the scatterer can be approximated such as with a plane wave incident, the second and higher-order terms are of the order of $(a/\lambda)\vec{E}(\vec{r}_0)$, $(a/\lambda)^2\vec{E}(\vec{r}_0), \dots)$. For the nonmagnetic material, the relation between $\vec{P}$ (or $\vec{D}$) and $\vec{E}$ is non-local. The expressions of electric displacement and magnetic field for spatially dispersive anisotropic medium under monochromatic excitation are given respectively as

$$D_i = (\epsilon_0 \delta_{ij} + \chi_{ij})E_j + \chi_{ijk}(\nabla_k E_j) + \chi_{ijkl}(\nabla_l \nabla_k E_j) + \dots, \tag{1.11}$$

and

$$H_i = \frac{1}{\mu_0} B_i, \tag{1.12}$$

where i is the Cartesian coordinates, δ_{ij} is the Kronecker delta, χ_{ij}, χ_{ijk}, and χ_{ijkl} are the susceptibility tensors. When the first two terms cannot be neglected, it indicates first-order spatial dispersion. In this case, the relation can be described by called bianisotropic constitutive relations and expressed as

$$\begin{aligned} \vec{D} &= \bar{\bar{\epsilon}}.\vec{E} - j\bar{\bar{\xi}}.\vec{B}, \\ \vec{H} &= \frac{1}{\mu_0}\vec{B} - j\bar{\bar{\xi}}^T.\vec{E}, \end{aligned} \tag{1.13}$$

where $\bar{\bar{\epsilon}}$ and $\bar{\bar{\xi}}$ represent the permittivity and reciprocal coupling tensors for bianisotropic medium, respectively. In first-order spatial dispersion, electric polarization is not directly induced by the magnetic field $\vec{B}$; rather, it arises from the circulating electric field.

While second-order spatial dispersion is weaker than first-order, it can dominate in certain engineered inclusions, such as the double split-ring resonator. Considering only the first two derivatives and assuming the medium is isotropic, the constitutive relation is given by

$$\begin{aligned} \vec{D} &= \epsilon \vec{E} - j\xi \vec{B} + \beta \nabla\nabla . \vec{E}, \\ \vec{H} &= \frac{1-\omega^2\mu_0\gamma}{\mu_0}\vec{B} - j\xi\vec{E}. \end{aligned} \tag{1.14}$$

Here, ϵ, ξ, β, and γ are scalar parameters determining the strength of the polarization effects. The second-order derivative terms are $\beta\nabla\nabla\cdot\vec{E}$, representing electric quadrupole polarization, which is very weak and thus neglected, and $\{(1-\omega^2\mu_0\gamma)/\mu_0\}\,\vec{B}$, corresponding to magnetic dipole moments that create artificial magnetic materials. For isotropic materials with negligible quadrupole polarization, considering only second-order spatial dispersion and artificial magnetism, the constitutive relation simplifies to

$$\begin{aligned} \vec{D} &= \epsilon_s . \vec{E} - j\sqrt{\epsilon_0\mu_0}\kappa\vec{H}, \\ \vec{B} &= \mu\vec{H} + j\sqrt{\epsilon_0\mu_0}\kappa\vec{E}, \end{aligned} \tag{1.15}$$

where $\epsilon_s = \epsilon + \mu\xi^2$ ($_s$ denotes spatial dispersion), $\mu = \mu_0/(1-\omega^2\mu_0\gamma)$, and $\kappa = \xi\mu/\sqrt{\epsilon_0\mu_0}$ is the chirality parameter. First-and second-order spatial dispersion, also called weak spatial dispersion, occurs when electromagnetic (or magnetoelectric) coupling coefficients are weaker than the local polarization response. The general expression for a bianisotropic medium is given by

$$\begin{aligned} \vec{D} &= \bar{\bar{\epsilon}}.\vec{E} + \bar{\bar{\xi}}.\vec{H}, \\ \vec{B} &= \bar{\bar{\zeta}}.\vec{E} + \bar{\bar{\mu}}.\vec{H}. \end{aligned} \tag{1.16}$$

ξ and ζ are called magnetoelectric (or magneto-optic) and electromagnetic coupling tensors, respectively. In the most general case, these are complex and expressed explicitly as

$$\bar{\bar{\xi}} = \bar{\bar{\nu}} - j\bar{\bar{\kappa}}^T \qquad \text{and} \qquad \bar{\bar{\zeta}} = \bar{\bar{\nu}} + j\bar{\bar{\kappa}}. \tag{1.17}$$

The new dyadics $\bar{\bar{\kappa}}$ and $\bar{\bar{\nu}}$ are related with reciprocal (or nonreciprocal) behavior in bian-isotropic medium. They are respectively expressed by

$$\bar{\bar{\nu}} = \frac{\bar{\bar{\zeta}} + \bar{\bar{\xi}}^T}{2} \qquad \text{and} \qquad \bar{\bar{\kappa}} = \frac{\bar{\bar{\zeta}} - \bar{\bar{\xi}}^T}{2}. \tag{1.18}$$

Four bianisotropic coupling phenomena are classified based on reciprocity/nonreciprocity and symmetry/asymmetry of the coupling dyadic: chiral, omega, Tellegen, and moving medium coupling, as shown in Figure 1.7.

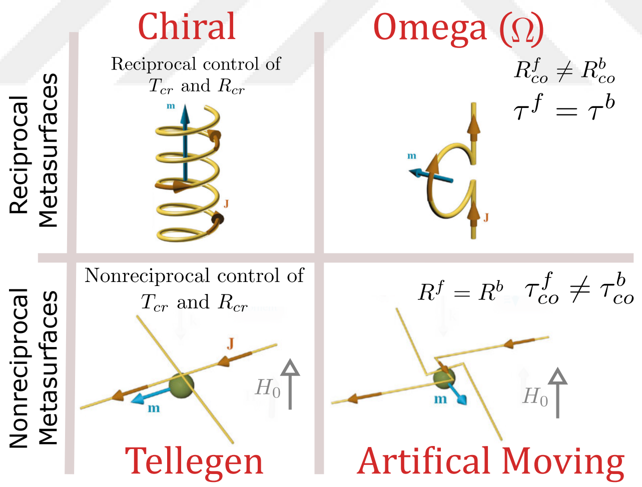

Figure 1.7. Example particles for types of bianisotropic media according to being reciprocal: metal wire loop for chiral particle, and a metal wire for omega (Ω) particle, or nonreciprocal: a metal wire with ferrite particle for Tellegen particle, and metal wire with chirality and ferrite particles for moving medium (Asadchy et al., 2018).

A bianisotropic medium can be classified based on the nonreciprocal coupling dyadic $\bar{\bar{\nu}}$. If $\bar{\bar{\nu}}$ is zero, reciprocal bianisotropic coupling can be either chiral or omega (Ω) type. Chiral coupling occurs when the reciprocal coupling dyadic $\bar{\bar{\kappa}}$ is symmetric

($\bar{\bar{\kappa}} = \bar{\bar{\kappa}}^T$), while omega coupling occurs when $\bar{\bar{\kappa}}$ is anti-symmetric ($\bar{\bar{\kappa}} = -\bar{\bar{\kappa}}^T$). Chirality results from specific geometric structures with mirror-asymmetry causing polarization rotation, while omega media are realized with asymmetric metallic inclusions and directional asymmetry, resulting in direction-dependent asymmetric properties.

By enhanced design flexibility and field transformation capabilities, bianisotropic metasurfaces are suitable for the application goals discussed in this thesis. Their ability to incorporate time-varying features allows for flexible manipulation of wave characteristics, including beam-forming, beam-steering, and control over reflectivity, transmission, absorption, polarization, and phase (Quevedo-Teruel, 2019; Asadchy et al., 2018; Ataloglou et al., 2021; Taravati and Eleftheriades, 2022). In the thesis, we study the bianisotropic metasurface to achieve field transformations and integrate time-varying attributes. As a preliminary work, we numerically and experimentally analyzed the double negative (DNG) index metamaterial slab, examining its anisotropic and bianisotropic properties due to the excitation dependence of its principal axis components (Önder Yılmaz and Yaman, 2022).

1.4. Wave Transformation on Metasurface

Metasurfaces provide comprehensive control over reflection, transmission, and surface waves. The surface wave is transverse waves that propagate along an interface and decay exponentially away from it. A characterization matrix can be used to determine the surface impedance necessary for achieving desired field transformations on both sides.

In the literature, most research has concentrated on impenetrable metasurfaces. They are typically designed to manipulate propagating waves by engineering surface impedances, often within a parallel-plate waveguide configuration, where one wall is a metasurface and the other a perfect conductor. They focus on controlling reflected waves through coupled surface waves by tuning or modulating surface impedance. They are also employed to control leaky wave radiation through direct excitation of surface waves. Recent studies (Tcvetkova et al., 2018; Epstein and Eleftheriades, 2016; Popov et al., 2019; Tcvetkova et al., 2019; V. Popov, 2016) have explored the generation of surface waves under specific conditions. They open routes for controlling both transmission and reflection via surface waves. This thesis proposes replacing the perfect conductor wall with a phase-conjugate surface of the other to create a penetrable surface capable of supporting surface waves. A suitable solution to satisfy these requirements is utilizing bianisotropic constitutive relations based on an impedance model. The initial objective of this thesis is to contribute to the literature by proposing a surface wave-supported penetrable metasurface through analytical and numerical solutions in 2D, as illustrated in Figure 1.8 (Yılmaz and Yaman, 2024).

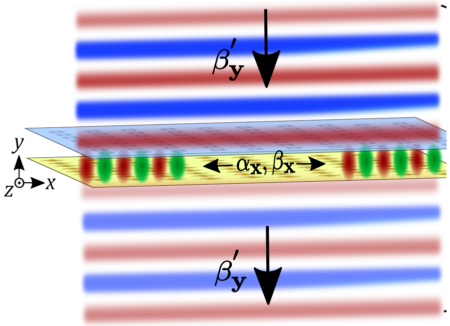

Figure 1.8. Illustration of penetrable metasurface supporting surface wave generation (Yılmaz and Yaman, 2024).

1.4.1. Dynamic Control of Metasurface

While metasurfaces can be designed with various functionalities, their properties remain stationary in real-time operation. Introducing active components into the unit cells (meta-atoms) can enable dynamic field transformation. In the microwave and millimeter-wave spectrum, tunable active components include semiconductors (e.g., diodes, transistors), graphene, vanadium oxide (V_2O_5), liquid crystals, phase-change materials (PCM), micro and nano electro mechanical systems (MEMS/NEMS) (Shao and Zhu, 2021; A. Li and Sievenpiper, 2018).

The main difficulty lies in modeling slow or fast time-varying active components. While slow variations (e.g., with DC) can often be solved using three dimensional (3D) numerical methods, fast time-varying systems (e.g., time modulation) lack ready-to-use 3D simulation techniques. This thesis addresses this by developing numerical solutions using the impedance transfer-matrix method (ITMM) and harmonic balance (HB), which are applied to impedance-based equivalent circuits. We present constructing the equivalent circuit model through the proposed 3D unit cell which converts incident waves into transmission and surface waves manipulated by time-varying components (Yılmaz and Yaman, 2024).

1.5. Electromagnetic Nonreciprocity

Reciprocity is a fundamental principle in various branches of physics for passive systems. In EM, it refers to a principle that states the electrical current at a particular point due to a source at another point is equal to the current at the second point due to the same source placed at the first point. So, nonreciprocity refers to a system that exhibits different transmission ratios depending on the wave propagation direction. It is often referred to as asymmetric transmission, but not all media with asymmetric transmission are nonreciprocal (Kord et al., 2020; V. S. Asadchy and Tretyakov, 2020). Figure 1.9 illustrates nonreciprocal transmission as one-way, which is called isolation.

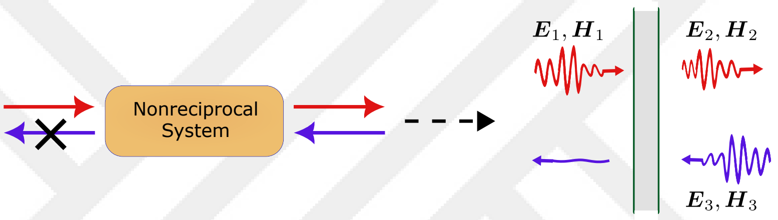

Figure 1.9. Illustration of example nonreciprocal transmission: isolator on system model and surface (Christophe Caloz and Deck-Leger, 2018).

Lorentz analytically expresses the reciprocity theorem by (Balanis, 2005)

$$-\nabla.\left(\vec{E}_1 \times \vec{H}_2 - \vec{E}_2 \times \vec{H}_1\right) = \vec{E}_1.\vec{J}_2 + \vec{H}_2.\vec{M}_1 - \vec{E}_2.\vec{J}_1 - \vec{H}_1.\vec{M}_2, \tag{1.19}$$

where $\vec{E}_{1,2}$ and $\vec{H}_{1,2}$ are the field radiated by the set of current $\vec{J}_{1,2}$ and $\vec{M}_{1,2}$. In other words, a system is nonreciprocal if it is asymmetric under time-reversal, as Maxwell's equations are time-symmetric (Kord et al., 2020; Christophe Caloz and Deck-Leger, 2018). In terms of medium parameters, reciprocity requires $\bar{\bar{\epsilon}} = \bar{\bar{\epsilon}}^T$ and $\bar{\bar{\mu}} = \bar{\bar{\mu}}^T$ in the anisotropic case, and $\bar{\bar{\zeta}} = -\bar{\bar{\xi}}^T$ for the bianisotropic case (Asadchy, 2017).

Many microwave-to-optical systems demand nonreciprocity at fundamental or subharmonic/inter-harmonic frequencies for applications such as unidirectional transmission (isolation), asymmetric wave amplification/attenuation, and anomalous reflections (Tianshuo Qiu and Qu, 2020; Taravati and Eleftheriades, 2021; Zang et al., 2019; Cardin et al., 2020; Mikheeva et al., 2022). Historically, ferrite materials have been used to construct nonreciprocal devices such as isolator, circulator, and phase shifter. For instance, an isolator is a two-port device with unidirectional transmission, and its ideal scattering matrix is given by

$$[S] = \begin{bmatrix} 0 & 0 \\ 1 & 0 \end{bmatrix}, \tag{1.20}$$

which indicates that both ports are matched, but transmission occurs only from port 1 to port 2. The $[S]$ matrix is non-unitary and asymmetric because the isolator must be lossy and is non-reciprocal (Pozar, 2012). Nonreciprocal systems, whether with gain or loss, are called non-Hermitian systems (V. S. Asadchy and Tretyakov, 2020).

The classical approach to nonreciprocity uses the Faraday effect in ferrite materials biased with magnetic fields. However, ferrites require large magnetic fields and are bulky, expensive, prone to interference, and incompatible with modern fabrication. Newer methodologies offer significant potential to overcome these limitations, providing enhanced performance for applications such as full-duplex communication, radar systems, and quantum computing (Taravati and Eleftheriades, 2020; Kord et al., 2020; Nagulu and Krishnaswamy, 2021; Bardin et al., 2021). These methods can be categorized into three main approaches:

- Time-odd biasing (mimicking ferrite behavior) (Ra'di and Grbic, 2016; Ra'di and Alu, 2020; Kodera et al., 2013),
- Nonlinearity-based systems (Mahmoud et al., 2015; Cotrufo et al., 2021; Sounas and Alù, 2018),
- Space-time modulation (Zang et al., 2019; Wang et al., 2020; Ptitcyn et al., 2019; Taravati and Kishk, 2020; Taravati and Eleftheriades, 2022).

Time-odd biasing, such as active-biased transistor-based surfaces, uses the anti-symmetric behavior of circulating currents but suffers from high noise, limiting its use in low-noise radar and communication systems. Despite this, it offers low cost, simplicity, and ease of fabrication. Nonlinear-based methods create passive nonreciprocal systems, as the medium's nonlinearity depends on incident energy but is limited by incident power range and power losses. "Dynamic reciprocity" limits the performance as nonlinearity-based systems cannot achieve nonreciprocity for simultaneously opposing excitation (Shi and Fan, 2015). These systems are promising for the optics domain, where the implementation of other techniques is challenging. Inspired by parametric modulation in low-noise amplifiers (LNAs), space-time modulation (or spatiotemporal) can enable isolation in one direction and amplification in another. It offers tunable isolation and low-noise operation, making it ideal for communication and radar systems, but is challenging to implement due to the complexity of modulating the medium's components. Typical techniques in RF/microwave involve permittivity modulation via varactor diodes (Bahamonde, 2020) and conductance modulation via transistors (Reiskarimian, 2020), both of which suffer from high power consumption.

Space-time modulation stands out for its design flexibility, offering tunable characteristics, strong isolation, and low-noise behavior, even extending to the optical regime (Mikheeva et al., 2022). It has the ability to break reciprocity at both fundamental and subharmonic frequencies and its applications outside electromagnetics, including acoustics (Shen et al., 2019). However, practical implementation requires complex modulation schemes and precise synchronization, making it a challenging technique. In the study by X. Wang et al. (Wang et al., 2020; Ptitcyn, 2021), they propose using uniform time modulation in a linear bianisotropic system to achieve nonreciprocal transmission for a penetrable metasurface. Asymmetric phase and amplitude responses raised by space modulation are provided by an asymmetric response of an Ω-type bianisotropic medium. Their work is based on numerical impedance-matrix solutions and remains theoretical in terms of establishing the individual feeding and equivalent functions for time-varying circuit elements.

This thesis introduces a novel method for achieving nonreciprocal transmission. The method is based on using time modulation on a penetrable metasurface, which generates π-phase delayed surface waves based on excitation direction. Nonreciprocal behavior under solely time modulation requires a time delay between opposing waves. A π-phase delay between forward and backward waves with equal amplitudes is optimal for isolation and amplification through constructive or destructive interference. Our approach involves using surface waves to interact with time-modulated elements. It enables distinct modeling of time-invariant and time-varying components through impedance-based characterization, and so the numerical solutions by the ITMM and HB. The use of π-phase delayed surface waves on a penetrable surface presents a novel contribution to the literature (Yılmaz and Yaman, 2024).

1.6. Space-Time and Time Modulated Metasurfaces

This section reviews analytical solutions for space-time and time-modulated homogeneous media. Before the analyses, we need to look at the Floquet analysis, which is a crucial mathematical tool for solving time-periodic systems. Floquet analysis is employed for ordinary differential equations with periodic functions (Wang et al., 2020; Koutserimpas and Fleury, 2018). For a basic differential equation given as

$$\dot{\mathbf{x}}(t) = \mathbf{A}(t)\mathbf{x}(t), \tag{1.21}$$

if time dependence is periodic,

$$\mathbf{A}(t+\tau) = \mathbf{A}(t), \tag{1.22}$$

the solution coefficient will have the same periodicity indicated as

$$\mathbf{x}(t) = \mathbf{P}(t)e^{t\mathbf{B}} \qquad \text{where} \qquad \mathbf{P}(t) = \mathbf{P}(t+\tau). \tag{1.23}$$

$\mathbf{P}(t)$ can be expanded in Fourier series to obtain Floquet harmonics (modes).

1.6.1. Time-Modulated Metasurface

The permittivity of the medium is assumed to have periodically time-modulated with a sinusoidal signal given by (Taravati and Kishk, 2020; Jorge R. Zurita-Sánchez and Cervantes-González, 2009)

$$\epsilon(t) = \epsilon_{av} + \epsilon_m \cos(\omega_m t). \tag{1.24}$$

The incident monochromatic plane wave propagating through the time-modulated medium is expressed as

$$\vec{E}_i(z,t) = \hat{y}E_0 e^{-j(k_0 z - \omega_0 t)}. \tag{1.25}$$

Figure 1.10 illustrates such a scenario for given coordinates. The solution of the wave equations for such a problem results in all Floquet harmonics, $\omega_0 + n\omega_m$, are introduced, where n is an integer. Here, E_0 represents the amplitude of the incident wave, and the

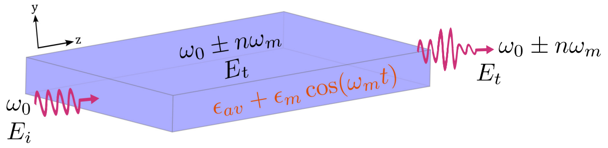

Figure 1.10. Illustration of wave propagation through time-modulated medium (Taravati and Kishk, 2020).

propagation constant of free space is $k_0 = \omega_0/\nu_0$. The phase velocity of the medium is $\nu_b = c/\sqrt{\epsilon_r}$. After the solution, the total fields on the medium is expressed by

$$\vec{E}_m(z,t) = \hat{y} \sum_{n,p=-\infty}^{\infty} \left(A^{+}_{np} e^{-j\beta_{np}z} + A^{-}_{np} e^{j\beta_{np}z}\right) e^{j(\omega_0+n\omega_m)t}, \tag{1.26}$$

where n represents the number of space-time harmonics. Each integer number of $\beta_{0p}(\omega_0)$ represents a mode of the medium. There is possible to exist an infinite number of space-time harmonics corresponding to modes at other frequencies since each harmonic is a solution of the given wave equation. The final expression for transmitted electric field is found as

$$\vec{E}_T(z,t) = \hat{y} \sum_{n=-\infty}^{\infty} E_{t,n} e^{-j[k_{0n}z-(\omega_0+n\omega_m)t]}. \tag{1.27}$$

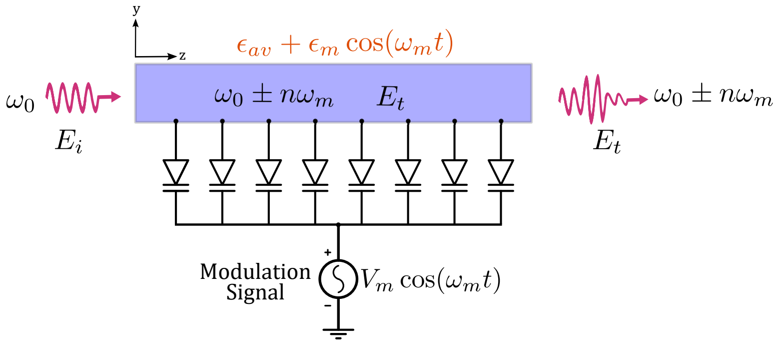

Figure 1.11. Illustration of realization of time-modulated transmission line with varactor diodes (Taravati and Kishk, 2020).

For example, in microwave systems, time-varying permittivity in the medium can be achieved by using varactor capacitors distributed with subwavelength separation and connected to the transmission line, as illustrated in Figure 1.11. In the transmission line

(TL) equivalence, fields are represented by voltage (V) and current (I), with material parameters modeled as lumped elements as capacitance and inductance. Equation 1.28 expresses the modulation voltage and the corresponding capacitance function of the varactor under negative bias, assuming it operates in the linear region of the C-V characteristic.

$$V(t) = V_{dc} + V_{m,n} cos(\omega_m t) \quad \text{and} \quad C(t) = C_{av} + C_m cos(\omega_m t). \tag{1.28}$$

The modulation depth is defined as the ratio of the maximum amplitude of the sinusoidal part to the average, i.e. DC part, expressed as $M = C_m / C_{av}$.

Conversely, commercially available, ready-to-use products designed explicitly for permeability modulation are not yet available, and this remains a subject of ongoing research (Kodama et al., 2023).

1.6.2. Space-Time Modulated Metasurface

In the space-time-modulated scenario, the permittivity of the slab medium is modulated both spatially and temporally expressed as (Taravati and Kishk, 2020; Sajjad Taravati and Caloz, 2017)

$$\epsilon(z,t) = \epsilon_{av} + \epsilon_m \cos(\beta_m z - \omega_m t). \tag{1.29}$$

By considering wave propagation through both sides of the medium ($+z$ and $-z$ propagation), the incident field is expressed by

$$\vec{E}_i = \hat{y} E_0 e^{\mp j(k_0 z - \omega_0 t)}. \tag{1.30}$$

Figure 1.12 illustrates this scenario for the given configuration. The total electric field on the medium is calculated as

$$\vec{E}_m(z,t) = \hat{y} \sum_{n,p=-\infty}^{\infty} \left(A_{np}^{+} e^{-j(\beta_{0p}^{+} + n\beta_m)z} + A_{np}^{-} e^{+j(\beta_{0p}^{-} - n\beta_m)z} \right) e^{j(\omega_0 + n\omega_m)t}. \tag{1.31}$$

The total transmitted electric field outside the slab for the forward ($+\hat{z}$) and backward $-\hat{z}$ illuminations are given by

$$\vec{E}_T(z,t) = \hat{y} \sum_{n=-\infty}^{\infty} E_{t,n} e^{\mp j[k_{0n} z - (\omega_0 + n\omega_m)t]}. \tag{1.32}$$

where $+$ and $-$ denote forward and backward illumination, respectively. Here, we observe that phase-coherent nonreciprocal transmissions can be enabled in a space-time-modulated medium for forward and backward illuminations.

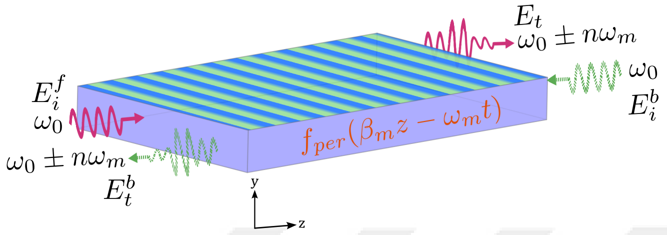

Figure 1.12. Illustration of the wave propagating through space-time modulated medium (Taravati and Kishk, 2020).

Figure 1.13 illustrates an example of a space-time-modulated transmission line using varactor diodes.

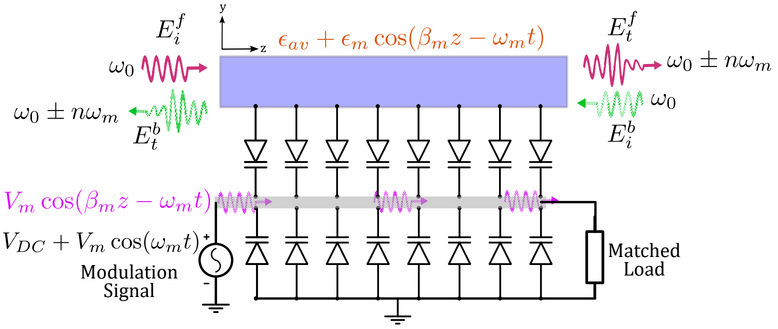

Figure 1.13. Illustration of realization of space-time modulated transmission line with varactor diodes (Taravati and Kishk, 2020).

Equation 1.32 confirms the discussions on asymmetric transmission for forward and backward illuminations, as detailed in Section 1.5. It shows that an asymmetric response to waves propagating in opposite directions through the medium is necessary. Thus, if the medium produces an asymmetric response to incoming waves from both sides, time modulation alone is sufficient. This can be accomplished using phase-conjugate surfaces with Ω-type bianisotropy through phase-delayed surface waves on the medium (Yılmaz and Yaman, 2024).

1.7. Varactor Diode Modeling

The varactor diode can be employed to realize the time-varying feature of the proposed medium. A varactor is a p-n junction diode that exhibits voltage-dependent capacitance when reverse-biased. The general representation and energy-band diagram of the p-n junction are shown in Figure 1.14. This section reviews the analytical expressions derived for the capacitance function of the p-n junction (Bahamonde, 2020; Golio, 2008).

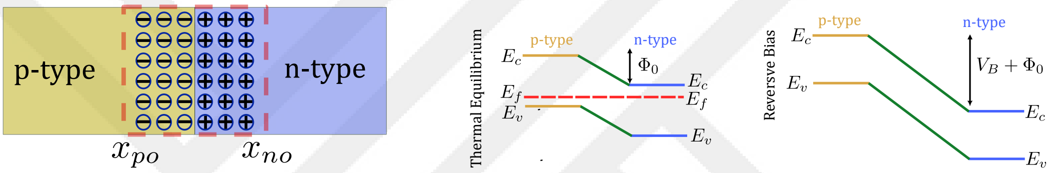

(a) (b)

Figure 1.14. (a) Illustration of p-n junction and (b) energy band diagram in thermal equilibrium and under reverse bias (Bahamonde, 2020).

The charge density along the medium can be written as a function of position in one dimension (1D) by

$$\rho_0(x) \simeq \begin{cases} -qN_A, & -x_{P0} \geq x \geq 0 \\ qN_D, & 0 \geq x \geq x_{N0} \end{cases}, \tag{1.33}$$

where q represents the charge of an electron, N_A and N_D are the acceptor and donor concentrations, respectively, and x_{P0} and x_{N0} represent the depletion width extending into the p-side and n-side. The principle of charge conservation indicates that

$$x_{P0}N_A = N_D x_{N0}. \tag{1.34}$$

The solution of Poisson's equation in thermal equilibrium gives

$$\frac{d^2\Phi}{dx^2} = \frac{\rho}{\epsilon} = \frac{q}{\epsilon} x_{P0} \big[(p_0 - n_0) + (N_D - N_A)\big], \tag{1.35}$$

where Φ represents the potential between the junctions, and p_0 and n_0 denote the intrinsic carrier concentrations of the semiconductor. As the depletion region is the area of interest, where $p_0 = n_0 = 0$, the integration result in

$$\Delta\Phi = \frac{q}{2\epsilon} \frac{N_A N_D}{N_A + N_D} (x_{p0} + x_{N0})^2. \tag{1.36}$$

Total depletion width is $W = x_{p0} + x_{N0}$ defined by

$$W = \sqrt{\frac{2\epsilon}{q} \frac{N_A + N_D}{N_A N_D} \Delta\Phi}, \tag{1.37}$$

where $\Delta\Phi = V_B + \Phi_0$ and Φ_0 is the potential at thermal equilibrium given by

$$\Phi_0 = \frac{k_B T}{q} \ln(\frac{N_A N_D}{n_0 p_0}) \tag{1.38}$$

where k_B is the Boltzmann constant and T is temperature. When an external negative bias is applied ($V_B < 0$ V), the depletion region expands, increasing the energy barrier between the p and n regions and thus the depletion region's volume. The capacitance of the depletion region is related as

$$C_j = \frac{\epsilon_S}{W}, \tag{1.39}$$

where ϵ_S is the permittivity of semiconductor material.

To verify the $C - V$ characteristic of the diode (Skyworks SMV2019) used in our simulations and experiments, we simulated its SPICE model using Keysight ADS: HB simulation software. Figure 1.15 shows the varactor diode circuit model. The junction capacitance C_J of the varactor diode is determined by the applied reverse DC voltage V_R, zero-bias junction capacitance C_{J0}, grading coefficient M, and junction potential V_J. The relationship is given by

$$C_j(V_R) = \frac{C_{J0}}{(1+\frac{V_R}{V_J})^M}. \tag{1.40}$$

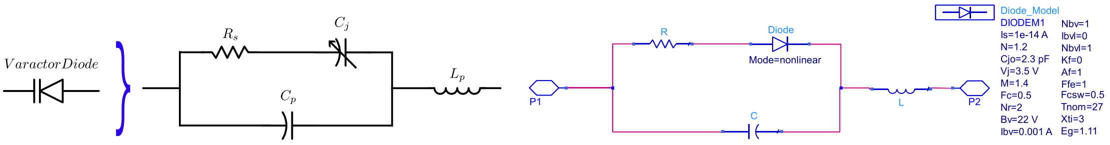

(a) (b)

Figure 1.15. Circuit schematic for varactor diode, (a) equivalent circuit model, (b) SPICE varactor diode models for Skyworks SMV2019

The total capacitance is the parallel combination of C_J and the package capacitance C_p:

$$C_T(V_R) = C_J(V_R) + C_p. \tag{1.41}$$

We calculate the capacitor value based on a basic circuit based on the change in resonance frequency under the negative DC bias of the diode. The resonance frequency is given by

$$\omega_0 = \frac{1}{\sqrt{LC}}. \tag{1.42}$$

Here, $\omega_0 = 2\pi f_0$, with L remaining constant while C varies with voltage. The calculated capacitance (C) as a function of the bias voltage is shown in Figures-1.16. This $C - V$ characteristic well-matches the values provided in the data sheet.

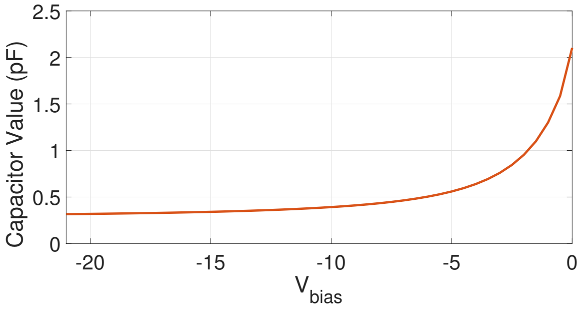

Figure 1.16. Calculated capacitance value versus negative DC bias for varactor diode of Skyworks SMV2019

1.8. Numerical Solution Techniques

In this thesis, we employ different numerical techniques to address both time-invariant and time-varying problems, including 2D analytical solutions, a proposed 3D structure model, and a time-varying transmission line (TL) equivalent circuit. For time-invariant cases in 2D and 3D, we use the Finite Difference Time Domain (FDTD) method, the Finite Element Method (FEM), and the Eigensolver (E-Solver). The FDTD method provides the most promising solution for wave propagation through complex media. The FDTD in the free and open-source MEEP library is implemented for the 2D problem in Section 2 (A. Oskooi and Johnson, 2010). For 3D models, we use the FEM in commercial software CST Microwave Studio, which excels in analyzing complex geometries and multi-resonances in metasurfaces. The FEM, effective for intricate designs, divides the problem space into finite elements, such as tetrahedrons, for precise analysis. In addition, the Eigensolver in CST Microwave Studio is employed throughout the thesis, which provides a specialized solution for determining resonant frequencies and mode shapes, which are essential for designing waveguides and cavities.

For time-varying problems where standard solutions are not available, we develop a numerical solution using the ITMM, rooted in Floquet analysis (Li et al., 2019; Alvarez-Melcon et al., 2019; Wang et al., 2020). We also use HB simulation in Keysight ADS software (ADS, 2019) to account for realistic scenarios. The HB method combines time and frequency domain analysis to simulate nonlinear effects and harmonic mixing in microwave circuits, incorporating real semiconductor models like varactor diodes. These methods are detailed in Chapters 5 and 6.

1.9. Thesis Motivation and Scope

The recent advancement in metasurface technology has enabled superior control over EM waves. Bianisotropy has significantly enhanced metasurface design flexibility by introducing coupling parameters for versatile field transformation capabilities, which are essential for many applications, including those addressed in this thesis. Time variance in metasurfaces further expands their potential in practical scenarios by dynamically controlling wave characteristics such as beam-forming, steering, and tunable reflectivity, transmission, and absorption. This thesis aims to develop a novel methodology for dynamic transmission control on penetrable metasurfaces through surface waves. Then, it is employed for improving performances while offering solutions for complexity and difficulties in nonreciprocity and beam-steering applications, which are validated by numerical simulations and experimental results. The scope of the thesis includes designing a penetrable bianisotropic metasurface that enables desired field transformations between incident and transmitted fields through surface waves. It involves the implementation of nonreciprocity and electronically reconfigurable radiation through, respectively, fast (time-modulation) and slow time variations. It further includes the impedance-based characterization for an equivalent circuit, then its modeling with time-domain-based components, and the development of numerical solutions for time modulation on the model. Experimental results have been conducted to confirm the theoretical and numerical results founded on the proposed methods and the models.

The thesis is structured as follows: Chapter 2 presents the theoretical and numerical analysis of a penetrable metasurface supporting surface-wave generation in 2D. Chapter 3 outlines the design procedure for the 3D model and its simulation results and it includes the retrieval of bianisotropy couplings and impedance-based characterization used to construct a TL equivalent circuit model. Chapter 4 introduces a 3D design where variable capacitance interacts with excited surface waves on the unit cell-in-cavity model, and its equivalent circuit model incorporating variable capacitance. The consistency of this equivalent model is demonstrated through comparisons with full-wave simulations. In Chapter 5, numerical analyses for the equivalent circuit model with time-varying capacitance are developed. Here, results of nonreciprocal transmission achieved through ITMM and HB simulation techniques are presented. Chapter 6 firstly revisits the 3D simulation and the numerical solution for the time-modulated circuit for the case of incorporating all losses and utilizing a real waveguide. Then, experiment setups to observe nonreciprocal transmission via time modulation are given, and measured results are compared with simulations and numerical techniques. Chapter 7 analyzes eigenmode solutions for the infinite periodic proposed metasurface, focusing on slow time-varying changes with only DC. It presents an electronically reconfigurable wavefront application through surface waves on a metasurface fed by a horn antenna. The metasurface is applied to the aperture of a 3D-printed compact horn antenna for beam-steering applications of the directive radiation. The chapter involves 3D designs, simulations, and proof-of-concept experiments for the proposed goals.

CHAPTER 2

ANALYTICAL SOLUTION OF SURFACE WAVE SUPPORTED METASURFACE IN 2D

This chapter begins with an overview of the analytical background of DNG materials, perfect lensing phenomena, phase conjugate surfaces, and surface-wave converter metasurfaces. An analytical solution is developed for the penetrable metasurface, which supports anti-symmetric surface waves based on conjugate bianisotropic surfaces. We demonstrate the control of transmission coefficients by manipulating the surface wave that is coupled to the incident and propagating waves. 2D numerical simulations are presented to verify the analytical solutions.

2.1. Double Negative Index Medium

When a medium exhibits negative values for both permittivity (ϵ) and permeability (μ), it is termed a DNG or left-handed medium (LHM). This concept was initially theoretically studied by V. G. Veselago (Veselago, 1968). This section reviews the electromagnetic wave solutions for the case of effective negative parameters. We start the analysis with Maxwell's equations, which show the relation of electric and magnetic field quantities. They are expressed as follow (Cheng, 1983)

$$\begin{aligned} \nabla \times \vec{E} &= -\frac{\partial \vec{B}}{\partial t} - \vec{M}_s, & \nabla \cdot \vec{D} &= \rho_e \\ \nabla \times \vec{H} &= \vec{J}_s + \frac{\partial \vec{D}}{\partial t}, & \nabla \cdot \vec{B} &= \rho_m, \end{aligned} \tag{2.1}$$

where, $\vec{J}_s$ and $\vec{M}_s$ are, respectively, electric (A/m^2) and magnetic (V/m^2) current density vectors, and ρ_e and ρ_m are, respectively, scalar electric (C/m^3) and magnetic (Wb/m^3) charge densities. ∇ and $\frac{\partial}{\partial t}$ are, respectively, spatial and temporal differentiation operators.

Constitutive relations in an isotropic medium are given as

$$\vec{D} = \epsilon \vec{E} \qquad \text{and} \qquad \vec{B} = \mu \vec{H}. \tag{2.2}$$

The wave equation is derived from Maxwell's equations as

$$\nabla^2 \psi - \epsilon\mu \frac{\partial^2 \psi}{\partial t^2} = 0, \tag{2.3}$$

where ψ represents either $\vec{E}$ or $\vec{H}$. The term $\epsilon\mu$ is not effected by changes of signs of ϵ and μ at the same time due to squared of refractive index ($n^2/c_0^2 = \epsilon\mu$, c_0 is the speed of light in vacuum). In the phasor domain, the relations between electric and magnetic fields for the lossless and source-free case, are expressed as

$$\begin{aligned} \nabla \times \vec{E} &= -j\omega\mu\vec{H}, \\ \nabla \times \vec{H} &= j\omega\epsilon\vec{E}, \end{aligned} \tag{2.4}$$

where $j = \sqrt{-1}$ and plane wave with space and time dependence is ; $\vec{E} = \vec{E}_0 e^{(-j\vec{k}.\vec{r}+j\omega t)}$ and $\vec{H} = \vec{H}_0 e^{(-j\vec{k}.\vec{r}+j\omega t)}$, where $\vec{k}$ is the propagation vector. The relations can be written in complex domain as

$$\begin{aligned} \vec{k} \times \vec{E} &= \omega\mu\vec{H}, \\ \vec{k} \times \vec{H} &= -\omega\epsilon\vec{E}. \end{aligned} \tag{2.5}$$

These solutions are different in a DNG medium, as discussed in the literature (Ziolkowski and Heyman, 2001; Ricardo Marques and Sorolla, 2008). In a medium where both permittivity (ϵ) and permeability (μ) are positive, it is referred to as a "right-handed" vector system. However, when both ϵ and μ are negative, and the equations are becomes as

$$\vec{k} \times \vec{E} = -\omega|\mu|\vec{H}, \tag{2.6}$$

$$\vec{k} \times \vec{H} = \omega|\epsilon|\vec{E}. \tag{2.7}$$

This vector system is termed "left-handed" or "backward" media due to the existence of backward wave propagation. The real part of the Poynting vector specifies the direction of the time-averaged energy flux. It is not affected by a simultaneous change of signs of ϵ and μ, as indicated in Equation 2.8. In a so-called left-handed medium, energy and wavefront propagate in opposite directions (Ricardo Marques and Sorolla, 2008; Nader Engheta, 2006).

$$\vec{S} = \frac{1}{2}\vec{E} \times \vec{H}^{*}, \tag{2.8}$$

where $(*)$ denotes the complex conjugate Poynting vector. The vector representations of right and left-handed medium are given in Figure 2.1.

(a) RHM (b) LHM

Figure 2.1. Illustration of vector system for EM waves.

When losses are introduced to a finite region of left-handed medium without sources, the power flow is calculated by taking the divergence of the complex Poynting vectors, given as

$$\nabla \cdot \{\vec{E} \times \vec{H}^{*}\} = j\omega(\vec{E} \cdot \vec{D}^{*} - \vec{B} \cdot \vec{H}^{*}), \tag{2.9}$$

and the statement for the net power flow can be expressed by integral form using divergence theorem as follows (Ricardo Marques and Sorolla, 2008)

$$\Re\left\{ \oint \vec{E} \times \vec{H}^{*} \cdot \hat{n}\, dS \right\} = \omega \Im\left\{ \int \left(\mu \mid \vec{H} \mid^{2} - \epsilon^{*} \mid \vec{E} \mid^{2} dV \right) \right\} < 0, \tag{2.10}$$

which indicates

$$Im(\epsilon) \ < \ 0 \qquad \text{and} \qquad Im(\mu) \ < \ 0. \tag{2.11}$$

A plane wave propagating in a lossy left-handed medium with $\Re(\epsilon \ < \ 0)$ and $\Re(\mu \ < \ 0)$ has a propagating constant squared as $k^2 = \omega^2 \mu \epsilon$, and Equation 2.11 indicates $Im(k^2) \ > \ 0$, implying

$$\left\{ \Re(k) > 0 \ \text{ and } \ \Im(k) > 0 \right\} \qquad \text{or} \qquad \left\{ \Re(k) < 0 \ \text{ and } \ \Im(k) < 0 \right\}. \tag{2.12}$$

This implies that waves amplify in the direction of the wavefront propagation, aligning with the previously mentioned backward-wave propagation. The time-averaged energy density for a transparent, non-dispersive medium can be expressed as follows

$$U_{nd} = \frac{1}{4} \{ \epsilon \mid \vec{E} \mid^{2} + \mu \mid \vec{H} \mid^{2} \}. \tag{2.13}$$

If both ϵ and μ are negative as in given medium, Equation 2.13 results in a negative energy density, which is non-physical. Any real physical medşum exhibits some degree of dispersion, except for a vacuum. The energy density for a dispersive medium can be expressed as

$$U = \frac{1}{4} \left\{ \frac{\partial(\omega\epsilon)}{\partial\omega} \mid \vec{E} \mid^{2} + \frac{\partial(\omega\mu)}{\partial\omega} \mid \vec{H} \mid^{2} \right\}. \tag{2.14}$$

Hence, the condition of a positive energy density implies,

$$\frac{\partial(\omega\epsilon)}{\partial\omega} > 0 \qquad \text{and} \qquad \frac{\partial(\omega\mu)}{\partial\omega} > 0, \tag{2.15}$$

and this aligns with $\epsilon \ < \ 0$ and $\mu \ < \ 0$ with $\partial\epsilon/\partial\omega \ > \ |\epsilon|/\omega$ and $\partial\mu/\partial\omega \ > \ |\mu|/\omega$, as suggested by the low-loss Drude-Lorentz model for ϵ and μ, in a highly dispersive medium, just above the resonance frequency, ϵ and/or μ can become negative. This is consistent with the concept that a left-handed medium must exhibit high levels of dispersion. The propagation in backward media is described by opposite signs of phase and group velocities as

$$\frac{\partial k^2}{\partial \omega} = 2k\frac{\partial k}{\partial \omega} \equiv 2\frac{\omega}{\nu_p \nu_g}, \tag{2.16}$$

where $\nu_p = \omega/k$ and $\nu_g = \partial\omega/\partial k$ represent the phase and group velocities, respectively. From $k^2 = \omega^2\epsilon\mu$ and Equation 2.15, the following equations are derived

$$\frac{\partial k^2}{\partial \omega} = \omega\epsilon\frac{\partial(\omega\mu)}{\partial \omega} + \omega\mu\frac{\partial(\omega\epsilon)}{\partial \omega} < 0. \tag{2.17}$$

By equations 2.16 and 2.17, we can write as

$$\nu_p \nu_g \; < \; 0. \tag{2.18}$$

The phase and group velocities propagate reversely, indicating backward wave propagation for a medium with negative ϵ and μ.

2.2. Negative Refraction and Perfect Lensing

The refraction at the interface of a left-handed medium ($n_2 < 0$) when an optical ray comes from an ordinary right-handed medium ($n_1 > 0$) is illustrated in Figure 2.2. The applying EM boundary conditions at the interface through phase matching is called Snell's law of reflection and which is expressed by (Ricardo Marques and Sorolla, 2008)

$$\frac{\sin(\theta_i)}{\sin(\theta_r)} = -\frac{|\vec{k}_2|}{|\vec{k}_1|} \equiv \frac{n_2}{n_1} < 0. \tag{2.19}$$

Such a medium is also called negative refractive index media. This implies that the refraction is anomalous, with the refracted angle on the same interface side normal as the incident angle. The wave vectors and Poynting vectors resulting from the oblique scattering problem are given in the following (Nader Engheta, 2006)

$$\vec{k}_{inc} = k_1 \left[\cos(\theta_1)\hat{z} + \sin(\theta_1)\hat{x}\right],$$

$$\vec{k}_2 = k_1 \left[-\cos(\theta_1)\hat{z} + \sin(\theta_1)\hat{x}\right], \tag{2.20}$$

$$\vec{k}_1 = k_2 \left[\cos(\theta_2)\hat{z} + \sin(\theta_2)\hat{x}\right],$$

$$\vec{S}_{inc} = \frac{1}{2}\frac{|E_0|^2}{\eta_1}\left[\cos(\theta_1)\hat{z} + \sin(\theta_1)\hat{x}\right],$$

$$\vec{S}_{refl} = \frac{1}{2}\frac{|TE_0|^2}{\eta_1}\left[-\cos(\theta_1)\hat{z} + \sin(\theta_1)\hat{x}\right], \tag{2.21}$$

$$\vec{S}_{trans} = \frac{1}{2}\frac{|\tau E_0|^2}{\eta_2}\left[\cos(\theta_2)\hat{z} + \sin(\theta_2)\hat{x}\right],$$

where $\eta_{1,2}$ are the characteristic impedance of the media, Γ and T are the reflection and transmission coefficients, respectively.

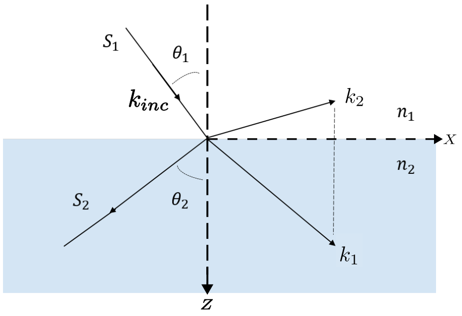

Figure 2.2. Negative refraction between right-handed (n_1) and left-handed (n_2) medium. $S_{1,2}$ and $k_{1,2}$ are Poynting and propagation vectors of medium$_{1,2}$, respectively (Önder Yılmaz, 2018).

The Poynting and wave vectors align if the transmitted wave propagates in a DPS medium. However, for a transmitted wave in a DNG medium, where the index is less than zero, expressions become as

$$\vec{k_2} = -|n_2|\frac{\omega}{c}\left[\cos(|\theta_2|)\hat{z} - \sin(|\theta_2|)\hat{x}\right],$$
$$\vec{S}_{trans} = \frac{1}{2}\frac{|\tau E_0|^2}{\eta_2}\left[\cos(|\theta_2|)\hat{z} - \sin(|\theta_2|)\hat{x}\right]. \tag{2.22}$$

The wave and Poynting vectors point in opposite directions, with the Poynting vector directed causally away from the interface.

When the $\epsilon_r = -1$ and $\mu_r = -1$ simultaneously, the extraordinary properties of left-handed media arise. As a breakthrough, J. B. Pendry demonstrated that negative refraction could create a perfect lens (Pendry, 2000). For an infinitesimal dipole in front of a lens with ω frequency radiating wave, A $2D$ Fourier expansion that gives the electric component of the field can be written by

$$\vec{E}(r,t) = \sum_{\sigma,k_x,k_y} \vec{E_\sigma}(k_x,k_y)e^{jk_z z + jk_x x + jk_y y - j\omega t}, \tag{2.23}$$

where σ denotes the spatial harmonics of the electric field. Considering normal propagation in the $z-$axis, Maxwell's equations and dispersion relation indicate that

$$k_z = +\sqrt{\omega^2 c^{-2} - k_x^2 - k_y^2} \qquad \text{and} \qquad \omega^2 c^{-2} > k_x^2 + k_y^2. \tag{2.24}$$

The lens corrects the phase of each Fourier component so that they converge at a distance, forming an image of the dipole source. For larger transverse wave numbers, the evanescent waves decay exponentially with z, and there is possible phase correction to restore their exact amplitude. The dispersion for the component of propagating direction is given as

$$k_z = +\sqrt{k_x^2 - k_y^2 - \omega^2 c^{-2}} \qquad \text{and} \qquad \omega^2 c^{-2} < k_x^2 + k_y^2. \tag{2.25}$$

They are effectively excluded from the image and only contribute to propagating waves. The resolution of the image cannot surpass this limit, as determined by the confinement of propagating waves within $k_x^2 + k_y^2 < \omega^2 c^{-2}$,

$$\Delta \approx \frac{2\pi}{k_{max}} = \frac{2\pi c}{\omega} = \lambda. \tag{2.26}$$

This holds true regardless of the perfection of the lens or the size of the aperture. A unique alternative to a lens is a material exhibiting a negative refractive index, capable of focusing light even in the form of a parallel-sided (flat) slab. Figure 2.3 depicts the focusing behavior of such a slab, assuming a refractive index of $n = -1$. Light is bent at a negative angle to the surface, which is normal in a medium with a negative refractive index. Consequently, light diverging from a point source is reversed and converges back to a point. Upon exiting the slab medium, the light achieves focus once again.

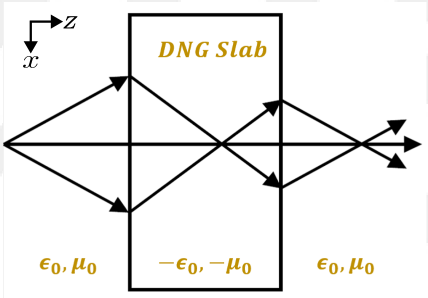

Figure 2.3. Illustration of negative refraction between DNG slab with $n = -1$ and free spaces.

In addition to negative refraction, a notable characteristic is the double-focusing effect depicted in a straightforward ray diagram. Light passing through a slab of thickness d_2, situated at a distance d_1 from the source, converges to a second focus when $z = d_2 - d_1$. Here, the critical factor is the negative values of the dielectric permittivity, ϵ, and the magnetic permeability, μ. In the scenario of chosen $\epsilon = -1$ and $\mu = -1$, the refractive index is equivalent to that of vacuum, given by $n = \sqrt{\epsilon\mu}$. A negative square root must be chosen for n. The medium impedance is given by

$$Z = \sqrt{\frac{\mu\mu_0}{\epsilon\epsilon_0}}, \tag{2.27}$$

which keeps its positive sign so the medium perfectly matches free space by eliminating reflections at interfaces. At the far boundary, another impedance match enables transparent light transmission into the vacuum. All energy transmission into the medium in the $+z$ direction can be shown in calculations given as

$$k_z^{'} = -\sqrt{\omega^2 c^{-2} - k_x^2 - k_y^2}. \tag{2.28}$$

The transmission coefficient is found as

$$T = e^{jk_z^{'}d} = e^{-j\sqrt{\omega^2 c^{-2} - k_x^2 - k_y^2}d}, \tag{2.29}$$

where d is the slab thickness. The negative phase arising from the wave vector choice is due to causality. This allows the medium to refocus light by canceling the phase acquired during propagation. The medium can negate the decay of evanescent waves. But, evanescent waves diminish in amplitude rather than phase as they propagate. Thus, amplification, not phase correction, is necessary for focusing. Across the slab, evanescent waves emerge from the far side and are amplified without violating energy conservation as they transport no energy. Transmission and reflection coefficients for the $y-$polarized wave in vacuum and the $x-$polarized evanescent wave are expressed as following

$$\begin{gathered} \lim_{\epsilon,\mu \to -1} T = e^{-jk_z^{'}d} = e^{-jk_z d}, \\ \lim_{\epsilon,\mu \to -1} \Gamma = 0. \end{gathered} \tag{2.30}$$

The medium amplifies evanescent waves. In this way, both propagating and evanescent waves contribute to the overall image resolution.

2.3. Perfect Lens with Phase Conjugate Sheets

Phase conjugate surfaces have been proposed as an alternative solution for perfect lensing instead of bulky DNG slabs (Maslovski and Tretyakov, 2012; Alu and Engheta, 2006). Negative refraction occurs only at the interfaces of the DNG slab rather than inside.

A parallel conjugate pair of surfaces can effectively mimic the operation of a perfect lens having negative refraction. If the surfaces support surface modes in the condition of $k_t > k_0$, impinging evanescent waves will resonate across the sheets and be tunneled through the lens with amplified amplitude. This effect arises from the electromagnetic coupling between surface modes excited on the sheets. This mechanism resembles a DNG slab with a coupled surface wave (Alu and Engheta, 2006).

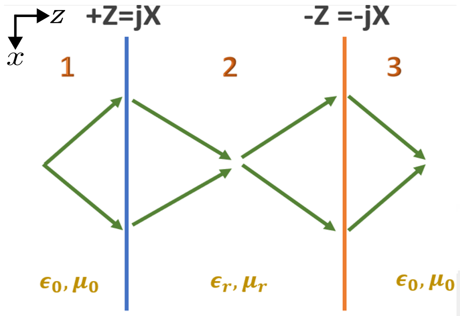

Figure 2.4. Illustration of perfect lens phenomena through phase conjugate surfaces.

Figure 2.4 illustrates the equivalent mechanism shown in Figure 2.3 for the DNG slab. The propagating plane wave is negatively refracted at the interfaces, and the evanescent modes are boosted due to the excitation of coupled surface plasmon-polariton pairs (surface waves). We review the analytical expressions presented in the literature for the problem (Maslovski and Tretyakov, 2012). For such a scenario, the tangential fields on the boundaries are assumed as

$$\vec{E}_{t,(1,3)} = \vec{E}^*_{t,(2)}. \tag{2.31}$$

The complex-conjugate surfaces hold symmetric properties on both sides. Under ideal refraction conditions, the field amplitudes should remain unchanged across the sheets. Consider a single phase-conjugating surface at $z = 0$; the tangential electric and magnetic fields on both sides of the surface can be decomposed into plane waves as follows

$$\vec{E}_t(x,y)|_{z=\pm 0} = \frac{1}{(2\pi)^2}\int\int \vec{E}_t(k_x,k_y)|_{z=\pm 0}e^{-j(k_x x+k_y y)}dk_x dk_y,$$
$$\vec{H}_t(x,y)|_{z=\pm 0} = \frac{1}{(2\pi)^2}\int\int \vec{H}_t(k_x,k_y)|_{z=\pm 0}e^{-j(k_x x+k_y y)}dk_x dk_y. \tag{2.32}$$

The boundary conditions imply those

$$\vec{E}_t(k_x,k_y)|_{z=+0} = \vec{E}_t^*(-k_x,-k_y)|_{z=-0},$$
$$\vec{H}_t(k_x,k_y)|_{z=+0} = \vec{H}_t^*(-k_x,-k_y)|_{z=-0}. \tag{2.33}$$

At the conjugating interface, propagating modes undergo negative refraction due to the reversal of the tangential component of the wave vector $\vec{k}_t = kx\hat{x} + k_y\hat{y}$. In contrast, negative refraction occurs in the DNG slab when the wave vector's normal component (k_z) reverses the sign.

For each of the phase-conjugating surfaces illuminated by an obliquely incident plane wave in free space, the tangential fields on both sides satisfy the following relation

$$\vec{E}_t(k_x,k_y)|_{z=\pm 0} = -Z_{TM,TE}\hat{z}\times\vec{H}_t(k_x,k_y)|_{z=\pm 0}, \tag{2.34}$$

where

$$Z_{TM} = \eta_0\frac{\sqrt{k_0^2-k_t^2}}{k_0} \qquad \text{and} \qquad Z_{TE} = \eta_0\frac{k_0}{\sqrt{k_0^2-k_t^2}}, \tag{2.35}$$

and $k_0 = \omega/c$ is the free-space wavenumber, $\eta_0 = \sqrt{\mu_0/\epsilon_0}$ and $k_t^2 = k_x^2 + k_y^2$. At the same time, according to the boundary condition, the tangential fields are expressed by

$$\vec{E}_{t+} = \vec{E}_{t-}^* \qquad \text{and} \qquad \vec{H}_{t+} = \vec{H}_{t-}^*. \tag{2.36}$$

This leads to

$$\vec{E}_t(k_x,k_y)|_{z=-0} = -Z^*_{TM,TE}\hat{z}\times\vec{H}^*_t(-k_x,-k_y)|_{z=+0} = -Z^*_{TM,TE}\hat{z}\times\vec{H}_t(k_x,k_y)|_{z=+0}. \tag{2.37}$$

When a wave incident the sheet, it interacts with the surface impedance which is the complex conjugate of the free space impedance. The reflection coefficient is expressed by

$$\Gamma_{TM,TE} = \frac{Z^*_{TM,TE} - Z_{TM,TE}}{Z^*_{TM,TE} + Z_{TM,TE}}. \tag{2.38}$$

Conjugate surfaces can excite surface waves coupled to the incident free-space wave for both transverse and normal wave vectors. For a propagating wave ($k_t = \sqrt{k_x^2 + k_{y^2}} < k_0$), the wave impedance is real and it is leading to zero reflection and negative refraction without reflection. For an evanescent wave ($k_t > k_0$), where the wave number is imaginary, so becoming the wave impedances purely imaginary, it results in an infinite reflection coefficient as given by Equation 2.38. Similarly, the transmission coefficient becomes infinite due to the boundary condition in Equation 2.36. Note that this applies only to the evanescent wave, which does not transport real power. The characteristic impedance of the TM evanescent wave is capacitive, while it appears inductive from the other side of the interface.

We can observe the equivalent characteristic for the interfaces of the DNG slab and DPS media (Alu and Engheta, 2006). Inside the DNG slab, evanescent waves experience growth rather than decay. When an evanescent wave propagates, the transverse impedances of the two regions become complex conjugates, resulting in infinite Fresnel reflection and transmission coefficients. This scenario does not contradict physical laws, as these coefficients illustrate the interaction between incident and reflected/transmitted evanescent waves, which do not carry real power. Instead, a surface wave propagates infinitely along the interface and decays exponentially away from surfaces. An equivalent circuit can be represented by phase conjugate reactances, which compensate each other by resonating at the same or near frequency. The ideal phase-conjugating surface should induce both electric and magnetic polarization currents. This implies the solution is to be a metasurface with magnetoelectric (or electromagnetic) coupling, so $\Omega-$ bianisotropy.

2.4. Surface-Wave Supported Penetrable Metasurface

In this section, we derive the analytical expression for the penetrable metasurface capable of generating surface waves. We will establish the design procedure and solutions based on the DNG and phase-conjugation surfaces. The electric and magnetic surface polarization currents and the surface impedance matrix are derived for the metasurface having the desired wave transformation. Our analysis begins by reviewing bianisotropic metasurfaces capable of near-perfect conversion between space and surface waves.

2.4.1. Bianisotropic Metasurface for Surface Wave Generation

Bianisotropic multilayered sheets have been analyzed in the literature to achieve near-perfect conversion of free-space propagating waves into surface waves (Epstein and Eleftheriades, 2016; Tcvetkova et al., 2018; Popov et al., 2019). V. Popov et al. used auxiliary surface waves to determine parameters for an Ω bianisotropic metasurface capable of splitting a normally incident plane wave into two equally propagating TE waves with opposite angles, such as θ and $-\theta$ (V. Popov, 2016).

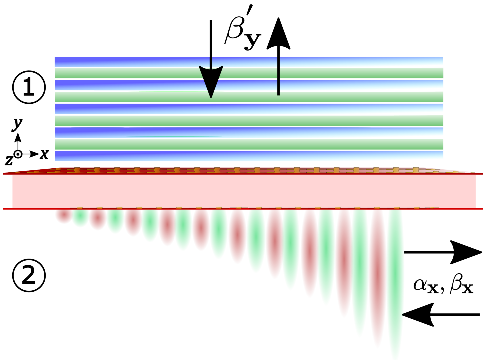

Figure 2.5. Illustration of wave transformation between normal plane wave to surface-wave (Popov et al., 2019).

Similarly, A. Epstein and G.V. Eleftheriades investigated arbitrary field transformations between two regions separated by a bianisotropic metasurface (Epstein and Eleftheriades, 2016). Their approach involves determining an impedance matrix for a passive, lossless, and reciprocal metasurface that transforms between the incident and desired fields. In subsequent years, S. N. Tcvetkova et al. examined the near-perfect conversion between incident plane waves and surface waves on impenetrable metasurfaces, providing exact solutions (Tcvetkova, 2019; Tcvetkova et al., 2018, 2019). In a related study, V. Popov et al. demonstrate numerically that bianisotropic metasurfaces can efficiently convert inhomogeneous plane waves into concentrated surface waves along the metasurface to a near-perfect degree as illustrated in Figure 2.5 (Popov et al., 2019). They consider a small growth condition that enables them to treat inhomogeneous plane waves as approximately uniform and homogeneous. Their findings on the impedance matrix in Equation 2.44 indicate the metasurface must exhibit Ω-coupling bianisotropy.

2.4.2. Two Conjugate Surface-Wave Converters

This section presents analytical and numerical solutions in 2D for a continuous penetrable surface that supports the generation of surface waves. We explore field transformations involving slightly inhomogeneous plane waves propagating on both sides and concentrated TM surface waves on the metasurface (Yılmaz and Yaman, 2024).

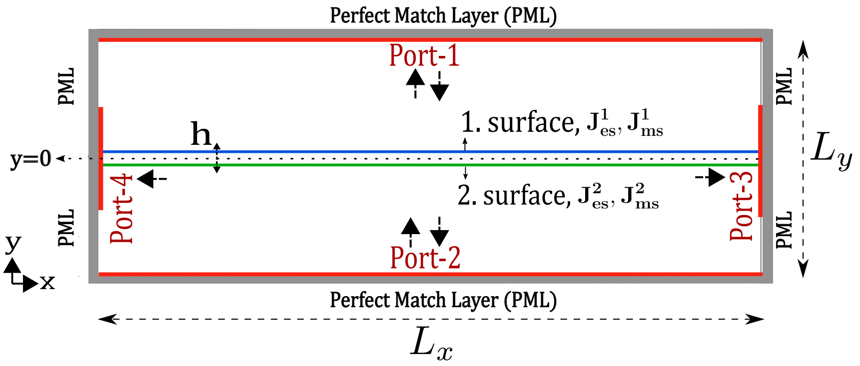

Figure 2.6. Schematic configuration for analytical solution and simulation setup in 2D (Yılmaz and Yaman, 2024).

We start by introducing a second surface that separates the desired fields in each region from the others. The separation distance between these surfaces is much smaller than the wavelength, $h << \lambda_0$, allowing the entire structure to be effectively considered a metasurface. We express the fields for each region given in Equation 2.39 for the configuration illustrated in Figure 2.6 for $x \in [-L_x/2,\ \ L_x/2]$.

$$
\begin{aligned}
H_{z1} &= e^{j\beta_y^{'}y+\alpha_x x}, && y \in [h/2,\ \ L_y/2]\,, \\
H_{z3} &= Te^{j\beta_y^{'}y+\alpha_x x}, && y \in [-h/2,\ \ -L_y/2]\,, \\
H_{z2} &= A_{sw}e^{(\alpha_y+j\beta_y)y}e^{(\alpha_x-j\beta_x)x}, && y \in [-h/2,\ \ h/2]\,, \\
E_{x1} &= \frac{\eta_0\beta_y^{'}}{k_0}e^{j\beta_y^{'}y+\alpha_x x}, && y \in [h/2,\ \ L_y/2]\,, \\
E_{x3} &= \frac{T\eta_0\beta_y^{'}}{k_0}e^{j\beta_y^{'}y+\alpha_x x}, && y \in [-h/2,\ \ -L_y/2]\,, \\
E_{x2} &= -j\frac{A_{sw}\eta_0(\alpha_y+j\beta_y)}{k_0}e^{(\alpha_y+j\beta_y)y}e^{(\alpha_x-j\beta_x)x}, && y \in [-h/2,\ \ h/2]\,,
\end{aligned}
\tag{2.39}
$$

where A_{sw} and T are the complex surface wave amplitude and transmission coefficient, k_0 and η_0 are the free-space wavenumber and impedance, $\mp$ refers to the $k_t < k_0$ or $k_t > k_0$, and the subscripts $_1$, $_2$, $_3$ refer to the region of $y > h/2$, $h/2 > y > -h/2$ and $y < -h/2$, respectively. The first surface is at $y = h/2$ and the second one is at $y = -h/2$. All the parameters of α and β are positive. The dispersion relation is given as

$$
\begin{aligned}
(\alpha_y + j\beta_y)^2 + (\alpha_x - j\beta_x)^2 &= -k_0^2, \\
\alpha_y^2 - \beta_y^{'2} &= -k_0^2.
\end{aligned}
\tag{2.40}
$$

The coefficients α_y and α_x are responsible for the attenuation and gain of the surface wave as it moves away from and along the surface. At the boundaries of the surfaces, the effective electric and magnetic surface currents leading to discontinuities in the tangential fields are expressed by

$$
\vec{J}_s(x) = \hat{y} \times \Delta\vec{H}_t(x) \qquad \text{and} \qquad \vec{M}_s(x) = -\hat{y} \times \Delta\vec{E}_t(x). \tag{2.41}
$$

where $\Delta\vec{E}_t(x) = \vec{E}_t^{+}(x) - \vec{E}_t^{-}(x)$ and $\Delta\vec{H}_t(x) = \vec{H}_t^{+}(x) - \vec{H}_t^{-}(x)$. $^{+}$ and $^{-}$ refer to the first and second regions at each boundary with respect to the normal vector. The surface electric and magnetic polarization currents for each surface, respectively, are given in Equation 2.42 and Equation 2.43.

$$\begin{aligned} \vec{J}_{es,1} &= \hat{x}(A_{sw}e^{(\alpha_x + j\beta_x)x} - e^{\alpha_x x}), \\ \vec{J}_{es,2} &= \hat{x}(Te^{\alpha_x x}) - \hat{x}(A_{sw}e^{(\alpha_x + j\beta_x)x}), \end{aligned} \tag{2.42}$$

$$\begin{aligned} \vec{J}_{ms,1} &= \hat{z}\big(\frac{j\eta A_{sw}}{k_0}(\alpha_y + j\beta_y)e^{(\alpha_x + j\beta_x)x} + \frac{-\eta\beta_y^{'}}{k_0}e^{\alpha_x x}\big), \\ \vec{J}_{ms,2} &= \hat{z}\big(\frac{-T\eta\beta_y^{'}}{k_0}e^{\alpha_x x} - \frac{j\eta A_{sw}}{k_0}(\alpha_y + j\beta_y)e^{(\alpha_x + j\beta_x)x}\big). \end{aligned} \tag{2.43}$$

For forward excitation, the expressions for field transformation by surface impedance matrix are given for the first and second surfaces in equations 2.44-2.47.

$$\begin{bmatrix} E_{x2}(x,0) \\ E_{x1}(x,0) \end{bmatrix} = \begin{bmatrix} Z_{11}^{1}(x) & Z_{12}^{1}(x) \\ Z_{21}^{1}(x) & Z_{22}^{1}(x) \end{bmatrix} \begin{bmatrix} -H_{z2}(x,0) \\ +H_{z1}(x,0) \end{bmatrix}, \tag{2.44}$$

$$\begin{bmatrix} -j\frac{A_{sw}\eta_0}{k_0}(\alpha_y + j\beta_y)e^{(\alpha_x - j\beta_x)x} \\ \dfrac{\eta_0\beta_y^{'}}{k_0}e^{\alpha_x x} \end{bmatrix} = \begin{bmatrix} jX_{11}^{1} & jX_{12}^{1} \\ jX_{21}^{1} & jX_{22}^{1} \end{bmatrix} \begin{bmatrix} A_{sw}e^{(\alpha_x - j\beta_x)x} \\ -e^{\alpha_x x} \end{bmatrix}, \tag{2.45}$$

$$\begin{bmatrix} E_{x2}(x,0) \\ E_{x3}(x,0) \end{bmatrix} = \begin{bmatrix} Z_{11}^{2}(x) & Z_{12}^{2}(x) \\ Z_{21}^{2}(x) & Z_{22}^{2}(x) \end{bmatrix} \begin{bmatrix} +H_{z2}(x,0) \\ -H_{z3}(x,0) \end{bmatrix}, \tag{2.46}$$

$$\begin{bmatrix} -j\frac{A_{sw}\eta_0}{k_0}(\alpha_y + j\beta_y)e^{(\alpha_x - j\beta_x)x} \\ \dfrac{T\eta_0\beta_y^{'}}{k_0}e^{\alpha_x x} \end{bmatrix} = \begin{bmatrix} jX_{11}^2 & jX_{12}^2 \\ jX_{21}^2 & jX_{22}^2 \end{bmatrix} \begin{bmatrix} -A_{sw}e^{(\alpha_x - j\beta_x)x} \\ Te^{\alpha_x x} \end{bmatrix}. \tag{2.47}$$

Since the surfaces are lossless, the impedance matrix is purely imaginary and given by $\bar{Z}_1 = j\bar{X}_1$. The reactance matrix for the first surface is expressed in Equation 2.48. Being inherently passive, it must exhibit reciprocity, meaning $Z_{12} = Z_{21}$, which leads to $A_{sw} = \sqrt{\beta_y^{'}/\beta_y}$. These impedance matrices align with the findings of V. Popov et al., who analyzed the near-perfect conversion of incident waves into surface waves (Popov et al., 2019).

$$\bar{X}_1(x) = \begin{bmatrix} \dfrac{\eta_0\alpha_y}{k_0} - \dfrac{\eta_0\beta_y}{k_0}\cot(\beta_x x) & -\dfrac{\eta_0 A_{sw}\beta_y}{k_0\sin(\beta_x x)} \\ -\dfrac{\eta_0\beta_y^{'}}{A_{sw}k_0\sin(\beta_x x)} & -\dfrac{\eta_0\beta_y^{'}}{k_0}\cot(\beta_x x) \end{bmatrix}. \tag{2.48}$$

We derive the impedance matrix for the second surface by considering the opposite normal vectors for Equation 2.44 and Equation 2.46. The result reveals that the second surface is the complex conjugate of the first one, i.e., $\bar{Z}_2(x) = \bar{Z}_1^*(x)$. We can express as $\bar{Z}_2 = -j\bar{X}_1$ as given in Equation 2.49 for the lossless case.

$$\bar{X}_2(x) = \begin{bmatrix} -\dfrac{\eta_0\alpha_y}{k_0} + \dfrac{\eta_0\beta_y}{k_0}\cot(\beta_x x) & \dfrac{\eta_0 A_{sw}\beta_y}{k_0\sin(\beta_x x)} \\ \dfrac{\eta_0\beta_y^{'}}{A_{sw}k_0\sin(\beta_x x)} & \dfrac{\eta_0\beta_y^{'}}{k_0}\cot(\beta_x x) \end{bmatrix}. \tag{2.49}$$

By applying the conservation of averaged power flow across the rectangular enclosure around the surfaces, the relation between surface wave amplitude (A_{sw}) and transmission ratio (T) can be derived. The time-averaged power flow density vector is defined by

$$\vec{S}_{av} = \frac{1}{2}\Re(\vec{E} \times \vec{H}^*). \tag{2.50}$$

For the first region, power density is found as

$$\vec{S}_{av,1} = \frac{1}{2}\Re\Big\{\Big[\frac{\eta_0\beta_y^{'}}{k_0}e^{j\beta_y^{'}y+\alpha_x x}\hat{x}\Big] \times \Big[e^{-j\beta_y^{'}y+\alpha_x x}\hat{z}\Big]\Big\} \tag{2.51}$$

and we found the expression for first region as

$$\vec{S}_{av,1} = \big(-\frac{\eta_0\beta_y^{'}}{2k_0}e^{2\alpha_x x}\big)\hat{y}. \tag{2.52}$$

Similarly, it is calculated for the third region as

$$\vec{S}_{av,3} = \frac{1}{2}\Re\Big\{\Big[\frac{T\eta_0\beta_y^{'}}{k_0}e^{j\beta_y^{'}y+\alpha_x x}\hat{x}\Big] \times \Big[Te^{-j\beta_y^{'}y+\alpha_x x}\hat{z}\Big]\Big\}, \tag{2.53}$$

then, we found the expression as

$$\vec{S}_{av,3} = \big(-\frac{\eta_0|T|^2\beta_y^{'}}{2k_0}e^{2\alpha_x x}\big)\hat{y}. \tag{2.54}$$

For the second region, we write the expression for power density through the metasurface as

$$\begin{aligned}\vec{S}_{av,2} =& \frac{1}{2}\Re\Big\{\Big[\mp j\frac{A_{sw}\eta_0(\alpha_y+j\beta_y)}{k_0}e^{(\alpha_y+j\beta_y)y}e^{(\alpha_x-j\beta_x)x}\hat{x} \\ &+\frac{j\eta_0A_{sw}}{k_0}(\alpha_x-j\beta_x)e^{\pm(\alpha_y+j\beta_y)y}e^{(\alpha_x-j\beta_x)x}\hat{y}\Big] \times \Big[A_{sw}e^{(\alpha_y-j\beta_y)y}e^{(\alpha_x+j\beta_x)x}\hat{z}\Big]\Big\},\end{aligned} \tag{2.55}$$

and it is simplified to

$$\vec{S}_{av,2} = \big(-\frac{\eta_0|A_{sw}|^2\beta_y}{2k_0}e^{2\alpha_y y}e^{2\alpha_x x}\big)\hat{y} + \big(\frac{\eta_0|A_{sw}|^2\beta_x}{2k_0}e^{2\alpha_y y}e^{2\alpha_x x}\big)\hat{x}. \tag{2.56}$$

The total power over the rectangular enclosure is calculated by integration as

$$\oiint_{S} \vec{S}_{av}.d\vec{S}. \tag{2.57}$$

For each port (see Figure 2.6), we found the expressions for the total average power of incoming and outgoing waves are respectively as

$$P_1 = \int_{\frac{-L_x}{2}}^{\frac{L_x}{2}} -\frac{\eta_0 \beta_y^{'}}{2k_0} e^{2\alpha_x x} dx = -\frac{\eta_0 \beta_y^{'}}{4k_0 \alpha_x} e^{2\alpha_y y}(e^{\alpha_x L_x} - e^{-\alpha_x L_x}), \tag{2.58}$$

$$P_3 = \int_{\frac{-L_x}{2}}^{\frac{L_x}{2}} -\frac{|T|^2 \eta_0 \beta_y^{'}}{2k_0} e^{2\alpha_x x} dx = -\frac{|T^2| \eta_0 \beta_y^{'} h}{4k_0 \alpha_x} e^{2\alpha_y y}(e^{\alpha_x L_x} - e^{-\alpha_x L_x}), \tag{2.59}$$

$$P_2 = \int_{\frac{-h}{2}}^{\frac{h}{2}} \frac{\eta_0 |A_{sw}|^2 \beta_x}{2k_0} e^{2\alpha_y y} e^{2\alpha_x x} dy = \frac{\eta_0 |A_{sw}|^2 \beta_x}{4k_0 \alpha_y} e^{2\alpha_x x}(e^{h\alpha_y} - e^{-h\alpha_y}). \tag{2.60}$$

The principle of power conservation implies that $P_1 = P_2 + P_3$. Considering the limitations $\alpha_x L \ll 1$ and $\alpha_y h \ll 1$, and employing Maclaurin's expansion, we have

$$e^x = \sum_{n=0}^{\inf} \frac{x^n}{n!} = 1 + x + \frac{x^2}{2!} + \frac{x^3}{3!} + \ldots, \tag{2.61}$$

and approximating expressions by the followings

$$\begin{aligned} e^{\alpha_x L_x} - e^{-\alpha_x L_x} &\approx 2\alpha_x L_x, \\ e^{\alpha_y h} - e^{-\alpha_y h} &\approx 2\alpha_y h. \end{aligned} \tag{2.62}$$

After evaluating the average power flow around the surfaces, we obtain relations for the transmission coefficient (T), surface wave amplitude A_{sw}, surface length (L_x), and the distance between surfaces (h), as follows

$$T = \sqrt{1 - \frac{\beta_x h}{\beta_y L_x}} \qquad \text{and} \qquad A_{sw} = \sqrt{\frac{\beta_y' L_x}{\beta_x h}(1 - T^2)}. \tag{2.63}$$

2.4.3. Results of 2D Numerical Simulations

For numerical solutions, we employed the MEEP software package using the FDTD method to solve for the surfaces defined by induced currents. Figure 2.6 shows the simulation configuration and boundaries. Initially, we simulated for non-imaginary propagation constant $k_t < k_0$ stated in Section 2.3, aiming to observe negative refraction without surface wave excitation. Figure 2.7 shows the negative refraction of normalized tangential magnetic field (H_z) distribution for the cases: (i) $B_x = 0.4k_0$, (ii) $B_x = 0.7k_0$.

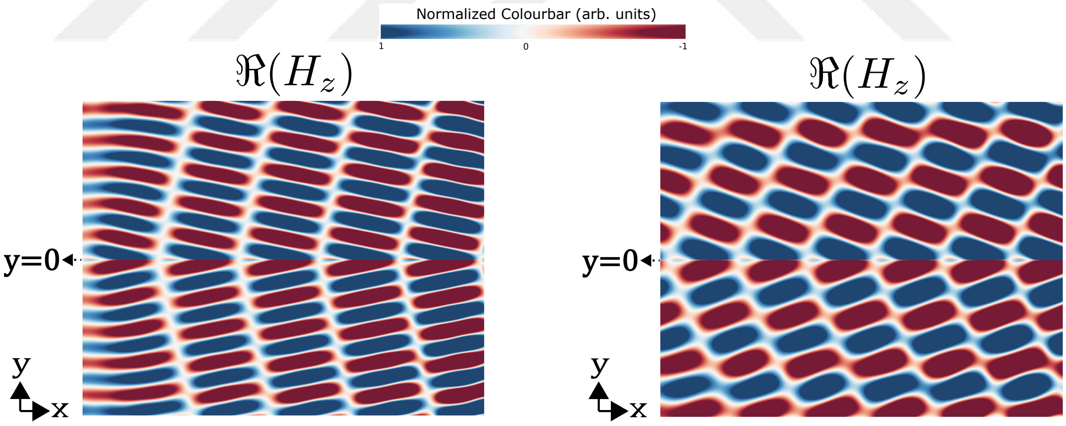

(a) (b)

Figure 2.7. $2D$ MEEP simulation results for negative refraction without surface wave excitation when $k_t < k_0$: tangential component of magnetic field (H_z) distribution for continuous source simulation (a) $B_x = 0.4k_0$, (b) $B_x = 0.7k_0$. For both simulations, $h = \lambda_0/300$, $L_x = 3.75\lambda_0$, $|T|^2 = 1$ and $\alpha_x = 0.002k_0$.

Then, we simulated the situation of imaginary propagation wavenumber, $k_t > k_0$. We first apply the Gaussian source having $f_{center} = c/\lambda_0$, $f_{width} = 0.01 f_{center}$ for power flow calculations. Figure 2.8 shows the normalized power flows in each port for forward and backward illumination cases. The results are obtained for $|T|^2$ values ranging from low to high by the tangential propagation constants α_x and β_x while maintaining fixed values for h and L_x. The conditions ar given as $0 \leq |T|^2 \leq 1$, $h \ll \lambda_0$ and $\alpha_x L_x \ll 1$.

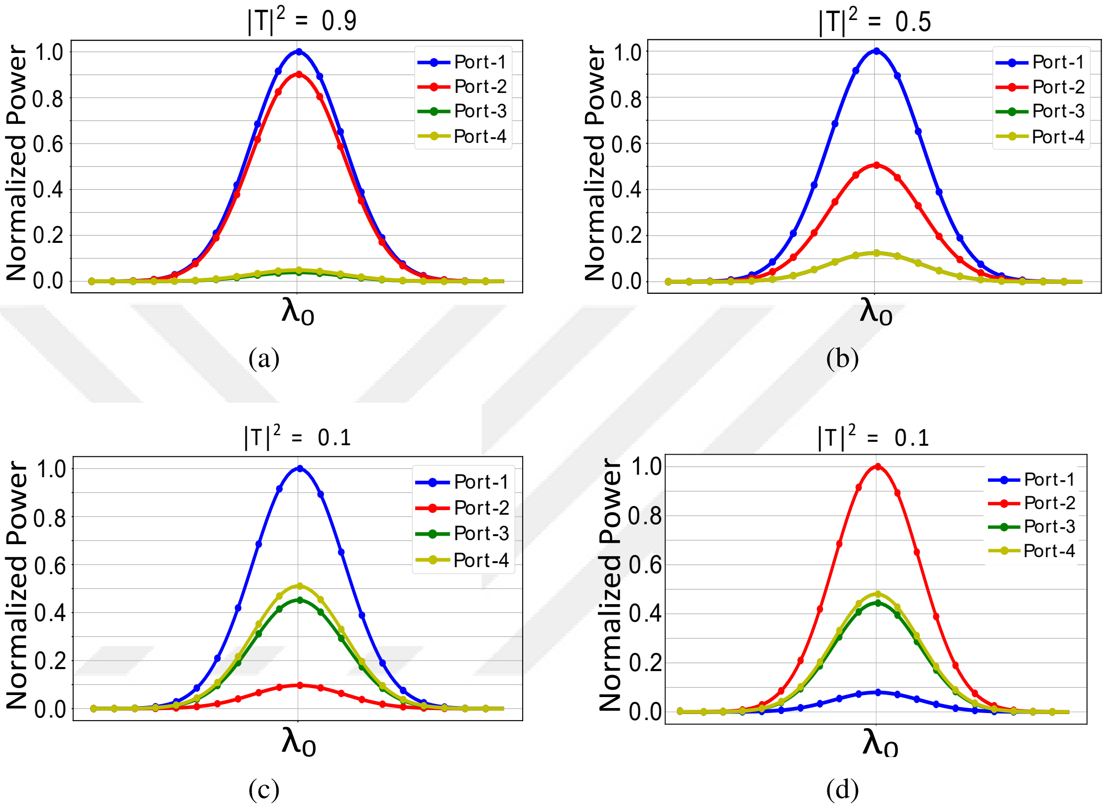

Figure 2.8. $2D$ MEEP simulation results of average power flows through each port when $k_t > k_0$ for a Gaussian source ($f_{center} = c/\lambda_0$, $f_{width} = 0.01 f_{center}$): (a)-(c) forward, (d) backward. For all simulations, $h = \lambda_0/300$ and $L_x = 3.75\lambda_0$. (a) $|T|^2 = 0.9$, $\alpha_x = 0.005k_0$, $\beta_x = 1.3k_0$. (b) $|T|^2 = 0.5$, $\alpha_x = 0.002k_0$, $\beta_x = 1.4k_0$. (c) and (d): $|T|^2 = 0.1$, $\alpha_x = 0.001k_0$, $\beta_x = 1.5k_0$ (Yılmaz and Yaman, 2024).

After, we re-simulated the same configuration for a continuous sinusoidal source ($f_0 = c/\lambda_0$). Figure 2.9 displays the normalized tangential electric field (E_x) distributions at steady-state for forward and backward incidences. These results demonstrate surface wave excitation and its coupling with the transmitting wave, allowing effective control over transmission, reflection, and absorption coefficients by adjusting the surface wave wavenumber (i.e., varying medium constituents). Figures 2.9e and 2.9f show the normalized tangential magnetic field (H_z) distribution for $|T|^2 = 0.5$ under both forward and backward illuminations in the same configuration.

Focusing on backward excitation (Port-2 as the source, see Figure 2.6), the odd-symmetry of the magnetic field causes the excited surface wave to have a π-phase delay compared to forward excitation (Port-1 as the source) while maintaining $k_x^{(2)} = k_x^{(1)}$. Applying the backward incident field in Equation 2.64 to the impedance matrix of the second surface ($\bar{Z}^{(2)}$) leads to fields as given in Equation 2.66 and Equation 2.67:

$$H_{z3}^{b} = -e^{-j\beta_y' y + \alpha_x x}, \tag{2.64}$$

$$\begin{bmatrix} E_{y2}^{b} \\ \frac{\eta_0\beta_y'}{k_0} e^{\alpha_x x} \end{bmatrix} = \begin{bmatrix} -\dfrac{\eta_0\alpha_y}{k_0} + \dfrac{\eta_0\beta_y}{k_0}\cot(\beta_x x) & \dfrac{\eta_0 A_{sw}\beta_y}{k_0\sin(\beta_x x)} \\ \dfrac{\eta_0\beta_y'}{A_{sw}k_0\sin(\beta_x x)} & \dfrac{\eta_0\beta_y'}{k_0}\cot(\beta_x x) \end{bmatrix} \begin{bmatrix} H_{z2}^{b} \\ e^{\alpha_x x}. \end{bmatrix} \tag{2.65}$$

$$H_{z2}^{b} = -A_{sw}e^{-(\alpha_y + j\beta_y)y}e^{(\alpha_x - j\beta_x)}, \tag{2.66}$$

$$E_{y2}^{f,b} = \pm\frac{j\eta_0 A_{sw}}{k_0}(\alpha_x - j\beta_x)e^{\pm(\alpha_y + j\beta_y)y}e^{(\alpha_x - j\beta_x)x}. \tag{2.67}$$

Here, the indices ^{f} and ^{b} refer to forward and backward illuminations. Figure 2.8d shows the power flow for $|T|^2 = 0.1$ under backward illumination, consistent with the forward case in Figure 2.8c.

Figure 2.10 presents the normalized normal electric field (E_y) components for both forward and backward illuminations in the same configuration, ranging from low to high transmission coefficients, as in previous simulations. The results confirm that the concentrated TM surface wave exhibits a precise π-phase difference with identical amplitude, indicating anti-symmetric surface wave generation. This allows asymmetric control of the transmission coefficient through fast time-scale manipulation, such as time modulation, allowing for potential nonreciprocal transmission.

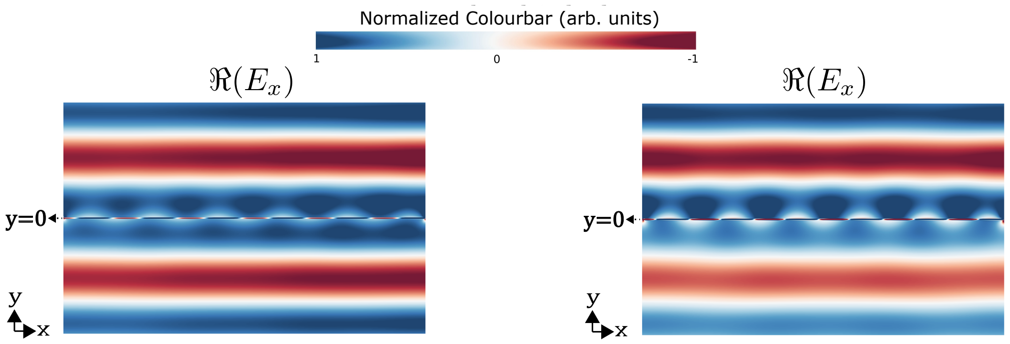

$\Re(E_x)$ $\Re(E_x)$

(a) Forward, $|T^2| = 0.9$ (b) Forward, $|T^2| = 0.5$

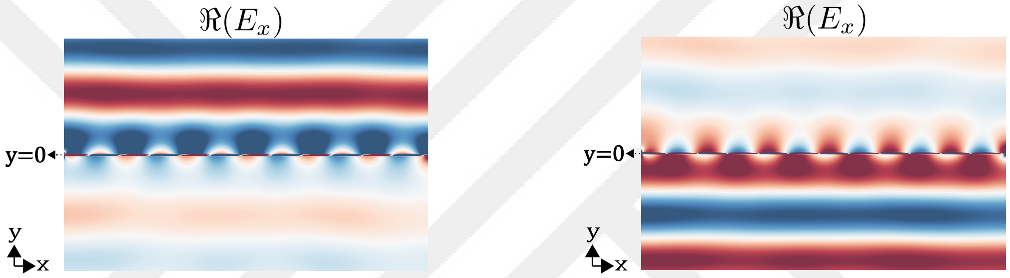

$\Re(E_x)$ $\Re(E_x)$

(c) Forward, $|T^2| = 0.1$ (d) Backward, $|T^2| = 0.1$

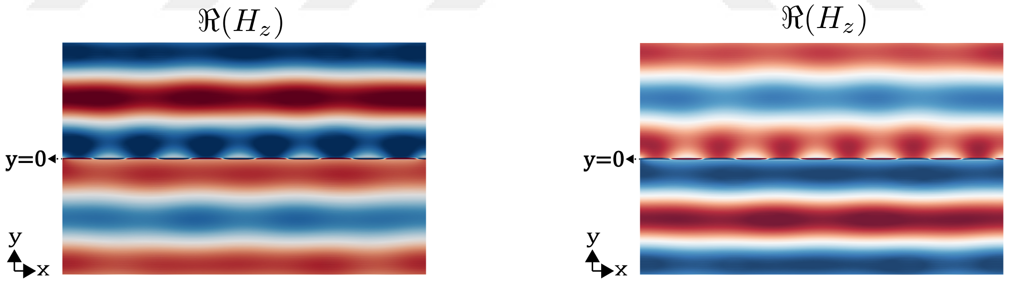

$\Re(H_z)$ $\Re(H_z)$

(e) Forward, $|T^2| = 0.5$ (f) Backward, $|T^2| = 0.5$

Figure 2.9. $2D$ MEEP simulation results of tangential fields (a)-(d) electric field E_x, (e), (f) magnetic field H_z distributions for continuous sinusoidal source when $k_t > k_0$: (a)-(c), (e) forward, (d), (f) backward illumination. For all simulations, $h = \lambda_0/300$ and $L_x = 3.75\lambda_0$. (a) $|T|^2 = 0.9$, $\alpha_x = 0.005k_0$, $\beta_x = 1.3k_0$. (b), (e), (f) $|T|^2 = 0.5$, $\alpha_x = 0.002k_0$, $\beta_x = 1.4k_0$. (c), (d): $|T|^2 = 0.1$, $\alpha_x = 0.001k_0$, $\beta_x = 1.5k_0$ (Yılmaz and Yaman (2024)).

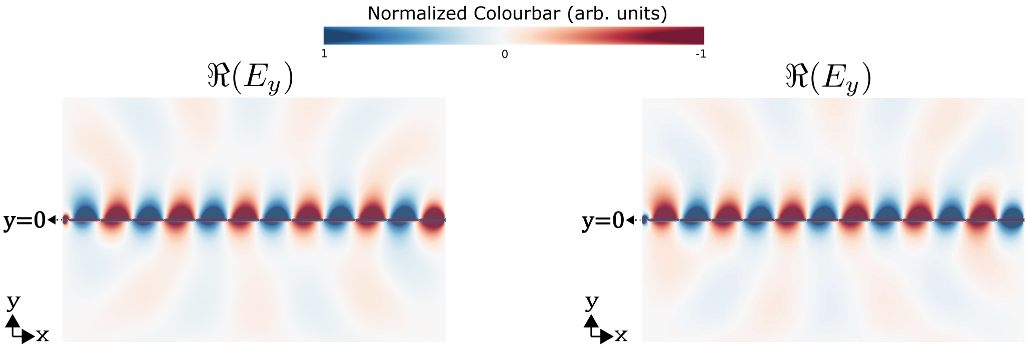

(a) Forward, $|T^2| = 0.1$ (b) Backward, $|T^2| = 0.1$

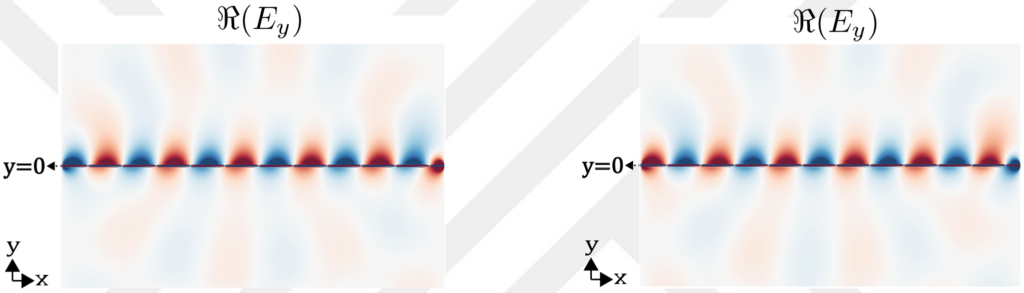

(c) Forward, $|T^2| = 0.5$ (d) Backward, $|T^2| = 0.5$

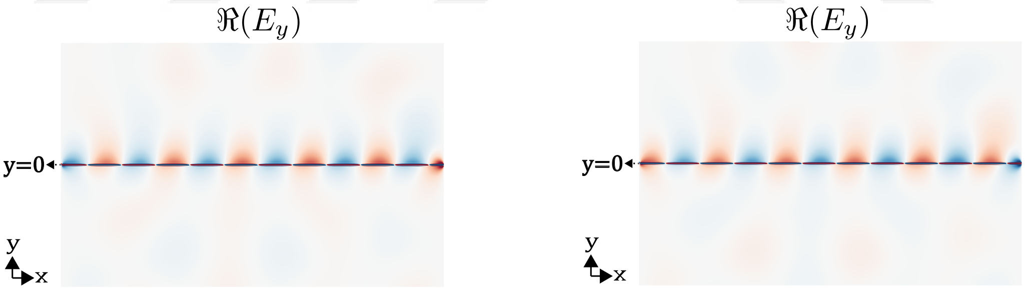

(e) Forward, $|T^2| = 0.9$ (f) Backward, $|T^2| = 0.9$

Figure 2.10. $2D$ MEEP simulation results of electric field normal component (E_y) distributions for continuous sinusoidal source when $k_t > k_0$ (a), (c), (e) forward, (b), (d), (f) backward illumination. (a), (b) $|T|^2 = 0.1$, $\alpha_x = 0.001k_0$, $\beta_x = 1.5k_0$. (c), (d) $|T|^2 = 0.5$, $\alpha_x = 0.002k_0$, $\beta_x = 1.4k_0$. (e), (f) $|T|^2 = 0.9$, $\alpha_x = 0.005k_0$, $\beta_x = 1.3k_0$. For all simulations, $h = \lambda_0/300$ and $L_x = 3.75\lambda_0$ (Yılmaz and Yaman, 2024).

CHAPTER 3

DESIGN AND CHARACTERIZATION OF BIANISOTROPIC PENETRABLE METASURFACE

Metasurfaces are characterized by effective polarizability, susceptibility, and surface impedance obtained through homogenization. This provides a practical design methodology using wave transformation matrices. Metasurfaces provide a comprehensive framework for wave engineering by extending the capabilities of the earlier artificial surfaces such as diffraction gratings, reflectarrays, frequency-selective surfaces (FSSs), and high impedance surfaces (HISs). Figure 3.1 shows a chart of artificial surfaces in terms of being homogenizable and resonant or non-resonant inclusion type (Wang, 2020; Achouri and Caloz, 2021).

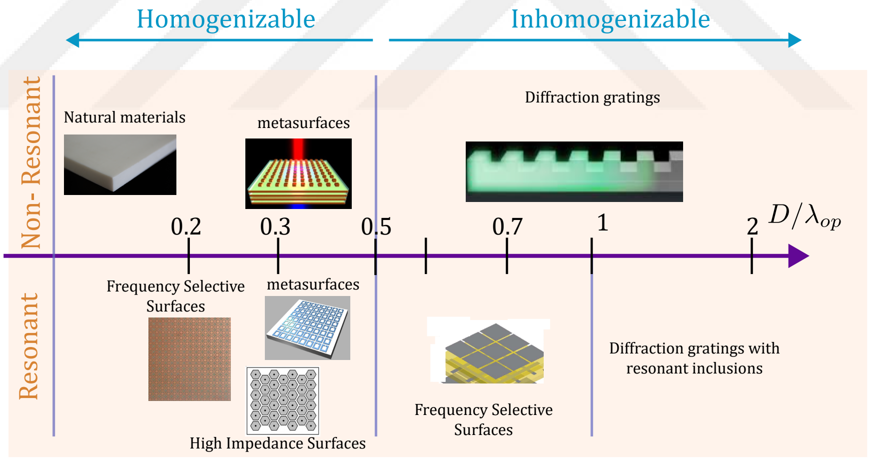

Figure 3.1. Classification of artificial thin planar structures (surfaces) by the ratio of size and wavelength and being resonance or non-resonance type (Wang, 2020).

We start with a review of the electromagnetic properties of bianisotropic metasurfaces and explore the conditions under which homogenization is possible. We then examine the boundary conditions known as generalized sheet boundary conditions (GSTCs) developed for bianisotropic surfaces. We study the impedance-based equivalent model via averaged fields and reflection/transmission coefficients. Subsequent sections present the simulation results and equivalent circuit model for the proposed 3D model designed based on the analytical findings in Chapter 2.

3.1. Electromagnetic Properties of Metasurface

Figure 3.2 shows an example design of an electrically thin metamaterial slab called a metasurface in a $d << \lambda$ condition. It can be electromagnetically characterized by susceptibility (χ), polarizability (α), and impedance (Z) based models. They define the metasurface from different analytical and modeling perspectives and can be transformed into one another. For the most general bianisotropic case, they are represented by $\bar{\bar{\chi}}$, $\bar{\bar{\alpha}}$ and $\bar{\bar{Z}}$ tensors.

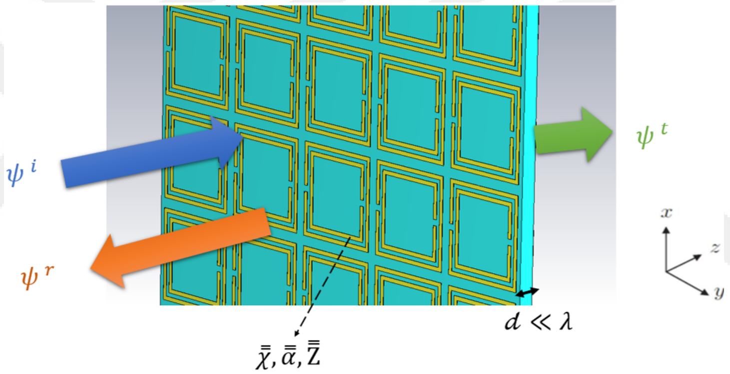

Figure 3.2. An example for illustration of metasurface in free-space with characterization matrices.

For a bianisotropic medium, the electric and magnetic polarization vectors in Equation 1.9 can be written in terms of polarizability (Tretyakov-Simovski model) and susceptibility tensors, respectively, given as (Achouri and Caloz, 2021; Albooyeh, 2015)

$$\begin{aligned} \vec{P} &= \hat{\bar{\alpha}}_{ee} \cdot \vec{E}^i + \hat{\bar{\alpha}}_{em} \cdot \vec{H}^i, \\ \vec{M} &= \hat{\bar{\alpha}}_{me} \cdot \vec{E}^i + \hat{\bar{\alpha}}_{mm} \cdot \vec{H}^i, \end{aligned} \tag{3.1}$$

$$\vec{P} = \epsilon_0 \bar{\bar{\chi}}_{ee} \cdot \vec{E} + \frac{1}{c_0} \bar{\bar{\chi}}_{em} \cdot \vec{H},$$
$$\vec{M} = \epsilon_0 \bar{\bar{\chi}}_{mm} \cdot \vec{H} + \frac{1}{\eta_0} \bar{\bar{\chi}}_{me} \cdot \vec{E}, \tag{3.2}$$

where $c_0 = 1/\sqrt{\epsilon_0 \mu_0}$, $\eta_0 = \sqrt{\mu_0/\epsilon_0}$, $\hat{\bar{\bar{\alpha}}}_{ee}$, $\hat{\bar{\bar{\alpha}}}_{em}$, $\hat{\bar{\bar{\alpha}}}_{me}$, and $\hat{\bar{\bar{\alpha}}}_{mm}$ are called electric, magnetoelectric, electromagnetic, and magnetic collective polarizability tensors, respectively. Here, ^{i} denotes the incident wave and the hat ($\hat{a}$) denotes the collective term, which establish the relationship between the incident fields and the surface polarizations. Substituting Equation 3.2 into Equation 1.9, the constitutive relation is expressed as

$$\vec{D} = \epsilon_0 (\bar{\bar{I}} + \bar{\bar{I}} \bar{\bar{\chi}}_{ee}) \cdot \vec{E} + \frac{1}{c_0} \bar{\bar{\chi}}_{em} \cdot \vec{H},$$
$$\vec{B} = \mu_0 (\bar{\bar{I}} + \bar{\bar{I}} \bar{\bar{\chi}}_{mm}) \cdot \vec{H} + \frac{1}{c_0} \bar{\bar{\chi}}_{me} \cdot \vec{E}, \tag{3.3}$$

where $\bar{\bar{I}}$ is the unity dyadic tensor. This relation can be represented in a more compact form as

$$\vec{D} = \bar{\epsilon} \cdot \vec{E} + \bar{\bar{\xi}} \cdot \vec{H},$$
$$\vec{B} = \bar{\bar{\zeta}} \cdot \vec{E} + \bar{\mu} \cdot \vec{H}, \tag{3.4}$$

where $\bar{\epsilon}$ (F/m), $\bar{\mu}$ (H/m), $\bar{\bar{\xi}}$ (s/m) and $\bar{\bar{\zeta}}$ (s/m) are the permittivity, permeability, magnetoelectric coupling and electromagnetic coupling tensors, respectively. Each contains $3 \times 3 = 9$ susceptibility components, so there are a total of $4 \times 9 = 36$ susceptibilities. If temporal dispersion (or time-varying) is considered, they can be mathematically expressed, for example, in the case of simple isotropic materials, as (Achouri and Caloz, 2021)

$$\mathcal{D}(t) = \epsilon_0 \mathcal{E}(t) + \int_{-\infty}^{T} \left(\epsilon_0 \hat{\chi}_{ee}(t - t') \cdot \mathcal{E}(t') + \frac{1}{c_0} \hat{\chi}_{em}(t - t') \cdot \mathcal{H}(t') \right) dt', \tag{3.5}$$

$$\mathcal{B}(t) = \mu_0 \mathcal{H}(t) + \int_{-\infty}^{T} \left(\mu_0 \hat{\chi}_{mm}(t - t^{'}) \cdot \mathcal{H}(t^{'}) + \frac{1}{c_0} \hat{\chi}_{me}(t - t^{'}) \cdot \mathcal{E}(t^{'}) \right) dt^{'}, \tag{3.6}$$

where $\mathcal{D}(t)$, $\mathcal{B}(t)$, $\mathcal{E}(t)$ and $\mathcal{H}(t)$ are time-domain forms of the electric and magnetic flux densities and fields, respectively. These expression implies the convolution of the susceptibilities over the fields themselves, as given by the following

$$\mathcal{D}(t) = \epsilon_0 \mathcal{E}(t) + \epsilon_0 \hat{\chi}_{ee}(t) * \mathcal{E}(t) + \frac{1}{c_0} \hat{\chi}_{em}(t) * \mathcal{H}(t), \tag{3.7}$$

$$\mathcal{B}(t) = \mu_0 \mathcal{H}(t) + \mu_0 \hat{\chi}_{mm}(t) * \mathcal{H}(t) + \frac{1}{c_0} \hat{\chi}_{me}(t) * \mathcal{E}(t). \tag{3.8}$$

In the absence of external bias, Lorentz reciprocity conditions ensure the following (Asadchy, 2017)

$$\bar{\bar{\epsilon}} = \bar{\bar{\epsilon}}^T, \qquad \bar{\bar{\mu}} = \bar{\bar{\mu}}^T \qquad \text{and} \qquad \bar{\bar{\xi}} = -\bar{\bar{\zeta}}^T, \tag{3.9}$$

and similarly in terms of susceptibilities can be written as

$$\bar{\bar{\chi}}_{ee} = \bar{\bar{\chi}}_{ee}^T, \qquad \bar{\bar{\chi}}_{mm} = \bar{\bar{\chi}}_{mm}^T \qquad \text{and} \qquad \bar{\bar{\chi}}_{me} = -\bar{\bar{\chi}}_{em}^T. \tag{3.10}$$

According to causality and the Kramers-Kronig Relation, in the case of a lossless and passive medium (without gain), the self susceptibilities are purely real, while the coupling susceptibilities are purely imaginary, indicated as

$$\Im(\bar{\bar{\chi}}_{ee,mm}) = 0 \qquad \text{and} \qquad \Re(\bar{\bar{\chi}}_{me,em}) = 0. \tag{3.11}$$

We introduced the four types of bianisotropy in Chapter 1. Those are chiral (χ) and omega (Ω) coupling for reciprocal, and Tellegen and moving-media for nonreciprocal medium. We concluded in Chapter 2 with the necessity of Ω-type bianisotropy to design a metasurface with proposed functionalities. We now review that condition detailed in the literature (Achouri and Caloz, 2021; Asadchy, 2017). The magnetoelectric and electromagnetic coupling terms of the susceptibility tensor, $\bar{\bar{\chi}}_{em}$ and $\bar{\bar{\chi}}_{me}$ can be split into tensors as

$$\bar{\bar{\chi}}_{em} = \bar{\bar{\nu}} - j\bar{\bar{\kappa}} \qquad \text{and} \qquad \bar{\bar{\chi}}_{me} = (\bar{\bar{\nu}} + j\bar{\bar{\kappa}})^T, \tag{3.12}$$

where $\bar{\bar{\nu}}$ and $\bar{\bar{\kappa}}$ are respectively related to nonreciprocity and chirality. The arbitrary tensor $\bar{\bar{U}}$ may represent the either $\bar{\bar{\kappa}}$ (reciprocal medium) or $\bar{\bar{\nu}}$ (nonreciprocal medium), can be decomposed as

$$\bar{\bar{U}} = \bar{\bar{D}} + \bar{\bar{N}} \tag{3.13}$$

Here, $\bar{\bar{D}}$ represents the diagonal tensor, and $\bar{\bar{N}}$ is a traceless tensor that can be decomposed into symmetric and anti-symmetric components given by

$$\bar{\bar{S}} = \frac{\bar{\bar{N}} + \bar{\bar{N}}^T}{2} \qquad \text{and} \qquad \bar{\bar{A}} = \frac{\bar{\bar{N}} - \bar{\bar{N}}^T}{2}, \tag{3.14}$$

and so the tensor $\bar{\bar{U}}$ can be expressed by

$$\bar{\bar{U}} = \bar{\bar{D}} + \bar{\bar{S}} + \bar{\bar{A}}. \tag{3.15}$$

If the $\bar{\bar{D}} = 0$, $\bar{\bar{S}} = 0$ and $\bar{\bar{A}} \neq 0$, coupling type is called as Ω-type. One of the fundamental attributes of an Ω-bianisotropic medium is the giving of different reflection responses for the opposite incident waves.

3.2. Periodic Structures and Bloch-Floquet Modes

This section reviews the expressions for homogenizing metasurfaces and the associated conditions using the Bloch-Floquet analysis (Achouri and Caloz, 2021). Metamaterial/metasurface phenomena mainly are based on the homogeneity theory of EM medium. While viewing an array of scattering particles (e.g., gratings) as a spatially varying refractive index structure, there are restrictions in treating a periodic arrangement as fully homogenized. In an example in literature (Achouri and Caloz, 2021), they consider the one-dimensional (1D) periodic structure shown in Figure 3.3, consisting of a unit cell of length L_{per} with two segments having refractive indices n_a and n_b, respectively.

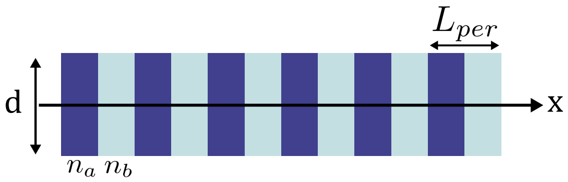

Figure 3.3. Illustration of 1D periodic scattering array with period L_{per} (Achouri and Caloz, 2021).

Based on the Bloch-Floquet theorem, the wave $\Psi(x)$ interacting with this structure must satisfy the translation symmetry condition expressed by

$$\frac{\Psi(x+L_{per})}{\Psi(x)} = \frac{\Psi(x+2L_{per})}{\Psi(x+L_{per})} = \cdots = \frac{\Psi(x+pL_{per})}{\Psi(x+(p-1)L_{per})} = C. \tag{3.16}$$

Here, p is an integer (i.e., $\cdots -2, -1, 0, 1, 2, \dots$), and C represents a complex coefficient with unit magnitude. The field at a given point in neighboring cells can differ solely by a phase factor, such as

$$C = e^{-jk_x L_{per}}, \tag{3.17}$$

where k_x is the x component of the wavenumber. Equation 3.16 now can be expressed as

$$\Psi(x+pL_{per}) = C\Psi\big[x+(p-1)L_{per}\big] = C\big\{C\Psi\big[x+(p-2)L_{per}\big]\big\} = \cdots = C^p\Psi(x). \tag{3.18}$$

The function $\Psi(x)$ is associated with a periodic function $A(x)$ given by

$$A(x) = e^{jk_x x}\Psi(x). \tag{3.19}$$

Further $A(x)$ can be expressed as a Fourier series expansion given as

$$A(x) = \sum_{m=-\infty}^{+\infty} A_m e^{j\frac{2m\pi}{L_{per}}x}. \tag{3.20}$$

Substituting this expansion into Equation 3.19, the wave function is written as

$$\Psi(x) = \sum_{m=-\infty}^{+\infty} A_m e^{-jk_{x,m}x} \qquad \text{where} \qquad k_{x,m} = k_x + \frac{2m\pi}{L_{per}}. \tag{3.21}$$

This represents the final expression of the Bloch-Floquet Theorem by a combination of plane waves, where the propagation constant $k_{x,m}$ is associated with the periodicity L_{per} of the structure. For subwavelength-thin ($d << \lambda$) gratings positioned between media with lossless refractive indexes n_1 and n_2, respectively, in case of obliquely incident, the scattering of both the reflected and transmitted waves at $y = 0$ are expressed in following

$$\begin{gathered}\Psi_r(x,0) = \sum_{m=-\infty}^{+\infty} A_{r,m} e^{-jk_{x,m}x}, \\ \Psi_t(x,0) = \sum_{m=-\infty}^{+\infty} A_{t,m} e^{-jk_{x,m}x}.\end{gathered} \tag{3.22}$$

The normal component of propagation constants (k_y) for the reflected and transmitted diffraction orders is expressed as

$$k_{r,y} = -\sqrt{k_1^2 - k_{x,m}^2} \qquad \text{and} \qquad k_{t,y} = -\sqrt{k_2^2 - k_{x,m}^2}, \tag{3.23}$$

where $k_1 = k_0 n_1$, $k_2 = k_0 n_2$ and k_x refers to the tangential wavenumber of the incident wave Ψ_i. These formulas can help consider if the diffraction orders are propagating ($k_{y,m} \in \Re$) or evanescent ($k_{y,m} \in \Im$) in the z-direction.

We continue the review with the conditions for homogenizing the metasurface into a thin, uniform layer described by effective parameters. To achieve homogeneity, only waves corresponding to $m = 0$ should propagate into the far field, while all other waves must remain confined as surface waves. This establishes a relationship between the array period and the wavelength of the incident wave.

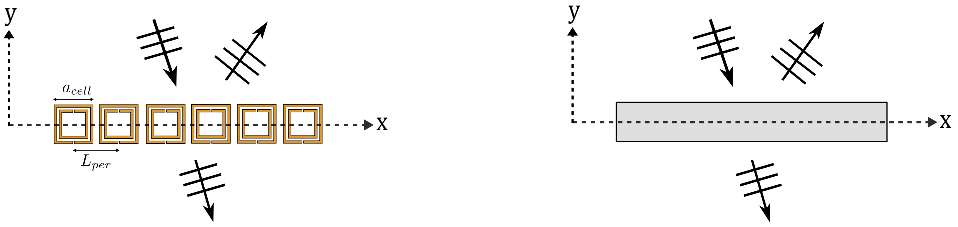

(a) Metasurface (b) Homogenized Medium

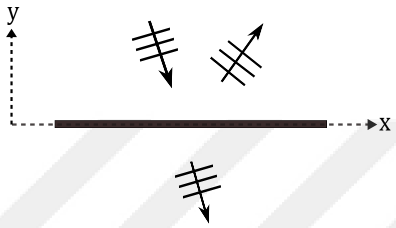

(c) Zero Thickness Model

Figure 3.4. Illustrations of representative steps for the metasurface homogenization concept: (a) an example metasurface composed of a subwavelength periodic array of split-ring resonators, (b) a slab with homogenized effective material parameters corresponding to the metasurface, (c) a zero-thickness sheet model characterized by effective parameters (Achouri and Caloz, 2021).

In one-dimensional (1D) cases, this relationship is given by

$$\sqrt{k^2 - k_{x,m}^2} = \sqrt{k^2 - \left(k_x + \frac{2m\pi}{L_{per}}\right)^2}, \tag{3.24}$$

where k represents either k_1 or k_2. To prevent nonzero diffraction orders, the term inside the square root must be negative for $m \neq 0$. This is achieved if the following condition holds true,

$$\pm k < k_x + \frac{2m\pi}{L_{per}}. \tag{3.25}$$

To suppress the diffraction orders associated with $m \neq 0$, it is necessary to limit the value of L_{per} sufficiently so that Equation 3.25 is satisfied for $|m| = 1$. This condition ensures Equation 3.25 for $|m| > 1$, suppressing all nonzero diffraction orders, such as,

$$L_{per} < |\frac{2\pi}{k - k_x}|. \tag{3.26}$$

For the incident wave coming from medium n_1 at an angle θ, where $k_x = k_1 \sin(\theta_i)$, setting $\theta_i = 90^\circ$ as the upper bound results in

$$L_{per} < \frac{\lambda_{av}}{2}, \tag{3.27}$$

where average of wavelength is defined as $\lambda_{av} = 2\lambda_0/(n_a + n_b)$. An important point is if the incident wave is perpendicular to the array ($\theta_i = 0$), then the requirement becomes $L_{per} < \lambda_{av}$. This implies that homogenization of the metasurface is more feasible for near-normal incidences than grazing angles.

We reviewed the analysis that an electromagnetically thin periodic array with a subwavelength period can be homogenized into a thin slab exhibiting effective material parameters, as illustrated in Figure 3.4a and Figure 3.4b. It is necessary to develop an appropriate theoretical model to derive its effective medium parameters. Given its electrical thickness ($d/\lambda \to 0$), the spatial variations of the fields across it are negligible. Hence, it can be represented as a zero-thickness sheet, as depicted in Figure 3.4c. Mathematically, this representation can be expressed by

$$\frac{\partial \Psi(x,y)}{\partial y} \approx 0 \qquad \text{for} \qquad y = [-d/2, d/2], \tag{3.28}$$

where $\Psi(x,z)$ refers to the total field through the metasurface.

3.3. Generalized Sheet Transition Conditions

Bianisotropic surfaces can induce electric and magnetic polarizations, as shown in Figure 3.5. In this part, we review the boundary conditions called GSTCs developed for such a medium (Albooyeh, 2015; Holloway and Kuester, 2016). Assume that the elements of the unit cell are embedded in a host medium characterized by the permittivity

(ϵ) and permeability (μ). Metasurface is situated at the interface of two half-spaces with characteristic impedances $\eta_1 = \sqrt{\mu_1/\epsilon_1}$ and $\eta_2 = \sqrt{\mu_2/\epsilon_2}$.

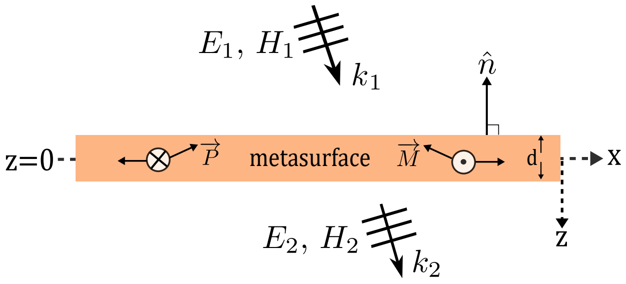

Figure 3.5. Equivalent boundary model for the bianisotropic metasurface with electric and magnetic polarizations.

The phasor forms of Maxwell's equations are written in Equation 3.30 considering the bulk electric and magnetic polarizations within the homogeneous slab of thickness d.

$$\nabla \times \vec{E} = -j\omega\mu\big(\vec{H} + \frac{\vec{M}}{\mu}\big), \qquad \nabla \times \vec{H} = j\omega\epsilon\big(\vec{E} + \frac{\vec{P}}{\epsilon}\big),$$
$$\nabla.(\epsilon\vec{E} + \vec{P}) = 0, \qquad \nabla.(\mu\vec{H} + \vec{M}) = 0, \tag{3.29}$$

where $\vec{P}$ and $\vec{M}$ represent the electric and magnetic bulk polarizations inside the slab. They are averaged over the unit cell area. Further, decomposing fields and polarizations into normal (denoted by subscript $_n$) and transverse (denoted by subscript $_t$) components allows to establish the relationship between the tangential electric and magnetic fields on the two sides of the slab (Albooyeh, 2015; Wang, 2020). The fields and polarizations can be rewritten as

$$\vec{E} = \vec{E}_t + \hat{n}E_n \qquad \text{and} \qquad \vec{H} = \vec{H}_t + \hat{n}H_n, \tag{3.30}$$

$$\vec{P} = \vec{P}_t + \hat{n}P_n \qquad \text{and} \qquad \vec{M} = \vec{M}_t + \hat{n}H_n, \tag{3.31}$$

and similarly for the ∇ operator, i.e.,

$$\nabla = \nabla_t + \frac{\partial}{\partial z}\hat{n}. \tag{3.32}$$

Here, the normal direction is along the z-axis. After substitution into Maxwell's equations, two sets of equations are obtained. The tangential components are given by

$$\begin{aligned} \nabla_t \times \hat{n}E_n + \frac{\partial}{\partial z}(\hat{n} \times \vec{E}_t) &= -j\omega\mu\vec{H}_t - j\omega\vec{M}_t, \\ \nabla_t \times \hat{n}H_n + \frac{\partial}{\partial z}(\hat{n} \times \vec{H}_t) &= j\omega\mu\vec{E}_t + j\omega\vec{P}_t, \end{aligned} \tag{3.33}$$

and transversal parts are given by

$$\begin{aligned} \hat{n}E_n &= \frac{1}{j\omega\epsilon}\nabla_t \times \vec{H}_t - \hat{n}\frac{P_n}{\epsilon}, \\ \hat{n}H_n &= -\frac{1}{j\omega\mu}\nabla_t \times \vec{E}_t - \hat{n}\frac{M_n}{\mu}. \end{aligned} \tag{3.34}$$

The incident fields can be assumed to be uniform over the subwavelength inclusions (unit cell). The total fields on the metasurface plane may change rapidly and dramatically due to magnetic and electric polarization induced by the incident fields. The effective values can be obtained by using averaged quantities described as

$$\vec{E}_{t,ave} = \frac{1}{d}\int_0^d \vec{E}_t dz \qquad \text{and} \qquad \vec{H}_{t,ave} = \frac{1}{d}\int_0^d \vec{H}_t dz. \tag{3.35}$$

Equations 3.33-3.34 are integrated over the surface thickness, considering that the field distributions inside the slab are locally quasi-static in the normal direction z. This assumption remains valid when the thickness of the slab is electrically significantly smaller than the wavelength. The surface polarization densities are averaged by

$$\vec{P}_{ave} = \frac{1}{d}\int_0^d \vec{P} dz \qquad \text{and} \qquad \vec{M}_{ave} = \frac{1}{d}\int_0^d \vec{M} dz, \tag{3.36}$$

and effective surface polarizations are found by

$$\tilde{P} = \vec{P}_{ave}d \qquad \text{and} \qquad \tilde{M} = \vec{M}_{ave}d. \tag{3.37}$$

Continuous electric and/or magnetic current sheets can replace finite-size inclusions by employing the equivalence theorem. The expressions for the electric and magnetic surface currents as a time-derivation of effective polarization surface densities $\tilde{P}$ and $\tilde{M}$, are given in the following

$$\vec{J}_e = \frac{\partial \tilde{P}}{\partial t} \qquad \text{and} \qquad \vec{J}_m = \mu \frac{\partial \tilde{M}}{\partial t}, \tag{3.38}$$

and these can be decomposed into their tangential and normal components given as

$$\tilde{P} = \tilde{P}_t + \hat{n}P_n \qquad \text{and} \qquad \tilde{M} = \tilde{M}_t + \hat{n}M_n. \tag{3.39}$$

The equations 3.33-3.34 now can be written explicitly considering the field on both sides. Taking the limit as the slab thickness tends to zero ($d \rightarrow 0$), the GSTCs equations can be written as (Albooyeh, 2015; Achouri and Caloz, 2021)

$$\begin{aligned}
\hat{n} \times (\vec{E}_t^2 - \vec{E}_t^1) &= j\omega\mu_0 \hat{n} \times \vec{M}_t - \nabla_t \frac{P_n}{\epsilon_0}, & \qquad \hat{n} \cdot (\vec{E}_t^2 - \vec{E}_t^1) &= -\nabla \cdot \frac{\vec{P}_t}{\epsilon_0}, \\
\hat{n} \times (\vec{H}_t^2 - \vec{H}_t^1) &= j\omega \vec{P}_t - \hat{n} \times \nabla_t M_n, & \qquad \hat{n} \cdot (\vec{H}_t^2 - \vec{H}_t^1) &= -\nabla \cdot \vec{M}_t.
\end{aligned} \tag{3.40}$$

The discontinuity of the fields refers to the effective total electric and magnetic currents defined as

$$(\vec{E}_t^2 - \vec{E}_t^1) \times \hat{n} = \vec{M}_s \qquad \text{and} \qquad \hat{n} \times (\vec{H}_t^2 - \vec{H}_t^1) = \vec{J}_s. \tag{3.41}$$

A relationship between the effective currents and the averaged field can be established via the tensors $\bar{\bar{Z}}se$ and $\bar{\bar{Y}}sm$, which are defined as surface electric impedance and surface magnetic admittance, respectively, and expressed as (Chen, 2021)

$$\vec{E}_{t,ave} = \bar{\bar{Z}}_{se}\vec{J}_s \qquad \text{and} \qquad \vec{H}_{t,ave} = \bar{\bar{Y}}_{sm}\vec{M}_s. \tag{3.42}$$

In the literature, GSTCs can defined based on the susceptibility model expressed by (Budhu and Grbic, 2021; Albooyeh, 2015)

$$\begin{aligned} \vec{P} &= \hat{\bar{\bar{\chi}}}_{ee} \cdot \vec{E}_{ave} + \hat{\bar{\bar{\chi}}}_{em} \cdot \vec{H}_{ave}, \\ \vec{M} &= \hat{\bar{\bar{\chi}}}_{me} \cdot \vec{E}_{ave} + \hat{\bar{\bar{\chi}}}_{mm} \cdot \vec{H}_{ave}. \end{aligned} \tag{3.43}$$

Here, $\hat{\bar{\bar{\chi}}}$ indicates effective surface susceptibility tensors which are defined as, $\hat{\bar{\bar{\chi}}}_{ee} = \epsilon_0\bar{\bar{\chi}}_{ee}$, $\hat{\bar{\bar{\chi}}}_{em} = \sqrt{\mu_0\epsilon_0}\bar{\bar{\chi}}_{em}$, $\hat{\bar{\bar{\chi}}}_{me} = \sqrt{\frac{\epsilon_0}{\mu_0}}\bar{\bar{\chi}}_{me}$ and $\hat{\bar{\bar{\chi}}}_{mm} = \bar{\bar{\chi}}_{mm}$. The averaged fields are calculated in terms of incident, reflected, and transmitted fields as

$$\vec{E}_{ave} = \frac{\vec{E}_i + \vec{E}_r + \vec{E}_t}{2} \qquad \text{and} \qquad \vec{H}_{ave} = \frac{\vec{H}_i + \vec{H}_r + \vec{H}_t}{2}. \tag{3.44}$$

Note that all these fields are surface averaged over unit cell areas, so only propagating Floquet harmonics contribute to these equations, and they are taken at the metasurface plane ($z = 0$).

The bianisotropic surface can also be characterized with the surface impedance-based model. It provides a relationship between the tangential fields and surface currents ($\vec{J}_s$ and $\vec{M}_s$, respectively) induced on the magnetodielectric surface. When normal surface polarization and magnetization densities are neglected, i.e., $P_{s,n} = 0$ and $M_{s,n} = 0$, the GSTCs can be expressed in terms of surface impedances and bianisotropic couplings as

$$\begin{aligned} \hat{z} \times \vec{E}_{ave} &= \bar{\bar{Z}}_{se} \cdot [\hat{z} \times \Delta\vec{H}_{ave}] + \bar{\bar{K}}_{me} \cdot [\hat{z} \times \Delta\vec{E}_{ave}], \\ \hat{z} \times \vec{H}_{ave} &= \bar{\bar{K}}_{em} \cdot [\hat{z} \times \Delta\vec{H}_{ave}] + \bar{\bar{Y}}_{sm} \cdot [\hat{z} \times \Delta\vec{E}_{ave}], \end{aligned} \tag{3.45}$$

where $\bar{\bar{K}}me$, $\bar{\bar{K}}em$, $\bar{\bar{Z}}_{se}$ and $\bar{\bar{Y}}_{sm}$ are, respectively related to the inverses of the electromagnetic couplings ($\bar{\bar{X}}$), magnetoelectric couplings ($\bar{\bar{\gamma}}$), electric surface admittance ($\bar{\bar{Y}}_{se}$) and magnetic surface impedance ($\bar{\bar{Z}}_{sm}$) tensors, which are expressed in dimensionless form respectively as

$$\begin{aligned} \bar{\bar{X}} &= \left(j\omega\sqrt{\epsilon_0\mu_0}\right)\bar{\bar{\chi}}_{em}, & \bar{\bar{\gamma}} &= \left(j\omega\sqrt{\epsilon_0\mu_0}\right)\bar{\bar{\chi}}_{me}, \\ \bar{\bar{Y}}_{se} &= j\omega\epsilon_0\bar{\bar{\chi}}_{ee}, & \bar{\bar{Z}}_{sm} &= j\omega\mu_0\bar{\bar{\chi}}_{mm}. \end{aligned} \tag{3.46}$$

Finally, the impedance boundary condition (IBC) for bianisotropic surface can be expressed in the following form as set of equations;

$$\begin{bmatrix} \vec{J}_s \\ \vec{M}_s \end{bmatrix} = \begin{bmatrix} \bar{\bar{Y}}_{se} & \bar{\bar{X}} \\ \bar{\bar{\gamma}} & \bar{\bar{Z}}_{sm} \end{bmatrix} \begin{bmatrix} \vec{E}_{t,ave} \\ \vec{H}_{t,ave} \end{bmatrix}. \tag{3.47}$$

3.4. Equivalent Circuit Model For $\Omega-$Bianisotropic Metasurface

In the previous section, we reviewed the derivation for the tensor relation of GSTCs through the averaged fields and impedance-based parameters for Ω-bianisotropic metasurface. The general expression is for an anisotropic medium in Cartesian coordinates involving 3×1 field vectors and 3×3 electric and magnetic impedance (or admittance) and coupling matrices. In this section, we consider the fixed orientation and particular excitation fields while constructing the equivalent transmission-line (TL) circuit model. It is typically represented as a two-wire line for transverse EM (TEM) wave propagation (Pozar, 2012).

The impedance-based model of GSTCs is written in Equation 3.48 along the surface as a function of x for TEM waves propagating in the z direction, which is normal to the surface, as shown in Figure 3.6a.

$$\begin{aligned} \vec{E}_{t,ave}(x) &= Z_{se}(x)\vec{J}_s(x) - K_{em}(x)\left[\hat{z} \times \vec{M}_s(x)\right], \\ \vec{H}_{t,ave}(x) &= Y_{sm}(x)\vec{M}_s(x) - K_{em}(x)\left[\hat{z} \times \vec{J}_s(x)\right]. \end{aligned} \tag{3.48}$$

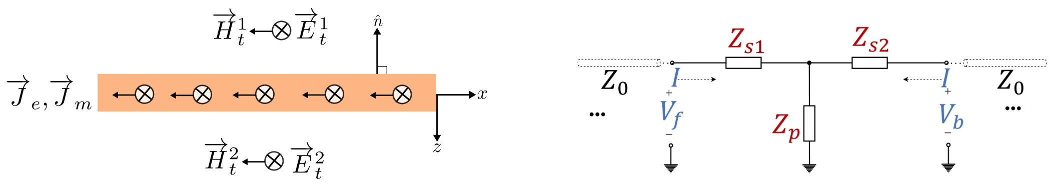

(a) (b)

Figure 3.6. Representation of metasurface model for TEM wave incident, (a) illustration of metasurface with equivalent surface currents and tangential fields, (b) equivalent TL T-circuit model. $V_{f,b}$ refer to the $E_t^{1,2}$, respectively, and I refers to $\hat{n} \times H_t^{1,2}$.

The surface is passive and lossless when both the impedance and admittance are purely reactive, along with the magnetoelectric coefficient being purely real, i.e., $\Re(Z_{se}) = \Re(Y_{sm}) = \Im(K_{em}) = 0$. Accordingly, these quantities are calculated using the equations 3.49-3.51 (Epstein and Eleftheriades, 2016) for the given problem.

$$K_{em} = \frac{1}{2} \frac{\Re\left\{ E_x^+ H_y^{-*} - E_x^- H_y^{+*} \right\}}{\Re\left\{ (E_x^+ - E_x^-)(H_y^+ - H_y^{-*}) \right\}}, \tag{3.49}$$

$$Y_{sm} = -j\left(\frac{1}{2}\Im\left\{ \frac{H_y^+ + H_y^-}{E_x^+ - E_x^-} \right\} - K_{em}\Im\left\{ \frac{H_y^+ - H_y^-}{E_x^+ - E_x^-} \right\} \right), \tag{3.50}$$

$$Z_{se} = -j\left(\frac{1}{2}\Im\left\{ \frac{E_x^+ + E_x^-}{H_y^+ - H_y^-} \right\} + K_{em}\Im\left\{ \frac{E_x^+ - E_x^-}{H_y^+ - H_y^-} \right\} \right). \tag{3.51}$$

For the normal incidence of a TEM wave, the TL equivalent circuit of the metasurface can be represented as a 2-port T circuit model (or $Y-$matrix for $\Pi-$Circuit) which is illustrated in Figure 3.6b. For an Ω-type structure, the asymmetric reflection depending on the illumination direction implies that $Z_{s1} \neq Z_{s2}$. The quantity $\Delta_Z = Z_{s1} - Z_{s2}$ quantifies the strength of the Ω coupling. The asymmetric phase response approaches the ideal π-phase delay when this coupling is sufficiently strong and dominant. The general representation of the two-port Z matrix of the T-circuit, which relates the tangential fields across the medium, is given as (Pozar, 2012)

$$\begin{bmatrix} E_{x,1} \\ E_{x,2} \end{bmatrix} = \begin{bmatrix} Z_{11}^T & Z_{12}^T \\ Z_{21}^T & Z_{22}^T \end{bmatrix} \begin{bmatrix} H_{y,1} \\ -H_{y,2} \end{bmatrix}, \tag{3.52}$$

where elements of the impedance matrix are expressed in equations 3.53-3.55 in terms of the derived surface impedances.

$$Z_{11}^T = Z_{se} + \frac{\frac{1}{4} - \frac{1}{2}K_{me} + \frac{1}{2}K_{em} - K_{em}K_{me}}{Y_{sm}}, \tag{3.53}$$

$$Z_{22}^T = Z_{se} + \frac{\frac{1}{4} + \frac{1}{2}K_{me} - \frac{1}{2}K_{em} - K_{em}K_{me}}{Y_{sm}}, \tag{3.54}$$

$$Z_{12}^T = Z_{21}^T = Z_{se} - \frac{1 \mp 2(K_{me} + K_{em}) + 4K_{em}K_{me}}{4Y_{sm}}. \tag{3.55}$$

For a reciprocal medium, the magnetoelectric coupling coefficient is $K_{me} = -K_{em}$. Finally, we can calculate the impedance matrix by

$$\begin{bmatrix} Z_{11}^T & Z_{12}^T \\ Z_{21}^T & Z_{22}^T \end{bmatrix} = \begin{bmatrix} \frac{1}{2} - K_{em} & \frac{1}{2} + K_{em} \\ -Y_{sm} & Y_{sm} \end{bmatrix}^{-1} \begin{bmatrix} Z_{se} & Z_{se} \\ -\frac{1}{2} + K_{me} & \frac{1}{2} + K_{me} \end{bmatrix}, \tag{3.56}$$

where the determinant (Δ_{det}) is found as

$$\Delta_{det} = \frac{1}{2}Y_{sm} + K_{em}Y_{sm} + \frac{1}{2}Y_{sm} - Y_{sm}K_{em} = Y_{sm}. \tag{3.57}$$

Then, the impedance matrix is found as

$$\begin{bmatrix} Z_{11}^T & Z_{12}^T \\ Z_{21}^T & Z_{22}^T \end{bmatrix} = \frac{1}{Y_{sm}} \begin{bmatrix} Y_{sm} & -\frac{1}{2} - K_{em} \\ Y_{sm} & \frac{1}{2} - K_{em} \end{bmatrix} \begin{bmatrix} Z_{se} & Z_{se} \\ -\frac{1}{2} + K_{me} & \frac{1}{2} + K_{me} \end{bmatrix}. \tag{3.58}$$

The series and parallel impedances of the equivalent circuit in Figure 3.6b are calculated by

$$Z_{s1} = \frac{1}{2} Z_{sm} + K_{em} Z_{sm}, \qquad Z_{s2} = \frac{1}{2} Z_{sm} + K_{me} Z_{sm}, \qquad Z_p = Z_{12}^T = Z_{21}^T. \tag{3.59}$$

3.4.1. Retrieval From Reflection/Transmission Coefficients

This section reviews the S-parameter retrieval method for the equivalent impedance model (Albooyeh et al., 2015). Figure 3.7 illustrates the problem's frame by a circuit model representing reflection (Γ) and transmission coefficients (τ) on the metasurface for forward and backward excitation.

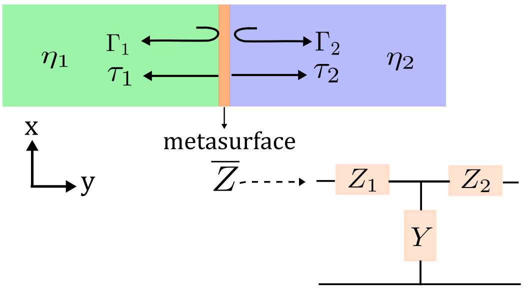

Figure 3.7. Representation of metasurface as an infinite thin homogeneous sheet model with reflection and transmission coefficients and $T-$circuit equivalent (Albooyeh et al., 2015).

The transmission matrix $[T]_{2,1}$, representing the relation between voltage and current at input and output ports, is given as

$$\begin{bmatrix} V_{2,1}^i \\ I_{2,1}^i \end{bmatrix} = \begin{bmatrix} 1+Z_{2,1}Y & Z_{2,1}+Z_{1,2}+Z_{2,1}Z_{1,2}Y \\ Y & 1+Z_{1,2}Y \end{bmatrix} \begin{bmatrix} V_{2,1}^o \\ I_{2,1}^o \end{bmatrix}, \tag{3.60}$$

where the subscript $_{2,1}$ indicate forward and backward illumination, respectively. The following equations express the reflection and transmission coefficients in terms of circuit parameters,

$$r_{2,1} = \frac{\eta_{1,2}(1+\frac{Z_{1,2}}{\eta_{1,2}}) - \eta_{2,1}(1-\frac{Z_{2,1}}{\eta_{2,1}}) - \eta_2\eta_1 Y(1-\frac{Z_{2,1}}{\eta_{2,1}})(1+\frac{Z_{1,2}}{\eta_{1,2}})}{\eta_2(1+\frac{Z_2}{\eta_2}) + \eta_1(1+\frac{Z_1}{\eta_1}) + \eta_2\eta_1 Y(1+\frac{Z_2}{\eta_2})(1+\frac{Z_1}{\eta_1})}, \tag{3.61}$$

$$t_{2,1} = \frac{2\eta_{1,2}}{\eta_2(1+\frac{Z_2}{\eta_2}) + \eta_1(1+\frac{Z_1}{\eta_1}) + \eta_2\eta_1 Y(1+\frac{Z_2}{\eta_2})(1+\frac{Z_1}{\eta_1})}. \tag{3.62}$$

Reciprocity states the relation as $t_2/\eta_1 = t_1/\eta_2$, and assume $t_{2,1}/\eta_{1,2} = t$. Now, the effective surface impedances and admittance can be obtained by

$$\frac{Z_{2,1}}{\eta_{2,1}} = \frac{1+r_{2,1}-\alpha_{2,1}t_{2,1}}{\alpha_{2,1}-\alpha_{2,1}r_{1,2}+t_{1,2}}, \tag{3.63}$$

$$\eta_{2,1}Y = \frac{1-r_{1,2}-t_{2,1}}{(1+\frac{Z_{2,1}}{\eta_{2,1}})t_{2,1}}, \tag{3.64}$$

where $\alpha_{2,1} = \big(1-r_{2,1}-t_{1,2}\big)/\big(1-r_{1,2}-t_{2,1}\big)$, and $r_{2,1}$, $t_{2,1}$ represent the reflection and transmission coefficients, respectively. Electric and magnetic surface impedances are now calculated via the following equations,

$$Z_m = Y_m^{-1} = Z_2 + Z_1 \qquad \text{and} \qquad Z_e = Y_e^{-1} = \frac{1}{Y} + \frac{Z_m}{4} - Z_{sm}K_{em}^2, \tag{3.65}$$

and couplings as

$$K_{em} = -K_{me} = \frac{Z_2 - Z_1}{2Z_m}. \tag{3.66}$$

3.5. 3D Model Design and Characterization

In Chapter 2, we examined that conjugate reactances with Ω-coupling bianisotropy can be used to design a penetrable metasurface that achieves high transmission and supports propagating surface waves. Under certain conditions, DNG slabs and phase conjugating surfaces exhibit equivalent field transformation, as seen in phenomena like the perfect lens, and can excite surface waves depending on k_t and k_n. The analytically investigated metasurface can be realized in 3D with a DNG slab, where one side is designed with an effective ϵ-negative (ENG) medium and the other with an effective μ-negative (MNG) medium. ENG and MNG unit cells are typically composed of electric and magnetic resonance structures, and they exhibit negative medium properties near resonance with complex conjugate impedances ($Z_{ENG} = Z^*_{MNG} = jX$).

A single negative medium has an imaginary wavenumber and infinite reflection for evanescent waves coupled with surface modes. By combining electric and magnetic negative structures closely ($<< \lambda_0$), transmission becomes infinite for evanescent waves. This behavior is equivalent to the response when an evanescent wave excites a conjugating surface, triggering surface wave propagation along the interface (Alu and Engheta, 2003).

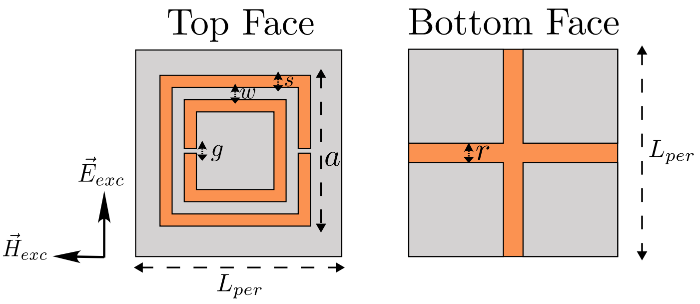

Figure 3.8. Unit cell design for the proposed bianisotropic metasurface. $\epsilon_r = 2.98$, and dimensions are respectively, $g = 0.6mm$, $w = 1mm$, $s = 1mm$, $a = 16mm$, $r = 1.6mm$, $L_{per} = 16mm$.

The proposed 3D model is designed through a concept of a DNG slab combined with ENG and MNG structures (D. R. Smith and Schultz, 2000; Asadchy et al., 2018; Önder Yılmaz and Yaman, 2022). This combination forms a magnetodielectric medium that induces electric and magnetic polarization currents similar to the analytical solutions for each conjugate surface (see Equations 2.42-2.43) (R. Marqués and Rafii-El-Idrissi, 2002). Split-ring resonators provide artificial magnetism with negative μ and strong

Ω-type bianisotropy (J. B. Pendry and Stewart, 1999; Smith et al., 2006; R. Marqués and Rafii-El-Idrissi, 2002; Albooyeh, 2015), while arrays of electrically thin wires create artificial dielectric media (J. B. Pendry and Youngs, 1996). By combining complementary ENG and MNG structures on each face of the DNG slab, we leverage their strong Ω bianisotropy couplings (Falcone et al., 2004; Smith et al., 2000; Önder Yılmaz and Yaman, 2022). The geometries of inclusions on each face on a thin substrate ($h << \lambda_0$, $\epsilon_r = 2.98$) are given in Figure 3.8. The sizes are optimized to overlap the resonances within the operating frequency range ($\approx 2.5 - 3$ GHZ).

The simulation setup in Figure 3.9 obtains the scattering and field distribution of the unit cell placed precisely in the middle. Here, the TEM plane wave is exited separately by $Port-1$ (forward illumination) and $Port-2$ (backward illumination). For such an impedance-matched two-port system, S-parameters refer to the reflections (S_{11} and S_{22}) and transmission (S_{21} and S_{12}).

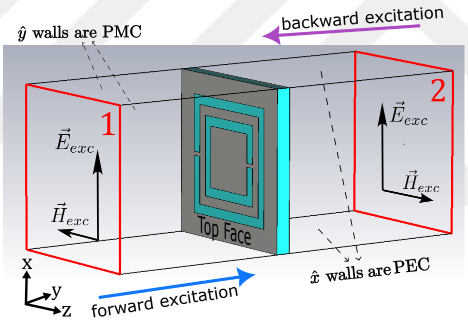

Figure 3.9. Simulation setup for unit cell in TEM waveguide (Yılmaz and Yaman, 2024).

A metasurface is constructed by periodically placing identical unit cell structures, except for the gradient ones. We stated that both the spatial period and the maximum size of the unit cell must be subwavelength (λ_{av}). When the boundary conditions are properly adjusted via Bloch-Floquet analysis in Section 3.2, the complete structure exhibits approximately equal EM properties of its unit cell. There are primarily three numerical solution approaches for the metasurface model in 3D which are: (i) exact structure with $n \times n$ unit cells, (ii) unit cell in unit cell boundary condition (UBC), which is a type of periodic boundary condition where the fields at the transverse boundaries reproduce themselves periodically, and (iii) unit cell in a rectangular waveguide.

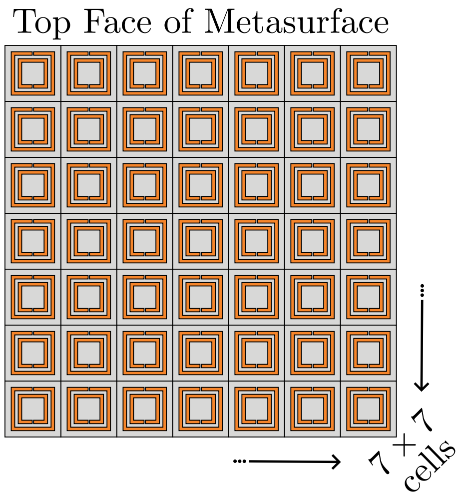

Figure 3.10. Proposed metasurface model formed by 7 × 7 unit cells.

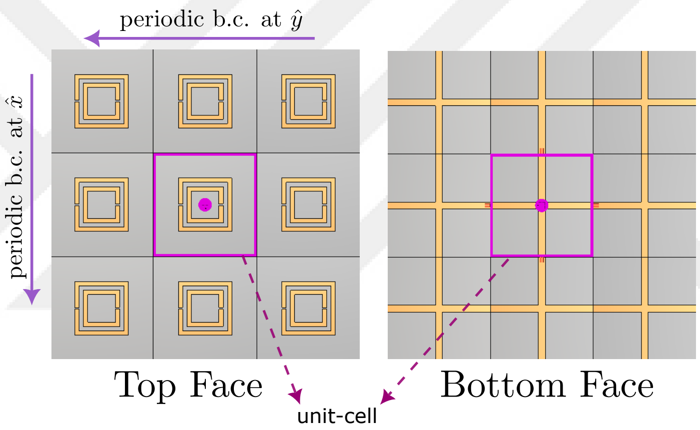

Figure 3.11. Simulation model of unit cell in unit boundary condition.

Figure 3.10 and Figure 3.11 show the metasurface model comprised of 7 × 7 cells, and its unit cell in the UBC configuration, respectively. The design parameters are optimized by using the FEM solver in the simulation package CST: Microwave Studio. For the UBC approach, the simulation only solves for a single cell in the solution domain (boundary box) and applies the periodic boundary conditions on its transverse plane. In all cases, the incident wave propagates in the $\mp z$ direction and impinges normally on the plane. We first focus on simulations in UBC setup in Figure 3.11. As clarified in Section 3.2, for larger values of L_{per}/λ_0, i.e., higher frequencies when L_{per} is fixed, higher order Bloch-Floquet modes are excited, and the medium becomes inhomogenizable. To analyze the influence of the period on both fundamental and higher modes, we simulated the unit cell within UBC for various L_{per}. Figure 3.12 shows the magnitude of transmission coefficients (in dB). As intended, the higher propagating modes are suppressed for $L_{per} =$ 20 mm and $L_{per} =$ 22 mm. Note that the fundamental mode (around $\approx 2.5 - 3$ GHz) does not depend on the period (see Equation 3.21). Although the UBC approach is very practical for analyzing a complete metasurface, one should remember that it is a mathematical solution that assumes the transverse plane goes to infinity on the plane.

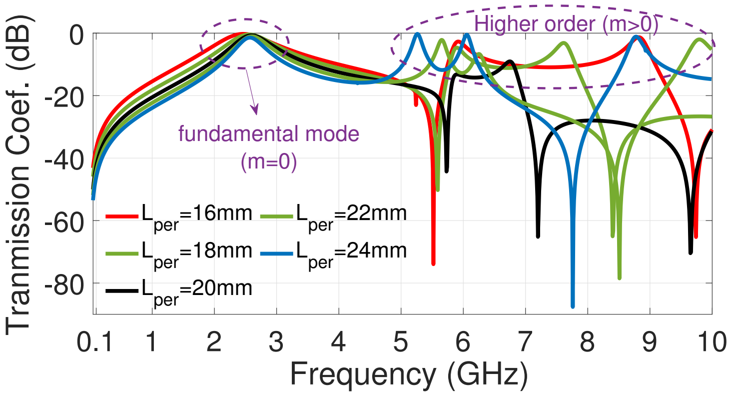

Figure 3.12. Simulation results of transmission coefficient (magnitude in dB) for unit cell in UBC setup.

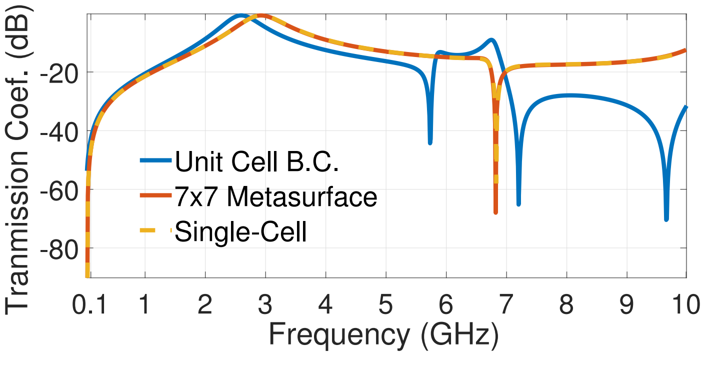

Figure 3.13. Simulation results of transmission coefficients (magnitude in dB) comparison of UBC, 7×7 metasurface and unit cell-in-waveguide simulations.

To compare the scattering responses, we then simulated the unit cell in the waveguide setup and metasurface consisting of 7×7 unit cells. Figure 3.13 shows the magnitude of transmission coefficients for the corresponding simulations when the period (L) is fixed to suppress the higher modes in the given spectrum ($0.1 - 10$ GHz). For $L_{per} = 20$ mm in the simulation with UBC, $L_{per} = 16$ mm in the 7×7 metasurface, and 4 mm spacing between the unit cell and PEC and PMC walls, we obtained well-matched results, especially for the fundamental transmission mode. The aforementioned theoretical assumptions on boundaries might cause a slight frequency shift in the results of UBC simulations.

3.5.1. Impedance-Based Characterization of The Unit Cell

We now retrieve the series (Z_{s1} and Z_{s2}) and parallel (Z_p) impedances for the T-circuit model in Figure 3.6b. We first calculate Z_{se}, Y_{sm}, K_{em} and K_{me} through averaged fields ($\vec{E}$ and $\vec{H}$) and reflection/transmission coefficients, which are obtained from the CST: MW simulation of the unit model in 3D. These were extracted from the 2D faces at the boundaries of the two sides of the structure as illustrated in Figure 3.9. This process was performed for each discrete frequency sample. We then applied the impedance-based characterization by equations 3.48-3.59 and equations 3.60-3.66, respectively. Figure 3.14 presents the surface impedances and coupling results of the proposed structure for the averaging field method in the given spectrum. The phase conjugation of the series impedances (Z_{s1} and Z_{s2}) can be seen in the given spectrum, and it is more clearly around the resonance frequency (≈ 3 GHz). The bianisotropic couplings (K_{em} and K_{me}) exhibit relatively higher values around the resonance frequency. Nevertheless, it is not zero across the spectrum seen in the zoomed Figure 3.14d. As we expect, the imaginary part of the coupling coefficients is zero across the spectrum, and the real parts are anti-symmetric (i.e., $\Re(K_{em}) \approx -\Re(K_{me})$) due to lossless and passive configuration. As discussed before, the difference between series impedances ($\Delta Z = |Z_{s1} - Z_{s2}|$) indicates how much strength the Ω coupling is and also means the asymmetric reflection. The results demonstrate strong Ω coupling and phase conjugate reactances of the proposed DNG slab. Those can be observable, especially around the resonance frequency. We determined sufficient field resolution during the numerical simulations for the field averaging method. By increasing the resolution, i.e., the total number of samples on the faces, we observe the influence of the total averaging number $N \times N$ on the transmission magnitude spectrum in Figure 3.15. When the sample size exceeds a certain threshold value, the results approach the true value, except for the vicinity of the resonance, where a higher sample size, such as $N = 640000$, is required.

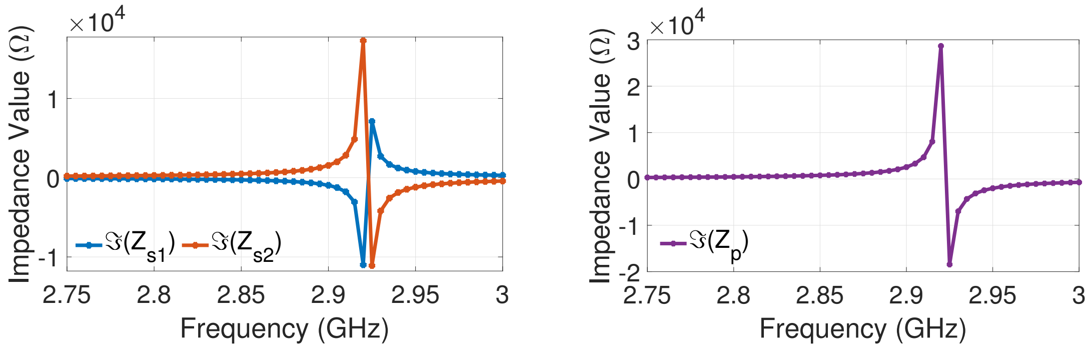

(a) Z_{s1} and Z_{s2} (b) Z_p

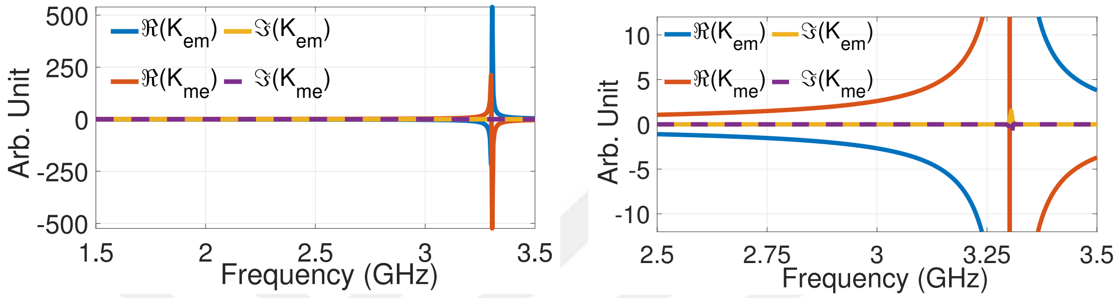

(c) K_{em} and K_{me} (d) K_{em} and K_{me} (zoomed around resonance)

Figure 3.14. Impedance-based characterization results of proposed unit cell structure for field averaging method in a given spectrum.

Following the averaging method, we implement the retrieval procedure of the reflection/transmission (Γ/τ) over a broadband spectrum (0.1–10 GHz). Figure 3.16 illustrates the series surface impedances and coupling coefficients. The results obtained using the Γ/τ retrieval method are consistent with those from the averaging method. We see higher-order resonance modes at higher frequencies, where the impedance and coupling coefficients significantly change due to the nature of resonance. However, these are higher-order Bloch-Floquet modes and are outside the metasurface context.

We then compute the reflection and transmission coefficients from the reconstructed lumped circuit (denoted as l. circuit in figures) derived from both methods for validation with the 3D simulation results. Figures 3.17a and Figure 3.17b present the magnitude of the transmission and reflection coefficients of the equivalent T-circuit. They compare the results of the 3D CST: MW simulation, respectively, with the averaging method and reflection/transmission retrieval method. Figure 3.17c displays the phase of the transmission coefficient, where the asymmetric reflection depending on the illumination direction can be observed. Well-matched consistency exists between the 3D simulation model and the proposed equivalent circuits, and it validates the proposed circuit under fixed orientation and specific excitation.

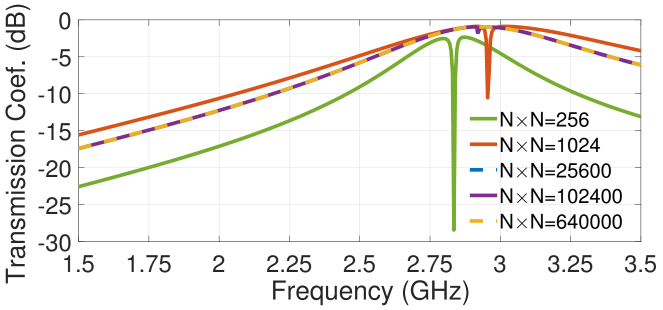

Figure 3.15. Simulation analysis of transmission coefficients (magnitude in dB) with respect to the total sample number ($N \times N$) in the field averaging method.

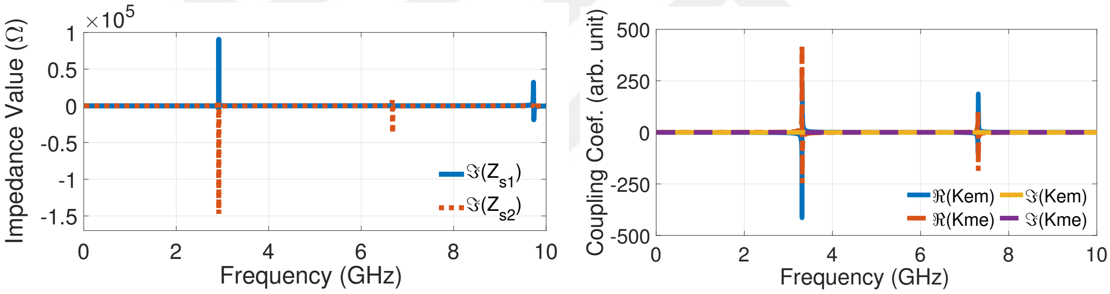

(a) Z_{s1} and Z_{s2}

(b) K_{em} and K_{me}

Figure 3.16. Impedance-based characterization results of proposed unit cell structure through $S-$parameter retrieval method.

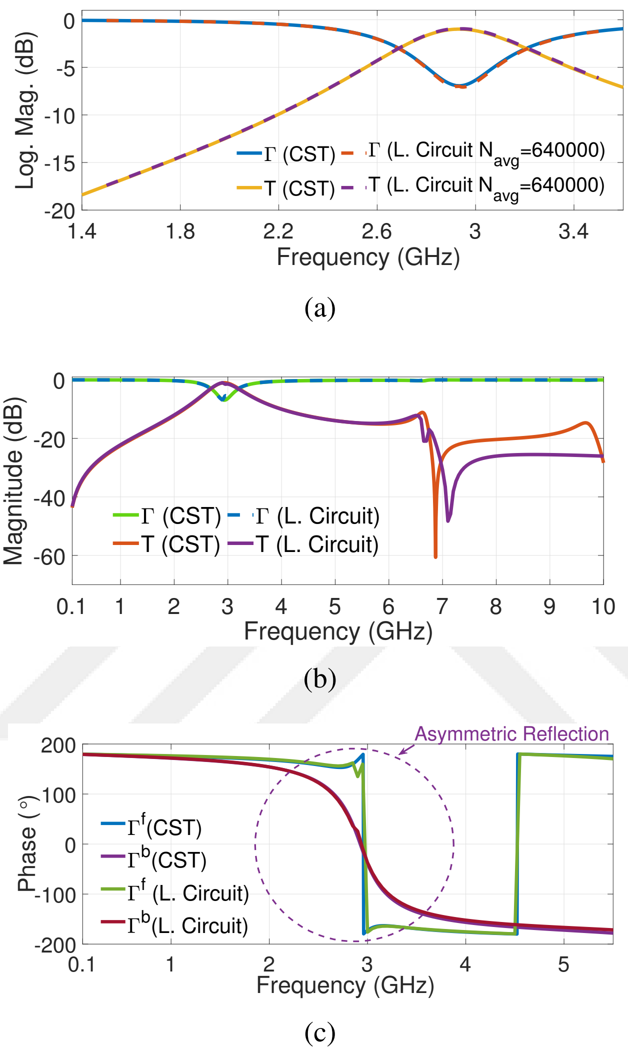

Figure 3.17. Results of transmission and reflection coefficients (magnitude in dB) calculated from equivalent circuit model constructed through the (a) averaging method, and (b) $S-$parameter retrieval method. (c) Results of reflection coefficients (phase °) calculated from equivalent circuit model constructed through $S-$parameter retrieval method for forward (^{f}, Port-1) and backward (^{b}, Port-2) excitation.

CHAPTER 4

DYNAMIC PENETRABLE METASURFACE ASSISTED BY SURFACE WAVE

This chapter focuses on surface wave excitation on the proposed metastructure and its manipulation by the variable capacitor (Yılmaz and Yaman, 2024). The design is enhanced to control the scattering parameters dynamically through surface waves in the surface cavity. The equivalent circuit model is developed for the surface cavity mode incorporated with the variable capacitor(s).

4.1. Surface Wave Supported Metasurface Design in 3D

This section presents optimizing the proposed design for constructing the penetrable metasurface that can generate the surface wave depending on the surface impedances. We redesigned the dimensions of the top and bottom structures as given in Figure 4.1 while optimizing them to get the desired induced currents for each face individually found analytically in Chapter 2. The averaged fields are calculated by boundary conditions in Equation 2.41 through fields obtained on faces indicated in the simulation setup in Figure 3.9.

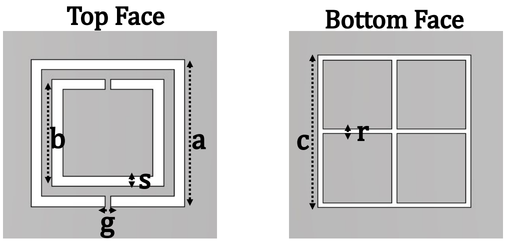

Figure 4.1. Top and bottom design of unit cell for surface wave assisted penetrable metasurface with the following dimensions: $a = 23.4mm$, $b = 17mm$, $g = 0.8mm$, $s = 1.6mm$, $c = 25mm$, and $r = 0.8mm.$ Grey and white areas indicate the conductor and dielectric (RT/duroid 5880, $\epsilon_r = 2.2$) (Yılmaz and Yaman, 2024).

Figure 4.2 shows the electric and magnetic surface polarization currents obtained from both 3D simulations and 2D analytical solutions through each surface and averaged over the unit cell dimension ($\approx \lambda_0/4$). These results demonstrate the magnetodielectric properties of the proposed structure and equivalent medium-response of the DNG slab and phase conjugate surfaces under specific geometry and boundary conditions. Dielectric ($\epsilon_r = 2.2$) substrate between the ENG and MNG faces may contribute to additional effective magnetic surface currents.

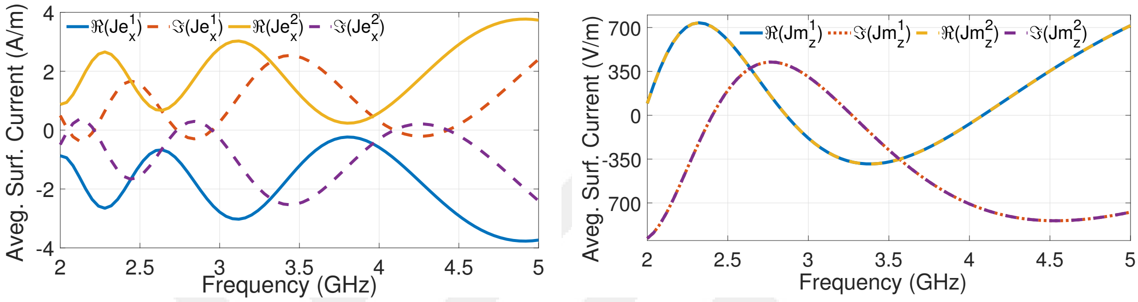

(a) Analytical model

(b) Analytical model

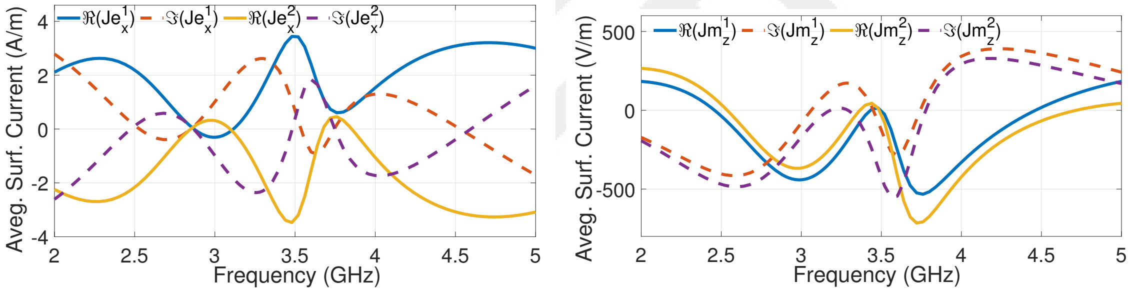

(c) 3D simulation model

(d) 3D simulation model

Figure 4.2. Effective electric and magnetic surface polarization currents which are calculated and averaged over a unit cell (Yılmaz and Yaman, 2024).

The design parameters were individually optimized to achieve the desired surface currents and then combined with the two faces to produce the intended coupling effect (Yılmaz and Yaman, 2020). This coupling results in new bianisotropy parameters. Figure 4.3 displays the calculated magnetodielectric coupling coefficient (K_{me}) of the Ω-type bianisotropy for both the simulated combined faces and the analytical surfaces. The couplings are calculated using Equation 3.49 with the averaged fields from both 3D simulations and the analytical expressions in Equation 2.39. While the coupling coefficient results show consistency across the spectrum, there is a strong matching around resonance frequencies where the surface parameters (geometries, dimensions, and materials) are optimized to match the analytical results.

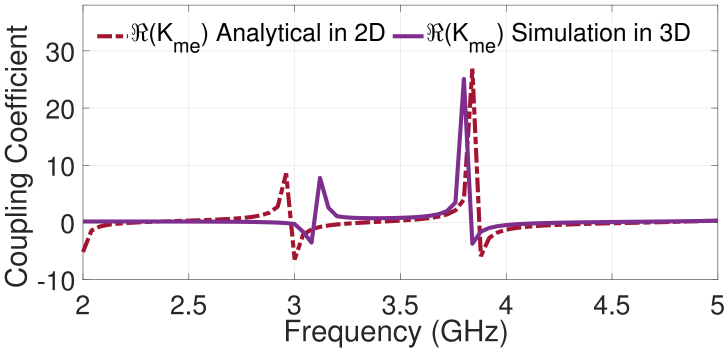

Figure 4.3. Magnetoelectric (K_{me}) coupling coefficient of Ω-type bianisotropy for calculated by analytical solutions and retrieved from 3D model simulation (Yılmaz and Yaman, 2024).

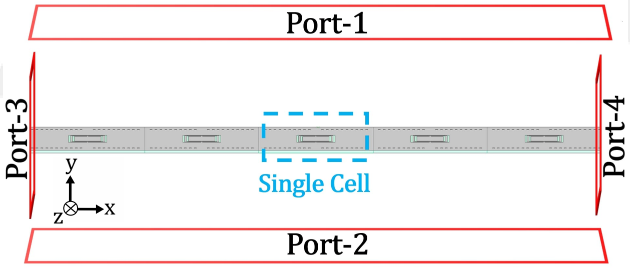

(a) 5×1 cells along $x-$direction

(b) Forward illumination

(c) Backward illumination

Figure 4.4. (a) $3D$ model metasurface formed with 5×1 cells in and simulation configuration, (b) and (c) normal component E_y of the electric field distribution (Yılmaz and Yaman, 2024).

To expand the analytical model into 3D, we construct a metasurface with 5×1 cells along the x-direction, as shown in Figure 4.4a. We aim to observe surface wave excitation along the x-direction on the transverse plane of the surface using CST Microwave Studio for 3D simulations. The side walls are set as perfect magnetic conductors (PMC) and perfect electric conductors (PEC) along the z and x axes, respectively, allowing normal incidence of a $\hat{x}$-polarized TEM plane wave. Ports 3 and 4 measure the power flow through the transverse plane. Figure 4.4 shows the normal component of the electric field (E_y) for both forward (Port 1) and backward (Port 2) illumination when the transmission coefficient is $|T|^2 = 0.5$, The results demonstrate concentrated surface waves and a π-phase difference based on the excitation direction, consistent with the analytical solution in Figure 2.10.

4.2. Equivalent Circuit Model For Time-Domain Solution

The numeric solution to the time-varying EM problem in 3D is very challenging, and, to our knowledge, there is no ready-to-use solution today. This problem can be solved by deriving an equivalent circuit in the time domain for a time-modulated unit cell. Specialized numerical techniques, ITMM and HB, will be employed to periodically analyze time-varying systems, presented in Chapter 5. The retrieved T-circuit impedances correspond to each face's electric and magnetic surface impedances (Wang, 2020). These impedances can be extracted into time-domain components such as L and C (in lossless cases). Each face's design involves resonator structures, resulting in impedances with multiple resonance characteristics (see Figure 4.6). We suggest modeling each impedance as a series of parallel LC resonators, as illustrated in Figure 4.5.

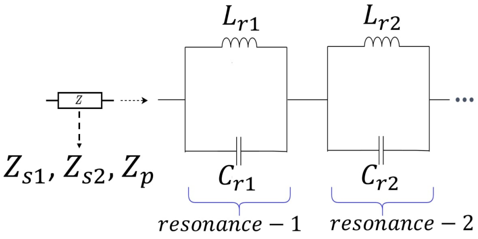

Figure 4.5. Extraction of the retrieved impedance to the lumped elements as series LC banks for the equivalent $T-$circuit.

The modeling by two series of parallel LC circuits is based on the metasurface's classification. J.W. Zang et al. previously modeled a unit cell patch resonator as a single LC bank when addressing a similar time-domain impedance transfer matrix problem (Zang et al., 2019). Even in the presence of dispersion in the medium, an effective parameter approach can provide a good approximation for its characterization (Holloway et al., 2012). However, it is inapplicable for higher frequencies (or larger periods). The designed scatterers have two resonances at frequencies lower than those of the higher-order Floquet modes. Thus, we use the first two resonance transmission modes to determine the effective parameters of LC resonance circuit blocks. These are inside the fundamental Floquet mode, as expressed in Equation 3.21, where $k_{x,m}$ are the propagation constants associated with the structure's periodicity L_{per}.

The impedance function for parameter extraction in the case of two resonance points is given as

$$Z_{eq}(\omega) = \frac{j\omega L_{R_1}}{1 - \omega^2 L_{R_1} C_{R_1}} + \frac{j\omega L_{R_2}}{1 - \omega^2 L_{R_2} C_{R_2}}, \tag{4.1}$$

where subscript $_{R1}$ and $_{R2}$ refer to the first and second resonance of LCs, respectively. We first express the relation of $L_{r_{1,2}}$ and $C_{r_{1,2}}$ from the frequencies of the first and second resonances. Those are, respectively, the fundamental mode and the upper band of the homogenization condition, and they are calculated by

$$\omega_{0_1} = \frac{1}{\sqrt{L_{r_1} C_{r_1}}} \qquad \text{and} \qquad \omega_{0_2} = \frac{1}{\sqrt{L_{r_2} C_{r_2}}}, \tag{4.2}$$

and we can express the capacitor values as

$$C_{r_1} = \frac{1}{\omega_{0_1}^2 L_{r_1}} \qquad \text{and} \qquad C_{r_2} = \frac{1}{\omega_{0_2}^2 L_{r_2}}. \tag{4.3}$$

By considering the given spectrum in impedance retrieving simulations, we select frequency points of $Z_{eq}(\omega_1)$ and $Z_{eq}(\omega_2)$ on $Z_{eq}(\omega)$ in Equation 4.1. After solving for L_{r_1} and L_{r_2} at the two frequency points of ω_1 and ω_2, we obtain the first inductance as

$$L_{r_1} = \frac{p_1 p_2 Z(\omega_1) - p_1 L_2 \omega_1 \omega_{0_2}^2}{\omega_1^2 \omega_{0_1}^2 p_2}, \tag{4.4}$$

where $p_1 = \omega_{0_1}^2 - \omega_1^2$ and $p_2 = \omega_{0_2}^2 - \omega_1^2$, and the second inductance is found as

$$L_2 = \frac{p_2 p_3 p_4 \omega_1 \omega_{0_1}^2 Z(\omega_2) - p_1 p_2 p_4 \omega_2 \omega_{0_1}^2 Z(\omega_1)}{p_2 p_3 \omega_1 \omega_2 \omega_{0_1}^2 \omega_{0_2}^2 - p_1 p_4 \omega_1 \omega_2 \omega_{0_1}^2 \omega_{0_2}^2}, \tag{4.5}$$

where $p_3 = \omega_{0_1}^2 - \omega_2^2$ and $p_4 = \omega_{0_2}^2 - \omega_2^2$.

We can now apply the retrieval methods to the proposed unit cell to obtain surface impedances. To maintain accuracy, we enhance surface resolution, especially as we approach below-resonance, which is of interest. However, this approach still may yield inaccuracies in being too close to resonance where wavelength shortening occurs (Simovski, 2018). Also, we discard the frequency samples very close to the resonance of the LCs, which gives the singularities in the impedance function for the lossless case. Table 4.1 presents the extracted circuit parameters. Here, the negative values confirm the left-handed behavior (LHM) and phase-conjugation of reactances. Figure 4.6 displays the retrieved through 3D simulation and calculated impedances from the LC model, while Figure 4.6d provides a zoomed view highlighting the conjugate values of series impedances around resonance.

We now calculate the reflection and transmission coefficients for the equivalent circuit constructed with impedances and lumped elements. Figure 4.7 shows the S_{21} (transmission) and S_{11} (reflection) coefficients for both the 3D simulation and equivalent models, where observing a well-matching between them. However, some discrepancies arise in the scattering parameters due to the degree of impedance function in Equation 4.1. Improving accuracy requires increasing the number of components, considering the limitations related to cell dimensions and wavelength. This results in the need for a more sophisticated curve-fitting analysis. Despite this, we think the proposed circuit model for the two transmission modes is sufficient for our purposes.

Table 4.1. The extracted values of LC parameters from the retrieved surface impedances in unit cell simulations.

	Z_{s1}	Z_{s2}	Z_p
C_1	17.6pF	-18.85pF	1.43pF
L_1	0.15nH	-0.14nH	1.84nH
C_2	-7.5pF	8.21pF	1.93pF
L_2	-0.23nH	0.21nH	0.89nH

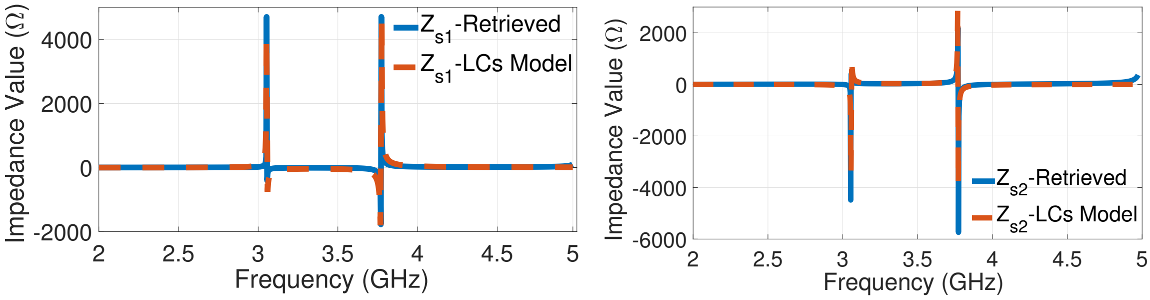

(a) Series impedance $\Im(Z_{s1})$ (b) Series impedance $\Im(Z_{s2})$

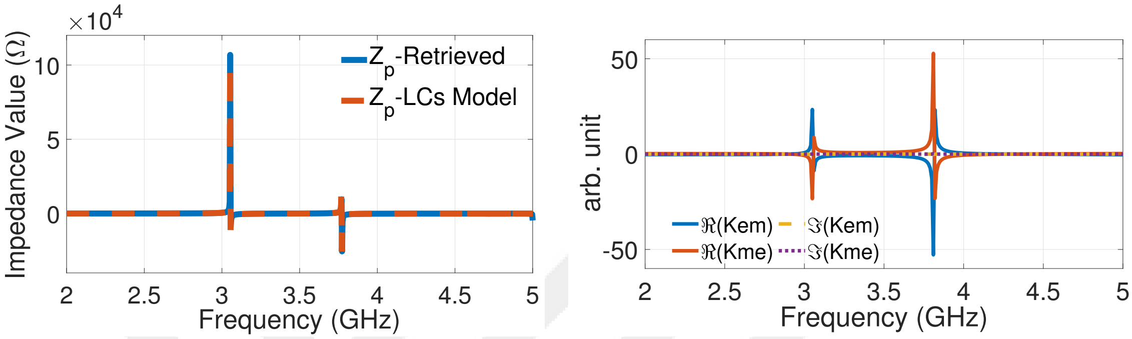

(c) Parallel impedance $\Im(Z_p)$ (d) Coupling coefficients (K_{em} and K_{me})

Figure 4.6. The retrieved series and parallel impedances of the equivalent circuit for the proposed unit cell (Yılmaz and Yaman, 2024).

4.3. Dynamic Control of Metasurface Through Surface Wave

As we explore in Chapter 2, surface and transmitted waves on the proposed medium can be controlled by manipulating the propagation constant of surface waves. This section presents a method for establishing the dynamic unit cell of the proposed metasurface by incorporating lumped variable capacitors into the design.

J. W. Zang et al. presented a similar idea, focusing on controlling reflection through surface waves on subharmonics of a time-modulated unit cell gradient metasurface (Zang et al., 2019). Their study is on the efficient conversion between two desired frequencies. By adjusting the phase delay applied to the modulation of each cell, they achieved nonreciprocity for the reflection. This was accomplished by setting drastically different phase gradients during the up/down conversion process and leveraging the interaction between specific nonlinear surface waves and reflected propagating waves. Their unit cell includes a resonant patch and multiple resonant slots coupled to a short-circuited substrate-integrated waveguide (SIW) with a shunt varactor diode connection. The process involves incident waves coupling to the SIW via resonances from the patch and slots,

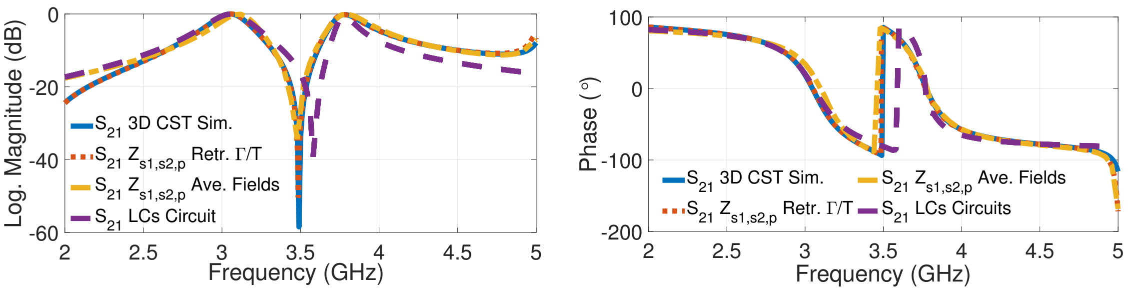

(a) $|S_{21}|$ (b) $\underline{/S_{21}}$

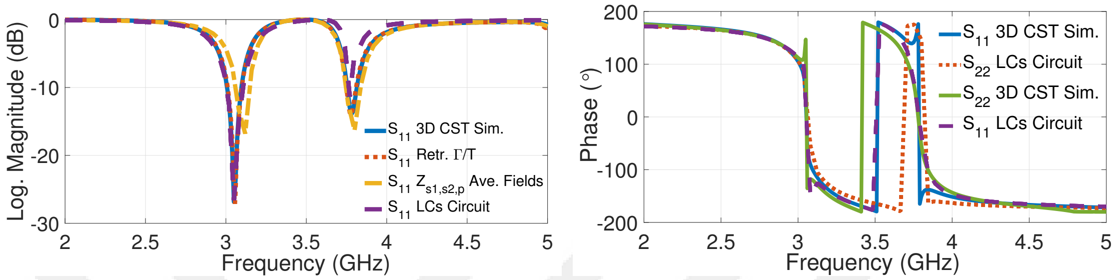

(c) $|S_{11}|$ (d) $\underline{/S_{11}}$ and $\underline{/S_{22}}$

Figure 4.7. S-parameter results for the 3D model simulation and the circuits constructed through retrieved impedances and LC model (Yılmaz and Yaman, 2024).

propagating along the SIW, reflecting at the short circuit, traveling back along the SIW, and re-radiating to free space. A tunable resonator is implemented by placing the varactor diode approximately $\lambda/4$ away from the SIW short circuit. For measurements, the unit cell is placed in a rectangular waveguide to simulate the behavior of a TE plane wave. They utilized the transfer matrix method for the numerical solution of time-modulated components in the resonance circuit coupled to the reflective metasurface. Inspired by the related study, we designed the proposed structure to support the standing surface wave, known as the surface cavity mode.

4.3.1. Design of Dynamic Unit Cell with Surface Cavity Mode

This section focuses on a 3D model of introducing time-varying element(s) into the medium where the surface wave is excited. We improve the proposed equivalent circuit model (Figure 3.6) now for having time-varying capacitor(s). Figure 4.8 illustrates the model having separated dielectric-backed ENG and MNG faces and including a time-varying capacitor in parallel that represents the surface wave in cavity mode. First, a single cell was extracted from the metasurface given in Figure 4.4a and placed within a waveguide. It is configured with a substrate-integrated waveguide (SIW), as shown in Figure 4.9.

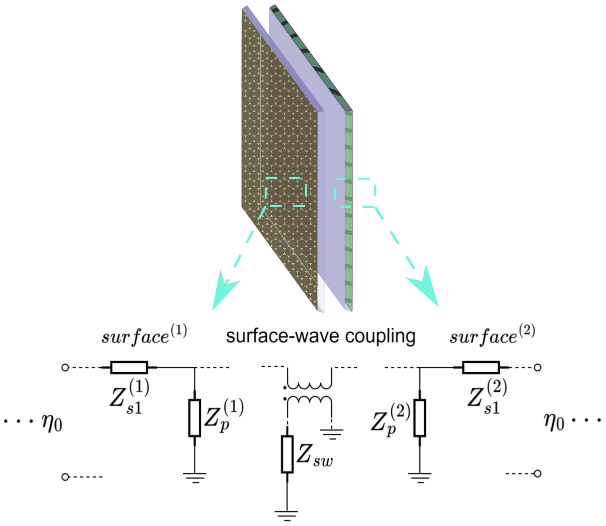

Figure 4.8. Visualizing metasurface through separated faces, and its equivalent circuit model that can transform surface waves in resonance (Yılmaz and Yaman, 2024).

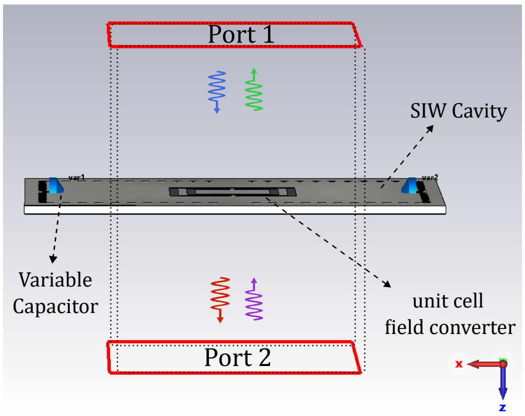

Figure 4.9. The view of the simulation model in xz plane for a unit cell with an SIW cavity terminated by variable capacitors at $\pm x$.

The variable capacitor is intentionally positioned outside the excitation waveguide for the unit cell to demonstrate that manipulation occurs only through the surface wave.

The SIW simulates a periodic metasurface for a unit cell, setting boundaries for standing-wave resonance. A time-variable capacitor is introduced via coaxial cross-section coupling in the fundamental mode. It creates a surface cavity mode coupled through the coaxial section between the top and bottom faces. This setup is shown in Figure 4.10.

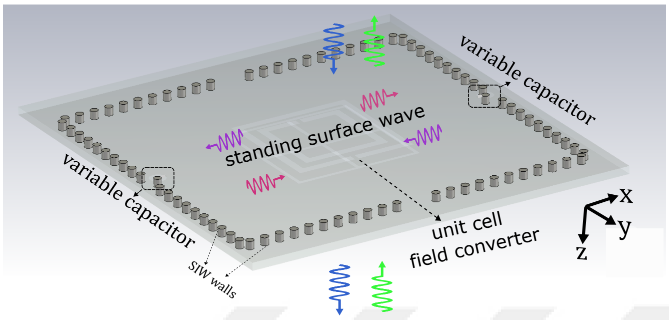

Figure 4.10. The perspective view which illustrates the wave transformation on a unit cell design with an SIW cavity terminated by variable capacitors at $\pm x$ (Yılmaz and Yaman, 2024).

SIWs exhibit propagation characteristics similar to rectangular metallic waveguides. SIW modes are essentially a subset of the TE_{n0} modes ($n = 1, 2, \ldots$) found in rectangular waveguides. Unlike rectangular waveguides, SIWs do not support TM modes due to the gaps between metal vias. The fundamental mode in a SIW corresponds to the TE_{10} mode of a rectangular waveguide, characterized by vertical electric current density on the side walls. This similarity has led to empirical relations between the SIW's geometric dimensions and the effective width w_{eff} of a rectangular waveguide with similar propagation characteristics (Nwajana and Obi, 2022; M. Bozzi, 2011; Balanis, 1989). It is expressed as

$$w_{eff} = w - \frac{d^2}{0.95s} \tag{4.6}$$

where d is the diameter of the metal vias, w and s represents their transverse and longitudinal spacing, respectively.Cut-off frequency is determined by $f_c = \dfrac{c}{2a}$ for the fundamental TE_{10} mode. The details and dimensions of the design are given in Figure 4.11a.

4.3.2. Simulation Results For Dynamic Unit Cell

This part presents the simulation results of a dynamic unit cell placed within a TEM waveguide, which converts incident waves into a surface cavity mode and incorporates time-variable capacitors. Antisymmetric (π-phase delayed) surface modes excitation will be employed to achieve nonreciprocal transmission.

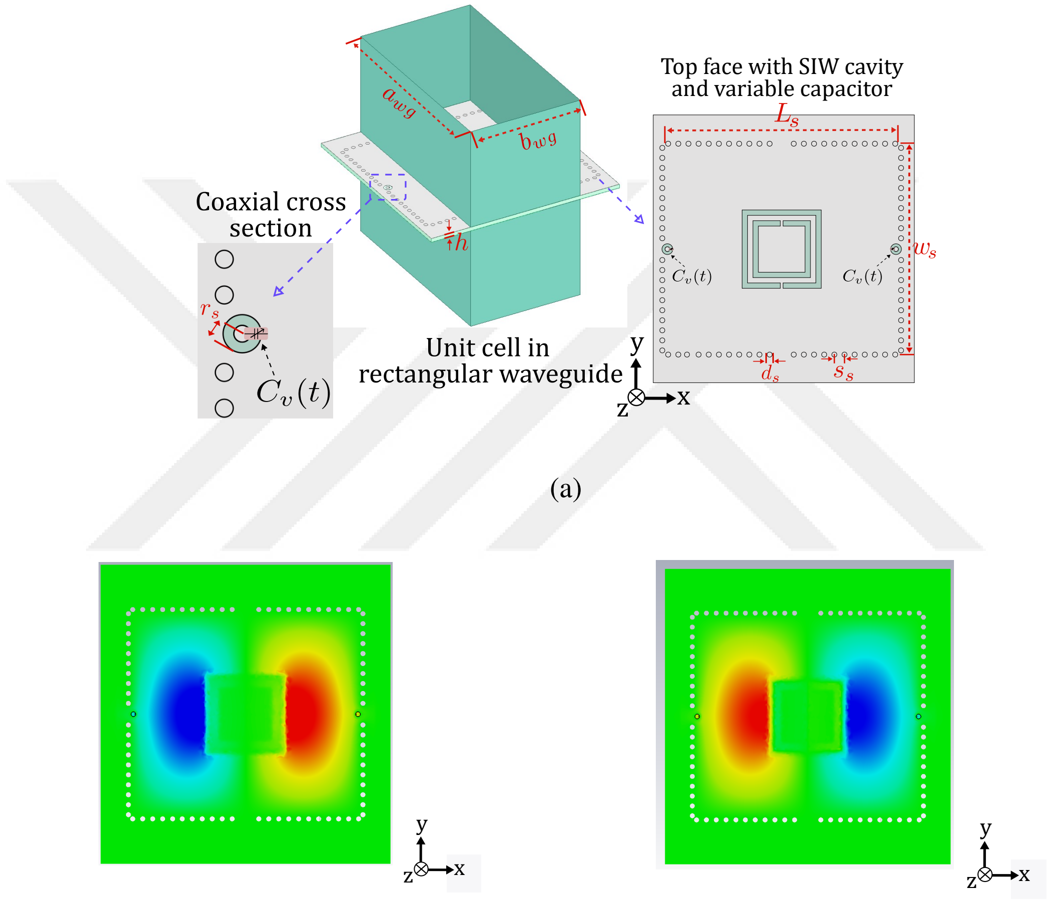

(a)

(b) E_z for forward illumination

(c) E_z for backward illumination

Figure 4.11. (a) Simulation setup for a unit cell exhibiting a surface cavity mode with a variable capacitor connected through a coaxial interface, (b) and (c) the distribution of the normal component of the electric field, E_z, at top view (normal to $\hat{z}$) under forward (Port 1) and backward (Port 2) illumination, respectively. Minimum and maximum electric field strength is adjusted as $\mp 10000 V/m$. Design parameter are: $r_s = 1.6mm$, $h = 1.5mm$, $a_{wg} \times b_{wg} = 83mm \times 46mm$, $d_s = 1.5mm$, $s_s = 3mm$, $w_s = 63mm$, $L_s = 68mm$ (Yılmaz and Yaman, 2024).

More clearly, an asymmetric signal is required on the variable capacitor due to signal mixing between the pump and the source signals in the 3D model. The electric field distribution (E_y) on the surface cavity for both forward and backward illuminations is shown in Figure 4.11, corresponding to the field distribution of a single cell in the 5×1 array depicted in Figure 4.4. Phase-asymmetric surface mode excitation can also be observed by analyzing the voltage at the lumped variable capacitor (C_v) terminals in the 3D simulation.

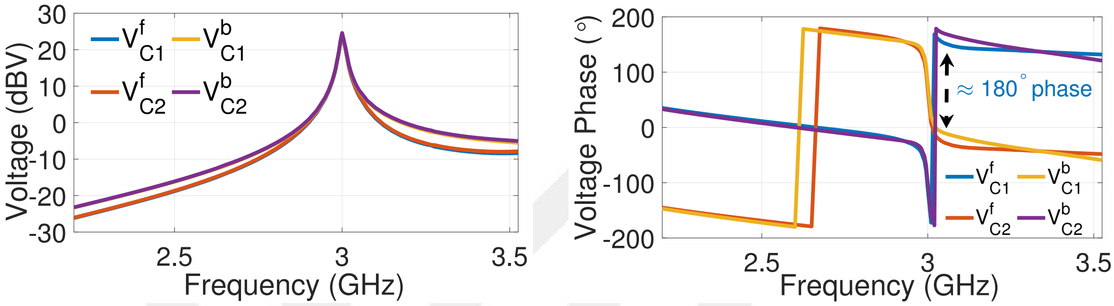

(a) Magnitude (in dBV)

(b) Phase (°)

Figure 4.12. Simulation results of the unit cell with a surface-cavity mode: voltages at variable capacitor terminals connected through a coaxial interface for forward (Port 1) and backward (Port 2) illumination (Yılmaz and Yaman, 2024).

Figure 4.12 displays the magnitude (dBV) and phase of voltages for forward and backward excitation. As expected, the voltages have identical amplitudes and approximately a π-phase difference, consistent with the E_y field observations in Figures 4.11b and 4.11c. The voltage amplitude compared to the source can reach 25 dBV (≈ 18 in linear ratio) due to the concentrated surface wave, which aligns with the analytical result in Equation 2.63. The modulation signal (pump) amplitude should be significantly higher than the source signal in practical scenarios with a varactor diode. If the source power is high or comparable, any change in source power could affect the modulation function of the variable capacitor due to nonlinearity. Maintaining a constant pump-to-source power ratio or limiting the source power should be kept. In addition, the TE_{10} mode on the surface has longitudinal, x, and transverse, y, components of the magnetic field. Figure 4.13 displays the related magnetic fields respectively. Figure 4.14 presents the simulation results of the electric and magnetic field vectors for the unit cell in the cavity for both port-1 and port-2 excitation, corresponding to forward and backward illuminations, respectively. We can observe the field transformation on and across the unit cell and, most importantly, the occurrence of $\pi-$phase difference depending on the stimulation direction. Additionally, Figure 4.15 shows the power flow vectors. Although we see the longitudinal power flow on the surface, the net power flow along the surface is zero except for the leakage and radiation since the surface wave is a standing wave. So nearly all power flows towards Port 1 and Port 2.

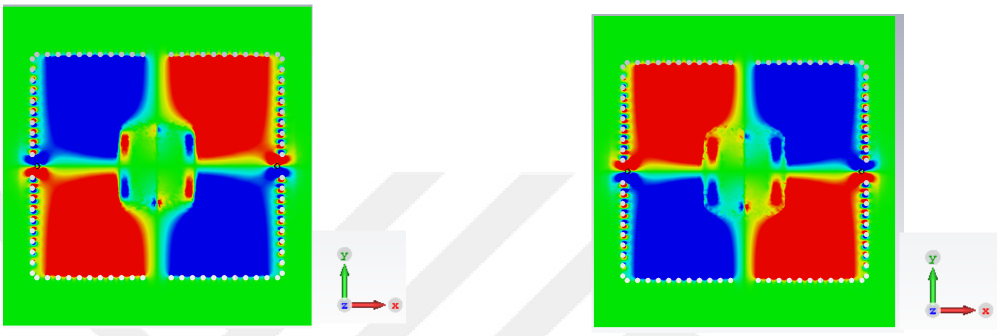

(a) H_x for forward illumination

(b) H_x for backward illumination

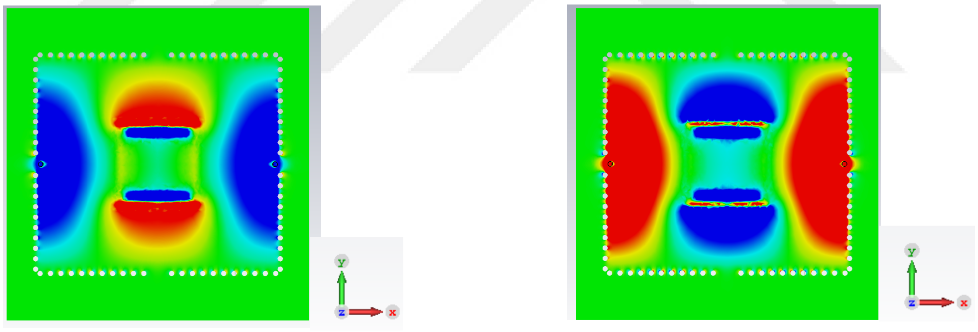

(c) H_y for forward illumination

(d) H_y for backward illumination

Figure 4.13. Simulation results for the magnetic field distribution on the dynamic unit cell with a surface-cavity mode. The results show the field distribution at the top view (normal to $\hat{z}$) for forward (Port 1) and backward (Port 2) illumination. Minimum and maximum magnetic field strength is adjusted as $\mp 10A/m$.

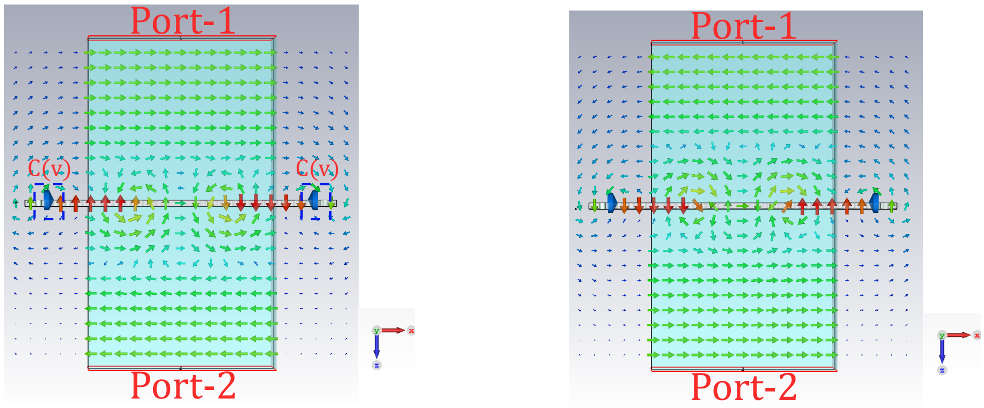

(a) $\vec{E}$ for forward illumination (b) $\vec{E}$ for backward illumination

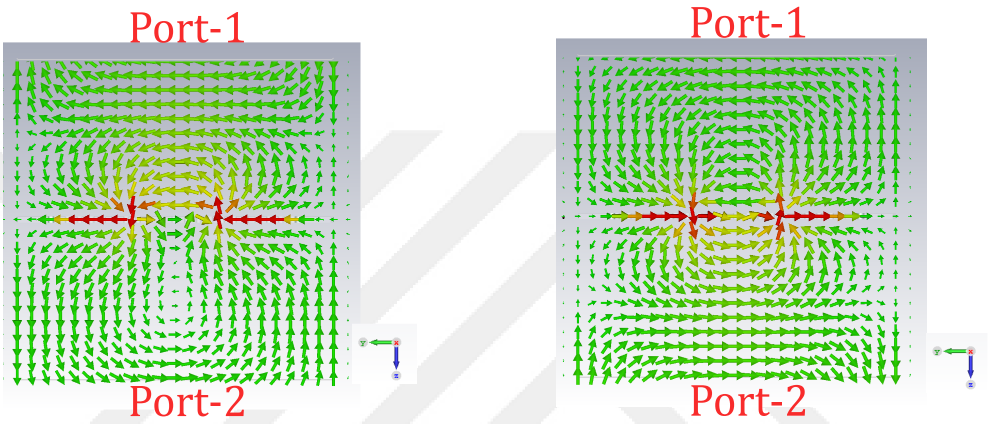

(c) $\vec{H}$ for forward illumination (d) $\vec{H}$ for forward illumination

Figure 4.14. Simulation results of the electric and magnetic field vectors for the dynamic unit cell with a surface-cavity mode. The results show the vector distributions at the side view (normal to $\hat{y}$ for $\vec{E}$ and normal to $\hat{x}$ for $\vec{H}$) for forward (Port 1) and backward (Port 2) illumination. Minimum and maximum field strengths of electric and magnetic fields are adjusted as $\mp 10000V/m$ and $\mp 10A/m$, respectively.

4.3.3. Equivalent Circuit Model For Dynamic Unit Cell

We have discussed that a DNG slab with the coupled surface wave can be considered a pair of phase conjugate surfaces separated within a subwavelength scale. This enables us to model the non-parsable complicated medium as three coupled media, as given in Figure 4.8. In this way, we can construct the impedance-based equivalent TL circuit with a parallel impedance equivalent connection as indicated in the figure for the coupled surface-cavity mode. We can model surface cavity mode by a resonance circuit with a variable capacitor in a LC bank. This equivalent model will allow us to apply

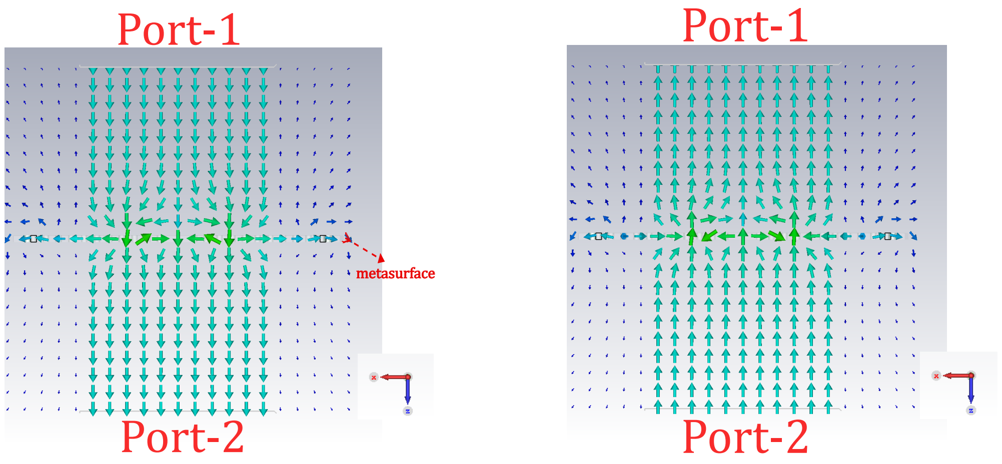

(a) $\vec{P}_{flow}$ for forward illumination
(b) $\vec{P}_{flow}$ for backward illumination

Figure 4.15. Simulation results of the power flow vectors for the dynamic unit cell with a surface-cavity mode. The results show the vector distributions at side view (normal to $\hat{y}$) for forward (Port 1) and backward (Port 2) illumination. Maximum power flow density is adjusted as $9.8 \times 10^6 V.A/m^2$.

numerical techniques (ITMM and HB simulation) to solve time-modulated unit cells for analyzing the nonreciprocal transmission.

Table 4.2. The extracted values of LC parameters from simulation of the unit cell in cavity-mode with variable capacitors.

	Z_{s1}	Z_{s2}	Z_p	Z_{sw}
C_1	17.6pF	-18.85pF	1.43pF	0.1pF
L_1	0.15nH	-0.14nH	1.84nH	20nH
C_2	-7.5pF	8.21pF	1.93pF	54.5pF
L_2	-0.23nH	0.21nH	0.89nH	0.5nH

The surface cavity mode, coupled to the time-varying capacitor parallel connected to the coaxial line cross-section, is modeled using cascade LC resonators represented by Z_{sw} as in Figure 4.8. Table 4.2 lists the extracted parameters based on the impedance characterization. Then, the equivalent circuit is reconstructed, which now has a variable capacitor. Figure 4.16a shows the transmission magnitude obtained through the 3D simulation and calculated through the circuit model. The results show that the equivalent model is approximately suitable to accomplish the proposed method with time modulation. We neglect the dispersion in the cavity mode for the 3D model. Thus, there is an approximation limit for the capacitor value range, as seen in Figure 4.16b. For the given simulation configuration, the limit is $C_V \leq 1pF$ for subsequent calculations.

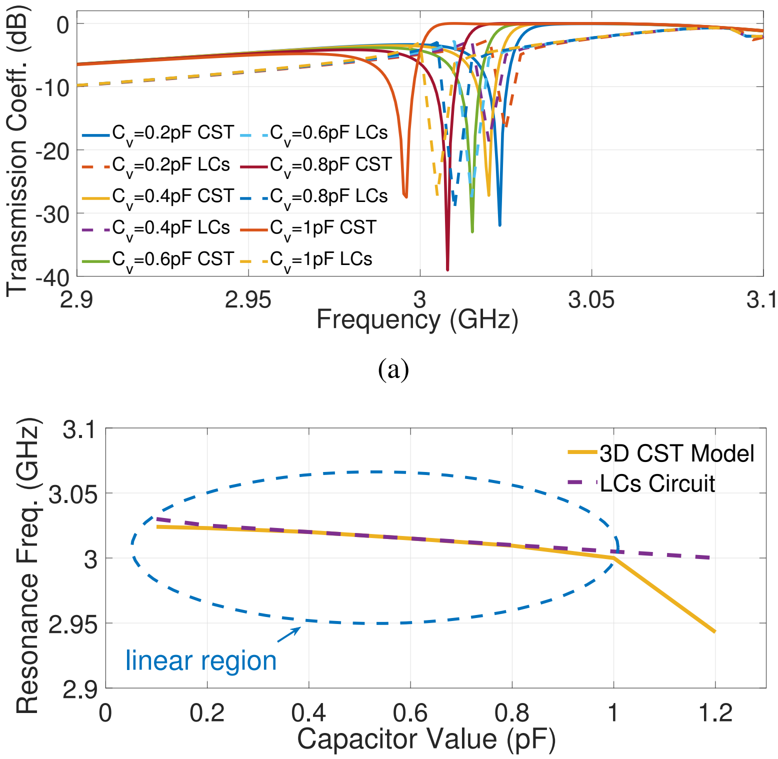

(a)

(b)

Figure 4.16. Simulation results of $3D$ simulation and the equivalent model for the unit cell in cavity-mode with variable capacitors: (a) magnitude of transmission coefficients (in dB) with respect to capacitor values (C_V), (b) resonance frequency as a function of the capacitor value (Yılmaz and Yaman, 2024).

CHAPTER 5

NONRECIPROCAL TRANSMISSION BY TIME-MODULATED UNIT CELL

This chapter begins with the time domain analysis of the simplified bi-isotropic circuit incorporating a time-varying component. We examine its time modulation response and identify the conditions for achieving nonreciprocal transmissions. We then develop the numerical techniques, impedance transfer matrix method (ITMM), and harmonic balance (HB) simulation to solve the developed circuit model of the unit cell, which has a variable capacitor that will be time-modulated. The results demonstrate that it is possible to enable partial (phase-coherent) and full (phase-incoherent) nonreciprocal transmissions by the proposed method.

5.1. Time-Domain Analysis of Bi-isotropic Circuit with Time-Varying Capacitance

Ω-coupling bianisotropic surface can be modeled as $T - circuit$ with $Z_{s1} \neq Z_{s2}$ under specific excitation and polarization. This circuit might be called bi-isotropic. For the time-domain analysis, Figure 5.1 shows its simplified type, including a time-varying parallel capacitor with $L_1 \neq L_2$ for forward and backward illumination.

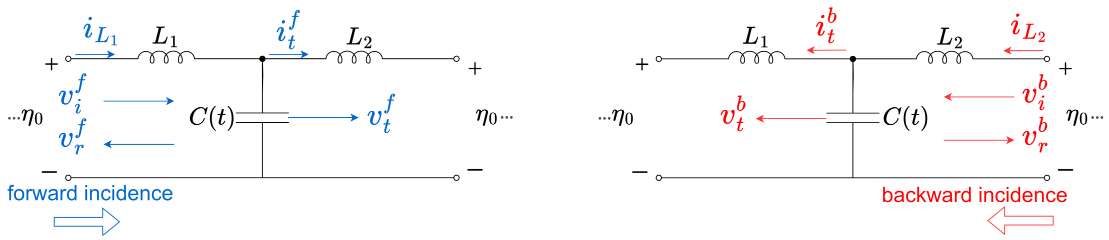

(a) Forward illumination

(b) Backward illumination

Figure 5.1. A simplified bi-isotropic circuit ($L_1 \neq L_2$) with a parallel-connected time-varying capacitor.

We first derive the solution for the forward incidence by following the analysis in the literature (Wang et al., 2020; Ptitcyn, 2021). We can express the currents on the middle node as

$$i_{L_2} = i_{L_1} + i_c. \tag{5.1}$$

For the incoming and leaving currents through the surface in terms of incident (i_i), reflected (i_r), and transmitted current (i_t) can be expressed as

$$\begin{aligned} i_i - i_r &= i_{L_2}, \\ i_t &= i_{L_1}, \end{aligned} \tag{5.2}$$

and reflected current is expressed as

$$i_r = i_i - i_t - i_c. \tag{5.3}$$

Similarly, we can write the relations for voltages as

$$\begin{aligned} &Vi + V_r = V_{L_2} + V_c, \\ &V_c = V_t + V_{L_1}, \\ &V_i + V_r = V_t + V_{L_1} + V_{L_2}. \end{aligned} \tag{5.4}$$

The relation of the current and voltage at the input port is given as

$$i_i + i_r = \frac{V_{L_2} + V_c}{\eta_0}. \tag{5.5}$$

So we follow similar expressions for the middle node as

$$2i_i - i_t - i_c = \frac{V_{L_2} + V_{L_2} + V_t}{\eta_0}, \tag{5.6}$$

$$2V_i = 2V_t + \eta_0 i_c + V_{L_1} + V_{L_2}. \tag{5.7}$$

The voltage of the inductance and the current of the capacitor can be expressed by

$$V_{L_{1,2}} = L_{1,2}\frac{di_{L_{1,2}}}{dt}, \tag{5.8}$$

$$i_c = \frac{dQ}{dt} = C\frac{dV_c}{dt} + \frac{dC}{dt}V_c. \tag{5.9}$$

Finally, we can express the relation between the incident and the transmitted voltages after substituting Equation 5.1,5.3 and Equation 5.8 into Equation 5.7. For the backward incidence, we obtain an equal expression except for the term of $(2L_{2,1} + L_{1,2})\frac{dC}{dt}$, where subscripts refer to respectively forward and backward cases. The final relation for both cases is given by

$$\begin{gathered}
2V_i^{\mathbf{b,f}} = \left[2 + \eta_0\frac{dC}{dt} + L_2\frac{d^2C}{dt_2}\right]V_t^{\mathbf{b,f}} + \left[\frac{L_1 + L_2}{\eta_0} + \eta_0 C + (\mathbf{2L_{2,1}} + \mathbf{L_{1,2}})\frac{\mathbf{dC}}{\mathbf{dt}}\right. \\
\left. + \frac{L_1L_2}{\eta_0}\frac{d^2C}{dt^2}\right]\frac{dV_t^{\mathbf{b,f}}}{dt} + \left[C(L_1 + L_2) + 2\frac{L_1L_2}{\eta_0}\frac{dC}{dt}\right]\frac{d^2V_t^{\mathbf{b,f}}}{dt^2} + \left[\frac{L_1L_2C}{\eta_0}\right]\frac{d^3V_t^{\mathbf{b,f}}}{dt^3}.
\end{gathered} \tag{5.10}$$

The highlighted in bold term in Equation 5.10 is responsible for differences in the ratio of transmitted and incident voltages unless $L_1 = L_2$. As discussed in Chapter 3, the bianisotropy creates unequal series impedances indicated as $L_1 \neq L_2$ in simplified case. To enable asymmetric transmission, the time-derivative of the capacitance must be non-zero, i.e., $\frac{dC}{dt} \neq 0$. These are the essential requirements of nonreciprocal transmission for the time-modulation technique in the ideal lossless and linear situation.

5.1.1. Sinusoidal Modulation of C(t)

Consider the parallel capacitor is temporally modulated as

$$C(t) = C_0 - AC_0 \sin(\omega_m t + \Phi), \tag{5.11}$$

and transmitted waves are assumed to be the same monochromatic for forward and backward, given as

$$v_t^f(t) = v_t^b(t) = \cos(\omega_0 t + \phi). \tag{5.12}$$

Substituting both into the Equation 5.10, we can write the final expressions in equations 5.13-5.15) by separating into the three harmonics, ω_0, $\omega_m - \omega_0$ and $\omega_m + \omega_0$ as follows

$$\begin{aligned} V_{i_1}^{b,f} &= \left[1 - \frac{C_0(L_1 + L_2)}{2}\omega_0^2\right] \cos\big(\omega_0 t + \phi\big) + \\ &\left[-\frac{(L_1 + L_2)}{2\eta_0}\omega_0 - \frac{\eta_0 C_0 \omega_0}{2} + \frac{L_1 L_2 C_0}{2\eta_0}\omega_0^3\right] \sin\big(\omega_0 t + \phi\big), \end{aligned} \tag{5.13}$$

$$\begin{aligned} V_{i_2}^{b,f} &= \left[\frac{\eta_0 C_0 A}{4}(-\omega_m + \omega_0) - \frac{L_1 L_2 C_0 A \omega_0}{4\eta_0}(\omega_m - \omega_0)^2\right] \cos\big((\omega_m - \omega_0)t + \Phi - \phi\big) \\ &+ \left[\frac{AC_0}{4}\bigg(L_{2,1}\omega_m^2 - (2L_{2,1} + L_{1,2})\omega_m\omega_0 + (L_1 + L_2\omega_0^2)\bigg)\right] \sin\big((\omega_m - \omega_0)t + \Phi - \phi\big), \end{aligned} \tag{5.14}$$

$$V_{i_3}^{b,f} = \left[\frac{\eta_0 C_0 A}{4}(-\omega_m - \omega_0) + \frac{L_1 L_2 C_0 A \omega_0}{4\eta_0}(\omega_m + \omega_0)^2\right] \cos((\omega_m + \omega_0)t + \Phi + \phi)$$

$$+ \left[\frac{C_0 A}{4}\Big(L_{2,1}\omega_m^2 + (2L_{2,1} + L_{1,2})\omega_m\omega_0 + (L_1 + L_2)\omega_0^2\Big)\right] \sin\big((\omega_m + \omega_0)t + \Phi + \phi\big). \tag{5.15}$$

These expressions help us to understand the source of the nonreciprocal response in the system under consideration. Specifically, we observe that the terms representing the static response of the circuit, $V_{1_1}^b = v_{1_1}^f$, and $v_{i_{2,3}}^b \neq v_{i_{2,3}}^f$ under the capacitor is time-varying ($\frac{dC}{dt} \neq 0$) and $L_1 \neq L_2$. To achieve nonreciprocal transmission, it is required to select the modulation frequency ω_m such that either $V_{i_2}^{f,b}$ or $V_{i_3}^{f,b}$ corresponds to the fundamental frequency ω_0. The third terms, $V_{i_3}^{f,b}$, only contribute to the fundamental frequency when $\omega_m = 0$. In this trivial situation, there will be no asymmetric transmission, $V_{i_3}^f = V_{i_3}^b$. The second terms, $V_{i_2}^{f,b}$, can contribute to the fundamental frequency when $\omega_m = 2\omega_0$, resulting in asymmetric contributions: $V_{i_2}^f \neq V_{i_2}^b$ (Wang et al., 2020).

Using the phasor notation, we can express the transmission coefficient for forward and backward cases when $\omega_m = 2\omega_0$. The complex amplitudes of transmitted waves are assumed to be as

$$\mathcal{V}_t^{f,b}(t) = \Re(V_t^{f,b} e^{j\omega_0 t}) \qquad \textit{where} \qquad V_t^f = V_t^b = e^{j\phi}. \tag{5.16}$$

Equation 5.17 defines the transmission coefficients at the fundamental frequency of the source signal, i.e. ω_0.

$$T^{\mathbf{b,f}}(\omega_0) = \frac{2e^{-j(\theta - 2\phi)}}{2 - \frac{C_0 L_s}{2}\omega_0^2 + j\omega_0\big(\frac{L_s}{\eta_0} + \eta_0 C_0 - \frac{L_m C_0}{\eta_0}\omega_0^2\big) - \frac{A C_0 \omega_0}{2}\big(\eta_0 + \frac{L_m \omega_0}{\eta_0} \mp \mathbf{j L_d \omega_0}\big)}, \tag{5.17}$$

where $L_s = L_1 + L_2$, $L_m = L_1 L_2$ and $L_d = L_1 - L_2$. The signal mixing in Equation 5.15 by $\omega_0 + w\omega_m$, results in the $3\omega_0$ harmonic for the modulation $\omega_m = 2\omega_0$, and it is given by

$$T^{b,f}(3\omega_0) = \frac{2}{\dfrac{-3\omega_0\eta_0 C_0 A}{2} + \dfrac{9\omega_0^3 L_1 L_2 C_0 A}{2\eta_0} + j\dfrac{3C_0 A\omega_0^2}{2}(3L_{1,2} + L_{2,1})e^{j\Phi}}. \tag{5.18}$$

To clarify the analytical expressions, we provide a numerical example for a given configuration with $L_1 = 10nH$, $L_2 = 60nH$, and a capacitance function $C(t) = 0.225 + 0.2025\sin(\omega_m t + \phi)$ pF, as visualized in Figure 5.2a.

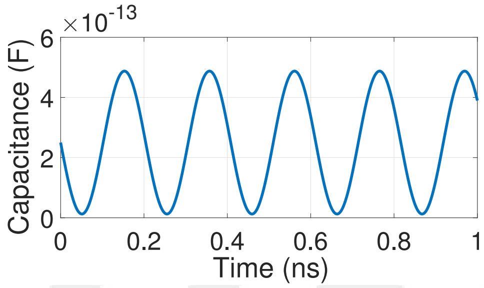

(a) $C(t) = 0.225 + 0.2025\sin(\omega_m t + \phi)$pF and $A_0 = \max(C(t)/C_0) = 0.9$.

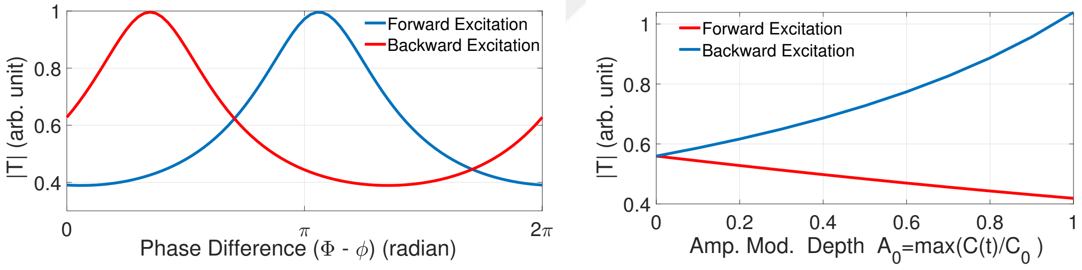

(b) (c)

Figure 5.2. Results for analytical solution of an example bi-isotropic circuit by time modulation ($\omega_m = 2 \times \omega_0$): (a) an example of a capacitance function with time, and magnitude of transmission coefficients (in linear) for (b) phase difference between source and modulation signals, (c) amplitude modulation depth.

The frequency of source and pump signal are given as $\omega_m = 2\omega_0$ where $\omega_0 = 2.45GHz$. Figure 5.2b shows the magnitude of transmission coefficient (in linear scale) results for the phase difference between the source and capacitor function. We observe the asymmetric transmission by the result; however, it is called partial or phase-coherent nonreciprocity in literature (Bahamonde, 2020; Wang et al., 2020) since the transmission depends on the phase of the source signal (assuming the modulation is fixed). Moreover, Figure 5.2c shows the maximum quantity in the difference of transmission magnitude for the amplitude of the modulation depth, which is expressed as $A_0 = \max(C(t)/C_0)$.

5.2. Numerical Techniques For Time-Modulated Circuit

Time-domain analysis is crucial for understanding nonreciprocity but it is not suitable for complex circuits with multiple time-varying components. To address this, techniques like the ITMM (Li et al., 2019; Alvarez-Melcon et al., 2019) and HB simulation (ADS, 2019) are developed. HB simulation is a ready-to-use commercial software tool. It combines time and frequency domains through iterative methods to model real components, including nonlinear elements like diodes and transistors. In contrast, ITMM solutions should be developed for each particular problem having a time-modulated system. It uses user-defined analytical expressions for time-varying components and applies Floquet analysis for time-periodicity.

5.2.1. Impedance Transfer Matrix Method

The transfer matrix method is applied to various applied-physic areas, and it has flexibility on modulation functions introduced to variable components (Shen et al., 2019; Li et al., 2019; Alvarez-Melcon et al., 2019). This part begins with a review of the derivation of ITMM analytical expressions (Wang et al., 2020). Subsequently, we develop solutions for the proposed equivalent circuit discussed in Chapter 4 to implement the ITMM. The arbitrary time-periodic variation of capacitance can be expressed by using the Fourier Series as

$$C(t) = \sum_{m=-\infty}^{+\infty} c_m e^{jm\omega_m t}, \tag{5.19}$$

where c_m represents the Fourier series coefficients. For the time-varying capacitor, the total charge is expressed as

$$Q(t) = C(t) \cdot V_C(t), \tag{5.20}$$

and the current through the capacitor, i.e. $\dfrac{dQ(t)}{dt}$ is given as

$$i_C(t) = \frac{d}{dt}\left[C(t) \cdot V_C(t)\right]. \tag{5.21}$$

Similarly, voltage and current can be written in the form of vector given as

$$V_C(t) = \sum_{n=-\infty}^{+\infty} v_n^C e^{\omega_n t}. \tag{5.22}$$

The capacitor and inductor can be expressed under the modulation by

$$V_C(t) \cdot C(t) = \int_0^t I_C(t')dt'. \tag{5.23}$$

Substituting equations 5.19-5.22 into Equation 5.23, the following expression is found as

$$\sum_{n=-\infty}^{+\infty} \sum_{m=-\infty}^{+\infty} c_m v_n^C e^{j\omega_{n+m} t} = \sum_{n=-\infty}^{+\infty} \frac{1}{j\omega_n} i_n^C e^{j\omega_n t}. \tag{5.24}$$

The basis functions on the left and right sides of the equation become the same after replacing n with $n - m$ on the left side. Modulation introduces to an infinite number of harmonics with frequencies $\omega_\mathbf{n} = \omega_\mathbf{0} + \mathbf{n}\omega_\mathbf{m}$. Considering harmonics from $n = -N$ to $n = +N$, the problem is formulated as a linear equation given as

$$\sum_{m=-\infty}^{+\infty} j\omega_n c_m v_{n-m}^C = i_n^C. \tag{5.25}$$

This expression is given in terms of admittance matrix as

$$\bar{Y}_C.\vec{v}_C = \vec{i}_C, \tag{5.26}$$

where admittance matrix $\bar{Y}_C$ explicitly given as

$$\begin{bmatrix} j\omega_{-N}C_0 & j\omega_{-N}C_{-1} & \dots & j\omega_{-N}C_{-2N} \\ j\omega_{1-N}C_1 & j\omega_{1-N}C_0 & \dots & \vdots \\ \vdots & \vdots & \vdots & \vdots \\ j\omega_N C_{2N} & j\omega_N C_{2N-1} & \dots & j\omega_N C_0 \end{bmatrix}_{(2N+1)\times(2N+1)} \tag{5.27}$$

Here, each row in the vector denotes the complex amplitude of each harmonic. In this way, impedance and admittance can be represented by matrices that relate the complex voltage and current vectors. The vectors of voltage and current harmonics under modulation are given as

$$\vec{v}_C = \begin{bmatrix} \dots \\ v^C_{-1} \\ v^C_0 \\ v^C_1 \\ \dots \end{bmatrix}_{(2N+1)\times 1} \quad \text{and} \quad \vec{i}_{L,C} = \begin{bmatrix} \dots \\ i^C_{-1} \\ i^C_0 \\ i^C_1 \\ \dots \end{bmatrix}_{(2N+1)\times 1} \tag{5.28}$$

Equation 5.25 stands for the convolution of the capacitor function over its voltage since multiplication in the time domain corresponds to the convolution in the frequency domain. In the frequency domain, the Fourier convolution theorem states that $\frac{d}{dt} \rightarrow j\omega$ and multiplication change with convolution, $. \rightarrow *$ for each harmonic.

The relation between voltage and current for a time-periodic inductance can be obtained following the same procedure. The final linear equation is given as

$$\sum_{m=-\infty}^{+\infty} j\omega_n l_m i^L_{n-m} = v^L_n, \tag{5.29}$$

and the impedance matrix relation is given as

$$\bar{\bar{Z}}_L.\vec{i_L} = \vec{v_L}. \tag{5.30}$$

In microwave engineering, many practical networks are often constructed by cascading two or more two-port networks. For such networks, a solution technique of impedance transfer matrix uses a 2×2 called $ABCD$ matrix for each two-port network. The ABCD matrix relates the voltage and current in each port of two-port networks. It is particularly useful for systems with two or more interconnected networks, as illustrated in Figure 5.3.

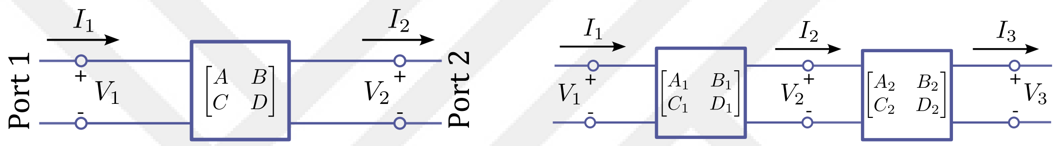

(a) single two-port network (b) cascaded two-port network

Figure 5.3. Illustration of $ABCD$ network (Pozar, 2012).

For each network, voltage and current relations between ports via $ABCD$ parameters are expressed as (Pozar, 2012)

$$\begin{aligned} V_1 &= AV_2 + BI_2, \\ I_1 &= CV_2 + DI_2, \end{aligned} \tag{5.31}$$

or in matrix form, given as

$$\begin{bmatrix} V_1 \\ I_1 \end{bmatrix} = \begin{bmatrix} A & B \\ C & D \end{bmatrix} \begin{bmatrix} V_2 \\ I_2 \end{bmatrix}. \tag{5.32}$$

For a cascade two-port system, the relation between the input and output ports will be the matrix multiplication of the $ABCD$ parameters of each network given by

$$\begin{bmatrix} V_1 \\ I_1 \end{bmatrix} = \begin{bmatrix} A_1 & B_1 \\ C_1 & D_1 \end{bmatrix} \begin{bmatrix} A_2 & B_2 \\ C_2 & D_2 \end{bmatrix} \begin{bmatrix} V_3 \\ I_3 \end{bmatrix}. \tag{5.33}$$

(a) Series impedance

(b) Shunt admittance

Figure 5.4. Illustration of two-port network for series impedance and parallel admittance.

For a series impedance in Figure 5.4a and a shunt admittance in Figure 5.4b, the formations of $ABCD$ matrices are given by

$$\Big[ABCD\Big]_Z = \begin{pmatrix} 1 & Z \\ 0 & 1 \end{pmatrix} \quad \text{and} \quad \Big[ABCD\Big]_Y = \begin{pmatrix} 1 & 0 \\ Y & 1 \end{pmatrix} \tag{5.34}$$

The $ABCD$ matrix technique is particularly useful when dealing with circuits that involve many harmonics, such as time-modulated capacitance and/or inductance circuits. In such cases, each parameter of the $ABCD$ matrix becomes a $(2N+1)\times(2N+1)$ matrix, and the overall $ABCD$ matrix now has a size of $(4N+2)\times(4N+2)$. For validation, the simplified T-circuit, which was solved analytically in Section 5.1.1, can now be represented in the form of impedance matrices, as shown in Figure 5.5 and solved by using the ITMM. The total $ABCD$ matrix, which relates the input and output quantities of the overall system, is calculated for forward (^{f}) and backward (^{b}) illumination by

$$\begin{aligned} \Big[\overset{=}{ABCD}\Big]^f_{total} &= \Big[\overset{=}{ABCD}\Big]_{L_1} \Big[\overset{=}{ABCD}\Big]_C \Big[\overset{=}{ABCD}\Big]_{L_2}, \\ \Big[\overset{=}{ABCD}\Big]^b_{total} &= \Big[\overset{=}{ABCD}\Big]_{L_2} \Big[\overset{=}{ABCD}\Big]_C \Big[\overset{=}{ABCD}\Big]_{L_1}. \end{aligned} \tag{5.35}$$

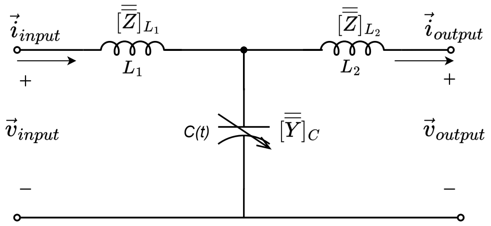

Figure 5.5. The simplified bi-isotropic $T-$circuit with a time-modulated capacitor, and its representation by series impedance and parallel admittance for ITMM solutions.

We can calculate the transmission and reflection matrices comprising the total number of harmonics in each row and column as (Wang et al., 2020; Pozar, 2012)

$$\begin{aligned} \bar{\bar{T}} &= 2\left(\bar{\bar{A}} + \bar{\bar{B}}\bar{\bar{Y}}_0 + \bar{\bar{Z}}_0\bar{\bar{C}} + \bar{\bar{Z}}_0\bar{\bar{D}}\bar{\bar{Y}}_0\right)^{-1}, \\ \bar{\bar{R}} &= \left(\bar{\bar{A}} + \bar{\bar{B}}\bar{\bar{Y}}_0\right)\bar{\bar{T}} - \bar{\bar{I}}, \end{aligned} \tag{5.36}$$

where $\bar{\bar{Y}}_0$ and $\bar{\bar{Z}}_0$ are the admittance and impedance matrices of free space, respectively, while $\bar{\bar{I}}$ denotes the unitary matrix.

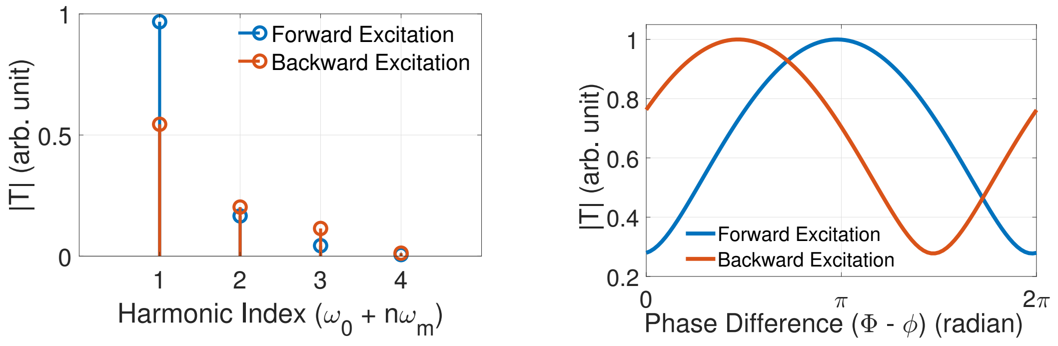

(a)

(b)

Figure 5.6. ITMM solution results for the simplified bi-isotropic circuit having a time-modulated capacitor: magnitude of transmission coefficients for (a) harmonics, (b) phase difference.

The simplified circuit with the same parameters in Section 5.1.1 is resolved to verify the developed ITMM solution. Figure 5.6 shows the results of the magnitude of the transmission coefficient in harmonics and for the input phase (phase of modulation function is fixed). The results are consistent with the time-domain solution in Figure 5.2b regarding the quantity of the asymmetric transmission and the response to the phase difference.

5.2.2. Harmonic Balance Simulation

Harmonic balance (HB) is an iterative simulation technique that uses both frequency and time domain approaches to simulate nonlinear effects in circuits and systems with multi-harmonics. This method evaluates nonlinear devices such as transistors and diodes in the time domain and then converts them to the frequency domain using the Fast Fourier Transform (FFT). The general algorithm procedure, along with the block diagrams, is illustrated in Figure 5.7 (ADS, 2019). The solution can be represented as a sum of steady-state sinusoidal functions corresponding to input frequencies and desired harmonics. For example, the waveform of a node voltage $v(t)$ in a single frequency HB simulation can be approximated by

$$v(t) = \left\{ \sum_{k=0}^{K} V_k e^{j2\pi k f_0 t} \right\}. \tag{5.37}$$

Here, f_0 is the fundamental frequency, V_k are the complex Fourier coefficients from HB analysis, and K is the truncation level (number of harmonics). A multi-tone simulation is needed for circuits with multiple input sources. The steady-state waveform is then approximated by a multi-dimensional truncated Fourier series, given as

$$v(t) = \left\{ \sum_{k_1=0}^{K_1} \sum_{k_2=0}^{K_2} \cdots \sum_{k_n=0}^{K_n} V_{k_1,k_2,\ldots,k_n} e^{j2\pi(k_1 f_1 + \cdots + k_n f_n)t} \right\}, \tag{5.38}$$

where, n is the number of tones (sources), $f_{1,\ldots,n}$ are the fundamental frequencies of each source, and $K_{1\ldots n}$ indicates the number of harmonics for each tone. Multiple frequency simulation generates the mixing products given in general by

$$g\{v(t)\} + \frac{d}{dt} q\{v(t)\} + y(t) \otimes v(t) = i(t), \tag{5.39}$$

and in the frequency domain is expressed by

$$F_k\big[g\{v(t)\}\big] + j\omega_k F_k\big[q\{v(t)\}\big] + Y(j\omega_k)V_k = I(\omega_k), \tag{5.40}$$

where, $g\{\cdot\}$ and $q\{\cdot\}$ are the nonlinear operators, F_k represents the k^{th} spectral component of a Fourier transform, with $\omega_k = 2\pi f k$. The $N * M$ nonlinear equations are solved iteratively for the V_k values. Nonlinear components are evaluated in the time domain by performing an inverse Fourier transform to convert V_k into the waveform $v(t)$. Each iteration transforms the current waveform and nonlinear charges into the frequency domain to apply their spectral values in frequency domain equations.

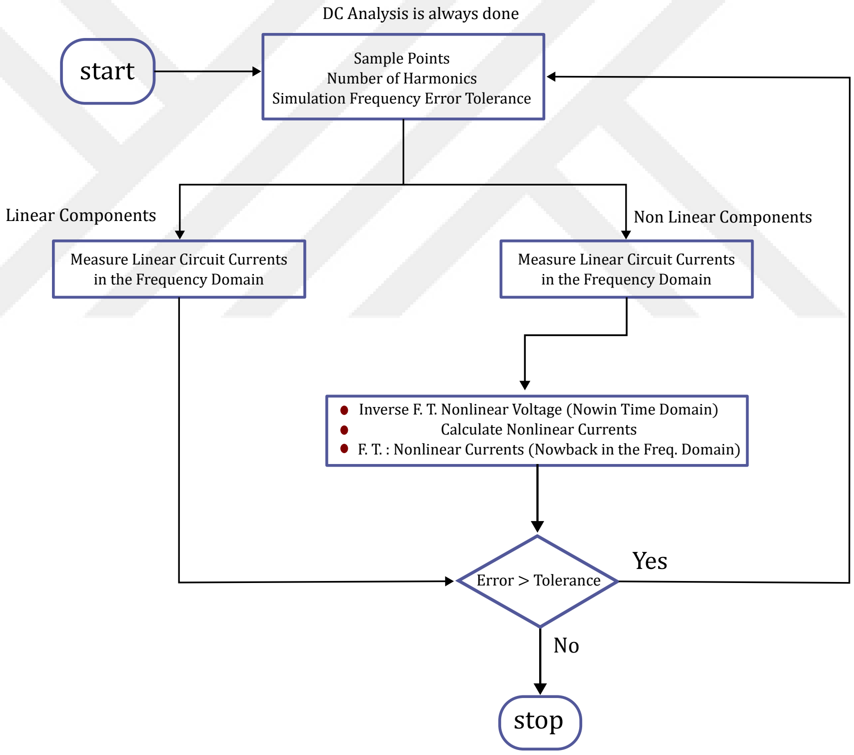

Figure 5.7. Block diagram of solution algorithm for harmonic balance simulation (ADS, 2019).

The HB simulation tool is in most commercial high-frequency simulation software packages. To verify the harmonic balance setup for the time modulation solution, we simulated the simplified T-circuit in Section 5.1.1 and Section 5.2.1 for the same parameters. The simulation schematic is given in Figure 5.8a for the forward illumination. For the backward illumination, the source port and load terminations are interchanged. We optimized the voltage supply of the varactor diode to have a similar modulation function. The time-varying capacitance function is calculated, and its curve is given in Figure 5.8b for several periods. The equations 5.41-5.43 give the calculation of the capacitance function by using time-domain voltage and current acquired from the simulation (M.S. Mirmoosa and Tretyakov, 2019; Biolek et al., 2007).

$$V_L(t) = \frac{d}{dt}\big(L(t)i_L(t)\big) = L(t)\frac{d}{dt}(i_L(t)) + i_L(t)\frac{d}{dt}(L(t)), \tag{5.41}$$

$$i_C(t) = \frac{d}{dt}\big(C(t)v_c(t)\big) = C(t)\frac{d}{dt}(v_c(t)) + v_c(t)\frac{d}{dt}(C(t)), \tag{5.42}$$

and the solutions for given differential equations are given as

$$\begin{aligned} i_L(t) &= \frac{L(0)i_L(0) + \int_0^t V_L(t)dt}{L(t)}, \quad \text{if} \quad L(t) \neq 0, \\ v_C(t) &= \frac{C(0)V_C(0) + \int_0^t i_C(t)dt}{C(t)}, \quad \text{if} \quad C(t) \neq 0. \end{aligned} \tag{5.43}$$

Figure 5.9 presents the magnitude of the transmission coefficient for harmonics and the source phase (phase of the pump signal is fixed), respectively. These results are well-matched with those obtained from ITMM solution and time-domain analysis, as shown in Figure 5.2 and Figure 5.6. However, unavoidable differences are observed in the transmission results and the capacitor function, as expected. This is because each solution method employs different analysis techniques and modulation parameters. For a linear system, time-domain analysis provides an exact analytic solution. ITMM offers a semi-analytical solution, which provides approximate results due to factors such as the truncated number of series and the inversion of large matrices. On the other hand, HB simulation is designed for nonlinear systems with multiple harmonics and employs realistic models of nonlinear components, yielding approximate but more realistic results. Thus, we avoid direct comparisons between the results obtained from ITMM and HB in the subsequent parts of this thesis. Instead, for both methods, we focus on optimized performance in terms of results and discuss the possible factors that would differ between theory and experiment.

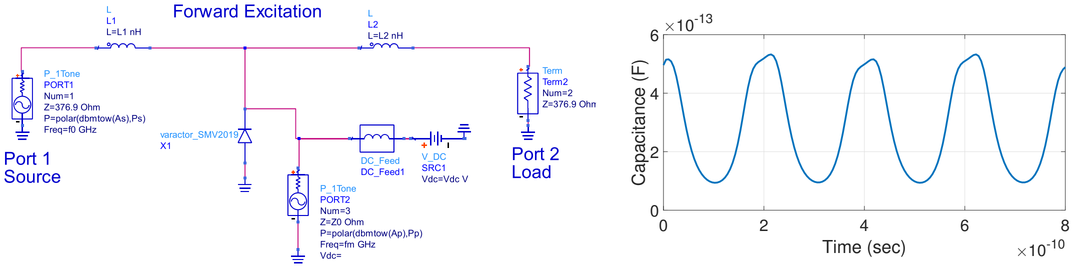

(a) (b)

Figure 5.8. (a) ADS:HB simulation configuration for simplified bi-isotropic T-circuit, (b) calculated capacitance as a function of time $(C(t))$ through time-domain voltage and current on varactor diode.

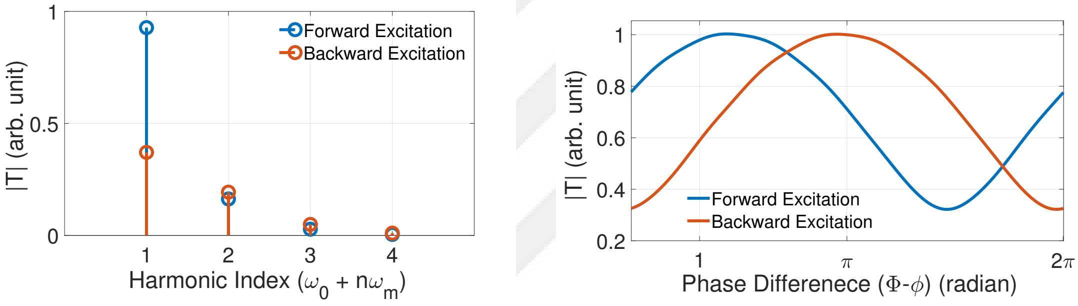

(a) (b)

Figure 5.9. HB simulation results for the simplified bi-isotropic circuit having a time-modulated capacitor: magnitude of transmission coefficients for (a) harmonics, (b) phase difference.

5.3. Numerical Solutions of The Time-Modulated Unit Cell

This section details the derivation of ITMM solutions and HB simulation configuration for the equivalent circuit with a time-varying capacitor proposed in Chapter 4. The results indicate phase incoherent and coherent nonreciprocal transmission for single and two time-varying capacitor $(C(t))$ configurations.

5.3.1. Derivation of Impedance Transmission Matrices

For the proposed penetrable medium supporting surface wave conversion, Figure 5.10 illustrates its unit cell response to free-space wave incidence under time-modulation (Zang et al., 2019).

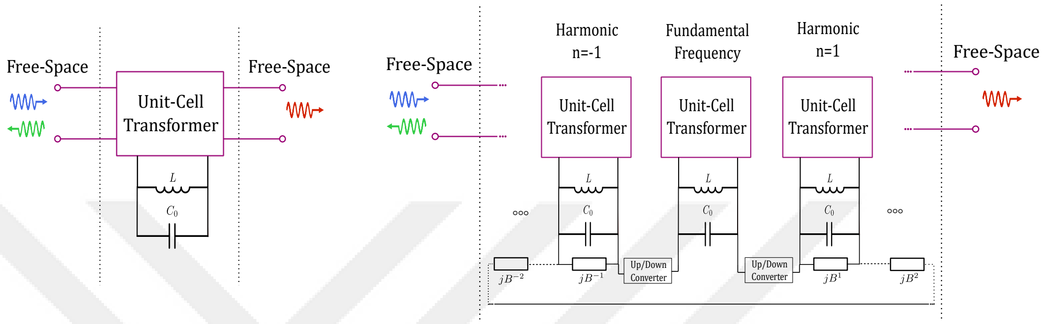

(a) without time-modulation

(b) with time-modulation

Figure 5.10. Illustration of unit cell field transformer with fundamental and mix harmonics by impedance block and time modulated shunt LCs (Zang et al., 2019).

The unit cell transformer represents the time-invariant converter comprising two phase-conjugate resonators in Figure 4.9. The parallel LC resonator represents the fundamental surface-cavity mode, where the inductance is time-invariant, and the capacitor is time-varying. Introducing time-modulation leads to harmonic mixing given as up/down conversion as depicted in Figure 5.10b.

We now develop the numerical solution of the impedance matrices for each cascade circuit block of the proposed circuit in Figure 5.11. This circuit diagram is for a single $C(t)$ configuration. Each circuit block of the surface impedances is modeled as two series LC banks since we consider the first two resonances regarding the homogenization conditions as discussed in Chapter 4. The $\left[\bar{\bar{T}}_{s1}\right]$, $\left[\bar{\bar{T}}_{p1}\right]$ and $\left[\bar{\bar{T}}_{s2}\right]$ are time-invariant impedance blocks. Their impedance matrices, as expressed in Equation 5.34, are constructed with only the diagonal terms given as

$$Z(\omega_{i,j}) = \Big(\frac{1}{j\omega_{i,j}C_1} \parallel j\omega_{i,j}L_1\Big) + \Big(\frac{1}{j\omega_{i,j}C_2} \parallel j\omega_{i,j}L_2\Big). \tag{5.44}$$

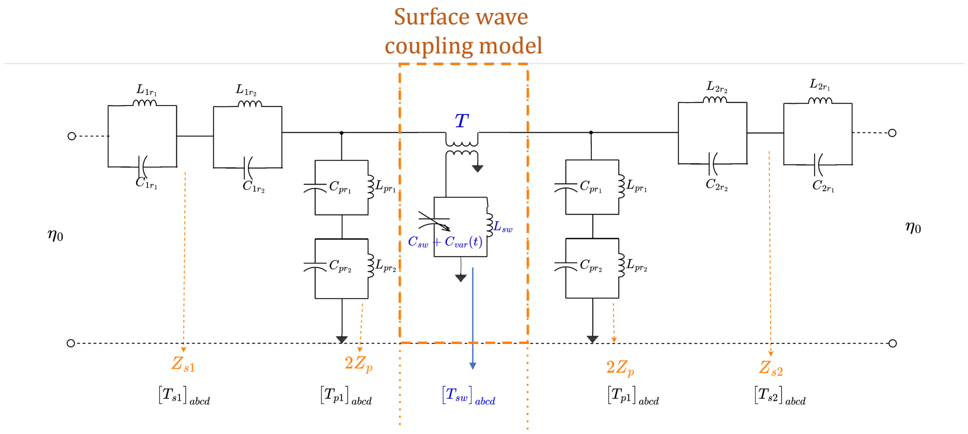

Figure 5.11. Impedance blocks of proposed circuit having single $C(t)$.

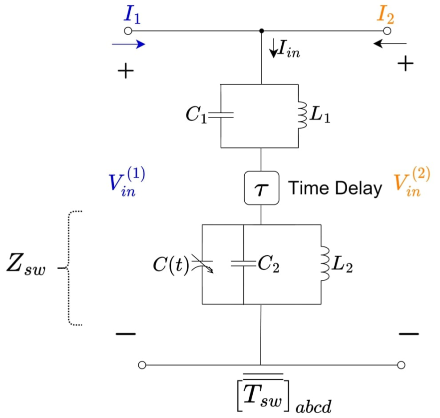

Figure 5.12. The circuit block for surface wave in cavity coupling with a time-varying capacitor, which is connected in parallel through the coaxial interface (Yılmaz and Yaman, 2024).

We first apply the time-domain solution to obtain the final transmission matrix expression for the time-varying circuit block in Figure 5.12 (Yılmaz and Yaman, 2024). We need to introduce a time-delay (τ) function to the equivalent circuit so the π-phase-delayed response in ITMM and HB solutions. Most HB package software (ADS, 2019) has a time-delay function component. However, ITMM is a semi-analytical solution, and the circuit block of time-delayed surface-wave coupling first must be solved in the time domain and subsequently modeled as a shunt circuit block characterized by $ABCD$ parameters. The time-delay function in the circuit is adjusted to represent an ideally π phase difference for each harmonic. We begin the time-domain analysis by applying

Kirchhoff's rules. For the given circuit block they are expressed as

$$\sum_n V_n^C e^{j\omega_n t} = \sum_n V_n^{in} e^{j\omega_n t} - \sum_n V_n^{L1} e^{j\omega_n t}, \tag{5.45}$$

$$\sum_n V_n^C e^{j\omega_n t} = \sum_n V_n^{in} e^{j\omega_n t} - \sum_n V_n^{C1} e^{j\omega_n t}. \tag{5.46}$$

The voltage and current relations can be written for the first LC bank as follows

$$V_n^{C1} = \frac{I_n^{C1}}{j\omega_n C_1}, \qquad I_n^{L1} = \frac{V_n^{L1}}{j\omega_n L_1} \qquad \text{and} \qquad I_n^{C1} = -\omega_n^2 L_1 C_1 I_n^{L1}. \tag{5.47}$$

The current relation at the top node is expressed as

$$\sum_n I_n^{in} e^{j\omega_n t} = \sum_n I_n^{L1} e^{j\omega_n t} + \sum_n I_n^{C1} e^{j\omega_n t}, \tag{5.48}$$

and by substituting this into Equation 5.47, we find the relation given as

$$I_n^{in} = \frac{V_n^{L1}}{j\omega_n L_1}(1 - \omega_n^2 L_1 C_1), \tag{5.49}$$

and it can be also expressed as

$$\sum_n V_n^{in} e^{j\omega_n t} - \sum_n \frac{I_n^{j\omega_n L_1}}{1 - \omega_n^2 L_1 C_1} e^{j\omega_n t} = \sum_n V_n^C e^{j\omega_n t}. \tag{5.50}$$

Now, we need to consider the second $L_2 \| C_2$ block to obtain the expression of V_n^C. Again, applying the voltage loop, we can write the following equation,

$$L_2 \sum_n I_n^{L2} e^{j\omega_n t} = \int_0^t \sum_n V_n^{in} e^{j\omega_n t} dt - \int_0^t \sum_n \big(\frac{I_n^{in}(j\omega_n L_1)}{1 - \omega_n^2 L_1 C_1}\big) e^{j\omega_n t} dt, \tag{5.51}$$

and we can arrive at the relation given as

$$I_n^{L2} = \frac{V_n^{in}}{j\omega_n L_2} - (\frac{L_1}{L_2})\frac{I_n^{in}}{1-\omega_n^2 L_1 C_1}. \tag{5.52}$$

Similarly, the expression for C_2 can be written as

$$I_n^{C2} = j\omega_n C_2 V_n^{in} + \frac{\omega_n^2 L_1 C_2}{1-\omega_n^2 L_1 C_1} I_n^{in}. \tag{5.53}$$

Applying the current conservation at the second node, we find the expression that gives the relation between input voltage and current as

$$\begin{aligned} \sum_n I_n^{in} e^{j\omega_n t} = \sum_n \left[\frac{V_n^{in}}{j\omega_n L_2} - (\frac{L_1}{L_2})\frac{I_n^{in}}{1-\omega_n^2 L_1 C_1}\right] e^{j\omega_n t} + \sum_n \Bigg[j\omega_n C_2 V_n^{in} + \\ \frac{\omega_n^2 L_1 C_2 I_n^{in}}{1-\omega_n^2 L_1 C_1}\Bigg] e^{j\omega_n t} + \sum_n I_n^C \sum_n \left[\frac{V_n^{in}}{j\omega_n L_2} - (\frac{L_1}{L_2})\frac{I_n^{in}}{1-\omega_n^2 L_1 C_1}\right] e^{j\omega_n t}. \end{aligned} \tag{5.54}$$

By substituting Equation 5.54 into Equation 5.50 and combining the harmonic expression of the time-varying capacitor from Equation 5.25, we obtain the final expressions for input voltage and current as

$$\begin{aligned} \sum_m j\omega_m C_m V_{n-m}^{in} + \sum_m \frac{\omega_n \omega_{n-m} L_1 C_m}{1-\omega_{n-m}^2 L_1 C_1} I_{n-m}^{in} = -V_n^{in}[\frac{1}{j\omega_n L_2} + j\omega_n C_2] + \\ I_n^{in}[1 + (\frac{L_1}{L_2})(\frac{1}{1-\omega_n^2 L_1 C_1}) - \frac{\omega_n^2 L_1 C_2}{1-\omega_n^2 L_1 C_1}]. \end{aligned} \tag{5.55}$$

To assign the time-delay function, we use the property of time delay in the frequency domain given as

$$V_{in}(t+\tau) = \sum_n V_n^{in} e^{j\omega_n(t+\tau)} = \sum_n V_n^{in} e^{j\omega_n \tau} e^{j\omega_n t}. \tag{5.56}$$

We finally obtain the matrices defining the voltage and current relation as given in Equation 5.57 and Equation 5.58, respectively. The relation of $\left[Y_{sw}\right] = \left[M_b\right]^{-1}\left[M_a\right]$ gives the admittance matrix of the circuit block, which is applied to Equation 5.59. In numerical calculations, time-delay (τ) is expressed to create a π-phase difference for each harmonic as $\tau_n = 2\pi/\omega_n$.

$$\left[M_a\right] = \sum_m -\omega_n^2\omega_{n-m}L_1C_m e^{j\omega_{n-m}\tau}V^{in}_{n-m} + \Big(\frac{e^{-j\omega_n\tau}}{L_2} - \omega_n^2 C_2 e^{-j\omega_n\tau}\Big)V^{in}_n, \tag{5.57}$$

$$\begin{aligned}\left[M_b\right] &= \sum_m \frac{-j\omega_n^2\omega_{n-m}L_1C_m e^{j\omega_{n-m}\tau}}{1-\omega_{n-m}^2L_1C_1}I^{in}_{n-m}\\ &+\left(j\omega_n e^{j\omega_n\tau} + \frac{j\omega_n e^{j\omega_n\tau}}{1-\omega_n^2L_1C_1}\Big(\frac{L_1}{L_2} - \omega_n^2 L_1C_2\Big)\right)I^{in}_n.\end{aligned} \tag{5.58}$$

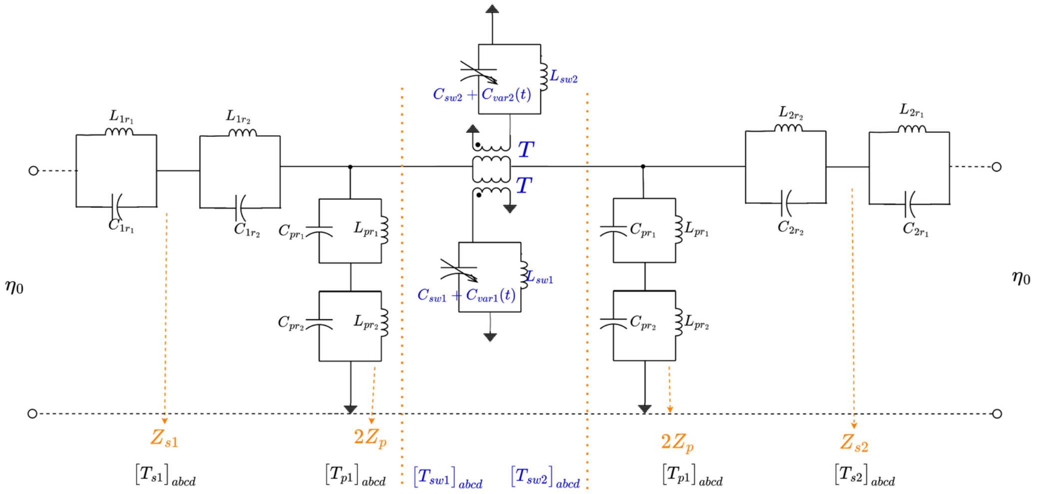

Figure 5.13. Circuit diagram represented by impedance blocks of two $C(t)$ configuration for ITMM solutions.

5.3.2. Numerical Solution Results of Time-Modulated Unit Cell

This part presents the result of the numerical techniques developed for the equivalent circuit model (Yılmaz and Yaman, 2024). Figure 5.13 illustrates the circuit blocks of two $C(t)$ configurations for ITMM solutions. The transmission matrices are computed through Equation 5.59 for forward and backward illumination.

$$\begin{aligned}\left[\bar{\bar{T}}\right]^{forward} &= \left[\bar{\bar{T}}\right]_{s1}\left[\bar{\bar{T}}\right]_{p1}\left[\bar{\bar{T}}\right]_{sw1}\left[\bar{\bar{T}}\right]_{sw2}\left[\bar{\bar{T}}\right]_{p1}\left[\bar{\bar{T}}\right]_{s2},\\ \left[\bar{\bar{T}}\right]^{backward} &= \left[\bar{\bar{T}}\right]_{s2}\left[\bar{\bar{T}}\right]_{p1}\left[\bar{\bar{T}}\right]_{sw2}\left[\bar{\bar{T}}\right]_{sw1}\left[\bar{\bar{T}}\right]_{p1}\left[\bar{\bar{T}}\right]_{s1}.\end{aligned} \tag{5.59}$$

Then, we first express the incident voltage in exponential form as in Equation 5.60 to calculate the transmission coefficient (Wang et al., 2020).

$$v(t) = \Re\left\{\sum_{n=-\infty}^{+\infty} v(\omega_n)e^{j\omega_n t}\right\}, \tag{5.60}$$

which is explicitly given by

$$\vec{v}_i = \begin{bmatrix} \vdots \\ v_i(\omega_{-2}) \\ v_i(\omega_{-1}) \\ v_i(\omega_0) \\ v_i(\omega_1) \\ v_i(\omega_2) \\ \vdots \end{bmatrix} \qquad \text{example for single frequency source:} \qquad \begin{bmatrix} \vdots \\ 0 \\ 0 \\ 1 \\ 0 \\ 0 \\ \vdots \end{bmatrix}. \tag{5.61}$$

The monochromatic incident signal as a source is given as

$$v_i(t) = \big(\frac{1}{2}e^{-j\omega_0 t} + \frac{1}{2}e^{+j\omega_0 t}\big) = \big(e^{-j\omega_0 t}\big) = \big(e^{+j\omega_0 t}\big). \tag{5.62}$$

Provided that $\omega_0 + \mathbf{n}\omega_\mathbf{m} = -\omega_0$, the n^{th} harmonic contributes to the fundamental frequency term ω_0. The magnitude ($|\cdot|$) and phase ($\angle\cdot$) of voltage amplitude for fundamental frequency ω_0, which is contributed by $v_{\omega_{+0}}$ and $v_{\omega_{-0}}$ are calculated by

$$|v_{\omega_0}| = \sqrt{\Re\left\{v_{\omega_{+0}} + v_{\omega_{-0}}\right\}^2 + \Im\left\{v_{\omega_{+0}} - v_{\omega_{-0}}\right\}^2},$$
$$\angle(v_{\omega_0}) = \arctan\left(\frac{\Re\left\{v_{\omega_{+0}} + v_{\omega_{-0}}\right\}}{\Im\left\{v_{\omega_{-0}} - v_{\omega_{+0}}\right\}}\right). \tag{5.63}$$

We can now calculate transmitted wave amplitudes by Equation 5.64 through Equation 5.36 for forward and backward illumination of the monochromatic source.

$$\vec{V_t}^f = \bar{\bar{T}}^f \vec{v_i} \qquad \text{and} \qquad \vec{V_t}^b = \bar{\bar{T}}^b \vec{v_i},$$
$$\vec{V_r}^f = \bar{\bar{R}}^f \vec{v_i} \qquad \text{and} \qquad \vec{V_r}^b = \bar{\bar{R}}^b \vec{v_i}, \tag{5.64}$$

where $\bar{\bar{T}}$ and $\bar{\bar{R}}$ are matrices, $\vec{v_i}$ and $\vec{V_t}^{f,b}$ are vectors, where each row represents the harmonic indices as given in Equation 5.61. We utilize the optimization tools for capacitor modulation functions to maximize asymmetric transmission and isolation quantity. We can define isolation quantity by $\max\left(|T^{f,b}(\phi|_{dB}\right) - \max\left(|T^{b,f}\phi|_{dB}\right)$.

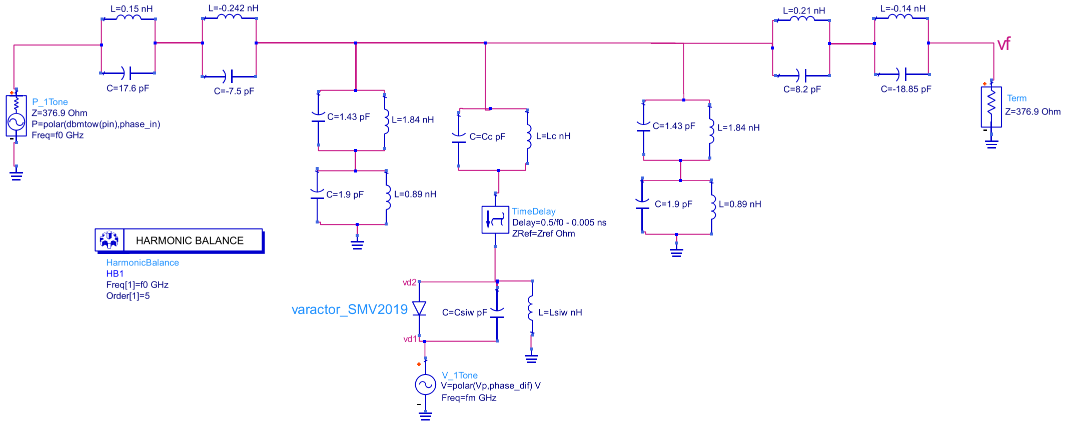

Figure 5.14. The circuit schematic for single-diode configuration in harmonic balance solver of Keysight ADS software for forward illumination. Parameters are indicated in Table 4.2.

In addition to ITMM solutions we employ the Keysight Advanced Design System (ADS) and HB simulation software. The Skyworks SMV2019 varactor diode model is used for the variable capacitor. The simulation setup of a single-diode configuration for forward excitation is illustrated in Figure 5.14. For the backward case, the setup remains the same but with reversed positions of the source power (P_1Tone) and load termination ($Term$). Note that for both numerical solutions (ITMM and HB), the value of the time delays is adjusted to have $\approx \pi-$phase difference on the time-varying capacitor in case of forward and backward illumination. For the results, we first focus on a single-diode configuration (assuming the other capacitor in Figure 4.11a is discarded). Figure 5.15a and Figure 5.15b present the optimized results of nonreciprocal transmission in magnitude and phase for the input phase, respectively. Source and modulation frequencies are $f_0 = 3GHz$ and $f_m = 2 \times f_0 = 6GHz$. The Fourier Series coefficients of the capacitor function derived from both methods are displayed in Figure 5.16.

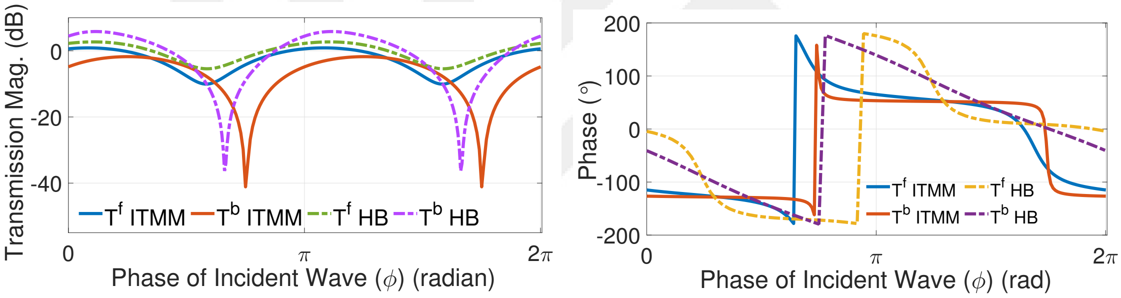

(a) in magnitude (dB)

(b) in phase (°)

Figure 5.15. Results of transmission coefficients with respect to the phase of source signal in the single $C(t)$ configuration.

As previously discussed, there are inevitable differences between the two numerical methods because they employ distinct techniques to model the time-varying capacitor. ITMM and HB cannot provide the same results regarding overall transmissions and modulation functions due to significant differences arising from the definition of linear time-varying capacitors and the nonlinear capacitor response of the negatively biased varactor diode. Differences in the numeric solution technique and optimization algorithms are another significant reason. Nonetheless, the results are assumed to be consistent considering the realization factors and methodological tolerances when we focus on the overall performances of the asymmetric transmission and its response to the source's phase.

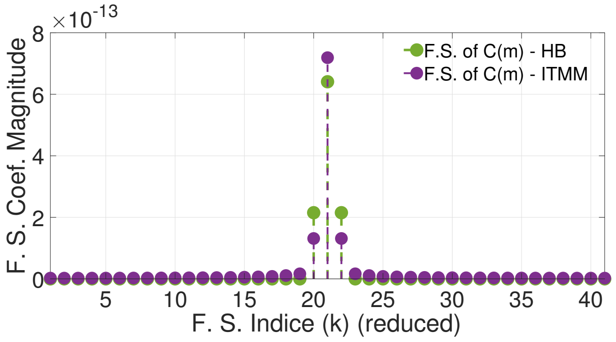

Figure 5.16. Fourier series (F.S.) coefficients of the optimized modulation function in single capacitor configuration.

We observe that nonreciprocal transmission with a single $C(t)$ configuration is phase-coherent, meaning isolation depends on the input phase. This makes it impractical as an isolator unless the input phases are known. To improve this, we propose using two capacitors symmetrically positioned on the top face, as shown in Figure 4.11a. Under the same illumination direction, these capacitors exhibit a π-phase difference, as demonstrated in Figure 4.11b for forward and Figure 4.11c for backward excitation. Consequently, the incoming voltage signals to the capacitors have a cross π-phase difference while maintaining approximately the same amplitude (Figure 4.12). The different modulation signals are required for both capacitors to achieve phase-independent nonreciprocal transmission. Optimal modulation functions are determined via optimization code. The direction of isolation can be switchable by interchanging the modulation functions of the capacitors with the help of cross $\pi-$phase differences. It means during forward excitation, the phase of the first capacitor matches that of the second capacitor in backward excitation, and vice versa (see Figure 4.12b). Figure 5.17 displays the optimized results for the two $C(t)$ configuration with isolation switched in reverse. Here, the transmission coefficient for the backward illumination (or forward in reverse operation) is always blocked (isolated). For the forward case, transmission varies between unity and near zero with respect to the phase of the incident wave (assuming the phase of the modulation signal is fixed). The isolation operation is switched by exchanging the modulation functions of capacitors. To achieve unity transmission (or amplification), the pumping signal should be synchronized with the forward incident signal, as suggested in the literature (Wang et al., 2020). This setup is practical for applications where the transmitter signal phase can be controlled, or the incoming signal can be detected during operation.

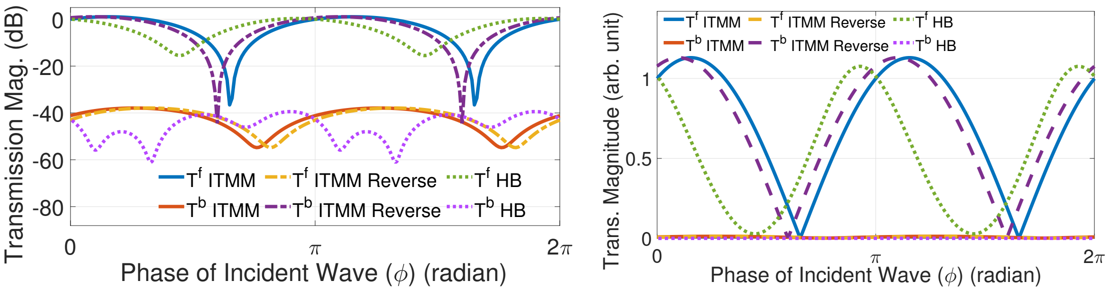

(a) in dB scale

(b) in linear scale

Figure 5.17. Results of transmission coefficients (magnitude in dB) with respect to the phase of source signal in two $C(t)$ configurations.

The operation frequency, i.e., f_0, can be changed by the DC component of the modulation function, i.e., C_0. However, there are certain limits for the total bandwidth. Essential factors can be listed as (i) the resonance characteristic of the single cell, which depends on geometric inclusions, its and host material, (ii) dimensions and material of surface cavity, (iii) the range variable of capacitance.

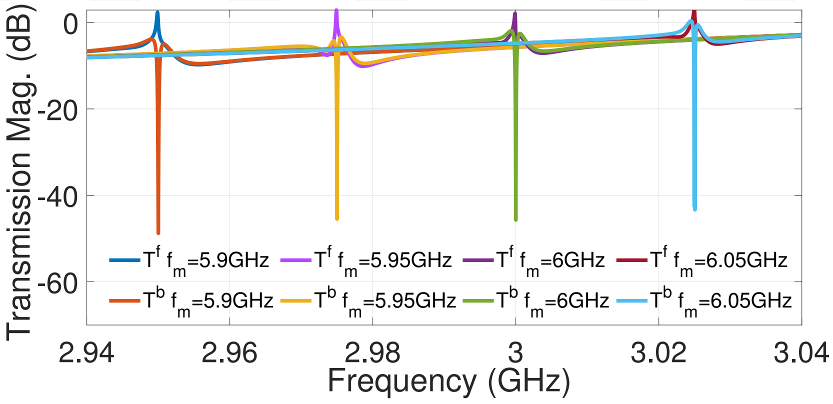

Figure 5.18. Results of transmission spectrum in two $C(t)$ configurations for $f_m = 5.9GHz$, $f_m = 5.95GHz$, $f_m = 6GHz$ and $f_m = 6.05GHz$. Bandwidth span is $100MHz$.

We obtain the results for a two-capacitor setup with the same diode model by varying the capacitor function to change the operation frequency. The modulation functions are optimized for the operation frequency varies between $f_0 = \{2.95, 2.975, 3, 3.025\}$ GHz. Figure 5.18 show the transmission spectrum within the bandwidth of $100MHz$, when modulation frequency varies between $f_m = 2f_0 = \{5.9, 5.95, 6, 6.05\}$ GHz. Modulation functions are found by optimization code as follows:

- for $f_m = 5.9GHz$: $C_1(t) = \{9.7 + 0.4\cos(\omega_m - 0.48)\} \times 10^{-13}F$, and $C_2(t) = \{7.2 - 5.5\cos(\omega_m + 0.81s)\} \times 10^{-13}F$,
- for $f_m = 5.95GHz$: $C_1(t) = \{8.7 - 0.3\cos(\omega_m + 0.18)\} \times 10^{-13}F$, and $C_2(t) = \{7 - 3.7\cos(\omega_m - 0.07)\} \times 10^{-13}F$,
- for $f_m = 6GHz$: $C_1(t) = \{7.6 + 0.7\cos(\omega_m - 1.23)\} \times 10^{-13}F$, and $C_2(t) = \{8 + 0.004\cos(\omega_m + 0.006)\} \times 10^{-13}F$,
- for $f_m = 6.05GHz$: $C_1(t) = \{10 - 0.3\cos(\omega_m - 1.35)\} \times 10^{-13}F$, and $C_2(t) = \{8.7 - 4\cos(\omega_m - 1)\} \times 10^{-13}F$.

Transmission curves are identical with respect to the source phase for each frequency, as expected. Figure 5.19 shows a version of zoomed into 10MHz at the $f_0 = 2.95GHz$ and its curve with respect to the source phase. Figure 5.20 shows the transmission coefficient (in dB) of harmonics that occurred by signal mixing. The higher harmonics have significantly low transmission since the phase of the mixed signal is precisely optimized to be matched for the fundamental frequency (ω_0).

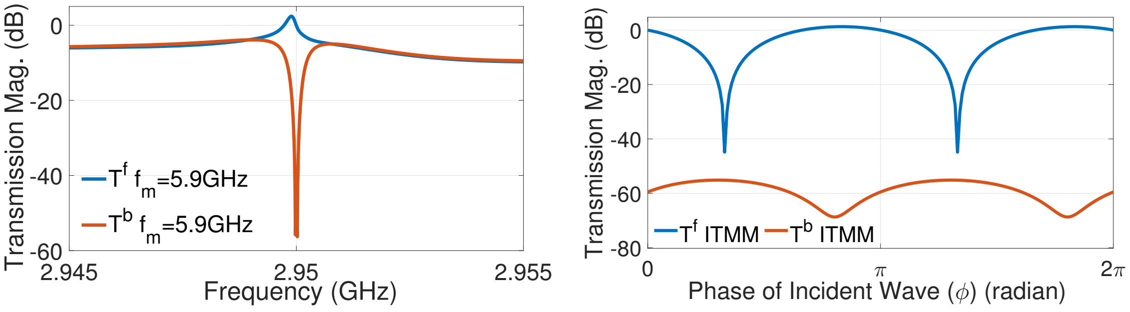

(a) Spectrum (dB) in $10MHz$ bandwidth

(b) vs. source phase

Figure 5.19. Results of transmission magnitude (in dB) in two capacitor configuration for $f_m = 5.9GHz$.

For the final analysis, we investigate how the amplitude of the source signal affects asymmetric transmission due to nonlinearity in diodes. This analysis is done in HB simulation involving nonlinearity. Figure 5.21 indicates the maximum isolation quantity for the input power. We see maximum source power limitation for practical applications with a fixed pump signal. In addition, considering practical realization, typical achievable time modulation frequencies today are estimated to exceed 100 GHz (Taravati and Eleftheriades, 2022). Alternatively, lowering the modulation frequency is also possible. For example, even significantly lower modulation frequency (e.g., $\omega_m = \omega_0/10$) can enable nonreciprocal transmission since the proposed design can contains multiple time-modulated elements (Wang et al., 2020).

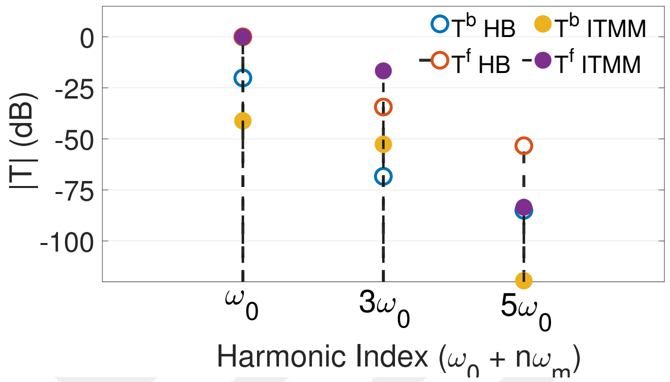

Figure 5.20. Results for transmission magnitudes (in dB) of mixed harmonics in two $C(t)$ configurations.

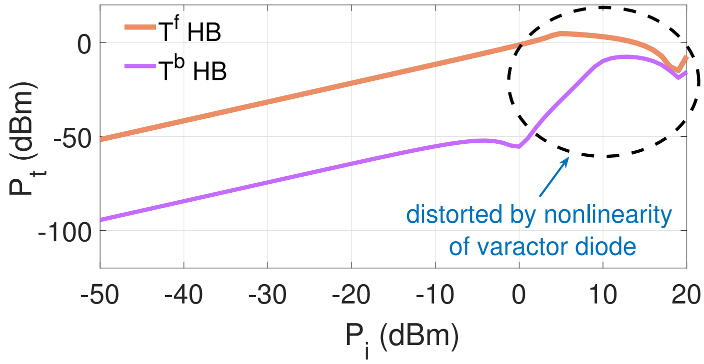

Figure 5.21. Results of transmitted power (in dBm) for input source power (in dBm) in HB simulation for two $C(t)$ configurations.

CHAPTER 6

EXPERIMENTS RESULTS FOR NONRECIPROCAL TRANSMISSION ON UNIT CELL BY TIME-MODULATION

This chapter first revisits the proposed unit cell simulations in 3D, considering losses and practical waveguide excitation factors. It is followed by deriving the impedance matrix of the proposed time-varying circuit block now having diode loss (R_s) and presenting the numerical results of the overall system with losses. After, we step into the experimental sections, presenting the experimental setups and the results while discussing their consistency with numerical results.

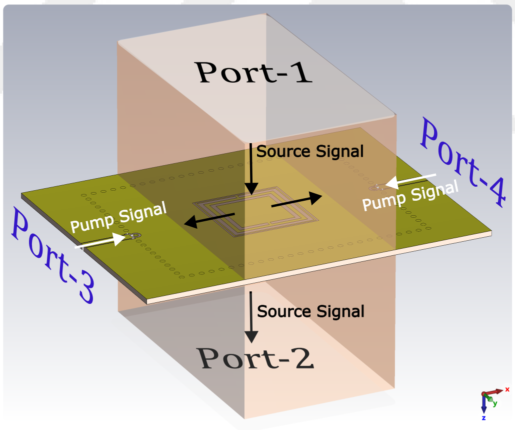

Figure 6.1. The simulation model of the unit cell in waveguide setup for the experimental scenario.

6.1. Revisiting Simulation Model for Experiment Setup

In the previous chapters, we have considered all materials and components lossless. We placed variable capacitors where the high field was concentrated in a unit cell cavity configuration. We then made the numerical calculations, assuming that time variations were introduced to them hypothetically. However, in practical experiments, the transmission lines must feed the variable capacitors by pump signals from the separated ports. Identical microstrip co-planar waveguides (CPW) are employed for pump signals (with negative DC bias) to the varactor diodes. Pump signals are fed through ports indicated as Port 3 and Port 4. We consider all losses and also change the TEM waveguide section with the realizable waveguide whose fundamental mode is TE_{10} incident wave in the spectrum. Figure 6.1 displays the general view of the simulation setup for the experimental scenario considering all losses. Here, PEC walls and the faces of inclusions are exchanged with the copper whose conductivity is $\sigma_{copper} = 5.8 \times 10^7 S/m$. The dielectric substrate is the same with $\epsilon_r = 2.2$ (Rogers RT/Duroid 5880) but now lossy with a dissipation factor $\tan\delta = 0.009$ at $10GHz$.

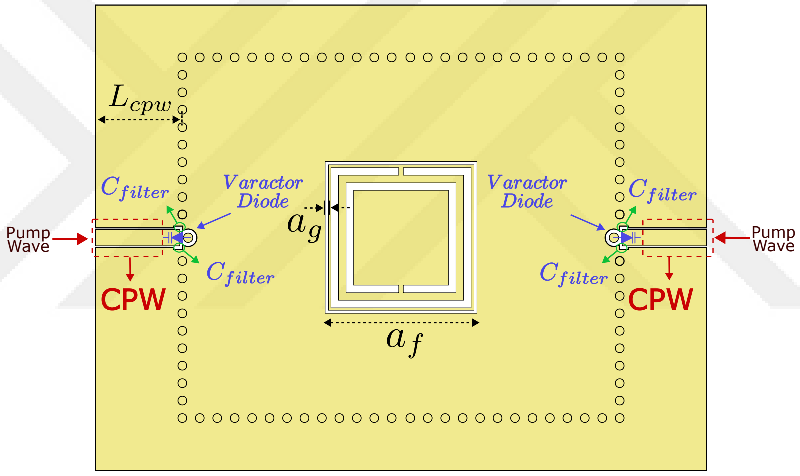

Figure 6.2. Top view of the proposed 3D model with the CPW feeding lines and SIW cavity for the experimental scenario. $a_g = 0.5mm$, $a_f = 25mm$, $L_{cpw} = 14mm$.

Connecting one terminal of the variable capacitor to the feeding line connects the equivalent circuit of the surface cavity to outside ports (Ports 3 and Port 4). Figure 6.2 shows the pump signal feeding line details. Here, filter capacitors are connected to each corner of the SIW wall and the CPW, so there are four filter capacitors. Precise adjustments of the design and lumped components are necessary for the filter circuit between the source and pump signals. The circuit seen from the source signal should remain mismatched in impedance to prevent a decrease in the cavity's quality factor and the manipulation level of the variable capacitor. Conversely, the circuit seen from the pump signal should be matched in impedance to deliver maximum power to the variable capacitor, ensuring high voltage. Hence, we need to develop a band-pass filter at the boundary of a coaxial cross-section where the variable capacitor is placed, which coincides with the end of the pump line. We optimized the geometrical parameters and lumped components through parametric sweeps during the 3D simulations. We aimed to achieve minimum leakage for the source wave in the cavity and maximum power transfer for the pump wave.

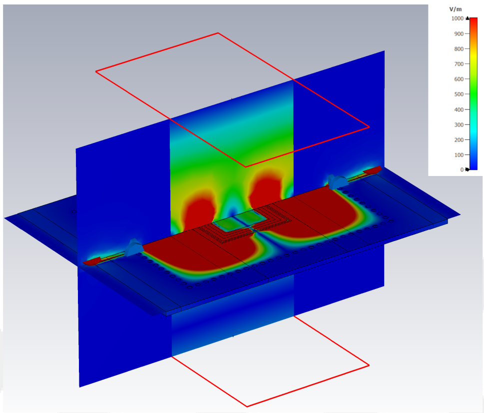

Figure 6.3. Simulation result for electric field distribution (magnitude, $|\vec{E}|$) showing the concentrated surface wave around the surface from a general perspective. Maximum electric field strength is adjusted as $1000V/m$.

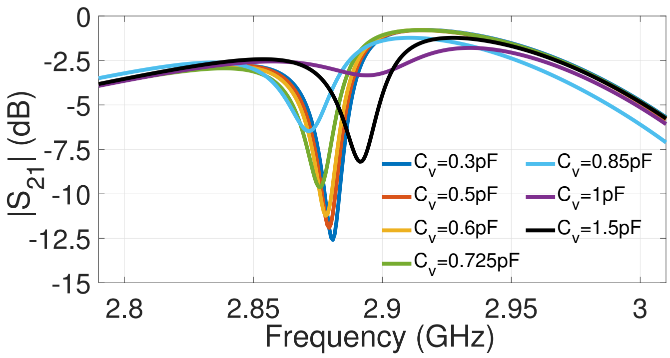

Figure 6.4. Simulation results of transmission magnitudes (S_{21} in dB) for the capacitor value ranging of Skyworks SMV 2019 varactor diode model in lossy case.

We redesign the unit cell structure by adding a new capacitor fence outside the split-ring resonator to increase the operating frequency bandwidth. This adjustment aims to enhance tolerance of frequency mismatch during the manufacturing process since the resonator structures are the highly affected by even the tiny changes in geometrical parameters. Figure 6.3 shows the distribution of the electric field magnitude excited from Port 1.

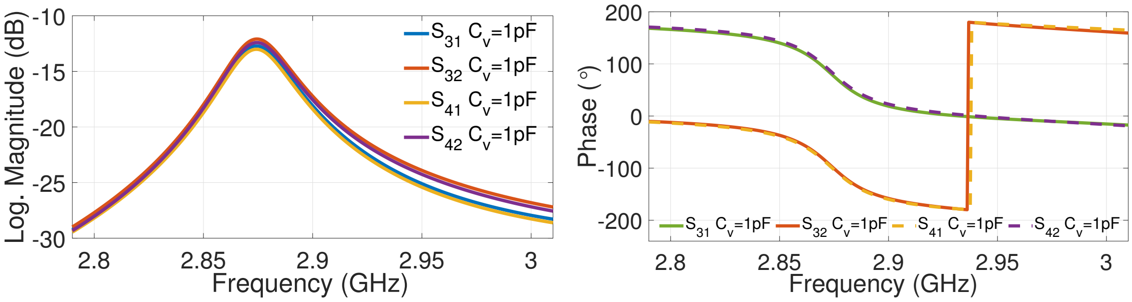

(a) Magnitude (in dB) (b) Phase (°)

Figure 6.5. Transmission coefficients of coupling between sources (Port−1 and Port−2) and feeding ports (Port−3 and Port−3) when $C_V = 1pF$.

The concentrated field around the surface demonstrates the separation of the incident field and the surface wave manipulation that occurred from outside the waveguide section. We can also observe the leakage field toward the pump ports. Figure 6.4 presents the magnitude (in dB) of the transmission coefficient (S_{21}) for the variable capacitor value within the range of the varactor diode model Skyworks SMV2019. Comparing this with the results without losses and pump line (see Figure 4.16a), we observe a drastic decrease in the impact of the capacitor changes. However, we can still control the transmission within a sufficient level, approximately $10dB$. Note that this is not the limit for the asymmetric transmission (isolation quantity) level, as there is no time modulation on the capacitor. Nonetheless, it illustrates how the performance decreases and allows for comparing the ideal and realized cases. The performance can be enhanced by reducing leakage and losses, for example, by replacing the Silicon (Si) varactor diode with Gallium Arsenide (GaAs) having low series resistance (R_s). Figure 6.5 presents the S-parameter results for coupling transmission between source wave excitation ports (Port 1 and Port 2) and feeding ports (Port 3 and Port 4). Here, the magnitude results indicate the leakage power through the surface wave, and the phase results demonstrate a cross-π ($180°$) phase difference. We have seen the same phase differences in the voltage of variable capacitors in Figure 4.12b. The cross-π phase differences occur for the situations: (i) at either Port-3 or Port-4 when excited by Port-1 and Port-2, and (ii) between Port-3 and Port-4 when excited by either Port-1 or Port-2.

6.1.1. Analysis of the Losses

Surface wave generation on such structures enhances the problem of losses (Maurizio Bozzi, 2009). We face this issue significantly, as the concentrated field on the lossy medium results in high amplitudes and boosts power dissipation. Despite efforts to reduce losses by using a substrate with a very low dissipation factor (RT/Duroid 5880) and employing copper, which is highly conductive, it is still a major factor in the overall performance of the structure.

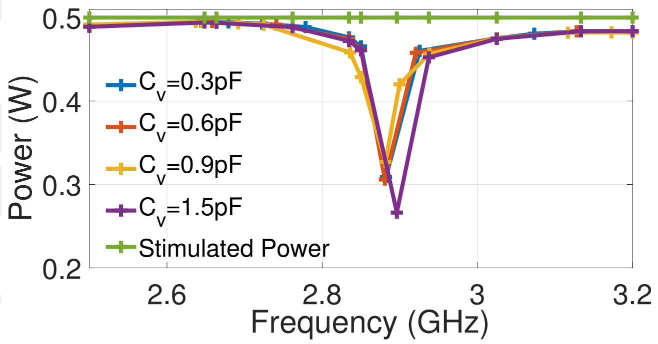

Figure 6.6. Simulation results of the total received power from all ports when the stimulated power is $0.5W$.

Figure 6.6 presents the simulation result for the total received powers in all ports when the stimulated power is $0.5W$. We observe the maximum losses occur around the frequency that matches the high surface wave conversion into cavity mode and the resonance of the unit cell DNG structure. Table 6.1 provides detailed information on the sources of these losses. Indeed, the mechanisms causing losses are highly complex and nonlinear. Our analysis is based on 3D numerical simulations. From simulation results, total efficiency frequency varies between $\%60 - \%90$ at around the operating frequency for the time-invariant situation.

Table 6.1. Simulation results of the losses and total received power P_r^{total} (in percentage) for different C_{var} values. R_s represents the varactor diode's series resistance.

	Dielectric	R_s	Metal	P_r^{total}
$C_{var} = 0.3pF$	$\%17.2$	$\%0.5$	$\%18$	$\%61.6$
$C_{var} = 0.6pF$	$\%14.8$	$\%4.6$	$\%17.4$	$\%61.2$
$C_{var} = 0.9pF$	$\%6.8$	$\%17.2$	$\%9.8$	$\%65.4$
$C_{var} = 1.5pF$	$\%10.8$	$\%20$	$\%13.6$	$\%53.2$

6.2. Revisiting Numerical Solutions For The Time-Modulated Circuit with Losses

We now analyze the impacts of losses on nonreciprocal transmission performance under time modulation. First, we revisited the time-modulated circuit block in Figure 5.12 for the impedance transfer matrix method. We derive its expression of the impedance matrix for the now series loss assigned into the variable capacitor. By following the solutions in Chapter 5, we obtain the final admittance matrix through $\Big[Y_{sw}\Big] = \Big[M_b\Big]^{-1}\Big[M_a\Big]$. Corresponding matrices are given in Equation 6.1 and Equation 6.2, respectively.

$$\Big[M_a\Big] = \sum_m \left(j\omega_n^2 + \frac{\omega_n^2 R}{\omega_{n-m}L_2 - \omega_n^2\omega_{n-m}C_2R}\right)C_m e^{j\omega_{n-m}\tau}V_{n-m}^{in} + \left(-\frac{-j}{L_2} + j\omega_n^2 C_2\right)e^{-j\omega_n\tau}V_n^{in}, \tag{6.1}$$

$$\Big[M_b\Big] = \sum_m \left(\frac{\omega_n^2\omega_{n-m}L_1}{1-\omega_{n-m}^2L_1C_1} + j\omega_n^2R - \frac{j\omega_n^2L_1R}{L_2(1-\omega_{n-m}^2L_1C_1)} + \frac{j\omega_n^2L_1C_2R\omega_{n-m}^2}{1-\omega_{n-m}^2L_1C_1}\right)C_m e^{j\omega_{n-m}\tau}I_{n-m}^{in} + \left(\omega_n - \frac{L_1\omega_n}{L_2(1-\omega_n^2L_1C_1)} + \frac{\omega_n^3L_1C_2}{1-\omega_n^2L_1C_1}\right)e^{-j\omega_n\tau}I_n^{in} \tag{6.2}$$

where R is the series resistance of the varactor diode.

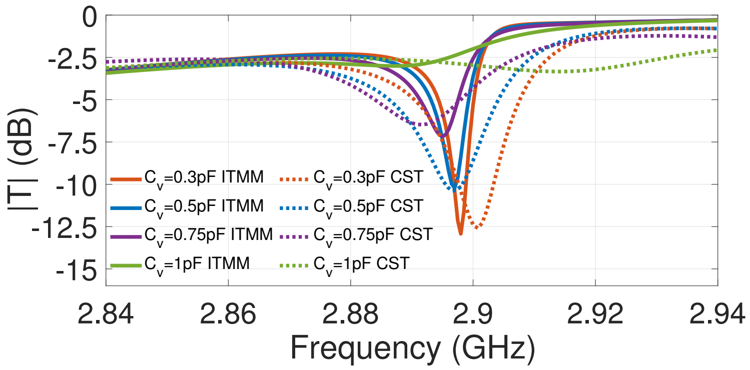

Figure 6.7. Transmission magnitudes (S_{21} in dB) of lossy ITMM solution for C_v values without modulation and comparison with 3D CST: MW simulation. The capacitor value is applied from $0.3pF$ to $1pF$, which is in the SMV 2019 varactor diode model range.

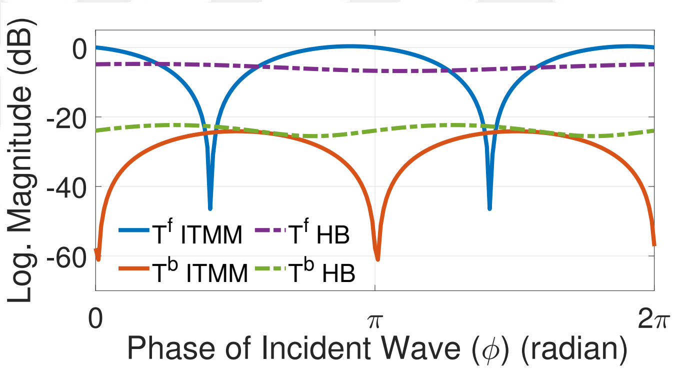

Figure 6.8. Results of transmission coefficients (magnitude in dB) with respect to the source's phase for the two $C(t)$ configuration when the losses are considered.

Figure 6.7 presents the calculated transmission magnitudes from the equivalent circuit for the capacitor values ranging from $C_{var} = 0.3 - 1pF$, as shown in Figure 4.16a for the lossless case. The response of the transmission coefficients for varying capacitor values is in good agreement with the simulation results in Figure 6.4. The quantity of manipulation impact is approximately $12dB$. When the capacitor's impedance exceeds the particular matching value, approximately $C_{var} > 1pF$, the equivalent circuit of the pump line becomes more effective. It changes the equivalent circuit parameters of the surface cavity. We consider the capacitor value as $C_{var} \leq 1pF$ for the time-varying solutions as we discuss for the related result given in Figure 4.16b. We then applied the numerical solutions for the time-modulated case considering the losses. Figure 6.8 presents the optimized result of the nonreciprocal transmission with respect to the source's phase for the two $C(t)$ configuration when the losses are considered. We could achieve the isolation quantity of approximately $20dB$ for both methods via optimization tools in HB simulation and Mathwork Matlab. A flat response to the variation of the source phase is observed in the HB simulation. This might be attributed to the domination of the nonlinear characteristic of the varactor diode when series resistance is introduced. When comparing the isolation quantity to the lossless scenario (see Figure 5.17a), we observe a performance degradation from $40dB$ to approximately $20dB$ for the lossy case. This discrepancy is expected since inevitable differences exist between the idealized case and real implementations. Nevertheless, a $20dB$ isolation quantity provides comparable performance for isolator applications compared to other methods and commercial products, which have major drawbacks for modern systems as discussed in the introduction. The performance can be enhanced by addressing the issues of losses and optimizing leakage to the feed port. Another significant issue is improving the time-variable capacitor performance using a diode with lower loss or an alternative technique. Note that the presented results are examples from the results within the limits of certain optimization conditions for given equivalent circuit elements, and they are not an upper limit in terms of performance output.

6.3. Experiment Results of The Time-Modulated Unit Cell

This section presents the experimental setups for the time-modulated unit cell within the SIW cavity placed in the waveguide section, followed by the measurement results that validate nonreciprocal transmission as proof-of-concept. The structure was fabricated according to the dimensions outlined in Figure 6.2. Figure 6.9a and Figure 6.9b show images of the manufactured structure from both top and bottom perspectives, respectively. For the experimental setup in Figure 6.1, we positioned the structure in the exact middle of a 3D-printed rectangular waveguide section with dimensions of 80 mm $\times$ 46 mm $\times$ 80 mm. Its operating frequency for only fundamental TE_{10} mode is approximately between $2.2 - 3.3$ GHz (Balanis, 1989). Figure 6.9c shows the unit cell structure within a 3D-printed waveguide section after soldering diodes and filter capacitors. Conductive tape was applied to the plastic wall to impart conductivity. The resulting conductivity level, and thus the wave-guiding performance, was sufficient for proof-of-concept experiments. A detailed analysis and performance results of the 3D-printed waveguide have been published in the literature (Anıl Karatay and Yaman, 2023). As discussed in Chapter 3, this setup allows the simulation of infinite identical cells with a particular period (Zang et al., 2019). The CPW feedings of the varactor diodes are outside the waveguide as we simulated in Chapter 4. So, this configuration prevents interference and cross-talk between the excitation and feeding waves and it demonstrates that the mixing operation only occurs on the varactor diodes.

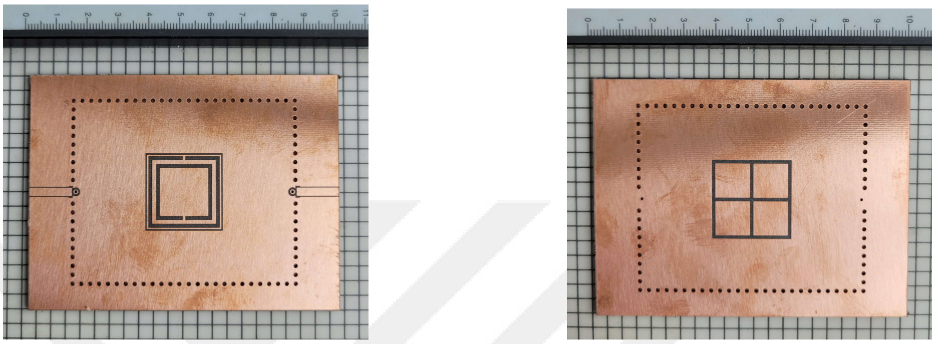

(a) Top face

(b) Bottom face

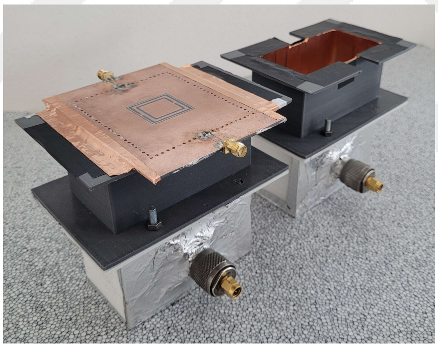

(c) In waveguide with soldered diode and filter capacitors

Figure 6.9. Photographs of the manufactured proposed structure and within 3D printed waveguide.

We first measured the S-parameters using the HP 8720D vector network analyzer (VNA) for the capacitor range of the varactor diode model by supplying only negative DC bias without a modulation pump signal. The voltage ranges from $0V$ to $20V$ according to the data sheet of the Skyworks SMV2019 varactor diode. Figure 6.10a presents the transmission coefficient (S_{21}) for the capacitor value ranging from minimum ($0.3pF$) to maximum ($2.2pF$) for the given diode model (Skyworks SMV2019). Figure 6.11a and Figure 6.11b present, respectively, the magnitude and phase of transmission coupling coefficients for source to feeding ports indicated as S_{31}, S_{32}, S_{41} and S_{42}.

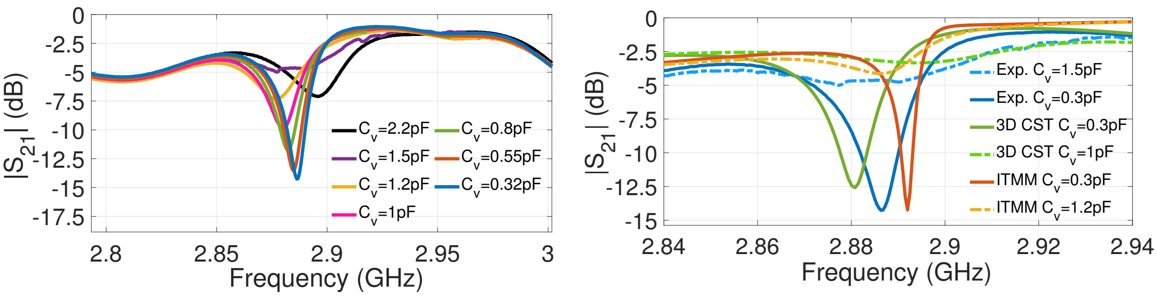

(a)

(b)

Figure 6.10. (a) Experiment results of transmission coefficients (magnitude, $|S_{21}|$ in dB) with respect to the negative DC bias of diodes, and (b) comparison with CST simulation with losses and ITMM solution of the equivalent circuit, when only negative DC bias is supplied without modulation.

To verify the experiment's setup, fabrication of the unit cell, and the soldering process, the experiment results are compared to the results of 3D CST: MW simulation and ITMM solution of the equivalent model. Figure 6.10b presents the magnitude of the transmission coefficients (S_{21}), comparing experimental results, 3D simulations, and the ITMM solution on the equivalent circuit for maximum dynamic transmission manipulation. This comparison verifies the consistency among the 3D simulation, equivalent circuit model, and experimental data.

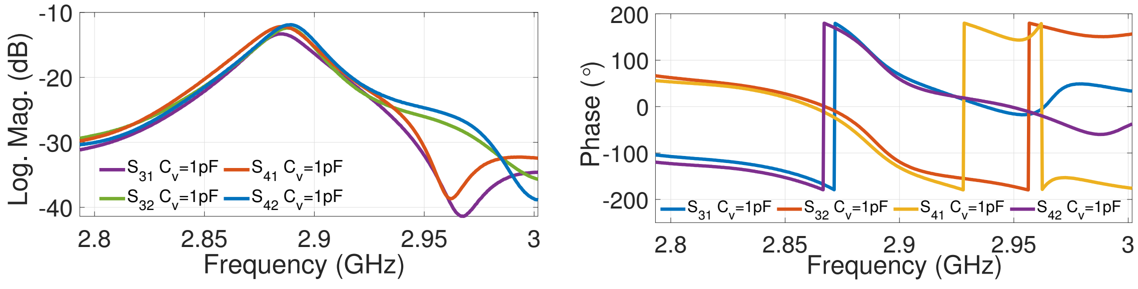

(a) Magnitude (in dB)

(b) Phase (°)

Figure 6.11. Experiment results of transmission coupling coefficients between source ports (Port-1 and Port-2) and feeding ports (Port-3 and Port-4) with respect to the negative DC bias of the diodes.

We proceed with the experiment on nonreciprocal transmission via time modulation. Figure 6.12a displays a view of the general experiment setup with measuring devices and the required equipment for the time modulation. Figure 6.12b presents a detailed photograph of the supplied source and pump signals and their related active and passive components, such as amplifiers, filters, bias-tee, and couplers.

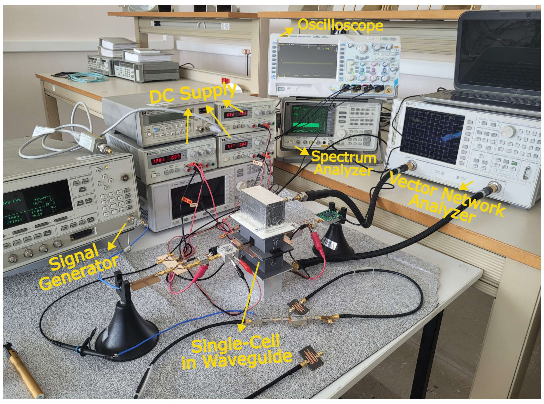

(a) General view

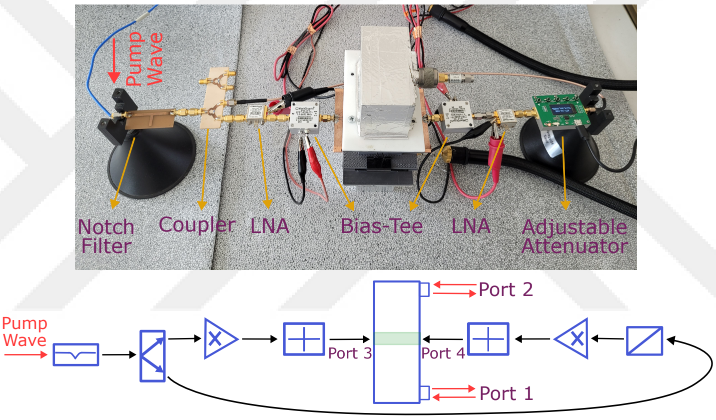

(b) Detail view of unit cell in waveguide section with components for pump signals

Figure 6.12. Experiment setup with measuring and source equipment for the time-modulation experiment of unit cell structure

The transmitted power spectrum was measured with a spectrum analyzer (HP 8565E) for the first experiment of the time modulation. The source signal is analytically expressed as

$$V_s = A_s \cos(\omega_0 t + \theta) \quad (V), \tag{6.3}$$

and the pump signals for the diodes which are supplied by HP 83620B swept signal generator and DC supplies generator, are expressed as

$$\begin{aligned} V_{m1} &= A_{01} + A_{m1}\cos(2\omega_0 t + \phi_1) \quad (V), \\ V_{m2} &= A_{02} + A_{m2}\cos(2\omega_0 t + \phi_2) \quad (V), \end{aligned} \tag{6.4}$$

where subscript $_{1,2}$ refers to the first and second diode, A_0 is the DC and A_m is the modulation (AC) amplitudes.

Figure 6.13a and Figure 6.13b present the measured powers P_t^f and P_t^b by the spectrum analyzer for respectively forward and backward illumination and when only DC biases are supplied as $A_{01} \approx 7.3V$ and $A_{02} \approx 10.5V$ without the modulation signal ($A_{m1} = A_{m2} = 0$). As it is supposed to be in the absence of time modulation, reciprocity is maintained, which means the transmission is symmetric for both illumination directions. The transmitted powers are measured as $P_t^f = -33.3dBm$ and $P_t^b = -33.7dBm$ for a normalized input power of $P_{in} = -20dBm$, respectively. Minor deviations in the measured powers for the forward and backward cases in the reciprocal situation could be attributed to factors such as the measuring resolution of the spectrum analyzer, cable and connection instabilities, and the nonlinearity of diodes.

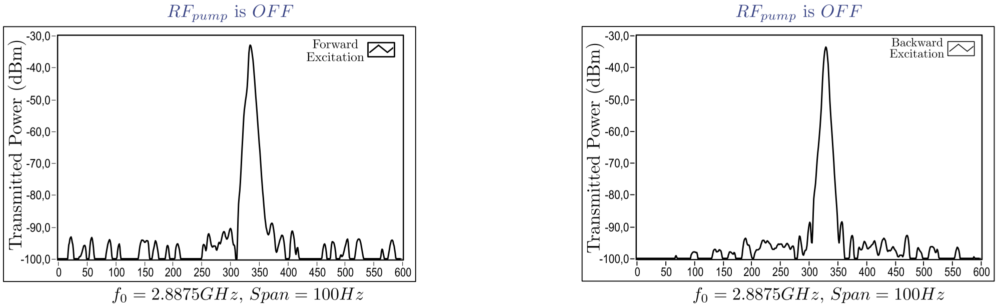

(a) Forward (Port-1) illumination

(b) Backward (Port-2) illumination

Figure 6.13. Experiment result of the transmitted power (in dBm) measured by the spectrum analyzer without pump signal ($RF_{pump} = 0$) for a normalized input power of $P_{in} = -30dBm$.

We then supplied the pump signals whose power was set to $12dBm$ from the signal generator, then split into two signals by a $3dB$ coupler. For the second diode, there is an adjustable attenuator before the amplifiers. The amplifiers and bias tees in the pump setup are identical, and their model are Mini-Circuits ZX6083LN and Mini Circuit ZFBT-6G, respectively. The relative phase between the pump signals ($\phi_1 - \phi_2$) was adjusted by the electrical length of the coaxial lines. So we can adjust the modulation signals for both diodes separately. The source frequency was adjusted as $f_0 = 2.8875GHz$, around the maximum surface wave conversion. Figure 6.14a and Figure 6.14b show the transmitted powers for the forward case when the modulation with frequency $\omega_m = 2\omega_0$ is supplied. To observe the precision of the harmonic mixing, we zoom into a narrow spectrum of $100Hz$. Two recorded samples show transmission blocking at multiple frequency points and maximum isolation levels are approximately –22 dB and -28 dB. In contrast, Figure 6.14c shows the not-blocked transmission for the backward case, which is approximately $-30.3dBm$. These results demonstrate the occurrence of signal mixing, which enables asymmetric transmission through the proposed unit cell. Nonetheless, those are screenshots after the relatively long measuring time ($\approx 4sec$) due to the signal sampling process of the spectrum analyzer. Therefore, we concluded that the spectrum analyzer could not accurately monitor the continuous process of signal mixing in our structure.

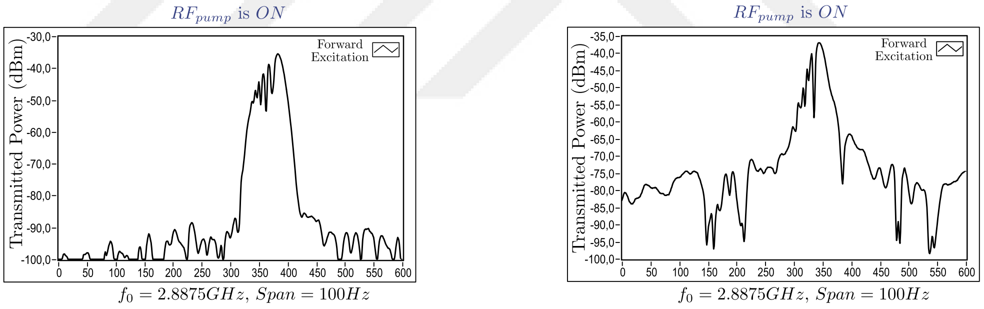

(a) Forward (Port$-$1) illumination (b) Forward (Port$-$1) illumination

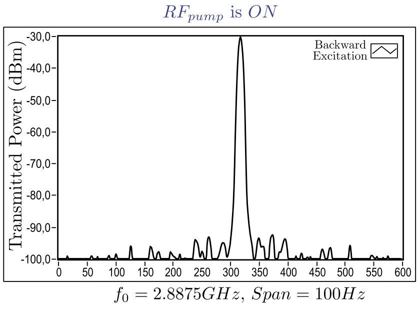

(c) Backward (Port$-$2) illumination

Figure 6.14. Experiment result of the transmitted power (in dBm) measured by the spectrum analyzer when RF_{pump} is ON for the normalized input power $P_{in} = -30dBm$.

We also faced the instabilities in each measuring sample. Therefore, we proceed with the time-modulation measurements using the HP 8720D Network Analyzer for the same modulation arrangements. Our system is a frequency translator system, including non-linear components and multi-harmonic mixing; the operation frequency of network analyzers should be precisely adjusted. The modulation frequency was precisely searched within the range of $\omega_m = 2\omega_0 \pm \%0.1$ to achieve maximum manipulation on the transmitted signal. Figure 6.15 displays two snapshot examples for the forward and backward transmission coefficients (magnitude $|S_{21}|$ and $|S_{12}|$ in dB) in a spectrum of 100kHz bandwidth when input power $P_{in} = -10$ dBm. Nonreciprocal transmission occurs at multiple frequency points around the $f_0 = 2.8875 GHz$. We observe the maximum isolation quantity reaching up to the $-30 dB$.

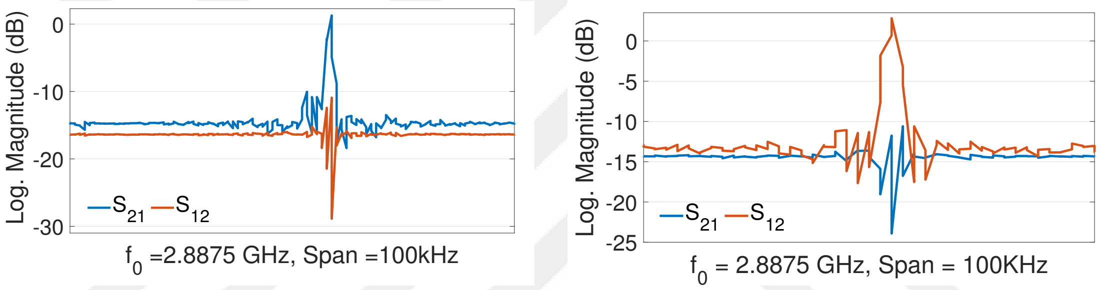

(a) Snapshot 1 (b) Snapshot 2

Figure 6.15. Experiment results of transmission magnitudes ($|S_{21}|$ and $|S_{12}|$ in dB) measured by VNA in spectrum of $100 kHz$ bandwidth.

Afterward, we made measurements using the single-frequency option in the VNA. The source frequency was adjusted again as $f_0 = 2.8875$ GHz, and the time duration accordingly the number of points (sample) to cover the total 2π input phase. For the first scenario, both pump signals were approximately adjusted to obtain phase-coherent (partial) nonreciprocity by emulating the numerical result of single $C(t)$ configuration in Figure 5.15a and Figure 5.15b. The experimental results of the transmission coefficient (S_{21} and S_{12}) are shown in Figure 6.16 in magnitude (dB) and its comparison with the numerical results, and phase (°). The pump signal parameters were adjusted as $A_{01} \approx A_{02} = 5.5$ V, $P_{pump} = 10$ dBm and attenuater is $0 dB$ while $P_{in} = -10 dBm$. Note that the measured phase is a relative phase to the input phase, i.e., $\phi_{trans.} - \phi_{source}$, while it was exact $\phi_{trans.}$ in the numerical simulations. There is good agreement for experiments and numerical simulations regarding the response and the quantity of the asymmetric transmission with respect to the source phase.

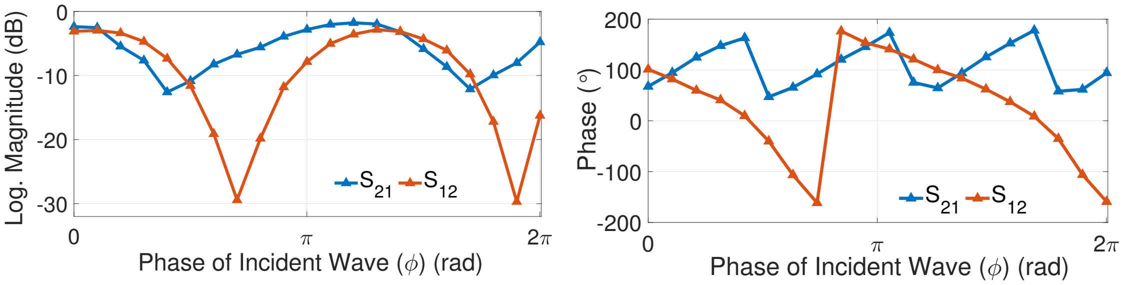

(a) Magnitude (in dB) (b) Phase (°)

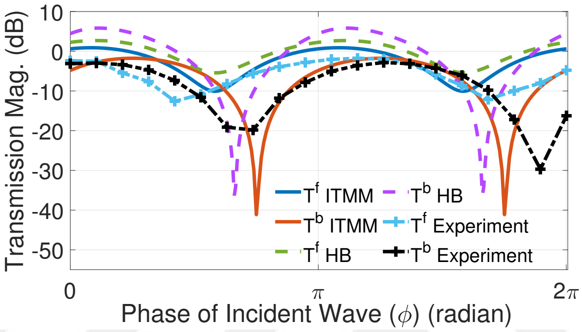

(c) Magnitude (dB) - comparison of experiment and numerical simulations

Figure 6.16. Experiment results of transmission magnitudes ($|S_{21}|$ and $|S_{12}|$ in dB) measured by VNA when approximately the same modulation functions are supplied, $V_{m1}(t) \approx V_{m2}(t)$. This shows phase-coherent nonreciprocity for forward and backward illumination.

Next, we performed measurements to achieve phase-incoherent nonreciprocity (isolation) by precisely adjusting the parameters of modulation functions. To optimize the maximum isolation quantity, we searched empirically for specific parameters around those found in the numerical simulation. As discussed in Chapter 5 for the numerical simulations, we can also amplify besides absorbing the input source depending on the adjustment of the input and pump signals. The primary limitation in practice is the ratio between the maximum pump power (P_{pump}) and the input source power (P_{in}). We also need to consider the maximum power handling of the varactor diodes. The output power of the amplifiers at $1dB$ compression (saturation point) is approximately 19 dBm. Thus, the maximum isolation quantity significantly depends on the input power for diodes. Figure 6.17 shows the transmission magnitudes (in dB) for input powers ranging from $P_{in} = 0$ dBm to $P_{in} = -30$ dBm. For measurements, the pump power is fixed at $P_{pump} = 12$ dBm, attenuater is $4dB$ and $A_{01} \approx 6.9V$, $A_{01} \approx 10.3V$. The isolation quantity convergences around $P_{in} \geq -20$ dBm.

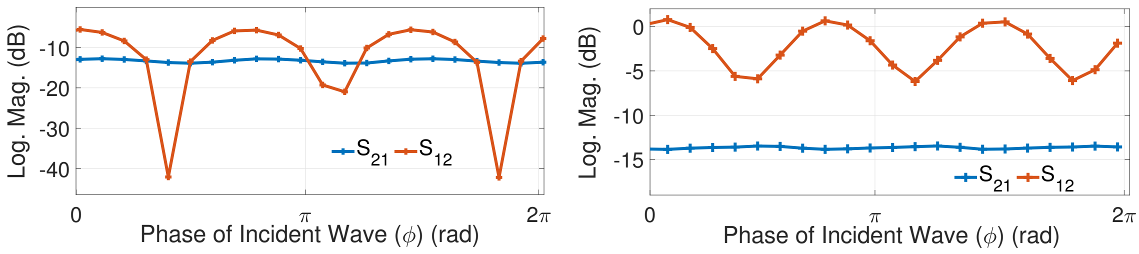

(a) $P_{in} = 0dBm$ (b) $P_{in} - 10dBm$

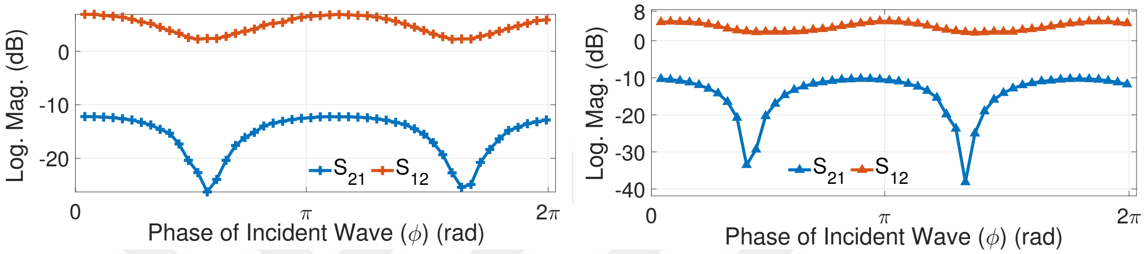

(c) $P_{in} = -20dBm$ (d) $P_{in} = -30dBm$

Figure 6.17. Experiment results of transmission coefficients (magnitude, $|S_{21}|$ and $|S_{12}|$ in dB) measured by VNA when modulation functions were adjusted to maximize the isolation quantity for input power (P_{in}) ranging from 0dBm to -30dBm.

The manner of its response to the input power is similar to the result of HB simulation in Figure 5.21. Therefore, we performed further measurements for $P_{in} \geq -20$ dBm, whose results are shown in Figure 6.19a. Figure 6.18 shows the phase of the transmission coefficient for the $P_{in} = -10dBm$. To keep the isolation quantity about constant with respect to the given input power (P_{in}), when the pump power (P_{pump}) is synchronized with P_{in}. Figure 6.19b shows the impact of the pump power P_{pump} variation around the saturation point while the source power was fixed at $P_{in} = -20$dBm. Here, we can observe how the gain factor on backward transmission (S_{12}) increases while forward (S_{21}) is always blocked as the pump power is increasing. The time duration and number of samples were adjusted to evaluate the system's stability. We consecutively recorded ten measurements for the time corresponding to the 12 periods of the source signal. Figure 6.20 displays the averaged magnitude of transmission coefficients ($|S_{21}$ and $S_{12}|$) in dB and linear ratio, respectively. We observe the stable behavior of nonreciprocal transmission when we compare the averaged results with single-taken results. The direction of isolation can be reversed by exchanging the modulation functions of the diodes, as discussed in Chapter 5 and the given result in Figure 5.17a.

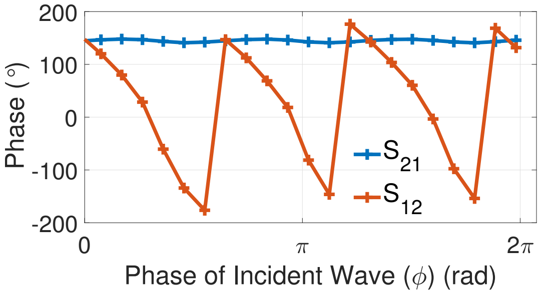

Figure 6.18. Experiment results of transmission phase ($\angle S_{21}$ and $\angle S_{12}$) measured by VNA when $P_{in} = -10dBm$ and $P_{pump} = 12dBm$.

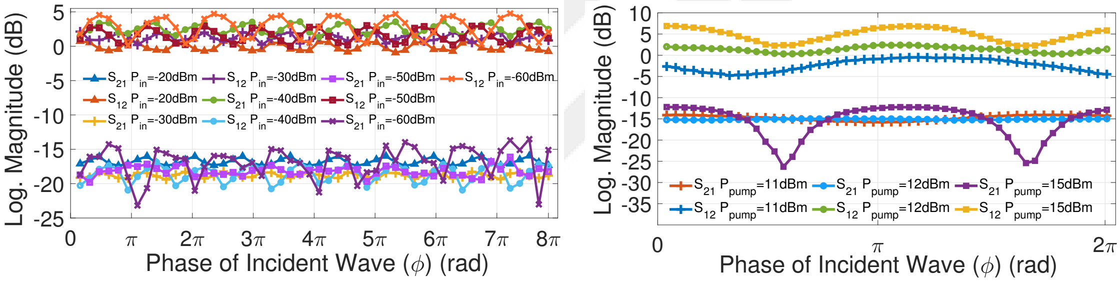

(a) (b)

Figure 6.19. Experiment results of transmission coefficients (magnitude $|S_{21}|$ and $|S_{12}|$ in dB) measured by VNA for variation of (a) input power P_{in} when P_{pump} is synchronized with P_{in}, and (b) P_{pump} when $P_{in} = -20$dBm.

In practice, exact reversal by swapping the modulation signals is not likely due to non-ideal and non-identical components, soldering processes, and fabrication constraints. We could only supply approximate reversed modulation functions. Figure 6.21 demonstrates this reversal operation with the results of transmission coefficient magnitudes ($|S_{21}|$ and $|S_{21}|$ in linear ratio). After, we performed longer measurements to emulate the real-time operation. Figure 6.22 presents the transmission magnitudes in dB and the linear ratio throughout 0.1 seconds. The number of points was adjusted to have approximately a 90 time period of the source signal. This allows us to observe the persistence of the isolation during extended real-time operation. We lastly optimized the phase difference between the source and pump signal ($\theta - \phi$) as kept settled to have maximum nonreciprocal transmission. Figure 6.23 presents a result of transmission magnitudes demonstrating the significant isolation quantity with between $\approx 35dB$-$\approx 60dB$. The modulation parameters were adjusted as: $A_{02} = 5.93V$, $A_{02} = 9.36V$, attenuater is $4dB$, and $P_{pump} = 15dBm$, when $P_{in} = -20dBm$.

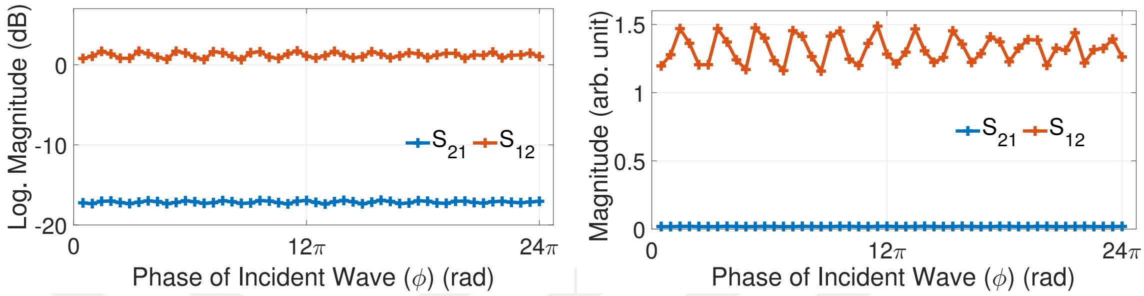

(a) in dB

(b) in linear ratio

Figure 6.20. Experiment results of averaged transmission cofficients (magnitude, $|S_{21}|$ and $|S_{12}|$) measured by VNA when $P_{in} = -20$dBm and $P_{pump} = 13$dBm. Averaging is performed by 10 discrete measurements for 12 time periods of the source signal.

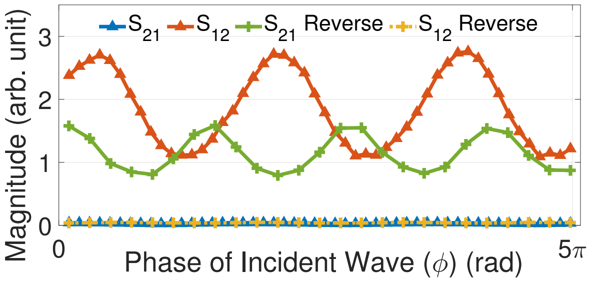

Figure 6.21. Experiment results of transmission magnitudes ($|S_{21}|$ and $|S_{12}|$, in linear ratio) measured by VNA when $P_{in} = -30dBm$ and $P_{pump} = 10dBm$. It demonstrates the switching of the direction of isolation.

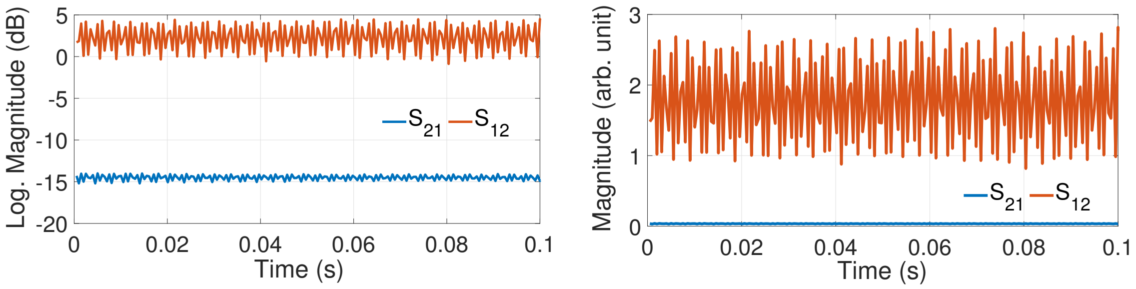

(a) in dB

(b) in linear ratio

Figure 6.22. Experiment results of transmission magnitudes (S_{21} and S_{12}) measured by VNA for a real-time scenario ($\approx$ 90 periods) when $P_{in} = -20dBm$ and $P_{pump} = 12dBm$.

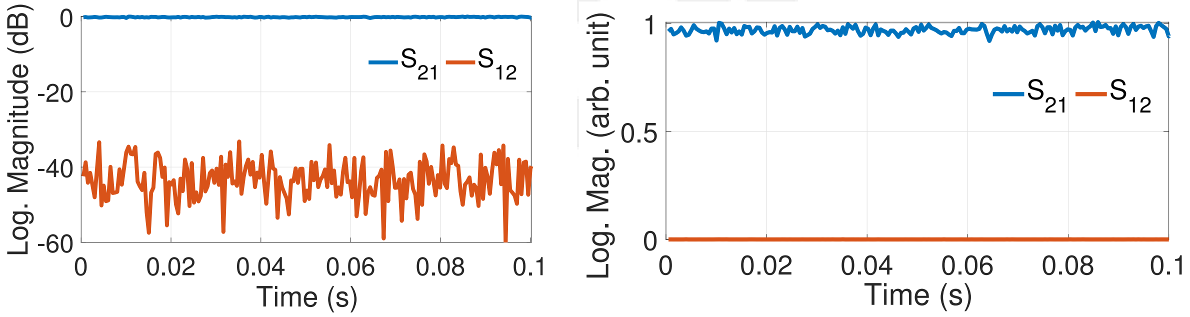

(a) in dB

(b) in linear ratio

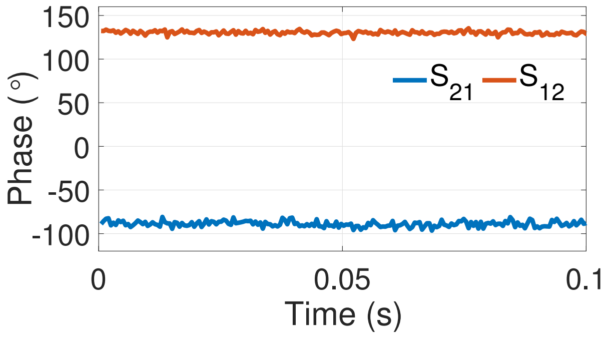

(c) Phase (°)

Figure 6.23. Experiment results of transmission (S_{21} and S_{12}) measured by VNA in case of a fixed phase difference $\theta - \phi$ when $P_{in} = -20dBm$ and $P_{pump} = 15dBm$.

6.3.1. Measurements Results of Synchronous Detection

We move to real-time scenario measurements by considering eliminating measurement tolerances of the general-purpose measurement devices VNA and spectrum analyzer. The measurement setup is established as given in Figure 6.25 for synchronous detection, called homodyne detection in optic engineering. Synchronous detection uses the continuous wave (CW) source signal as a reference signal to the downconverting mixer. The modulated or mixed harmonic signal output is downconverted by the mixer. This process is similar to heterodyne detection, with a difference in that the detected signal typically falls within the audio range, while it is DC for the homodyne detection (Jaggard and King, 1973). Figure 6.24 illustrates the operation of the synchronous detection.

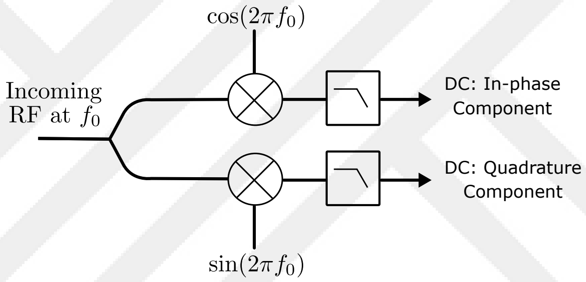

Figure 6.24. Illustration for the operation of the synchronous detection method.

For the synchronous detection setup, the mixer model is the Mini-Circuits ZX05-C60MH, and the pre-amplifier model is the Mini-Circuits ZX60-272LN. The IF signal was recorded via digital oscilloscope for the given situations given as: (i)$P_{in} = -5dBm$, $P_{pump} = 12dBm$, $A_{01} = 7.1V$ and $A_{02} = 10.8V$, (ii) $P_{in} = -5dBm$, $P_{pump} = 16dBm$, $A_{01} = 6.5V$ and $A_{02} = 11V$. Figure 6.26 and Figure 6.27 present the normalized transmitted power ratio for both measurements. They were recorded along 1 second. The dashed curves on the results represent the averaged values taken in a particular time interval along the duration. The maximum isolation quantity for the averaged values is $14dB$ and $12dB$, respectively. For the particular instants, it can reach up to $15dB$ and $23dB$, respectively. These results are consistent with the VNA measurements for the real-time scenario in Figure 6.22.

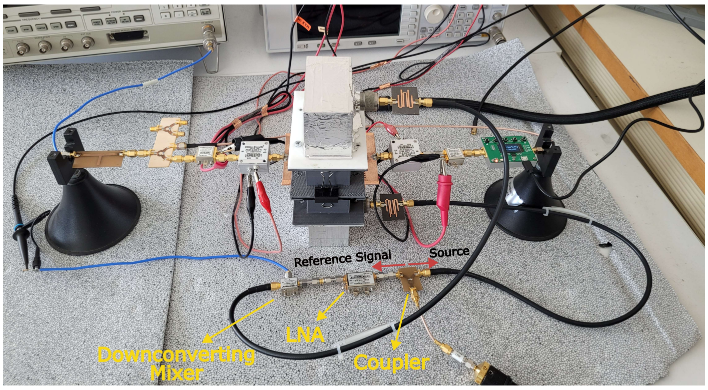

Figure 6.25. Photograph of the synchronous detection setup in general view.

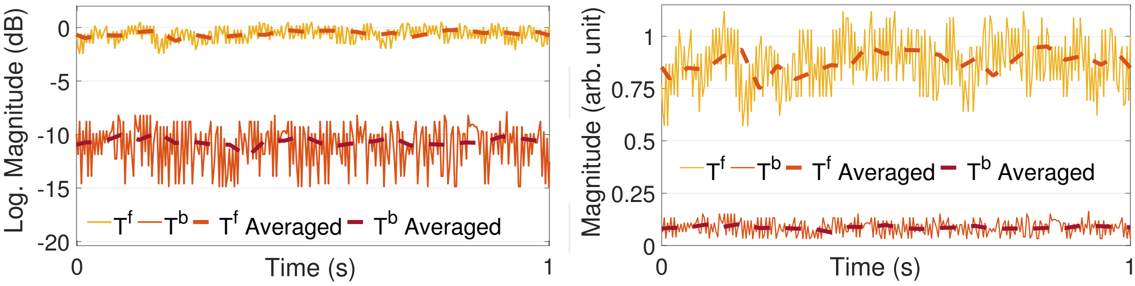

(a) in dB

(b) in linear ratio

Figure 6.26. Experiment results of transmitted power ratio (normalized) measured by synchronous detection experiment for forward and backward illumination. $P_{in} = -5dBm$, $P_{pump} = 12dBm$, $A_{01} = 7.1V$ and $A_{02} = 10.8V$.

We also analyzed the recorded intermediate frequency (IF) signal in the frequency domain by performing a Fast Fourier Transform (FFT). Figure 6.28 displays the power spectrum. The maximum frequency component is expected to be $1MHz$. The DC component indicates the fundamental frequency (f_0) and demonstrates the isolation quantity for forward and backward illumination. Away from the fundamental component, we observe a significant lowering in power levels. Only very close to the DC component can we observe relatively strong other harmonic-mixing products, possibly resulting from the nonlinear diodes. However, still, they are relatively low compared to the fundamental component (f_0). After that, we decrease the input power to be $P_{in} = -5dBm$ when the $P_{pump} = 15dBm$ and interchange the modulation functions to make the isolation direction reverse. Figure 6.29a shows the measured IF voltages of the in-phase and quadrature terms for forward and backward illumination. Figure 6.29b and Figure 6.29c shows the total transmitted powers in dB and linear scale.

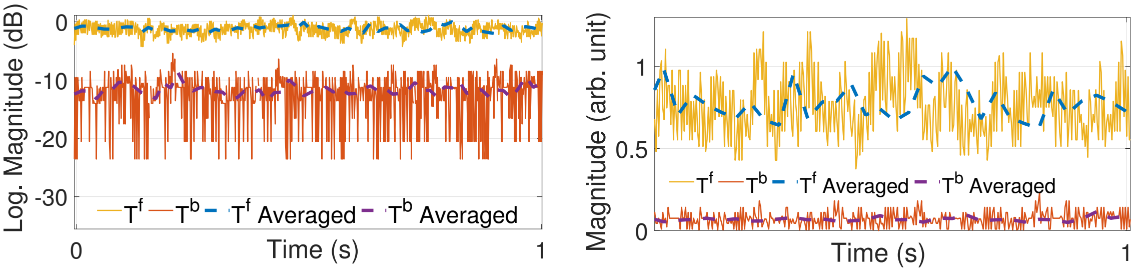

(a) in dB (b) in linear ratio

Figure 6.27. Experiment results of transmitted power ratio (normalized) measured by synchronous detection experiment for forward and backward illumination. $P_{in} = -5dBm$, $P_{pump} = 16dBm$, ${}_{01} = 6.5V$ and $A_{02} = 11V$.

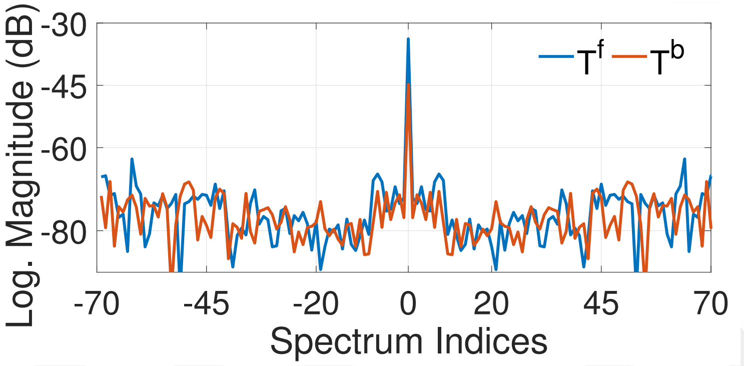

Figure 6.28. Experiment results of transmitted power spectrum measured by synchronous detection experiment for forward and backward illumination. $P_{in} = -5dBm$, $P_{pump} = 16dBm$, ${}_{01} = 6.5V$ and $A_{02} = 11V$.

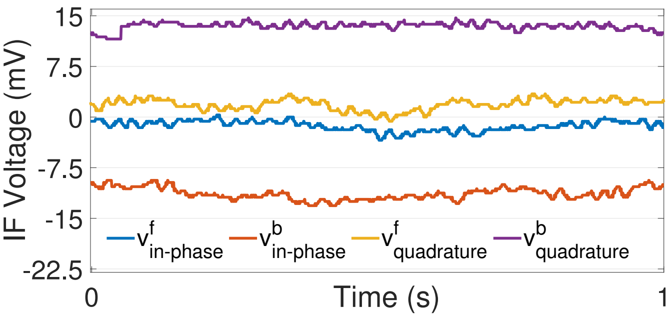

(a) Voltage of each channel

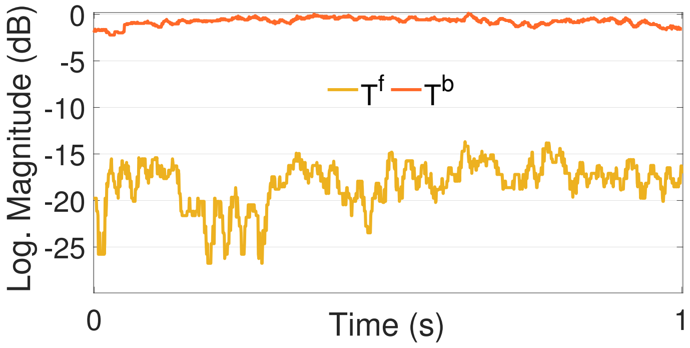

(b) in dB

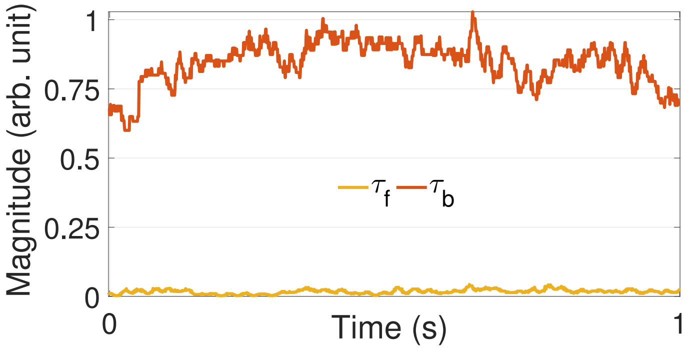

(c) in linear ratio

Figure 6.29. Experiment results of (a) voltages and (b) transmitted power ratio (normalized) measured by synchronous detection experiment for forward and backward illumination when isolation direction is reversed. $P_{in} = -10dBm$, $P_{pump} = 15dBm$, $A_{01} = 5.9V$ and $A_{02} = 9.8V$.

CHAPTER 7

RECONFIGURABLE METALENS ANTENNA THROUGH SURFACE WAVE

This chapter focuses on the reconfigurable radiation capabilities of the proposed surface wave-supported metasurface. We aim for this study to be a bridge for nonreciprocal metasurface having reconfigurable radiation properties, which will be in the future directions. We explore manipulating surface eigenmodes across multiple cells controlled only by a DC voltage without modulation. We initially review the beam-steering requirements for transmitarray surfaces, which involve identical radiation elements distinguished by their phase profiles. Subsequently, we introduce the proposed design, drawing on the analytical insights from Chapter 2, as well as the 3D model detailed in Chapters 3 and 4. Using Eigensolver in CST: MW numerical analysis, we evaluate its surface modes for variation of the variable capacitors. We demonstrate the beam-steering application of the dynamic metasurface positioned at the aperture of a horn antenna with simulation and experiment results.

7.1. Overview of Reconfigurable Transmitarray Antenna

A transmitarray antenna is a planar arrangement comprised of an illuminating feed source positioned at an equivalent focal point and a thin transmitting surface that hosts an array of radiating elements. Figure 7.1 shows the the conceptual illustration. These elements are generally identical resonance unit cells designed to have an ideal transmission coefficient of 1 (0 dB). Conversely, in a reflectarray, the reflection magnitude is constant at 1 (0 dB) due to a metal ground plane that reflects the entire incident wave. Reflectarray requires only phase control of the element reflection, while in a transmitarray, in addition to phase control, the magnitude of the transmission coefficient must be maintained. The radiating elements enable the conversion of the spherical phase front of feeding to a planar phase front, facilitating the generation of a focused radiation beam with high gain. Transmitarray antennas have great potential across various applications, for example, earth remote sensing, wireless communications, spatial power combining for high-power applications, THz imaging and sensors, and solar energy concentration

(Ahmed H. Abdelrahman and Nayeri, 2017; Kahrilas, 1968; McGrath, 1986).

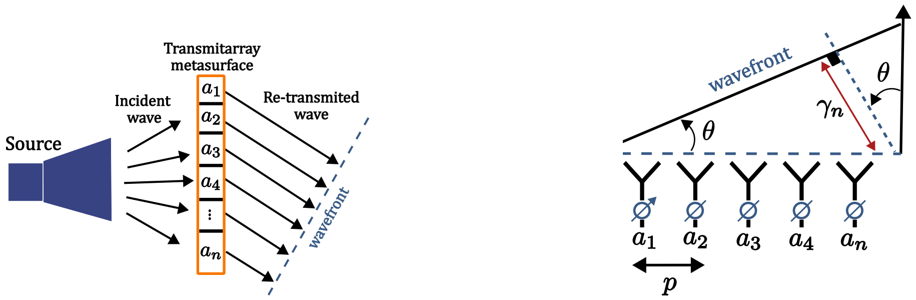

(a)

(b)

Figure 7.1. Transmitarray conceptual illustrations for showing the reshaping of the wavefront, (a) feeding source and the surface with radiating identical elements described by phase object, (b) modeling excitation of each element as phased-array radiators, (Reis et al., 2019)

Specialized feed sources such as horn antennas, microstrip patch antennas, or other UWB antennas are examples employed to illuminate the transmitarrays. Today, transmitarrays and reflectarrays are often designed under multilayer frequency-selective surfaces (FSS) and metasurfaces (Ali, 2022). Various dynamic technologies implants with reconfigurable characteristics enable electronic beamforming or beam steering, frequency tuning, and polarization control. These functionalities are achieved using solid-state electronic devices, including PIN diodes, varactors, MEMS/NEMS switches, tunable dielectric substances such as liquid crystals, microfluidic systems, and graphene (Ali, 2022; Reis et al., 2019). A transmitarray can manipulate the wavefront of both the source antenna and the incident wave. Figure 7.1a illustrates a typical radiation model of a transmitarray fed by a source horn antenna. For the classical multi-cascade approach, the first array layer is called the receiver, illuminated by an incident wave from the feed. The receiver is directly linked to a group of phase shifters responsible for controlling the beam wavefront in the desired direction. These phase shifters are connected to a transmitter layer at their other end, which modulates the incident wave in transmitter mode. As given in Figure 7.1b, each unit cell's phase shifter introduces a path difference of γn (n is integer) to the source point to achieve the desired scan angle θ. The direction of the incident wave is governed by radiation controlled by the transmission phase of the transmitarray. Now, we start the review of the theoretical model for beam-steering in 1D by expressing the phase profile of the n^{th} element as (Ali, 2022; Balanis, 2005)

$$\gamma_n = \frac{2\pi}{\lambda_0} pn \sin\theta = k_\theta pn \sin\theta \tag{7.1}$$

where the specified parameters are given in Figure 7.1b. α_n is transmission phase in the n^{th} element and can be defined as

$$\alpha_n = -\gamma_n + \alpha_0 + 2\pi i, \qquad i = 0, 1, 2, \ldots. \tag{7.2}$$

The re-transmitted wave direction θ as a function of phase difference ψ between adjacent elements, is given as

$$\psi = \alpha_n - \alpha_{n-1} = -\gamma_n + \gamma_{n-1} = -k_0 p \sin\theta. \tag{7.3}$$

By varying the phase of each array (α_n), the incident wave can be steered to a desired direction θ relative to the normal given as

$$\psi = -k_0 p \sin\theta \qquad \leftrightarrow \qquad \theta = -\sin^{-1}\big(\psi \frac{\lambda}{2\pi p}\big). \tag{7.4}$$

Controlling over phase manipulation is crucial when considering the beam-steering requirements of classical phased-array systems. Therefore, each element should have controllable phase variation. We propose employing dynamic control of surface waves on the proposed metasurface to manipulate the phase profile of each adjacent unit cell. This technique offers a practical alternative for phase control by decreasing the complexity of the classical approach since it has only a single layer with fewer and cheaper components rather than multiple stacked layers and expensive phase shifters.

To summarize the relationship between space and surface waves on the metasurface: (i) for a propagating wave ($k_t = \sqrt{k_x^2 + k_{y^2}} < k_0$), the wave impedance is real, resulting in zero reflection and negative refraction without reflection, (ii) for an evanescent wave ($k_t > k_0$), where the wave number is imaginary, the wave impedance is purely imaginary, leading to the excitation of a surface wave along the plane of the surface. The characteristic impedance evanescent wave (e.g., of TM) is capacitive, while it is seen as inductive in front of the other side of the interface. Therefore, we can control the phase of the excited surface wave (β_{sw}) along the surface by adding variable reactive components such as a varactor diode. We can conclude with two of the important outputs for the proposed approach as follows: (i) dynamic control of free-space transmitted/reflected waves by uncomplicated modification of the excited surface wave properties (e.g., phase profile), (ii) the feature to focus the excited fields due to the negative-refraction nature of DNG structures, which provides a lens effect that can be obtained from a flat structure. Thus, we can design the radiating surface with reconfigurable features, which have more directivity and compactness than structures in classical methods. Such surfaces are often called metalens.

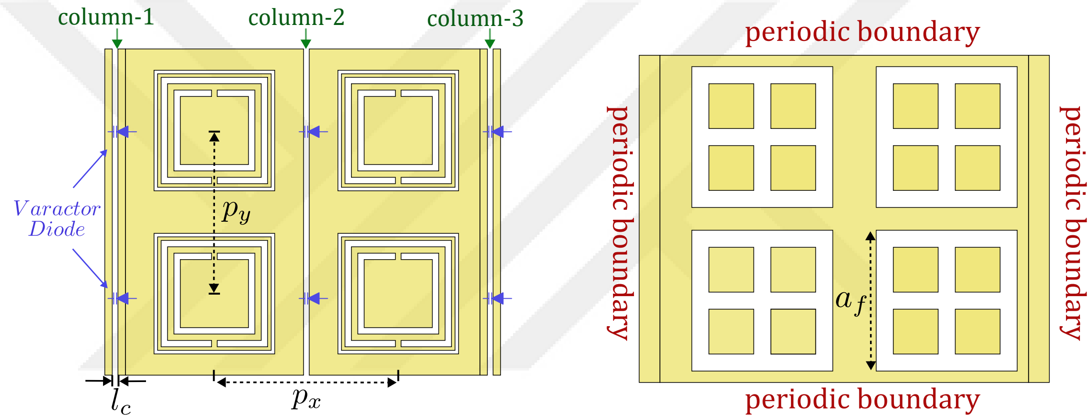

(a) Top face (b) Bottom face

Figure 7.2. Simulation model of 2 × 2 metasurface with variable capacitors configuration and boundary conditions. Design parameters are given as $\epsilon_r = 2.2$ (RT/duroid 5880) $l_c = 0.8mm$, $p_y = 23mm$, $25.9mm$, $a_f = 19.8mm$, $s = w = 0.9mm$, $g = 0.8mm$, $a_g = 0.5mm$, $s_x = s_y = 15mm$.

7.2. Simulation Model of The Dynamic Metalens and Its Eigenmode Solutions

This section presents the reconfigurable design based on the cell analyzed in Chapter 3, and numerical analysis of the surface modes on the 3D model by the CST Eigensolver. For the design, we etched the middle of adjacent cells with identical slits, and the varactor diodes were placed over them to manipulate the surface impedance by a variable lumped capacitor. In this way, the negative DC biasing of the diodes becomes easily possible since each column is now electrically separated from the other. This also makes the dynamic control on metasurfaces less complex. Figure 7.2 displays the top and bottom face of the simulation model for metasurface with 2×2 cells and variable capacitors' placement. Since the boundary conditions on the surface plane are periodic, the simulated surface is assumed to have infinite cells. The slit's capacitor value, as well as the dimension of the diode model, determines the width of the slit.

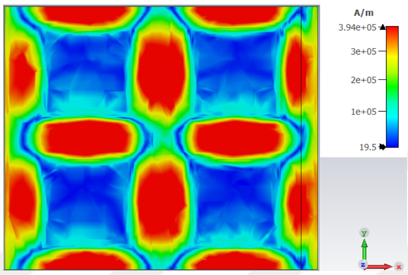

(a) $C_1 = C_3 = 0.3pF$, $C_2 = 0.3pF$

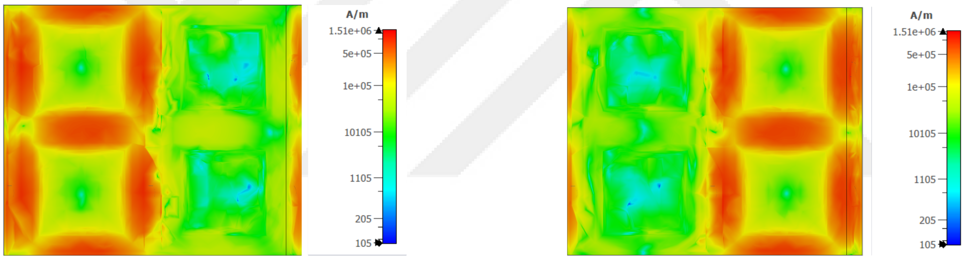

(b) $C_1 = C_3 = 0.8pF$, $C_2 = 1.2pF$

(c) $C_1 = C_3 = 1.2pF$, $C_2 = 0.8pF$

Figure 7.3. The simulation results of magnetic field distribution for C_i variations on a mode around $f_{mode} = 5.5GHz$ solved by CST Eigenmode solver.

We searched the surface modes through the CST Eigenmode solver, aiming for the maximum field concentrated on the lumped variable capacitor. Figure 7.3a shows the magnetic field distribution for one of the desired modes around $5.5GHz$. Figure 7.3b and Figure 7.3c show the magnetic field distribution, demonstrating the manipulated phase profile on the mode by controlling the values of the capacitors in each column. For these three states, the capacitors of each column are adjusted as (i) $C_1 = 0.3pF$, $C_2 = 0.3pF$, (ii) $C_1 = 0.8pF$, $C_2 = 1.2pF$, (iii) $C_1 = 1.2pF$, $C_2 = 0.8pF$. The C_i refers to the value of each capacitor in the ith column. The results indicate phase difference towards each side of the surface wave propagation direction. The analytical solution for the phase variation caused by capacitors in such media excited by the source is complex. Each unit cell contributes to the surface wave transformation of the inhomogeneous incident wave while they then are the re-emitter. So, calculating the phase profile for each neighboring column in the whole structure will be difficult. We make a simulation to analyze each column by monitoring the averaged magnetic field flow through them to address that. Figure 7.4a and Figure 7.4b present the magnitude (A/m) and the relative phase $(^\circ)$ of the average magnetic field on a plane between the adjacent columns. For the given design configuration and varactor diode (Skyworks SMV2019), we can manipulate the adjacent phases up to the 134°. According to Equation 7.4, the steering angle (θ) can reach approximately 48° for the proposed configuration in ideal conditions.

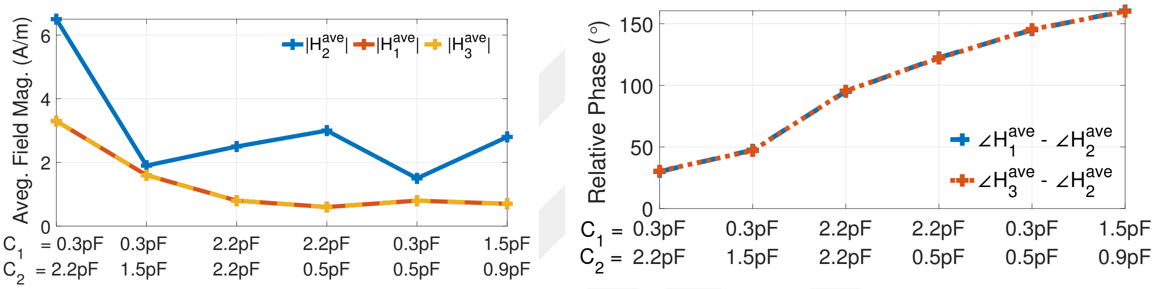

(a) Magnitude (A/m)

(b) Phase $(^\circ)$

Figure 7.4. The results of the average magnetic field on a plane between adjacent columns of 2×2 metasurface with respect to the capacitors variations.

7.3. Beam Steering on The Dynamic MetaLens Antenna

We begin by outlining the design of a 3×4 metasurface positioned at the aperture of a horn antenna, operating within the frequency range of 5.5 GHz to 6.0 GHz. This configuration forms a dynamic metalens (or flat lens) antenna. Additive manufacturing through 3D printer technology was used to fabricate the horn antenna. The conductivity was assigned by conductive tape to the PLA plastic walls of the 3D-printed horn antenna. We present the simulation and experimental findings for the beam-steering application of the proposed structure. Figure 7.5 shows the 3D model and details its dimensions. We performed simulations under open-space boundary conditions. Figure 7.6a displays the electric field distribution within the horn and on the metasurface at 5.8GHz. In addition, Figure 7.6b presents an example radiation pattern in 3D steered towards -30° from a side perspective. These visualizations demonstrate the excitation of the metasurface at the aperture by the horn antenna and the excitation of the desired surface mode for the particular frequency. We numerically optimized the phase profile of unit cells in each column by the variations of capacitor values to allow the beam to be focused at specific angles through elevation for indicated coordinates in Figure 7.6b. Figures 7.7 and Figure 7.7b present the simulation results of the reflection coefficient for variations of capacitor values. The metasurface comprises 3×4 cells, with 5×4 identical capacitor columns. The odd-numbered columns (C_1, C_3, and C_5) are identical to each other, as are the even-numbered columns (C_2 and C_4). These groups are respectively denoted as C_1 and C_2. The magnitude of reflection around 5.8 GHz exhibits slight variations with changes in capacitor values while maintaining impedance matching with reflections ≤ -10 dB. On the other hand, phase results show us the delays in reflections caused by surface wave manipulation due to variations in capacitor values.

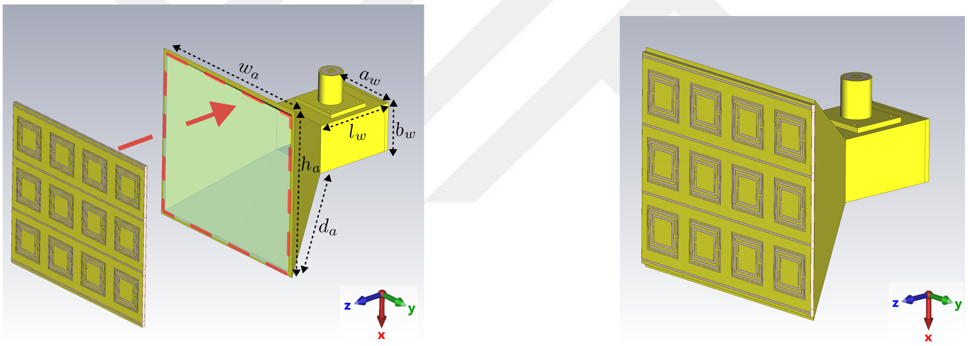

(a) Separated

(b) Combined (metasurface at the aperture)

Figure 7.5. Simulation models for the horn antenna, and metasurface with 3×4 cells. The design parameters are given as $w_{wa} = 91.7mm$, $h_a = 83.7mm$, $d_a = 60mm$, $l_w = 39.3mm$, $a_w = 32mm$ and $b_w = 24$.

We now focus on the directivity radiation pattern on 2D polar coordinates. Figure 7.8 presents simulation results of the directivity patterns (in dB) for variations of capacitor values. The patterns are taken from the cut planes, which correspond to both co-polarization and cross-polarization, and either $\theta = 0°$ or $\phi = 0°$ (see Figure 7.6b for the polar coordinates). For the given configuration and the diode model, we observe in Figure 7.8a as a maximum directivity of $D_{\text{max}} = 13$ dB and maximum steering of $68°$ (as $\pm 34°$) for θ angle when $\phi = 0$. As expected by the proposed design, there is no beam-steering for the ϕ angle, which can be seen in Figure 7.8c. Additionally, Figure 7.8b and Figure 7.8d reveal very low directivity and no beam steering for cross-polarization. It indicates that the proposed antenna configuration is linearly polarized and has the capability of beam-steering in only x-direction.

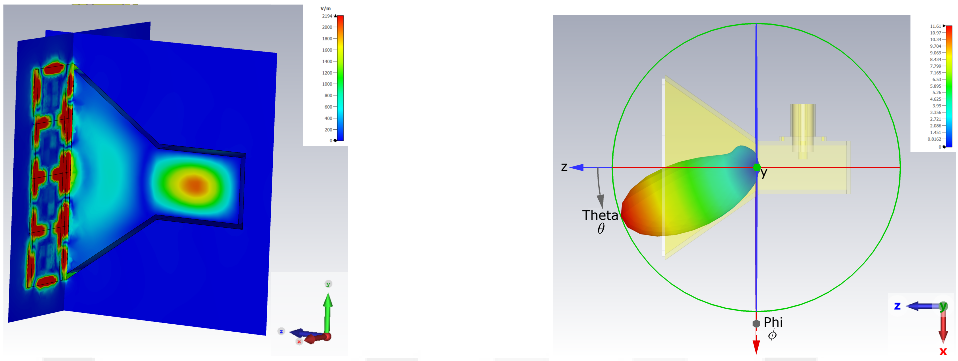

(a) (b)

Figure 7.6. Simulation result of dynamic metasurface supported horn antenna: (a) electric field distribution at 5.8 GHz within horn antenna and on metasurface, (b) an example 3D radiation pattern at $5.8GHz$ directed to $-30°$ from the side perspective.

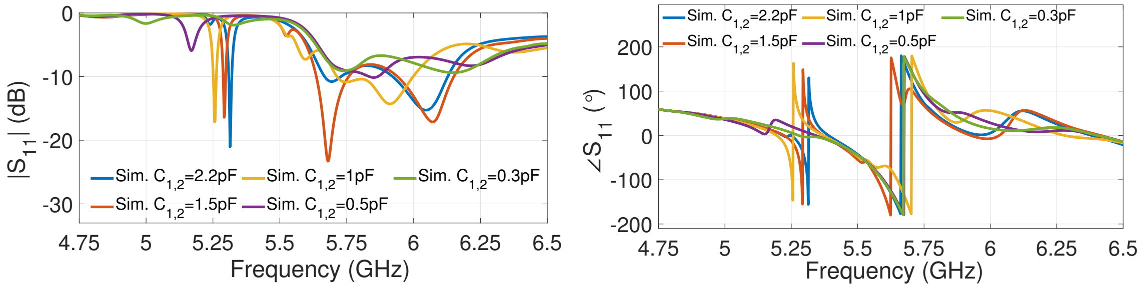

(a) Magnitude (in dB) (b) Phase (°)

Figure 7.7. Simulation results of reflection coefficients with respect to capacitor variations for the metasurface fed by horn antenna.

Figure 7.9 presents the directivity patterns in linear ratio individually for the steering angles of $\pm 34°$, $\pm 27°$, $\pm 20°$, and $\pm 16°$. Those are respectively obtained at frequencies 5.65 GHz, 5.7 GHz, 5.75 GHz, and 5.8 GHz. We can observe the beam-steering functionality achieved either along the frequencies or through active control by variable capacitors at a particular frequency. The proposed surface can be operated for beam-steering applications in active and passive modes across the given spectrum, which might be called a "hybrid" technique. Additionally, we can adjust the wavefront by optimizing numerically for a power divider application. Figure 7.10 illustrates an example radiation pattern where the main lobe is directed to the $\pm 34^\circ$ at $f = 5.65$GHz. Here, we performed approximately dividing the power as $\approx \%45$ to $+33^\circ$ and $\approx \%55$ to -35°.

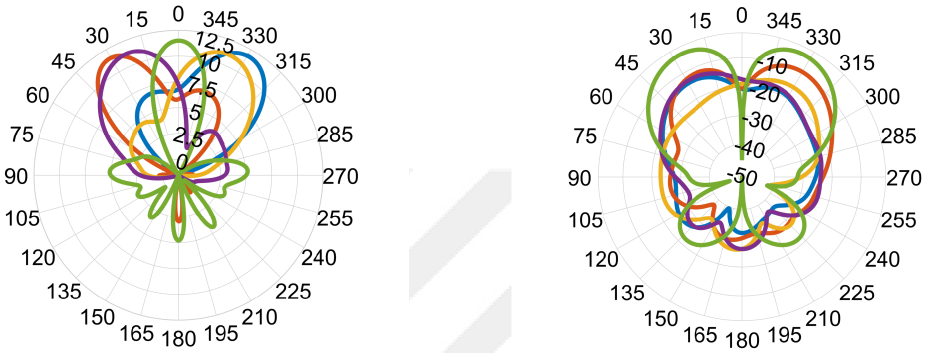

(a) Co-polarization, $\phi = 0$

(b) Cross-polarization, $\phi = 0$

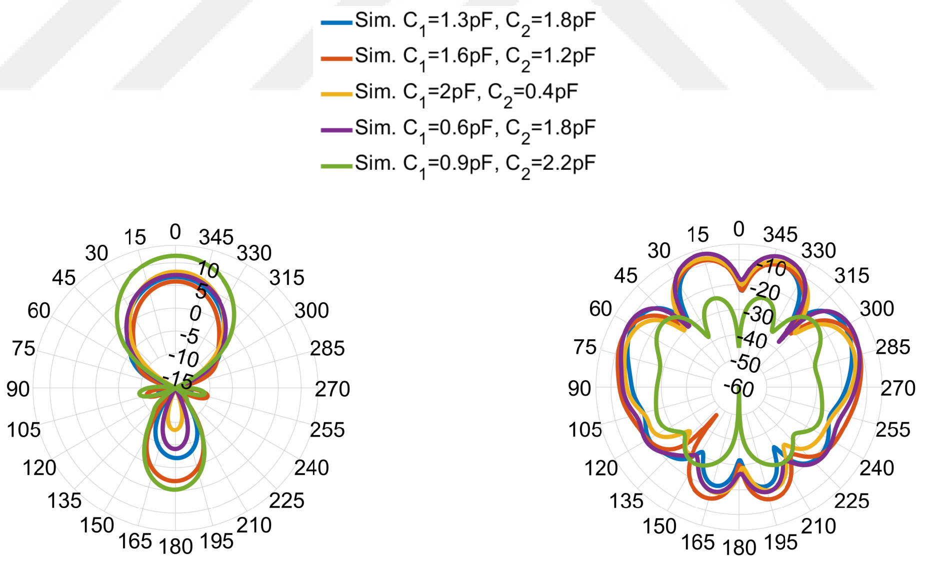

(c) Co-polarization, $\theta = 0$

(d) Cross-polarization, $\theta = 0$

Figure 7.8. Simulation results of radiation directivity patterns in each cut plane for θ and ϕ at $f = 5.65GHz$ with respect to the capacitor variations on the metasurface fed by the horn antenna.

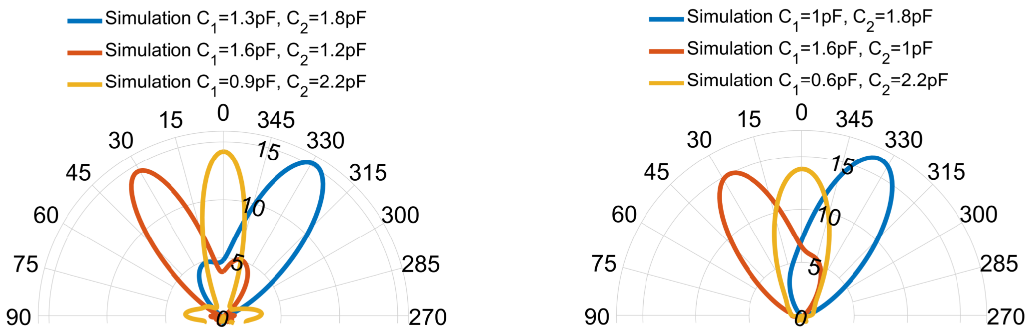

(a) $f = 5.65GHz$, steered at $\theta = \pm 34$ (b) $f = 5.7GHz$, steered at $\theta = \pm 27$

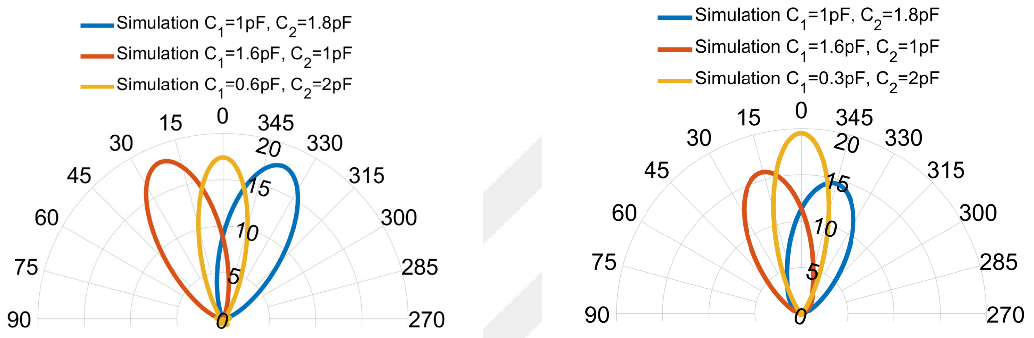

(c) $f = 5.75GHz$, steered at $\theta = \pm 22$ (d) $f = 5.8GHz$, steered at $\theta = \pm 17$

Figure 7.9. Simulation results of directivity patterns through a given spectrum with respect to capacitor variations on the metasurface fed by horn antenna It shows the beam-steering on azimuth angle (ϕ). Maximum directivity is $D_{max} = 13dB$.

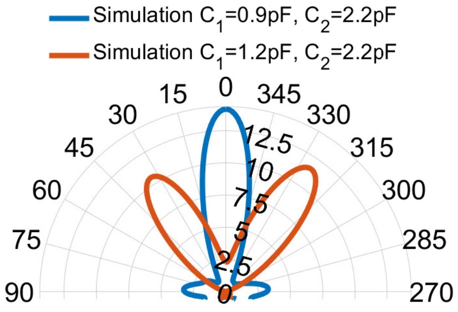

Figure 7.10. Simulation result of directivity pattern that shows power dividing application on the metasurface fed by horn antenna. Power is divided as $\approx \%45$ to $+33°$ and $\approx \%55$ to $-35°$ at $f = 5.65$ GHz.

7.3.1. Experiment Results

We fabricated the simulated model depicted in Figure 7.5 and Figure 7.2 to verify the beam-steering functionality with experiments. Figures 7.11a and 7.11b display pictures of the top and bottom faces, respectively. Figure 7.11c and Figure 7.11d show the metasurface combined with the horn antenna and its setup during measurement with DC control for each column.

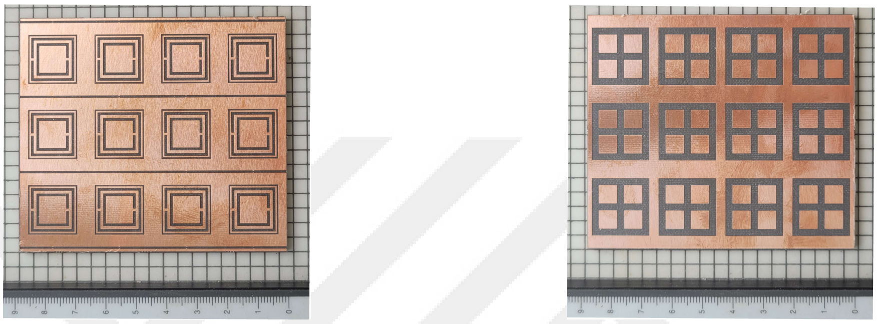

(a) Top face of metasurface

(b) Bottom face of metasurface

(c) Metasurface with soldered diodes combined with horn antenna

(d) On measurement with DC feeds

Figure 7.11. The pictures of manufactured metasurface and horn antenna.

We first measured the reflection coefficients (S_{11}) using the vector network analyzer (VNA HP 8720D). The separate DC feed was supplied for each column as given in Figure 7.11d. Figure 7.12 present S_{11} in magnitude (dB) and phase (degrees), respectively. There is a good impedance matching at frequencies between the 5.75 GHz and 6.0 GHz with return losses ≤ -10 dB for all capacitor combinations as in Figure 7.12a. We observe the manipulations between 5.75 GHz and 5.8 GHz in the measured reflection phases ($\angle S_{11}$) for the capacitor variations in Figure 7.12b. These results are consistent with the simulation results in Figure 7.7.

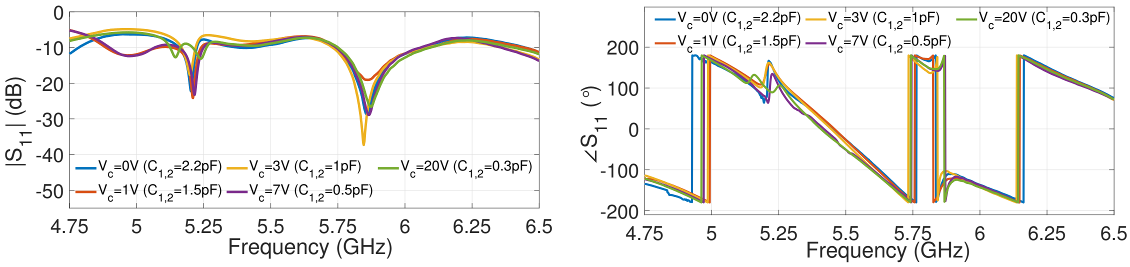

(a) Magnitude (in dB)

(b) Phase (°)

Figure 7.12. Experiment results of reflection coefficients (S_{11}) with respect to capacitor variations for the metasurface fed by horn antenna.

During the reflection (S_{11}) measurement, we faced challenges while adjusting the excitation probe of the SMA connector. A standard SMA model with a flange mount is used. The length and angle of the conductor extension were precisely adjusted empirically. Observed that even slight variations in the angle have a relatively significant effect on the impedance matching and the excitation of the surface mode. It is difficult to maintain consistent probe coupling to the horn waveguide adapter for the entire spectrum as in the simulation. Therefore, the parameters of the coupling probe were adjusted to be impedance-matched at the narrow frequency band around 5.75 GHz. This led to mismatched, i.e., high reflection (S_{11}) values for the remainder of the spectrum. Besides, we observed a low reflection response around 5.25GHz that is not particularly interesting to us since the radiation efficiency was close to zero ($\eta_r \ =\approx\ 0$), where most of the stimulated power was absorbed as losses.

We then measured the gain patterns at 5.75 GHz using the spectrum analyzer (HP 8565E). The radiation patterns in linear scale are given in Figure 7.13 compared with lossy simulation results. Here, we separately display the steering angles for capacitor combinations. The maximum gain was measured at 11.45 dB for the experiment and 11.5 dB for the simulation. We observed a maximum scanning angle of approximately $\pm 22.5^\circ$ so a total of approximately 45°, at 5.75GHz for the experiment and simulation results. There is a consistency between the experiment and simulation results regarding the quantity of gain and the steering angles. However, there are noticeable differences in the radiation patterns between them. As discussed for the reflection measurement, we encountered similar fluctuations while measuring the radiation pattern. During the rotation of the antenna under test, any slight changes in the coupling probe position and angle could have affected the measured power and, consequently, the radiation pattern. We also suppose that the nonlinearity of the varactor diodes and their possible non-identical production could cause inconsistency and fluctuations in radiation patterns. Nevertheless, we have experimentally demonstrated the proposed surface wave-assisted metalens, which offer beam-steering with relatively fewer components and a simpler control schema.

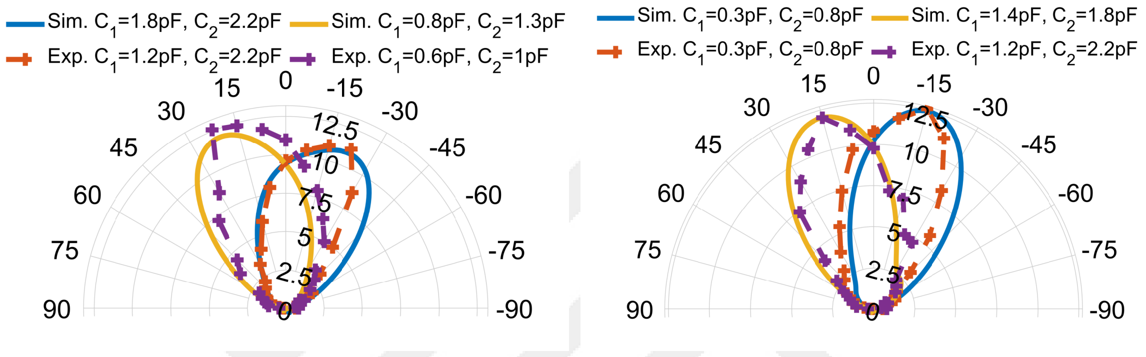

(a) Steered at $\theta = \pm 22.5°$ (b) Steered at $\theta = \pm 15°$

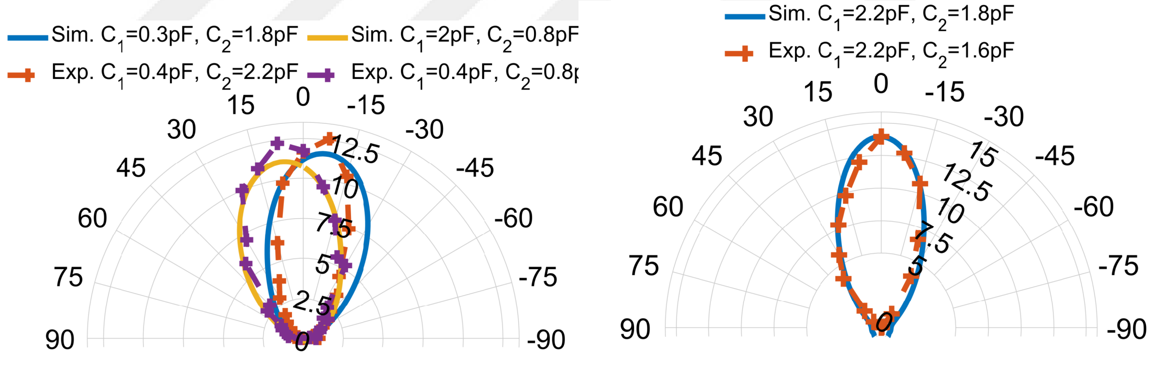

(c) Steered at $\theta = \pm 7.5°$ (d) Steered at $\theta = 0°$

Figure 7.13. Experiment and simulation results of radiation gain patterns at $f = 5.75GHz$ with respect to variations of capacitor values for metasurface fed by horn antenna. Maximum gain is $G_{max} = 11.45dB$ for the experiment and $G_{max} = 11.5dB$ for the simulation.

7.4. Doppler Radar Application

We set up a Doppler radar system to evaluate the performance of the fabricated metasurface-supported horn antenna in a real-time application. This metalens antenna was used as the receiving antenna, while antennas from a previous study were used as the transmitting and reference receiving antennas for comparison (Yılmaz and Yaman, 2020). Figure 7.14a shows a photograph of the pendulum experiment setup with the Doppler radar. In the first experiment, the pendulum was positioned at $0°$ and placed 1 meter from the receiving antenna. Following our previous study, the DNG antenna was used as the transmitter, and the near-zero index (NZI) antenna was used as the reference receiver (Yılmaz and Yaman, 2020). Initial measurements were taken with the NZI antenna for reference, after which the metasurface-supported horn antenna without DC biasing was integrated as a receiving antenna in the same position. Figures 7.14b and 7.14c show the normalized Doppler radar velocity measurements for both receiver antennas. As expected, the pendulum velocity and maximum received power match well for both antennas, given their close maximum gain values in both simulation and measured results.

The next experiment measurements were taken for the dynamic metalens antenna, which was mechanically rotated to angles of $\pm 15°$ and $0°$, while the pendulum position was fixed. For each mechanically rotated angle, the capacitance values in each column were electronically adjusted to antenna be steered approximately $\mp 15°$ during the pendulum experiment measurements. Figure 7.15 presents the measurements of the dynamic antenna, which is steered at $+15°$ and $-15°$ for each mechanical angle. These results show that the resolution and clarity of the pendulum velocity decrease (or increase) due to the reduced (or increased) levels of received power when the beam angle is rotated. The proposed dynamic metalens antenna has been validated both passively and actively in a real-time performance. We encountered similar measurement instabilities as the antenna parameter measurements, which stem from the feeding coupling of a 3D-printed horn antenna due to mechanical rotation. We recorded multiple measurements to obtain stable results. Improvements to the feeding coupling issue will be considered in future work.

(a) Photograph of measurement setup

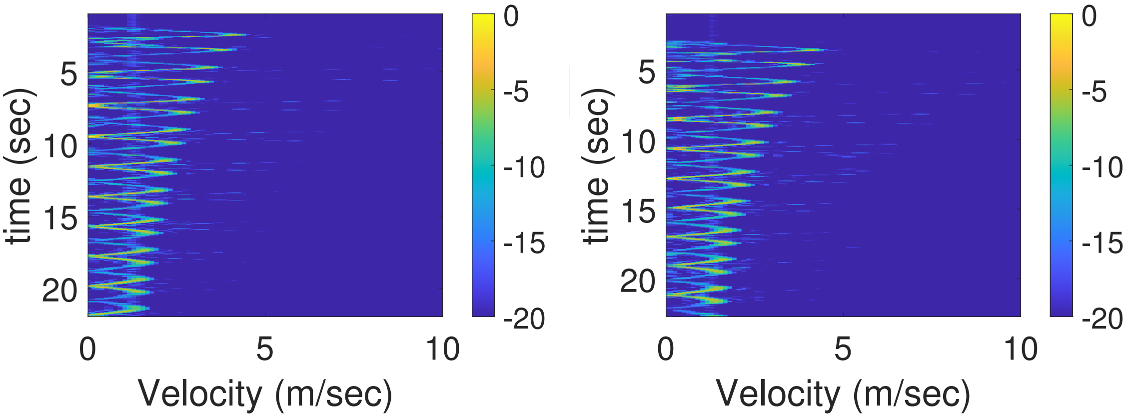

(b) NZI antenna as receiver, steering at $\theta = 0^\circ$

(c) Proposed metasurface horn antenna as receiver, steering at $\theta = 0^\circ$

Figure 7.14. Doppler radar results of pendulum experiment when steering angle and position of pendulum are at 0° when DNG and near-zero index (NZI) antennas in our published study (Yılmaz and Yaman, 2020) are respectively as transmitter and receiver reference.

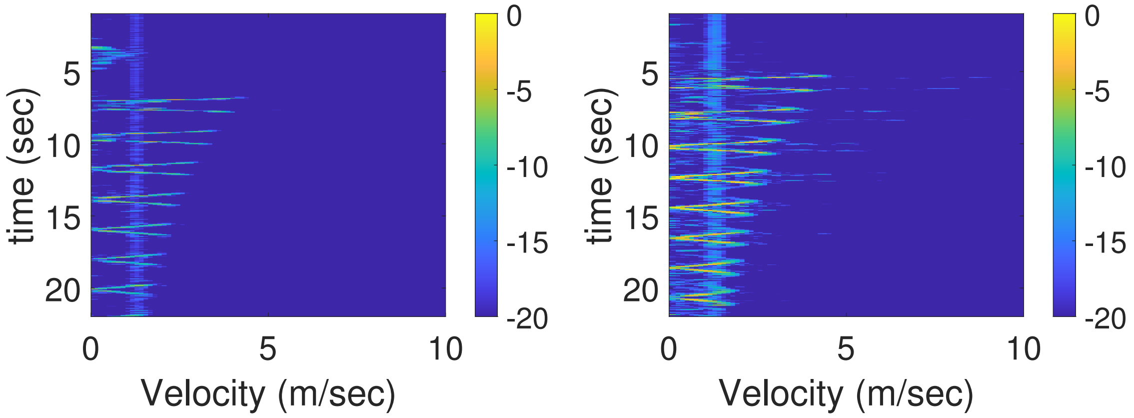

(a) Pendulum at $\theta = -15°$ (b) Pendulum at $\theta = -15°$

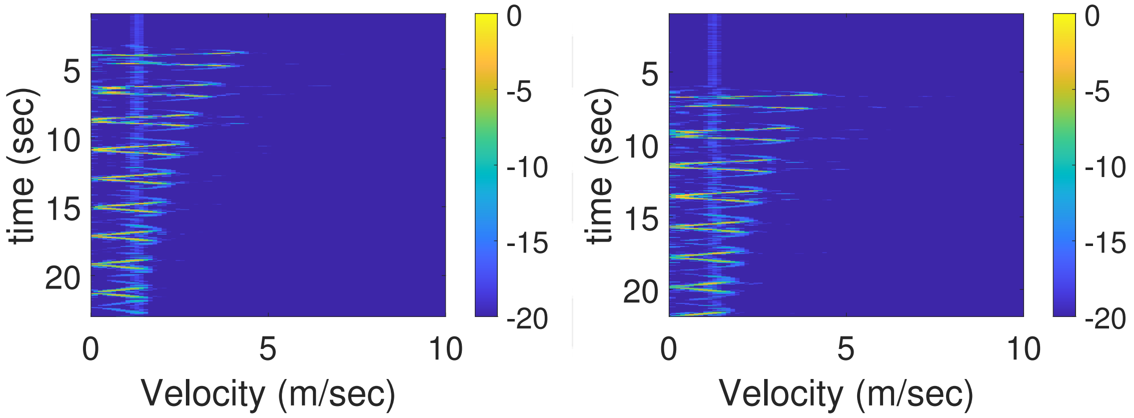

(c) Pendulum at $\theta = 0°$ (d) Pendulum at $\theta = 0°$

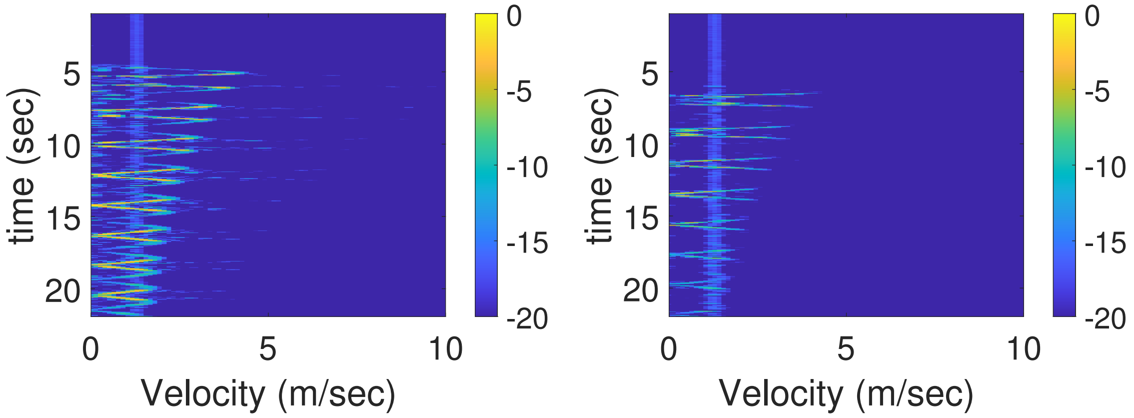

(e) Pendulum at $\theta = +15°$ (f) Pendulum at $\theta = +15°$

Figure 7.15. Pendulum experiment results of the metasurface supported horn antenna at angles $\mp\theta = +15°$ and $\theta = 0°$. Capacitor values (a)-(c) $C_1 = 0.3$ pF, $C_2 = 0.8$ pF, (d)-(f) $C_1 = 1.2$ pF, $C_2 = 2.2$ pF.

CHAPTER 8

CONCLUSIONS AND FUTURE DIRECTION

This thesis investigates surface wave-assisted penetrable metasurfaces applied to nonreciprocity and reconfigurable antenna systems through scattering control. The initial chapters present analytical and numerical solutions for 2D surface wave excitation on penetrable metasurfaces. These results confirm the generation of surface waves on analytically defined metasurfaces, their coupling with the transmission coefficient, and an anti-symmetric phase response that depends on the incident wave's direction. A 3D model was subsequently realized via simulation using a Double Negative (DNG) design approach. Our contribution introduces a design methodology based on bianisotropy, phase conjugate surfaces, and DNG media, providing a comprehensive framework for analyzing and designing such surfaces. An equivalent circuit model was constructed using impedance-based characterization derived from the effective parameters of unit cells via homogenization. The time-domain circuit model was developed by extracting impedances through LC resonators, enabling the numerical solution of time-modulated systems.

The proposed methodology for dynamic transmission manipulation was applied to nonreciprocity and beam-steering applications. The outcomes of these applications were studied through simulations and proof-of-concept experiments. By incorporating time modulation into the unit cell of the bianisotropic metasurface with phase conjugation layers, we introduced a novel approach for achieving nonreciprocal transmission. A 3D model was developed using a penetrable unit cell bounded by a substrate-integrated waveguide (SIW) cavity design, integrating time-varying capacitors via varactor diodes into the cavity mode. The numerical solution for the time-modulated unit cell was carried out on a time-domain circuit model, which now includes a parallel time-varying capacitor within the LC resonance, representing the cavity mode. The Impedance Transfer Transfer Method (ITMM) and Harmonic Balance (HB) numerical techniques were developed to solve this problem. The results were validated through numerical simulations and experiments, demonstrating both phase-coherent and phase-incoherent nonreciprocal transmission. Discussions addressed discrepancies between numerical simulations and practical experiments, focusing on observed and potential limitations, including power requirements, modulation speed of variable capacitors, nonlinearity from semiconductor components, stable phase conditions for extreme isolation, and challenges due to multi-harmonic generation. These insights highlight potential obstacles to a complete metasurface implementation. Satisfying accuracy was achieved in both the dynamic manipulation of transmission coefficients under DC control and in nonreciprocal transmission quantities and phase response for both phase-coherent and phase-incoherent scenarios. Key findings include: (i) under DC control, about 10 dB transmission coefficient manipulation in both experiment and simulations of the 3D model and equivalent circuit model, (ii) for time-modulation in phase-coherent nonreciprocity, maximum isolation of 30 dB in experiments, and 35 dB and 40 dB for ITMM and HB simulations, respectively; and (iii) for time-modulated, phase-incoherent scenarios, minimum isolation of 20 dB in experiments and simulations at $P_{in} \leq -20\text{dBm}$, and a maximum of 60 dB when source and pump signal phases are synchronized. These consistent results were obtained in Vector Network Analyzer (VNA) measurements, with approximately 10 MHz frequency difference in modulation signals. This might be likely the precision of VNA or the small frequency shift ($\mp 0.01\%\omega_m$) due to electron mobility in semiconductors (varactor diodes). To maintain linear isolation behavior for input power (P_{in}) variations, the modulation power (P_{pump}) must be synchronized with the input power, requiring minor tuning for DC biases. Ripples observed in the measured data can be attributed to slight mismatches in phase synchronization. This proposed method and design for nonreciprocity introduces several novelties to the literature, which can be summarized as follows: (i) the integration of bianisotropy, DNG, and complex conjugate impedances in the medium reduces the complexity of space-time modulation techniques for enabling nonreciprocity solely through time modulation, and (ii) a π-phase delay between forward and backward excitation achieves the ideal asymmetric response for extreme isolation; (iii) development of a 3D realization method and model within the microwave spectrum; (iv) creation of an equivalent time-domain circuit model for the unit cell; and (v) development of numerical solutions for time-modulated circuits, with results supported by proof-of-concept experimental data.

In the final chapter, we extended the application of the proposed surface wave-based approach to enable reconfigurable radiation. The focus was on beam-steering of the radiated wavefront by varying the phase of adjacent cells through surface wave manipulation. This approach was demonstrated on a metasurface consisting of a 3×4 cell array, incorporating varactor diodes for phase control and excited by a 3D-printed horn antenna. First, the phase variation in the surface eigenmode of adjacent cells with periodic boundaries was analyzed and optimized via numerical simulations using CST Eigensolver. The metasurface was then implemented on the aperture of a horn antenna for equivalent focal point feeding. Consistent results from both simulations and experiments demonstrated the beam-steering performance, reducing the complexity of traditional approaches. Next, the dynamic meta-lens antenna was integrated into a Doppler radar system for the velocity measurement of a simple pendulum. Results confirmed its real-time beam-steering capabilities and overall antenna gain performance. Discussions focused on the challenges encountered during the transition from theoretical design to practical implementation and measurement difficulties. These challenges include system stability, component limitations (e.g., tuning range of varactor diodes or alternative techniques), and increased metasurface losses due to concentrated surface waves. Adequate accuracy was maintained between simulations and experiments at 5.8 GHz for (i) in reflection loss (S_{11} results, impedance matching (always < -10 dB), phase delays due to dynamic surface wave manipulation; (ii) in gain patterns, maximum gain (11.45 dB and 11.5 dB) and steering angles ($\approx \pm 22.5^\circ$). However, measured gain patterns exhibited asymmetry around the steering angles, likely due to non-identical soldering, diode nonlinearity, and limited measurement sampling. By the developed surface wae assisted dynamic metalens, the contributions to the literature can be summarized as (i) the flat lens property of the DNG slab enhances directivity in a compact structure; (ii) for 1D beam-steering, each column's electrical separation via etched capacitor slits and interconnection by variable capacitors (varactor diodes) significantly simplifies biasing complexity; and (iii) the need for only one variable element between adjacent cells reduces the number of active components.

Future work will focus on integrating nonreciprocity with reconfigurable antenna applications to achieve a nonreciprocal beam-steering metasurface. Key objectives will include reducing the modulation frequency, enhancing system performance, and extending the method to operate at higher frequencies. Additionally, further research will address critical aspects such as integrated modulation feeding schemes, expanding applicability to wider bandwidths, and improving efficiency by minimizing losses.

REFERENCES

A. Li, S. S. and D. Sievenpiper (2018). Metasurfaces and their applications. *Nanophotonics, De Gruyter 7*.

A. Oskooi, D. Roundy, M. I. P. B.-J. J. and S. Johnson (2010). Meep: A flexible free-software package for electromagnetic simulations by the fdtd method. *Computer Physics Communications 181*, 687–702.

A. Serdyukov, I. Semchenko, S. T. and A. Sihvola (2001). *Electromagnetics of bi-anisotropic*. Gordon and Breach Science Publishers.

Achouri, K. and C. Caloz (2021). *Electromagnetic Metasurfaces Theory and Applications*. John Wiley & Sons, Inc.

ADS, K. (2019). *Advanced Design Harmonic Balance Simulation: System 2019 Update 1.0 Release Notes*. Keysight Technologies Incorporated.

Ahmed H. Abdelrahman, Fan Yang, A. Z. E. and P. Nayeri (2017). *Analysis and Design of Transmitarray Antennas*. Morgan & Claypool.

Albooyeh, M. (2015). *Electromagnetic Characterization of Metasurfaces*. Doctoral dissertations, Aalto University Publication Series.

Albooyeh, M., R. Alaee, C. Rockstuhl, and C. Simovski (2015). Revisiting substrate-induced bianisotropy in metasurfaces. *Phy. Rev. B 91*, 195304.

Ali, Q.; Shahzad, W. A. I. S. S.-B. X. A. S. S. H. (2022). Recent developments and challenges on beam steering characteristics of reconfigurable transmitarray antennas. *Electronics 11*(587).

Alu, A. and N. Engheta (2003, Oct.). Pairing an epsilon-negative slabwith a mu-negative slab: Resonance, tunneling and transparency. *IEEE Trans. Antennas Propag. 51*.

Alu, A. and N. Engheta (2006, Jan.). Physical insight into the "growing" evanescent fields of double-negative metamaterial lenses using their circuit equivalence. *IEEE*

Trans. on Antennas and Propagation 54(1), 49–55.

Alvarez-Melcon, A., X. Wu, J. Zang, X. Liu, and J. S. Gomez-Diaz (2019, Dec). Coupling matrix representation of nonreciprocal filters based on time-modulated resonators. *IEEE Trans. on Microwave Theory and Tech. 67*(12), 4751–4763.

Anıl Karatay, Hasan Önder Yılmaz, C. Ö. and F. Yaman (2023, May). Cost-effective experiments with additively manufactured waveguide and cavities in the s-band. *Measurement Science and Technology 34*.

Anthony Grbic, L. J. and R. Merlin (2008). Near-field plates: subdiffraction focusing with patterned surfaces. *Science 320*.

Asadchy, V. (2017). *Spatially dispersive metasurfaces*. Doctoral dissertations, Aalto University Publication Series.

Asadchy, V. S., A. Díaz-Rubio, and S. A. Tretyakov (2018). Bianisotropic metasurfaces: physics and applications. *Nanophotonics 7*(6), 1069–1094.

Ataloglou, V. G., M. Chen, M. Kim, and G. V. Eleftheriades (2021, Jan). Microwave huygens' metasurfaces: Fundamentals and applications. *IEEE Journal of Microwaves 1*(1), 374–388.

B. H. Fong, J. S. Colburn, J. J. O. J. L. V. and D. F. Sievenpiper (Oct. 2010). The reflectarray antenna. *IEEE Trans. Antennas Propag. 58*.

Bahamonde, J. A. (2020). *Non-Reciprocal Acoustic Devices For RF Communications*. Phd. thesis, Columbia University.

Balanis, C. (1989). *Advanced Engineering Electromagnetics*. John Wiley & Sons, Inc.

Balanis, C. A. (2005). *Antenna Theory Analysis and Design* (3rd ed.). John Wiley & Sons, Inc.

Bardin, J., D. Slichter, and D. Reilly (2021). Microwaves in quantum computing. *IEEE Journal of Microwaves 1*(1).

Biolek, D., Z. Kolka, and V. Biolková (2007). Modeling time-varying storage components in pspice.

Bose, J. C. (1897). On a complete apparatus for the study of the properties of electric waves. *The London, Edinburgh and Dublin Philosophical Magazine and Journal of Science 43*.

Bose, J. C. (1898.). On the rotation of plane of polarisation of electric waves by a twisted structure. *Proc. R. Soc. A 63*, 146–152.

Boutry, G.-A. (October 1948). Augustin fresnel: His time, life and work, 1788-1827. *Science Progress 36*.

Budhu, J. and A. Grbic (2021, Oct.). Recent advances in bianisotropic boundary conditions: theory, capabilities, realizations, and applications. *Nanophotonics 10*.

Buskirk, L. V. and C. Hendrix (May 1961). The zone plate as a radio-frequency focusing element. *IRE Transaction Antennas Propagation 9*.

Cardin, A., S. Silva, and S. e. a. Vardeny (2020). Surface-wave-assisted nonreciprocity in spatio-temporally modulated metasurfaces. *Nat Commun 11*, 1469.

Chen, M. (2021). *Design and Applications of Printed-Circuit-Board Huygens' Metasurfaces*. Doctoral dissertations, Department of Electrical and Computer Engineering University of Toronto.

Cheng, D. K. (1983). *Field and Wave Electromagnetics* (1st ed.). Addison-Wesley Publishing Company.

Christophe Caloz, Andrea Alu, S. T. D. S. K. A. and Z.-L. Deck-Leger (2018). Electromagnetic nonreciprocity. *Physical Review Applied 10*(047001).

Cotrufo, M., S. A. Mann, H. Moussa, and A. Alù (2021). Nonlinearity-induced nonreciprocity—part i. *IEEE Trans. on Microwave Theory and Tech. 69*(8), 3569–3583.

D. Berry, R. M. and W. Kennedy (Oct. 2010). Scalar and tensor holographic artificial impedance surfaces. *IEEE Trans. Antennas Propag. 11*.

D. R. Smith, Willie. J. Padilla, D. C. V. N.-N. and S. Schultz (May 2000). Composite medium with simultaneously negative permeability and permittivity. *Pyhsical Review Letters 84*(18).

Epstein, A. and G. V. Eleftheriades (2016). Arbitrary power-conserving field transformations with passive lossless omega-type bianisotropic metasurfaces. *IEEE Trans. on Antennas and Prog. 64*(9), Sept.

Falcone, F., T. Lopetegi, M. A. G. Laso, J. D. Baena, J. Bonache, M. Beruete, R. Marques, F. Martin, and M. Sorolla (2004, Nov). Babinet principle applied to design of metasurfaces and metamaterials. *Phy. Rev. Let. 93*(19).

Golio, M. (2008). *The RF and Microwave Handbook*. CRC Press, Taylor & Francis Group.

Hickie, W. J. (2023). *The Clouds, by Aristophanes*. Blue Heart Publications.

Holloway, C. L. and E. F. Kuester (2016, Nov.). A homogenization technique for obtaining generalized sheet-transition conditions for a metafilm embedded in a magnetodielectric interface. *IEEE Trans. on Antennas and Propagation 64*(11), 4802–4809.

Holloway, C. L., E. F. Kuester, J. A. Gordon, J. O'Hara, J. Booth, and D. R. Smith (2012, Apr). An overview of the theory and applications of metasurfaces: The two-dimensional equivalents of metamaterials. *IEEE Antennas and Prog. Mag. 54*(2), 10–35.

J. B. Pendry, A. J Holden, D. J. R. and J. Stewart (November 1999). Magnetism from conductors and enhanced nonlinear phenomena. *IEEE Transactions on Microwave Theory and Techniques 47*.

J. B. Pendry, A. J. Holden, W. J. S. and I. Youngs (1996). Extremely low frequency plasmons in metallic mesostructures. *Pyhsical Review Letters 76*.

Jaggard, D. L. and R. J. King (1973, Dec). Sensitivity and dynamic range considerations for homodyne detection systems. *Transactions on Instrumentation and Measurement 22*, 331–338.

Jorge R. Zurita-Sánchez, P. H. and J. C. Cervantes-González (2009). Reflection and transmission of a wave incident on a slab with a time-periodic dielectric function $\epsilon(t)$. *Physical Review A 79*(053821).

Kahrilas, P. J. (Nov. 1968). Hapdar 8212: an operational phased array radar. *Proceeding IEEE 56*.

Kodama, T., N. Kikuchi, S. Okamoto, S. Ohno, and S. Tomita (2023, Apr). Spin-current-driven permeability variation for time-varying magnetic metamaterials. *Phys. Rev. Appl. 19*, 044080.

Kodera, T., D. L. Sounas, and C. Caloz (2013). Magnetless nonreciprocal metamaterial (mnm) technology: Application to microwave components. *IEEE Trans. on Microwave Theory and Tech. 61*(3).

Kord, A., D. L. Sounas, and A. Alù (2020). Microwave nonreciprocity. *Proceedings of the IEEE 108*(10), 1728–1758.

Koutserimpas, T. T. and R. Fleury (2018). Nonreciprocal gain in non-hermitian time-floquet systems. *Physical Review Letters 120*(087401).

Lamb, H. (1897). On the reflection and transmission of electric waves by a metallic grating. *Proc. Lond. Math. Soc. 1*(1), 523–546.

Li, J., X. Zhu, C. Shen, X. Peng, and S. A. Cummer (2019, Oct 31). Transfer matrix method for the analysis of space-time-modulated media and systems. *Phys. Rev. B 100*(14), 144311.

Lindman, K. F. (1920). Über eine durch ein isotropes system von spiralförmigen resonatoren erzeugte rotationspolarisation der elektromagnetischen wellen. *Ann. Phys. 368*, 621–644.

Lubkowski, G. (2009). *Simulation of Electromagnetic Fields in Double Negative Metamaterials, Phd. Thesis*. Technischen Universitat Darmstadt.

M. Bozzi, A. Georgiadis, K. W. (2011). Review of substrate-integrated waveguide circuits and antennas. *Microwaves, Antennas & Propagation 5*, 909–920.

Mahmoud, A., A. Davoyan, and N. Engheta (2015). All-passive nonreciprocal metastructure. *Nat Commun 6*, 8359.

Maslovski, S. and S. Tretyakov (2012). Perfect lensing with phase-conjugating surfaces: toward practical realization. *New Journal of Physics 14*, 035007.

Maurizio Bozzi, Marco Pasian, L. P. K. W. (2009, Oct.). On the losses in substrate-integrated waveguides and cavities. *International Journal of Microwave and Wireless Technologies 1*, 395–401.

McGrath, D. (Jan. 1986). Planar three-dimensional constrained lenses. *IEEE Trans. Antennas Propag. 1*.

Mikheeva, E., C. Kyrou, F. Bentata, S. Khadir, S. Cueff, and P. Genevet (2022). Space and time modulations of light with metasurfaces: Recent progress and future prospects. *ACS Photonics 9*(5), 1458–1482.

M.S. Mirmoosa, G.A. Ptitcyn, V. A. and S. Tretyakov (2019). Time-varying reactive elements for extreme accumulation of electromagnetic energy. *Physical Review Applied 11*, 014024.

Munk, B. A. (2000). *Frequency selective surfaces: theory and design*. Wiley.

Nader Engheta, R. W. Z. (2006). *Metamaterials Physics and Engineering Explorations* (1st ed.). John Wiley & Sons, Inc.

Nagulu, A. and H. Krishnaswamy (2021). Non-magnetic non-reciprocal microwave components — state of the art and future directions. *IEEE Journal of Microwaves 1*(1), 447–456.

Nwajana, A. O. and E. R. Obi (2022). A review on siwand its applications tomicrowave components. *Electronics 11*(1160).

Önder Yılmaz, H. and F. Yaman (2022). Reconstructions of effective parameters for a metamaterial antenna via 3d-printed components. *Journal of Electromagnetic Waves and Applications*.

Pendry, J. B. (2000, Oct). Negative refraction makes a perfect lens. *Phys. Rev. Lett. 85*, 3966–3969.

Pietrow, A. (March 2023). Did christiaan huygens need glasses? a study of huygens' telescope equations and tables. *Notes and Records: the Royal Society Journal of the History of Science*.

Popov, V., A. Díaz-Rubio, V. Asadchy, S. Tcvetkova, F. Boust, S. Tretyakov, and S. N. Burokur (2019). Omega bianisotropic metasurface for converting a propagating wave into a surface wave. *Phy. Rev. B 100*(12), 125103.

Pozar, D. M. (2012). *Microwave Engineering* (4rd ed.). John Wiley & Sons, Inc.

Ptitcyn, G. (2021). *On electromagnetics of time-modulated structures*. Doctoral dissertations, Aalto University Publication Series.

Ptitcyn, G., M. S. Mirmoosa, and S. A. Tretyakov (2019). Time-modulated meta-atoms. *Phys. Rev. Research 1*, 023014.

Quevedo-Teruel, O. (2019). An overview of the theory and applications of metasurfaces: The two-dimensional equivalents of metamaterials. *J. Opt 21*(073002).

R. Marqués, F. M. and R. Rafii-El-Idrissi (2002, April). Role of bianisotropy in negative permeability and left-handed metamaterials. *Physical Review B 65*(144440).

Ra'di, Y. and A. Alu (2020). Nonreciprocal wavefront manipulation in synthetically moving metagratings. *Photonics 7*, 28.

Ra'di, Y. and A. Grbic (2016). Magnet-free nonreciprocal bianisotropic metasurfaces. *Phy. Rev. B 94*, 195432.

Reis, J. R., M. Vala, and R. F. S. Caldeirinha (2019). Review paper on transmitarray antennas. *IEEE Access 7*, 94171–94188.

Reiskarimian, N. (2020). *Fully-Integrated Magnetic-Free Nonreciprocal Components by Breaking Lorentz Reciprocity: from Physics to Applications*. Phd. thesis, Columbia University.

Ricardo Marques, F. M. and M. Sorolla (2008). *Metamaterials with Negative Parameters* (1st ed.). John Wiley & Sons, Inc.

Sajjad Taravati, N. C. and C. Caloz (2017, October). Nonreciprocal electromagnetic scattering from a periodically space-time modulated slab and application to a qasisonic isolator. *Physical Review B 96*(165144).

Schelkunoff, S. A. and H. T. Friis (1952). Antennas: theory and practice. *Wiley 639*.

Shaltout, A. M., V. M. Shalaev, and M. L. Brongersma (2019). Spatiotemporal light control with active metasurfaces. *Science 364*(6441), eaat3100.

Shao, L. and W. Zhu (2021, June). Reconfigurable microwave metasurfaces with active lumped elements: A mini review. *Frontiers Materials 8*.

Shen, C., X. Zhu, J. Li, and S. A. Cummer (2019, Aug.). Nonreciprocal acoustic transmission in space-time modulated coupled resonators. *Phys. Rev. B 100*, 054302.

Shi, Y., Y. Z. and S. Fan (2015). Limitations of nonlinear optical isolators due to dynamic reciprocity. *Nature Photon 9*, 388–392.

Shurcliff, W. A. (1962). *Polarized Light Production and Use*. Harvard University Press.

Sievenpiper, D. F. (1999). *High-Impedance Electromagnetic Surfaces*. Ph. D. thesis.

Sihvola, A. (2007). Metamaterials in electromagnetics. *Metamaterials 1*(1), 2–11.

Simovski, C. (2018). *Composite Media with Weak Spatial Dispersion*. Taylor & Francis Group, Pan Stanford Publishing.

Smith, D. R., J. Gollub, J. J. Mock, W. J. Padilla, and D. Schurig (2006, 07). Calculation and measurement of bianisotropy in a split ring resonator metamaterial. *Journal of Applied Physics 100*(2), 024507.

Smith, D. R., W. J. Padilla, D. C. Vier, S. C. Nemat-Nasser, and S. Schultz (2000, May). Composite medium with simultaneously negative permeability and permittivity. *Phys. Rev. Lett. 84*, 4184–4187.

Smith, D. R. and J. B. Pendry (2006, Mar). Homogenization of metamaterials by field averaging. *J. Opt. Soc. Am. B 23*(3), 391–403.

Smith, D. R. and J. B. Pendry (2011). First-principles homogenization theory for periodic metamaterials. *Physical Review B 84*(075153).

Sounas, D. L. and A. Alù (2018). Nonreciprocity based on nonlinear resonances. *IEEE Antenna and Wireless Prop. Let. 17*(11).

Taravati, S. and G. Eleftheriades (2020). Full-duplex nonreciprocal beam steering by time-modulated phase-gradient metasurfaces. *Phys. Rev. App. 14*, 014027.

Taravati, S. and G. Eleftheriades (2021). Full-duplex reflective beamsteering metasurface featuring magnetless nonreciprocal amplification. *Nat Commun 12*, 4414.

Taravati, S. and G. V. Eleftheriades (2022). Microwave space-time-modulated metasurfaces. *ACS Photonics 9*(2), 305–318.

Taravati, S. and A. Kishk (2020). Space-time modulation: Principles and applications. *IEEE Microwave Magazine 21*(4), 30–56.

Tcvetkova, S. (2019). *Metasurfaces For Wave Conversions*. Doctoral dissertations, Aalto University Publication Series.

Tcvetkova, S. N., D. H. Kwon, A. Díaz-Rubio, and S. A. Tretyakov (2018). Near-perfect conversion of a propagating plane wave into a surface wave using metasurfaces. *Phys. Rev. B 97*, 115447.

Tcvetkova, S. N., S. Maci, and S. A. Tretyakov (2019). Exact solution for surface wave to space wave conversion by periodical impenetrable metasurfaces. *IEEE Trans. on Antennas and Prog. 67*(5), May.

Tianshuo Qiu, Jiafu Wang, Y. L. Y. M. M. Y. and S. Qu (2020). Emulating nonreciprocity via direction-dependent excitation of spoof surface plasmon polaritons. *J. Phys. D: Appl. Phys. 53*.

V. Popov, A. Díaz-Rubio, V. A. S. T. F. B. e. a. (2016). Synthesis of passive lossless metasurfaces using auxiliary fields for reflectionless beam splitting and perfect reflection. *Phy. Rev. Letters 117*(256103).

V. S. Asadchy, M. S. Mirmoosa, A. D.-R. S. F. and S. A. Tretyakov (2020, Oct.). Tutorial on electromagnetic nonreciprocity and its origins. *Proceedings of the IEEE 108*(10), 1684–1727.

Vardaxoglou, Y. J. C. (2017). Additive manufacturing of meta-atoms for microwave structures. *2017 International Conference on Electromagnetics in Advanced Applications (ICEAA)*, 1836–1838.

Vehmas, J. (2015). *Transmission-Line Metamaterials, Bianisotropy, and Transmission-Line Bianisotropy*. Doctoral dissertations, Aalto University Publication Series.

Veselago, V. G. (1968). The electrodynamics of substances with simulatenously negative values of ϵ and μ. *Soviet Physics Uspekhi 10*.

Wang, X. (2020). *Surface-impedance engineering for advanced wave transformations*. Doctoral dissertations, Aalto University Publication Series.

Wang, X., G. Ptitcyn, V. S. Asadchy, A. Diaz Rubio, M. S. Mirmoosa, S. Fan, and S. A. Tretyakov (2020). Nonreciprocity in bianisotropic systems with uniform time modulation. *Phys. Rev. Lett. 125*, 266102.

Yılmaz, H. Ö. and F. Yaman (2024, 08). Nonreciprocal transmission enabled by time modulation of penetrable metasurface assisted by surface waves. *Journal of Applied Physics 136*(7), 073105.

Yılmaz, H. Ö. and F. Yaman (Apr. 2020). Metamaterial antenna designs for a 5.8-ghz doppler radar. *IEEE Trans. on Instrumentation and Meas. 69*(4), 1775–1782.

Zang, J., D. Correas-Serrano, J. Do, X. Liu, A. Alvarez-Melcon, and J. Gomez-Diaz

(2019). Nonreciprocal wavefront engineering with time-modulated gradient metasurfaces. *Phys. Rev. App. 11*, 054054.

Ziolkowski, R. W. and E. Heyman (October 2001). Wave propagation in media having negative permittivity and permeability. *PHYSICAL REVIEW E, 64*.

Önder Yılmaz, H. (2018, December). Metamaterial antenna design for 5.8 ghz doppler radar.

VITA

EDUCATION

2019 - 2024

Doctor of Philosophy in Electrical and Electronics Engineering

Izmir Institute of Technology

Thesis Title: *Active Metasurface Designs For Tunable Scattering Properties*

Supervisor: Prof. Dr. Mustafa Aziz Altınkaya

Co-Supervisor: Assoc. Prof. Dr. Fatih Yaman

2017 - 2019

Master of Science in Electrical and Electronics Engineering

Izmir Institute of Technology

Thesis Title: *Metamaterial Antenna Design For 5.8 GHz Doppler Radar*

Supervisor: Assoc. Prof. Dr. Fatih Yaman

2009 - 2014

Bachelor of Science in Electrical and Electronics Engineering

Dokuz Eylül University

PUBLICATIONS

Yılmaz, Hasan Önder, and Fatih Yaman. "Nonreciprocal Transmission Enabled by Time Modulation of Penetrable Metasurface Assisted by Surface Waves." *Journal of Applied Physics*, 21 August 2024, 136(7): 073105.

Karatay, Anıl, Hasan Önder Yılmaz, C. Ö., and Fatih Yaman. "Cost-Effective Experiments with Additively Manufactured Waveguide and Cavities in the S-Band." *Measurement Science and Technology*, 34, May 2023.

Yılmaz, Hasan Önder, and Fatih Yaman. "Reconstructions of Effective Parameters for a Metamaterial Antenna via 3D-Printed Components." *Journal of Electromagnetic Waves and Applications*, 2022.

Yılmaz, Hasan Önder, and Fatih Yaman. "Metamaterial Antenna Designs for a 5.8-GHz Doppler Radar." *IEEE Transactions on Instrumentation and Measurement*, vol. 69, no. 4, pp. 1775-1782, April 2020.